Controlled Hydrolysis and Solid State Chemistry: Two Approaches to the Synthesis of Actinide Oxide Materials

A thesis submitted to The University of Manchester for the degree of Doctor of Philosophy (PhD) in the Faculty of Engineering and Physical Sciences

2013

Carlos De La Fontaine

School of Chemistry

Table of Contents

Abstract 18

Declaration 19

Copyright statement 19

Acknowledgments 20

Thesis structure 21

Chapter 1: INTRODUCTION 22

1. NUCLEAR FUEL CYCLE 23

1.1. Mining 23

1.2. Conversion 24

1.3. Enrichment 24

1.4. Fuel fabrication 24

1.5. The nuclear reactor 24

1.6. Used fuel storage 25

1.7. Reprocessing 25

1.8. Final Disposal 26

2. GENERAL PROPERTIES/CHEMISTRY OF ACTINIDES 26

2.1. *f*-orbitals 29

2.2. Actinides oxidation states 29

3. CERAMIC WASTEFORMS 30

3.1. Oxide pyrochlores 33

3.2. The pyrochlore structure 33

3.3. Diversity of pyrochlore compositions 34

3.4. The zirconolite structure 35

3.5. Monoclinic (2M,4M) and hexagonal (3T) zirconolite structures 35-37

4. ACTINIDE HYDROLYSIS 38

4.1. Actinide metal ions in aqueous media 39

4.2. Hydrolysis of tetravalent actinides 40

4.2.1. Thorium hydrolysis 42

4.2.2. Uranium (IV) hydrolysis 44

4.2.3. Neptunium (IV) and plutonium (IV) hydrolysis 44

4.3. Metal alkoxides 44

4.3.1. Actinide alkoxides 45

5. PROJECT AIMS 47

5.1. Solid state project aim 47

5.2. Solution Chemistry Project Objectives 48

5.2.1. Controlled hydrolysis using a caping ligand in aqueous solution 48

5.2.2. Controlled hydrolysis from metal organic compounds 50

5.10. Actinide alkoxides as precursors for ceramics 51

6. ACTINIDE ALKOXIDES AS PRECURSORS FOR CERAMICS 51

6.1. Sol-Gel Process 52

7. REFERENCES 55

Chapter 2: EXPERIMENTAL TECHNIQUES AND METHODS 60

1. DIFFRACTION TECHNIQUES 61

1.1. Production of X-rays 61

1.2. X-raydiffraction (XRD) 61

1.3. Powder XRD 62

1.4. Neutron Diffraction (ND) 63

1.5. Data Processing 63

2. TRANSMISSION ELECTRON MICROSCOPY (TEM) 67

3. X-RAY ABSORPTION SPECTROSCOPY (XAS) 67

3.1. Principles of X-ray absorption spectroscopy 67

3.2. X-ray Absorption 68

4. SCANNING ELECTRON MICROSCOPY (SEM) 70

4.1. Principles of SEM 70

5. MÖSSBAUER SPECTROSCOPY 71

6. NUCLEAR MAGNETIC RESONANCE (NMR) 74

6.1. Spin 74

6.2. Nuclei with Spin 74

6.3. Transitions 75

6.4. Chemical Shift 75

6.5. Spin-Spin Coupling 76

7. UV-VIS SPECTROSCOPY 77

8. RAMAN SPECTROSCOPY 78

9. ERROR ESTIMATION 79

9.1. Gaussian distribution 79

9.2. Weighed averages 80

9.3. Least-squares fitting 81

9.3.1. Simple guideline to evaluate measurements results 81

10. REFERENCES 82

Chapter 3: SYNTHESIS AND CHARACTERISATION OF A POSSIBLE HOST FOR TETRAVALENT ACTINIDES: $Y_{2-x}Ce_xTi_{2-x}Fe_xO_7$ 83

1. INTRODUCTION 84

1.1. The pyrochlore structure 84

1.2. The zirconolite structure 85

1.3. $Y_{2-x}Ce_xTi_{2-x}Fe_xO_7$ 86

2. EXPERIMENTAL PROCEDURE 87

3. RESULTS AND DISCUSSION 89

3.1. X-ray diffraction data 89

3.2. Scanning electron microscopy (SEM) 92

3.3. Mössbauer data 94

3.4. Raman Spectroscopy 96

3.5. Structural refinement 100

3.5.1. Pyrochlore solid solution: $Y_{1-x}Ce_xTi_{1-x}Fe_xO_7$ with x = 0.1 100

3.5.2. Zirconolite-3T structure: $Y_{2-x}Ce_xTi_{2-x}Fe_xO_7$ with x = 0.6 103

4. CONCLUSION 111

5. FUTURE WORK 111

6. REFERENCES 112

Chapter 4 : SYNTHESIS AND CHARACTERISATION OF NEW PYROCHLORE ZIRCONOLITE SOLID SOLUTIONS FOR ACTINIDE IMMOBILISATION: $Y_2Ti_{2-2x}Fe_xNb_xO_7$ 115

1. INTRODUCTION 116

1.1. The zirconolite structure 116

1.2. The pyrochlore structure 117

1.3. $Y_2Ti_{2-2x}Fe_xNb_xO_7$ 118

2. EXPERIMENTAL PROCEDURES 119

3. RESULTS AND DISCUSSION 121

3.1. Powder X-ray diffraction 121

3.2. Scanning electron microscopy (SEM) 124

3.3. Transmission electron microscopy (TEM) 127

3.4. ^{57}Fe Mössbauer spectroscopy 130

3.5. X-ray absorption spectroscopy (XAS) 132

3.6. Raman spectroscopy 133

3.7. Structural refinement 137

3.7.1. Pyrochlore solid solution: $Y_2Ti_{2-2x}Fe_xNb_xO_7$ with $0.0 < x < 0.5$ 137

3.7.2. Zirconolite-3T structure: $Y_2Ti_{2-2x}Fe_xNb_xO_7$ with x = 0.7 143

3.8. Magnetic properties 152

4. CONCLUSION 154

5. FURTHER WORK 154

6. REFERENCES 155

Chapter 5: OLIGOMERIC COMPLEXES OF ACTINIDES FORMED THROUGH LIGAND CONTROLLED HYDROLYSIS AND THE PREPARATION OF A NOVEL URANIUM (IV) IODO ISOPROPOXIDE ISOPROPANOL 158

1. INTRODUCTION 159

2. EXPERIMENTAL PROCEDURES 162

3. RESULTS AND DISCUSSION 166

3.1. Potentiometric results 166

3.2. NMR Spectroscopy 170

3.3. UV-vis-nIR Spectroscopy 190

3.4. Synthesis and Characterisation of $[UI(O\text{-}i\text{-}Pr)_2.(HO\text{-}i\text{-}Pr)_4]I$ 197

4. CONCLUSION 203

5. FURTHER WORK 204

6. REFERENCES 205

Chapter 6: CONCLUSION AND SUGGESTIONS FOR FURTHER WORK 207

CONLUSION 208

FURTHER WORK 210

EXTERNAL CONTRIBUTIONS 210

List of Figures

Chapter 1

Figure 1: Nuclear fuel cycle in the UK. 26

Figure 2: Shape of the f-orbitals generated by solving the Schrödinger equation. 29

Figure 3: Oxidation states of actinides as bare ions and in their compounds. 30

Figure 4: Schematic of trans-dioxo actinides. 30

Figure 5: Relative radiotoxicity on inhalation of a spent fuel with a burnup of 38 megawatt days/kg U over a geological time scale. 31

Figure 6: Simplified schemes of the fluorite a), and, pyrochlore b) structures. Yellow and blue atoms represent cations, red atoms represent anions (O^{2-}or F^{-} for example). 34

Figure 7: Schematic of a 2M polytype zirconolite structure ($CaZrTi_2O_7$) (Coordination number is showed next to the atoms and HTB i.e. hexagonal tungsten bronze type motif). 36

Figure 8: Structure of $Y_2Ti_{0.6}Fe_{0.7}Nb_{0.7}O_7$. Single hexagonal tungsten bronze layer projected down c-axis. Y sites (N.C = 6) are shown by magenta, Ti/Fe (N.C = 6) sites are shown in red, and Fe (N.C = 5) sites are shown in orange. Oxygen anions are shown by blue spheres. (Fe (5) sites are shown at 50% occupancy). 37

Figure 9: Nature of ligand (H_2O) in the coordination sphere depending on ion charge (Z) and pH. 39

Figure 10: Schematic of the start of hydrolysis for plutonium (III), (IV), (V), and (VI) over the whole pH range. 40

Figure 11: Solubility of tetravalent actinides (Th, U, Np and Pu) at ionic strengths < 0.12 M. 41

Figure 12: Percentage distribution of Th(IV) at r.t and 1M NaClO4. Cth: a) 0.12 mM, b) 0.01 mM. Numbers in brackets correspond to the stoichiometry of the compound. The first number correspond to the number of metal centres: Th^{4+} in the compound, the second number correspond to the number of ligands: A- and the last to the number of hydroxyls: 43

HO-

Figure 13: Schematic of the main synthetic routes leading to metal alkoxide complexes (-X= halide and -R= alkyl, aryl groups). 45

Figure 14: Schematic possible structures of $[Th(H_2O)_9]$, $[Th(H_2O)_5(heidi)]^+$and $[Th(H_2O)(heidi)_2]^{4-}$. 49

Figure 15: a) $[(UO_2)(C_7H_3NO_4)]$ cluster and b) three-dimensional sheet of $[(UO_2)(C_7H_3NO_4)]$. Black lines are the 2,6-pyridinecarboxylic acid and the polyhedra are the uranium pentagonal bipyramids. 49

Figure 16: $[Pu_{38}O_{56}Cl_{54}(H_2O)_8]^{14-}$ cluster, where Pu(IV) (green), O_2^- (red), O from water (blue), Cl^- (yellow). 50

Figure 17: Scheme of the hydrolysis of a dimeric zirconium alkoxide *via* controlled hydrolysis. 51

Figure 18: Scheme for a possible sol-gel process. 52

Figure 19: Cubic pyrochlore structure from the $Gd_{2-2x}Bi2_xTi_2O_7$ showing Ti octahedral sites and Gd/Bi cations channels. Material obtained via a sol-gel route. 53

Chapter 2

Figure 1: Illustration of the Bragg law. 62

Figure 2: Steps followed to perform Rietveld analysis. 66

Figure 3: Illustration of the absorption edge labelling according to the electron shell. 69

Figure 4: Schematics of typical XAS absorption profiles. 70

Figure 5: Simple Mössbauer spectrum from identical source and absorber. 72

Figure 6: Resonant overlap, E_R represents the recoil energy, E_D illustrate the spread of values due to the Doppler Effect. 72

Figure 7: Absorption peak where source and absorber are identical. 73

Figure 8: Quadrupole splitting for I = 3/2 74

Figure 9: Schematic of the interaction of a photon with matter 79

Figure 10: Histogram for measurements of the same quantity. The curve is the data Gaussian distribution. 80

Chapter 3

Figure 1: Schematic representations of the crystal structures of (a) $AX_{1.75}$ defect fluorite, (b) $A_2B_2X_7$ pyrochlore, and (c) A_2X_3 C-type structures, projected along the [100] direction. Red spheres represent X anions, green spheres represent A cations, blue spheres represent B cations, and small black spheres represent anion vacancies. 85

Figure 2: Schematic of a 2M polytype zirconolite structure ($CaZrTi_2O_7$). Coordination number of cation site is showed next to the atoms. 86

Figure 3: Normalised X-Ray diffraction data of $Y_{2-x}Ce_xTi_{2-x}Fe_xO_7$. 90

Figure 4: Indexed XRD patterns of $Y_{2-x}Ce_xTi_{2-x}Fe_xO_7$, a) x = 0.1 (pyrochlore) and b) x = 0.6 (zirconolite-3T). 91

Figure 5: Secondary (left) and backscattered (right) electron micrographs representative of all specimen. 93

Figure 6: Room temperature ^{57}Fe Mössbauer spectrum of a) x = 0.1 sample (cubic pyrochlore) and b) x = 0.6 sample (hexagonal 3T-zirconolite). 95

Figure 7: Raman spectra of $Y_{2-x}Ce_xTi_{2-x}Fe_xO_7$ for x = 0 (violet), x = 0.1 (blue), x = 0.2 (red) and x = 0.3 (green). 98

Figure 8: Raman spectra of $Y_{1.6}Ce_{0.4}Ti_{1.6}Fe_{0.4}O_7$. 99

Figure 9: Raman spectra of x=0.8 where the blue line represents a fluorite structure (CeO_2) and the green a zirconolite lattice (yttria-titanate-oxide). 100

Figure 10: Showing fit (solid line) to high resolution neutron diffraction data (points) for $Y_{1.9}Ce_{0.1}Ti_{1.9}Fe_{0.3}Nb_{0.1}O_7$ (x = 0.1) at 25 °C in space group Fd-3m; tick marks show allowed reflections, the difference profile (lower solid line) demonstrates a good fit to the data, R_{wp} = 5.60% and χ^2 = 3.91 %. 103

Figure 11: Showing fit (solid line) to high resolution neutron diffraction data (points) for $Y_{1.4}Ce_{0.6}Ti_{1.4}Fe_{0.6}O_7$ (x = 0.6) at 25 °C in space group $P3_12_1$; tick marks show allowed reflections, for pyrochlore (red markers) and zirconolite 3T (black markers), the difference profile (lower solid line) demonstrates an adequate fit to the data. 109

Figure 12: Schematic representation of refined structural model for: Ln1(8), Ln2(8) and Ln3(7) sites are denoted by gold, green and yellow spheres, respectively; M1(6), M2(6) and M3(4) sites are shown by magenta, red and orange polyhedra, respectively; oxygen anions are shown by blue spheres. Note M3(4) sites are shown at 50% occupancy. 110

Chapter 4

Figure 1: Schematic of a 2M polytype zirconolite structure ($CaZrTi_2O_7$) Coordination number of cation site is showed next to the atoms). 117

Figure 2: Schematic representations of the crystal structures of (a) $AX_{1.75}$ defect fluorite, (b) $A_2B_2X_7$ pyrochlore, and (c) A_2X_3 C-type structures, projected along the [100] direction. Red spheres represent X anions, green spheres represent A cations, blue spheres represent B cations, and small black spheres represent anion vacancies. 118

Figure 3: Normalised X-Ray diffraction data of $Y_2Ti_{2-2x}Fe_xNb_xO_7$. 122

Figure 4: Indexed XRD patterns of $Y_2Ti_{2-2x}Fe_xNb_xO_7$, a) x = 0.2 (pyrochlore) a) and b) x = 0.7 (zirconolite-3T). 123

Figure 5: Secondary (left) and backscattered (right) electron micrographs representative of all specimen. From top to bottom: pyrochlore compositions $Y_2Ti_{1.8}Fe_{0.1}Nb_{0.1}O_7$ and $Y_2Ti_{1.2}Fe_{0.4}Nb_{0.4}O_7$, a biphasic composition $Y_2Ti_{0.8}Fe_{0.6}Nb_{0.6}O_7$, a zirconolite-3T sample $Y_2Ti_{0.4}Fe_{0.8}Nb_{0.8}O_7$ and Y_2FeNbO_7. 125, 126

Figure 6: Selected a) [110], b) [111], c) [112], and d) [113] zone axis diffraction patterns for $Y_2Ti_{1.4}Fe_{0.3}Nb_{0.3}O_7$ (x = 0.3). Patterns indexed assuming the space group and atomic positions from Harvey *et.al.* 128

Figure 7: Selected a) [001], b) [110], c) [112], and d) [121] zone axis diffraction patterns for $Y_2Ti_{0.8}Fe_{0.7}Nb_{0.7}O_7$ (x = 0.7). Patterns indexed assuming the space group and atomic positions from Mazzi and Munno. 129

Figure 8: Room temperature ^{57}Fe Mössbauer spectrum of a) x = 0.3 sample (cubic pyrochlore) and b) x = 0.7 sample (hexagonal 3T-zirconolite). 130

Figure 9: Fe K-edge XANES spectra of FeO, Fe_2O_3 and x = 0.3 composition. 133

Figure 10: Raman spectra of the pyrochlore samples. 134

Figure 11: Raman spectra of $Y_2Ti_{0.4}Fe_{0.8}Nb_{0.8}O_{7.}$ 136

Figure 12: Showing fit (solid line) to high resolution neutron diffraction data (points) for $Y_2Ti_{1.4}Fe_{0.3}Nb_{0.3}O_7$ (x = 0.3) at 25 °C in space group Fd-3m; tick marks show allowed reflections, the difference profile (lower solid line) demonstrates a good fit to the data. 138

Figure 13: Variation of unit cell a-parameter with nominal composition (x) in the $Y_2Ti_{2-2x}Fe_xNb_xO_7$ pyrochlore solid solution (space group Fd-3m) determined from Rietveld analysis of neutron powder diffraction data. Error bars represent 3 esds and are smaller than the data points. 139

Figure 14: Variation of unit cell x- co-ordinate of O1 atom (at the 48f oxygen position) with nominal composition (x) in the $Y_2Ti_{2-2x}Fe_xNb_xO_7$ pyrochlore solid solution (space group Fd-3m) determined from Rietveld analysis of neutron powder diffraction data. Error bars represent 3 esds. 141

Figure 15: Variation of key metal – oxygen bond lengths with nominal composition (x) in the $Y_2Ti_{2-2x}Fe_xNb_xO_7$ pyrochlore solid solution (space group Fd-3m) determined from Rietveld analysis of neutron powder diffraction data. Y-O1 and Y-O2 bonds are denoted by blue diamonds and red squares respectively (left hand axis); M-O1 bonds are denoted by green trianges (right hand axis). Error bars represent 3 esds and are smaller than the data point where not visible. 142

Figure 16: Showing fit (solid line) to high resolution neutron diffraction data (points) for $Y_2Ti_{0.6}Fe_{0.7}Nb_{0.7}O_7$ (x = 0.7) at 25 °C in space group $P3_12_1$; tick marks show allowed reflections, the difference profile (lower solid line) demonstrates a good fit to the data. 146

Figure 17: Schematic representation of refined structural model for : Y1(8), Y2(8) and Y3(7) sites are denoted by gold, green and yellow spheres, respectively; M1(6), M2(6) and M3(5) sites are shown by magenta, red and orange polyhedra, respectively; oxygen anions are shown by blue spheres. Note M3(5) sites are shown at 50% occupancy. 147

Figure 18: Single hexagonal tungsten bronze layer in $Y_2Ti_{0.6}Fe_{0.7}Nb_{0.7}O_7$, projected down c-axis.; M1(6), M2(6) and M3(5) sites are shown by magenta, red, and orange polyhedra, respectively; oxygen anions are shown by blue spheres. Note M3(5) sites are shown at 50% occupancy. 152

Figure 19: Magnetic susceptibility of $Y_2Ti_{2-2x}Fe_xNb_xO_7$ compositions over $0 < T < 300$ K. 153

Chapter 5

Figure 1: Schematic of N-(2-Hydroxyethyl)iminodiacetic acid (heidi). 159

Figure 2: Ball and stick representations of a) $[Zr(heidi)_2].9H_2O$ and b) $[Th_2(heidi)_4]^{4-}$. 161

Figure 3: Titration of zirconium (IV) at 5.10^{-3} M (red line), in presence of 2 eq. of heidi (blue line) and heidi by itself (green line), I=0.5 M (NaCl). 167

Figure 4: Titration of thorium (IV) at 5.10^{-3} M (red line), in presence of 2 eq. of heidi (blue line) and heidi by itself (green line), I=0.5 M ($NaNO_3$). 167

Figure 5: Titration of uranium (IV) at 5.10^{-3} M (red line) in a HCl (1M) solution, in presence of 2 eq. of heidi (blue line) and heidi by itself (green line), I=0.5 M (NaCl). 168

Figure 6: Titration of uranyl at 5.10^{-3}M (red line), in presence of 2 eq. of heidi (blue line) and heidi by itself (green line), I=0.5 M ($NaNO_3$). 168

Figure 7: pH difference between blank and potentiometric data for M and 2 heidi solution at 10^{-3} M, I = 0.5 M, where M = Zr(IV), Th(IV), U(IV), U(VI). 170

Figure 8: Labelled heidi (above) and ^{1}H NMR data for heidi in D_2O from pH 2 to 12. 171

Figure 9: ^{13}C NMR data for heidi (1M, I = 0.5 M) in D_2O from pH 2 to 12. 172

Figure 10: Change in chemical shift of C_1 (COOH) as a function of pD and the model fit for heidi. 174

Figure 11: ^{1}H NMR in D_2O for Zr (IV) : heidi at a 1:2 ratio, at 10^{-3} M and I = 0.5 M (NaCl). 175

Figure 12: ^{1}H NMR of Th (IV) : heidi at a 1:2 ratio (left) and heidi (right) at 10^{-3} M, I = 0.5 M. 179

Figure 13: ^{1}H NMR of U (IV) : heidi at a 1:2 ratio at 10^{-3} M, I = 0.5 M. 182

Figure 14: ^{1}H NMR of U(VI):heidi at a 1:2 ratio (left) and heidi (right) at 10^{-3} M, I = 0.5 M. 184

Figure 15: ^{1}H NMR of Np (IV) : heidi at a 1:2 ratio, I = 0.5 M. 186

Figure 16: ^{1}H NMR of Np (VI) : heidi at a 1:2 ratio, for pH values below 4, I = 0.5 M. 187

Figure 17: ^{1}H NMR of Np (VI) : heidi at a 1:2 ratio for pH values above 4, I = 0.5 M. 188

Figure 18: Comparison of UV-vis spectra of U (VI) and U (VI) : heidi at the 1:2 ratio, at 10^{-3} M, pH= 2 and 4, I = 0.5 M. 191

Figure 19: Comparison of UV-vis spectra of U (VI) and U (VI):heidi at the 1:2 ratio, 10^{-3} M, pH > 6, I = 0.5 M. 192

Figure 20: Solution nIR spectra of Np(V/VI) and Np(V/VI): heidi, at a 1:2 ratio, along a 0.7-10 pH range, I = 0.5 M 194

Figure 21: UV-vis spectra of U (IV) and U (IV) : 2 heidi at 10^{-3} M, I = 0.5 M. 195

Figure 22: Near IR spectra of free U (IV) metal ions in aqueous solution and U (IV) : 2 heidi at10^{-3} M, I = 0.5 M. 196

Figure 23: UV-vis spectra of Np(IV) and Np (IV) : 2 heidi at 10^{-3} M, I = 0.5 M. 197

Figure 24: ORTEP representation of $[UI(O\text{-}i\text{-}Pr)_2.(HO\text{-}i\text{-}Pr)_4]I$, hydrogen atoms are not displayed for clarity. 198

Figure 25: UV-vis spectrum of $[UI(O\text{-}i\text{-}Pr)_2.(HO\text{-}i\text{-}Pr)_2]I$, in toluene [8.10-3 M]. 202

List of Tables

Chapter 1

Table 1: Ground state electronic configurations of the actinide elements 28

Table 2: Formation constants of mononuclear species for plutonium (IV) and neptunium (IV) at 25°C. 44

Table 3: Mineral phases under investigation for plutonium disposal. 47

Chapter 2

Table 1: Properties of NMR-active nuclei 75

Table 2: Splitting pattern predicted by Pascal's triangle 77

Chapter 3

Table 1: Quantitative elemental analysis of $Y_{2-x}Ce_xTi_{2-x}Fe_xO_7$ compositions. 94

Table 2: Observed bands in the Raman spectra at room temperature of pyrochlore structures from $Y_{2-x}Ce_xTi_{2-x}Fe_xO_7$. 99

Table 3: Refined structural parameters for $Y_{1.9}Ce_{0.1}Ti_{1.9}Fe_{0.1}Nb_xO_7$ (x = 0.1), determined from Rietveld analysis of neutron powder diffraction data. 101

Table 4: Key bond lengths for $Y_{2-x}Ce_xTi_{2-x}Fe_xO_7$ determined from Rietveld analysis of neutron powder diffraction data and resulting cation bond valence sums. 102

Table 5: Refined structural parameters for $Y_{1.4}Ce_{0.6}Ti_{1.4}Fe_{0.6}O_7$ (x = 0.6) determined from Rietveld analysis of neutron powder diffraction data, occupancies for M sites are reported in Table 9. The goodness of fit parameters were R_{wp} = 8.81 % and χ^2 = 9.35. 106

Table 6: Key bond lengths for Ln sites in $Y_{1.4}Ce_{0.6}Ti_{1.4}Fe_{0.6}O_7$ (x = 0.6) determined from Rietveld analysis of neutron powder diffraction data and resulting cation bond valence sums. Ln site occupancies are given in Table 10. The expected bond valence sum assumes the nominal cation oxidation state together with occupancies given in Table 10. The mean bond valence sum is the weighted mean calculated bond valence sum derived from the refined site occupancies and bond valence sums determined from bond length data, given in Table 11. 107

Table 7: Key bond lengths for M in sites $Y_{1.4}Ce_{0.6}Ti_{1.4}Fe_{0.6}O_7$ (x = 0.6) determined from Rietveld analysis of neutron powder diffraction data. M site occupancies are given in Table 9. The expected bond valence sum assumes the nominal cation oxidation state together with occupancies given in Table 9. The mean bond valence sum is the weighted mean calculated bond valence sum derived from the refined site occupancies and bond valence sums 108

determined from bond length data, given in Table 10.

Table 8: Occupancies for Ln and M sites in $Y_{1.4}Ce_{0.6}Ti_{1.4}Fe_{0.6}O_7$ (x = 0.6) determined from ^{57}Fe Mössbauer spectroscopy and Rietveld analysis of neutron powder diffraction data. 108

Table 9: Bond valence sums for Ln and M sites in $Y_{1.4}Ce_{0.6}Ti_{1.4}Fe_{0.6}O_7$ (x = 0.6) determined from bond length data reported in Tables 7 and 8. 109

Chapter 4

Table 1: Quantitative elemental analysis of $Y_2T_{i2-2x}Fe_xNb_xO_7$ compositions. Values in parentheses indicate one standard deviation in final decimal place. 127

Table 2: ^{57}Fe Mössbauer parameters for single phase compositions in $Y_2Ti_{2-2x}Fe_xNb_xO_7$ system. 131

Table 3: Observed bands in the Raman spectra for pyrochlore structures of $Y_2Ti_{2-x}Fe_xNb_xO_7$ 135

Table 4: Refined structural parameters $Y_2Ti_{2-2x}Fe_xNb_xO_7$ pyrochlore solid solution, in space group Fd-3m, determined from Rietveld analysis of neutron powder diffraction data. M site occupancies are in accordance with the nominal stoichiometry x. M located at (0,0,0), Y at (0.5, 0.5, 0.5), O2 at (3/8, 3/8, 3/8), and O1 at (x, 1/8, 1/8) (corresponding to the 8a, 8b and 48f positions, respectively). 138

Table 5: Key bond lengths for $Y_2Ti_{2-2x}Fe_xNb_xO_7$ determined from Rietveld analysis of neutron powder diffraction data and resulting cation bond valence sums. 142

Table 6: Refined structural parameters for $Y_2Ti_{0.6}Fe_{0.7}Nb_{0.7}O_7$ determined from Rietveld analysis of neutron powder diffraction data, occupancies for M sites are reported in Table 10. The goodness of fit parameters were R_{wp} = 7.92 % and χ^2 = 3.67. 145

Table 7: Key bond lengths for Y sites in $Y_2Ti_{0.6}Fe_{0.7}Nb_{0.7}O_7$ (x = 0.7) determined from Rietveld analysis of neutron powder diffraction data and resulting cation bond valence sums. 150

Table 8: Key bond lengths for M in sites $Y_2Ti_{0.6}Fe_{0.7}Nb_{0.7}O_7$ (x = 0.7) determined from Rietveld analysis of neutron powder diffraction data. M site occupancies are given in Table 150

9. The expected bond valence sum assumes the nominal cation oxidation state together with occupancies given in Table 10. The mean bond valence sum is the weighted mean calculated bond valence sum derived from the refined site occupancies and bond valence sums determined from bond length data, given in Table 11.

Table 9: Cation occupancies of M sites in $Y_2Ti_{0.6}Fe_{0.7}Nb_{0.7}O_7$ (x = 0.7) determined from Rietveld analysis of neutron powder diffraction data and 57Fe Mössbauer spectroscopy. Errors are reported for cation occupancies refined in Rietveld analysis. Nb is assumed to be excluded from the M3 site. 151

Table 10: Bond valence sums for M sites in $Y_2Ti_{0.6}Fe_{0.7}Nb_{0.7}O_7$ (x = 0.7) determined from bond length data reported in Table 10. 151

Chapter 5

Table 1: X-ray Crystallographic data for $C_{18}H_{40}I_2O_6U$ (1) 164

Table 2: ^{13}C chemical shifts (ppm) from the carbons belonging to the carboxylate groups (C_1) within heidi on its own and Zr (IV): 2 heidi 177

Table 3: ^{13}C chemical shifts (ppm) from the carbons belonging to the carboxylate groups (C_1) within heidi on its own and Th (IV) : 2 heidi 180

Table 4: ^{1}H chemical shifts (ppm) from the protons neighbouring the carboxylate groups (previously labelled *Hc*) within heidi in presence of tetravalent elements (Zr, Th, U, Np) 189

Table 5: ^{13}C chemical shifts (ppm) from the carbon atoms neighbouring the carboxylate groups (previously labelled C_1) within heidi and in presence of zirconium (IV) and thorium (IV) ions 189

Table 6: Selected bonds lengths for $[UI(O\text{-}i\text{-}Pr)_2.(HO\text{-}i\text{-}Pr)_2]I$ (1) 199

Table 7: Representative angles for $[UI(O\text{-}i\text{-}Pr)_2.(HO\text{-}i\text{-}Pr)_2]I$ (**1**) 200

Table 8: Atomic coordinates (x 10^4) and equivalent isotropic displacement parameters ($Å^2$x 10^3) for $[UI(O\text{-}i\text{-}Pr)_2.(HO\text{-}i\text{-}Pr)_2]I$ (1). U(eq) is defined as one third of the trace of the orthogonalised Uij tensor 201

University of Manchester

Carlos De La Fontaine

Doctor of Philosophy

Abstract

The nuclear industry faces important technical challenges for HLW storage and designing new nuclear fuels. Such materials have to perform under severe conditions and accommodate defects safely. Few materials are suitable for those purposes but certain types of ceramics are promising candidates; among them oxide compounds such as pyrochlores and zirconolites. The aim of this PhD project was to synthesise novel actinide oxide particles, in which two different approaches were taken: controlled hydrolysis and solid state chemistry.

Some minerals were naturally doped with actinides and rare earth elements and inspired synthetic formulations of new targeted waste forms for High Level Waste (HLW) instead of other disposal routes. The choice of synthetic pyrochlore and zirconolites as actinide hosts was inspired by the existence of naturally occurring actinide rich minerals. Substitutions within the cubic $Y_2Ti_2O_7$ were investigated *via* the respective $Y_2Ti_{2-2x}Fe_xNb_xO_7$ and $Y_{2-x}Ce_xTi_xFe_xO_7$ solid solutions.

Controlled hydrolysis was based on previous work with Lewis acidic transition metal cations. It was shown that it was possible to control the hydrolysis products in the presence of chelating organic ligands by carefully controlling the experimental conditions of the system. The same principles should apply to the chemistry of the actinide ions as they too are Lewis acidic. Such chemistry has implications for understanding the behaviour of actinides in nuclear processes within aqueous and organic systems.

This project was a collaboration between Sheffield University (Immobilisation Science Laboratory, ISL) and The University of Manchester (Centre for Radiochemistry Research, CRR) through the DIAMOND (Decommissioning Immobilisation and Management of Nuclear waste for Disposal) University research consortium.

Declaration

No portion of the work referred to in this thesis has been submitted in support of an application for another degree or qualification of this or any other institute of learning.

Copyright

(i) The author of this thesis (including any appendices and/or schedules to this thesis) owns certain copyright or related rights in it (the "copyright") and he has given The University of Manchester certain rights to use such copyright, including for administrative purposes.

(ii) Copies of the thesis, either in full or in extracts and whether in hard or electronic copy, may be made **only** in accordance with the Copyright, Designs and Patents Act 1988 (as amended) and regulations issued under it or, where appropriate, in accordance with licensing agreements which the University has from time to time. This page must form part of any such copies made.

(iii) The ownership of certain Copyright, patents, designs, trademarks and any or all other intellectual property (the "Intellectual Property Rights") and any reproductions of copyright works in the thesis, for example graphs and tables ("Reproductions"), which may be described in this thesis, may not be owned by the author and may be owned by third parties. Such Intellectual Property Rights and Reproductions cannot and must not be made available for use without the prior written permission of the owner(s) of the relevant Intellectual Property Rights and/or Reproductions.

(iv) Further information on the conditions under which disclosure, publication and commercialisation of this thesis, the Copyright and any Intellectual Property and/or Reproductions described in it may take place is available in the University IP Policy (see http://www.campus.manchester.ac.uk/medialibrary/polices/intellectual-property.pdf), in any relevant Thesis restriction declarations deposited in the University Library's regulations (see http://www.manchester.ac.uk/library/aboutus/regulations) and in The University's policy on presentation of Theses.

Acknowledgements

I would like to thank my supervisors, Dr. Sarah Heath and Prof. Neil Hyatt for their support and guidance during my PhD.

I am especially grateful to Dr. Nicholas Bryan, Dr. Martin Stennet and Dr Stephanie Cornet who took a lot of their time to teach me a great deal of laboratory techniques and data analysis.

I also would like to thank all the good friends I made during my time in the CRR (especially Ryan Telchadder and Dr. Tamara (Martha) Griffiths), the entire Radiochemistry group and my sponsor (NDA, through the DIAMOND consortium).

Last but not least, I would like to thank my family for their love and support throughout my studies. Thank you for keeping me under a roof during the long writing journey of this PhD.

"Não diga que a vitória está perdida.
Se é de batalhas que se vive a vida,
Tente outra vez..."
Paulo Coelho

"Et, si de t'agréer je n'emporte le prix,
J'aurai du moins l'honneur de l'avoir entrepris."
Jean de La Fontaine

This thesis has been written in a series of related papers centred on the study of potential wasteforms, the investigation of actinide alkoxides, and the study of actinide behaviour in the presence of organic ligands relevant for environmental issues. One part has already been published in the proceedings of the Actinides 2009 conference, the rest are due to be submitted in relevant journals in the field.

Chapter one will review the literature on the relevant subjects treated in this thesis (*e.g.* pyroclhore and zirconolite ceramic structures and suitability as wasteforms, hydrolysis of actinides focussing on tetravalent elements, and synthesis of actinide alkoxides as potential precursors for controlled hydrolysis).

Chapter two introduces the experimental techniques used during this research project, which required solid state chemistry and analytical techniques. This chapter also gives a brief introduction to error estimation.

Chapters three and four describe the synthesis and structural investigation of metal oxides proposed as wasteforms. Those systems were prepared by consecutive solid state reaction. Chapter three describes the $Y_{2-x}Ce_xTi_{2-x}Fe_xO_7$ system, a potential suitable ceramic host for plutonium on the Y^{3+} site. Chapter four describes the $Y_2Ti_{2-2x}Fe_xNb_xO_7$ system, which was formulated for actinide disposal by substitution at the Ti^{4+} site. Both systems were inspired by a cubic pyrochlore structure renowned as a promising wasteform candidate, as its structural flexibility allows a high degree of incorporation and is chemically robust.

Chapter five present a solution chemistry study undertaken with several tetravalent actinide ions (Th^{4+}, U^{4+}, Np^{4+}) and actinyls (UO_2^{2+}, NpO_2^{2+}, NpO_2^{+}) in the presence of two equivalents of heidi ($HOCH_2CH_2N(CH_2COOH)_2$), an organic ligand relevant for environmental/decommissiong issues, due to its features found in amino acids ($-NH_2$, -OH, and –COOH). The experimental conditions were set to investigate previous crystallographic data obtained in this system as an attempt to control hydrolysis. Chapter five also describes the synthesis and characterisation of a novel U(IV) alkoxide compound, $[UI(O\text{-}i\text{-}Pr)_2.(HO\text{-}i\text{-}Pr)_4]I$, a promising organometallic precursor to be employed in controlled hydrolysis.

Finally, the last chapter will draw the conclusions from the previous chapters and summarise the future work to be developed.

Chapter 1:

INTRODUCTION

Ever since their discovery, the actinides have been used in a different number of applications such as power production, heat and fuel sources in submarines and space shuttles, as well as in several types of materials; for instance ceramics; this has resulted in a growing list of environmental and health concerns, whether accidental or malicious.

Our relatively limited understanding of the solution and coordination chemistry of the actinides (in comparison to transition metals) complicates the full understanding of the potential environmental and health issues.

The project presented in this thesis is based on the investigation and characterisation of metal oxides *via* two main different methods: solid state chemistry and a sol-gel approach (aqueous or organic precursors). Both are relevant for decommissioning and disposal issues. This chapter will give an overview of the nuclear fuel cycle and review the relevant literature in the several fields connected in this project (e.g. use of pyrochlore and zirconolite ceramics as waste, controlled hydrolysis of actinide ions, relevance of actinide alkoxides as precursors).

1. NUCLEAR FUEL CYCLE [1]

Coal, oil, natural gas and uranium can all be used for power production in various types of power plants. To prepare uranium for use in a nuclear reactor, it has to undergo mining and milling, conversion, enrichment and fuel fabrication. These steps are known as the 'front end' of the nuclear fuel cycle.

After spending about three to five years in a reactor generating electricity, the used fuel may undergo a further series of steps including temporary storage, reprocessing, and recycling before eventual disposal as waste. Collectively these steps form the 'back end' of the fuel cycle.

1.1. Mining

Uranium is usually mined by either surface or underground mining techniques, depending on the depth at which the ore body is found.

The mined uranium ore is then sent to a mill which is usually located close to the mine. The ore is subsequently crushed and ground to a fine slurry, which is leached in sulfuric acid to allow the separation of uranium from the waste rock. After this, the uranium is recovered from the solution and precipitated as uranium oxide (U_3O_8) concentrate, commonly known as yellowcake.

It is noted that some countries, such as Russia, and the United States of America, use the military stockpile as another source of uranium when it is no longer being conserved for use in nuclear weapons.

1.2. Conversion

Uranium needs to be in the form of a gas before it can be enriched; the U_3O_8 is converted into a gas: uranium hexafluoride (UF_6).

1.3. Enrichment

A small number of reactors, notably the Canadian CANDU reactors, do not require uranium to be enriched, however, the vast majority of all nuclear power reactors in operation (PWR) and those under construction require enriched uranium fuel in order to allow a controlled chain reaction. The proportion of the U-235 isotope has to be raised from its natural level of 0.7% to between 3.5% and 5%. The enrichment process removes about 85% of the U-238 by separating gaseous uranium hexafluoride into two streams: one stream is enriched to the required level and then passes to the next stage of the fuel cycle whilst the other stream contains depleted U-235 which is for the most part stored at the enrichment site. This separation process is based on physical properties and can be accomplished by gas diffusion or via centrifugation.

1.4. Fuel fabrication

The enriched UF_6 is transported to a fuel fabrication plant where it is converted to uranium dioxide (UO_2) powder and pressed into small pellets. These pellets are inserted into tubes, usually of a zirconium alloy (zircalloy) to form fuel rods. The rods are then sealed and gathered into clusters to form fuel assemblies for use in the core of the nuclear reactor.

1.5. The nuclear reactor

Several hundred fuel assemblies make up the core of a reactor. For a reactor with an output of 1000 megawatts (MW), the core would contain about 75 tonnes of slightly-enriched uranium. In the reactor core, the U-235 isotope undergoes fission producing heat in a continuous process called a chain reaction. The process depends on the presence of a moderator such as water, heavy water or graphite, and is fully controlled.

Some of the U-238 in the reactor core is converted into plutonium, by capturing thermal neutrons; around half would then undergo fission which can provide about a third of the reactor's energy.
The heat is used to produce steam to drive a turbine and an electric generator, just as in other electricity generating plants.

1.6. Used fuel storage

Used (spent) fuel assemblies taken from the reactor core are highly radioactive and release a lot of heat. Fuel rods are therefore stored for a number of years in special ponds or pools, which are usually located at the reactor site, to allow both their heat and radioactivity to decrease. The water in the ponds serves as a barrier against radiation whilst cooling the spent fuel.

Spent fuel rods can sometimes be dry stored in engineered facilities, cooled by air. However, both kinds of storage are intended only as an interim step, the longer they are stored, the easier it is to handle, due to decay of radioactivity, but there is an increase in damage of the rods due to corrosion.

There are two methods for final disposal of used fuel: reprocessing (to recover the fissionable portion) or direct disposal.

1.7. Reprocessing

Used fuel still contains approximately 96% of its original uranium, of which the fissionable U-235 content has been reduced to less than 1%. About 3% of used fuel comprises waste products and the remaining 1% is plutonium produced while the fuel was in the reactor and not burned.

Reprocessing techniques, such as the PUREX process, [2] used in the UK and overseas, separates uranium and plutonium from waste products (and from the fuel assembly cladding) by chopping up the fuel rods, dissolving them in nitric acid and adding compounds such as TBP to complex to U/Pu allowing the separation of various materials. Recovered uranium can be returned to the conversion plant for conversion to uranium hexafluoride and subsequent re-enrichment. The reactor-grade plutonium can be blended with enriched uranium to produce a mixed oxide (MOX) fuel in a fuel fabrication plant. The nuclear cycle in the UK is illustrated in the following scheme, Figure 1, and comprises all steps discussed previously.

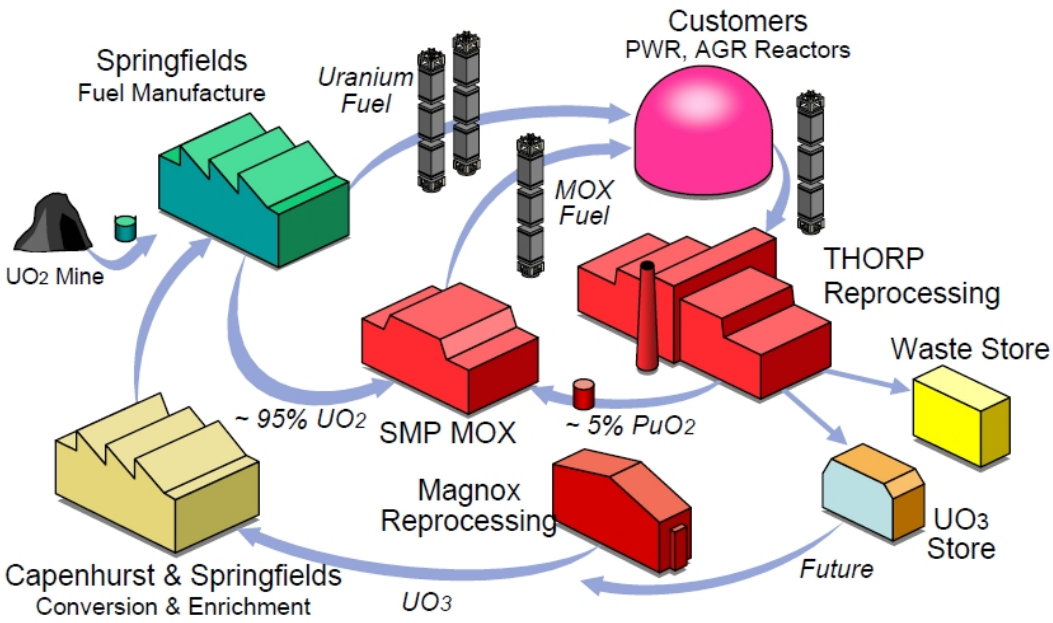

Figure 1: Nuclear fuel cycle in the UK. [3]

The remaining 3% of high-level radioactive wastes (some 750 kg per year from a 1000 MWe reactor) can be stored in liquid form and subsequently solidified as a glass waste form (vitrification).

1.8. Final Disposal

Most waste forms envisaged for disposal are sealed into stainless steel canisters or element specific ceramic matrices. It is intended to burry radioactive waste canisters into stable rock structures deep underground. It is noted that most national policies consider that spent fuel is not classified as waste, because it still contains a large amount of uranium (and plutonium) which can potentially be separated out through reprocessing and used to make new fuel.

2. GENERAL PROPERTIES/CHEMISTRY OF ACTINIDES

Uranium, the first f-element unveiled, was discovered in 1789 by the German chemist Martin Heinrich Klaproth. [4] It took another century before Becquerel discovered radioactive decay in 1895, [5] and so, inspiring other researchers, notably the Curies to isolate new elements such as polonium in 1896. The vital importance of uranium came after the discovery of the neutron by Chadwick in 1932 when Fermi *et al*. studied the radioactivity induced by (n,γ) reactions, leading to the discovery of transuranic elements as well as the nuclear fission by Hahn and Strassmann in 1938. [5,6] These discoveries showed the way to nuclear weapons during the Second World War and eventually to the present civil nuclear industry.

N. Bohr suggested, in 1923, the existence of a new group of elements at the end of the Periodic Table that would have similar chemical properties to the rare earth class. It was Seaborg who proposed that those new elements would form a new group starting with actinium. The accepted electronic ground state configurations of the actinides are shown in Table 1.

	Element	Ground State Electronic Configuration
Ac	Actinium	$[Rn]6d^1 7s^2$
Th	Thorium	$[Rn]6d^2 7s^2$
Pa	Protactinium	$[Rn]5f^2 6d^1 7s^2$
U	Uranium	$[Rn]5f^3 6d^1 7s^2$
Np	Neptunium	$[Rn]5f^4 6d^1 7s^2$
Pu	Plutonium	$[Rn]5f^6 7s^2$
Am	Americium	$[Rn]5f^7 7s^2$
Cm	Curium	$[Rn]5f^7 6d^1 7s^2$
Bk	Berkelium	$[Rn]5f^9 7s^2$
Cf	Californium	$[Rn]5f^{10} 7s^2$
Es	Einsteinium	$[Rn]5f^{11} 7s^2$
Fm	Fermium	$[Rn]5f^{12} 7s^2$
Md	Medelevium	$[Rn](5f^{13} 7s^2)$
No	Nobelium	$[Rn](5f^{14} 7s^2)$
Lr	Lawrencium	$[Rn](5f^{14} 6d^1 7s^2)$

Table 1: Ground state electronic configurations of the actinide elements [5]

2.1. f-orbitals

The quantum number, *n,* is equal to 4 for the lanthanide series and to 5 for the actinides and relates to the number of the electron shell. The angular quantum number, *l*, equals 3, which distinguishes a 7 fold degeneration for the f-orbitals. Their symmetry is *ungerade* in respect of parity. The shapes are generated by solving the Schrödinger equation and suggest that bonding to the f-orbitals is directional. They are generally represented as a *cubic set*, closely related to tetrahedral, octahedral and cubic ligand fields [7] but can also be represented by a *general set*.

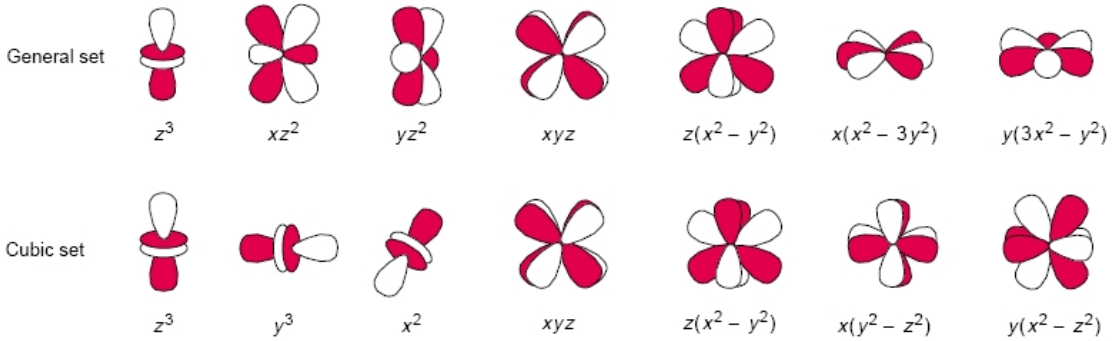

Figure 2: Shape of the f-orbitals generated by solving the Schrödinger equation. [8]

The orbitals shapes are complex, however, it is possible to see that the lobes of the f_{xyz} orbital point towards the corners of a cube. The $f_{z(x^2-y^2)}$, $f_{y(z^2-x^2)}$ and $f_{x(z^2-y^2)}$ have a similar shape to the f_{xyz} atomic orbital, but are rotated by the *z*, *y* and *x* axes respectively. It is f-orbitals that are responsible for the notable differences, both physical and chemical, for the lanthanide and the actinide elements when compared to the transition metals. Their effect on coordination chemistry is crucial to model the physical and chemical behaviour of the f-block elements.

2.2. Actinide oxidation states

The oxidation state patterns of the early actinides resemble those from the d-block metals in the sense that the maximum oxidation state corresponds to the number of outer shell electrons. Various oxidation states are exhibited by the early actinides due to the small difference in energy between the 5f, 6d and 7s orbitals. Hence, the chemistry of thorium is confined to the +IV state as are zirconium and hafnium, but uranium exhibits numerous oxidation states from +III to +VI and neptunium from +III to +VII. The +III oxidation state stability increases going across the An series, while the f-orbitals are gradually filled. Actinide oxidation states are shown in Figure 3.

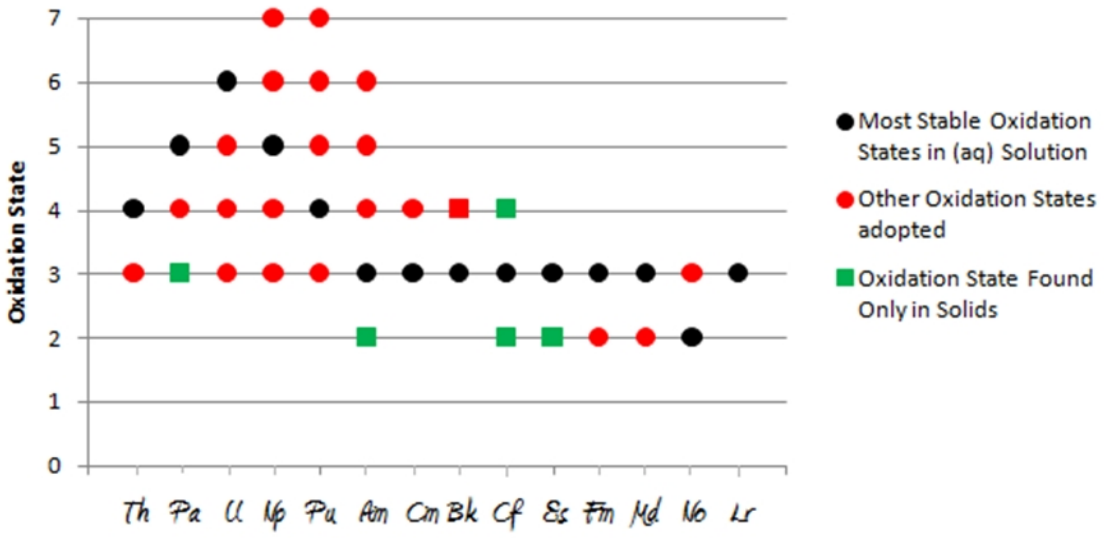

Figure 3: Oxidation states of actinides as bare ions and in their compounds.[9,10]

Early actinides in oxidation states +V and +VI are highly positively charged and readily strip oxygen atoms from water molecules to form a unique class of trans-dioxo cations (Fig. 4). This feature can also be seen with elements from the d- block such as tungsten, molybdenum and vanadium among them. [11,12] Their dioxo cations are usually bent.

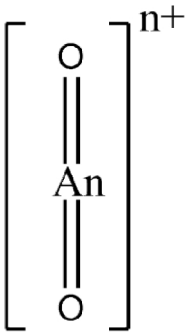

Figure 4: Schematic of trans-dioxo actinides.

3. CERAMIC WASTEFORMS

Actinides and their daughter products account for most of the radiotoxicity of nuclear waste after the first 500 years of disposal even if there are several fission products of high activity (^{137}Cs and ^{90}Sr for example) and long half-life (^{99}Tc, 200,000 years; ^{129}I, 1.6 x 10^7 years) in spent nuclear fuel. After several hundred of years, the radiotoxicity is dominated by ^{239}Pu (λ= 2,41 x 10^4 years) and ^{237}Np (λ =2 x 10^6 years). Thus, a major part of the long-term risk is directly related to the fate of these two actinides in the environment (Fig. 5). [13] The nuclear industry faces an important technical

challenge for HLW storage; materials for wasteforms have to accommodate radiation induced defects. Few materials are suitable as waste forms, but certain types of ceramic, such as pyrochlores and zirconolites, are among them. A ceramic wasteform is produced by the calcining of materials in a furnace, in the presence of air, at temperatures less than the system melting point. Waste is reacted with a suitable powdered mineral at a high temperature to cause a phase transition to occur; resulting in the formation of a new mineral phase which incorporates the waste in a stable form. The ceramic wasteform may then be sintered to form a solid monolithic material.

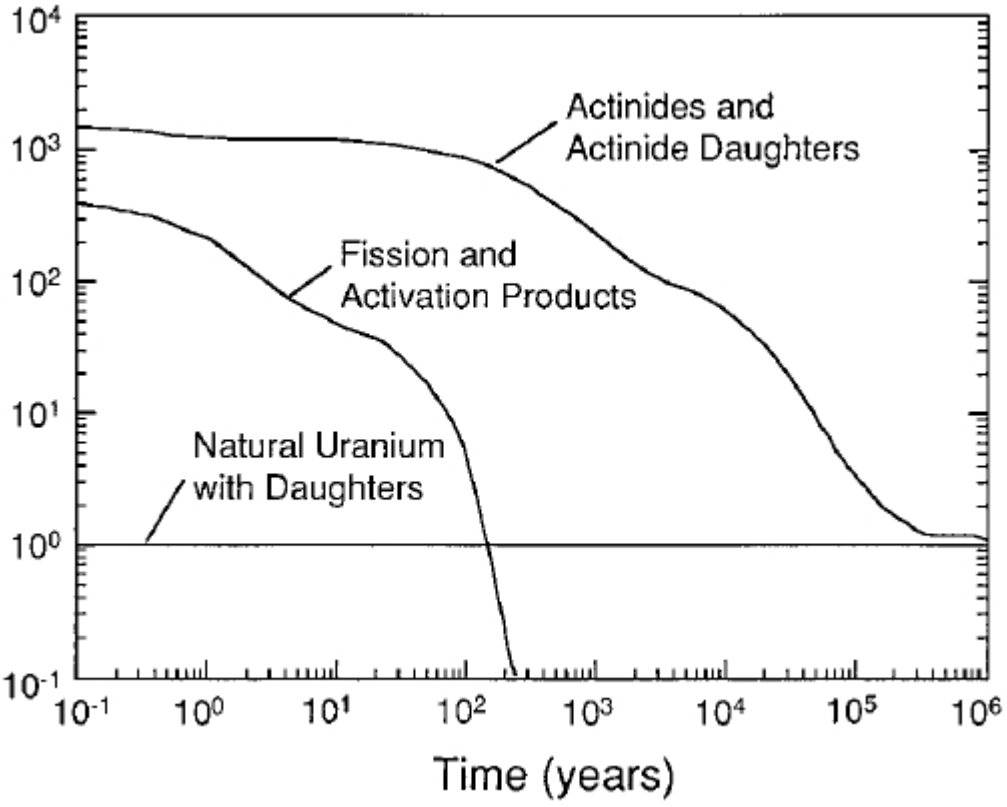

Figure 5: Relative radiotoxicity on inhalation of a spent fuel with a burnup of 38 megawatt days/kg U over a geological time scale. [13]

The interest in ceramics as actinide immobilisation phases is in part stimulated by their durability. Some natural ceramic samples have been found to incorporate up to 24 wt% UO_2, 22 wt% ThO_2 and 32 wt% REE_2O_3 for more than 2 000 Myr. [14] Those minerals inspired synthetic formulations of new targeted waste forms for High Level Waste (HLW) instead of the vitrification route.

High Level Waste (HLW) can decay to produce many atomic defects, and most materials cannot support such changes. The crystallinity can be extremely affected by the direct irradiation as well as the chemical changes due to decay in the ceramic and void swelling leading to amorphisation.

Chemical resistance and damage effects have been widely studied for targeted wasteform evaluation. [13,15,16]

Chemical durability is a broad term that includes various properties (*e.g.* corrosion resistance, thermodynamic stability) that are dependent on the geochemistry conditions (temperature, pH, redox conditions, composition of the solution, and flow rate). The chemical durability towards aqueous solutions is an important asset for waste forms. The release of radionuclides will certainly occur by their contact and reaction with water in a future geological disposal facility. The migration of radiotoxic materials will then be governed by dissolved and colloidal species. Dissolution rates are commonly measured for ceramics and ceramics altered by irradiation (self irradiation or external irradiation) in pure water at constant temperature in order to describe the alteration mechanism. An initial rate, r_0, is observed the first few hours or days, and the rate then diminishes drastically. Typically, dissolution rates of ceramics, for instance zirconolites, pyrochlores, present an initial rate, r_0, of about 10^{-2} $g.m^2.d^{-1}$ is observed in the first few hours or days. In comparison, borosilicate glasses, the most common wasteform for HLW, have been found to have leach rates higher than 1 $g.m^2.d^{-1}$. [17] Dissolution rates decrease with time by a few orders of magnitude, for example to around 10^{-5} $g.m^2.d^{-1}$ for titanate ceramics[18, 19, 20,21]. Two hypotheses can account for the decrease of the dissolution rate. The first is based on a thermodynamic equilibrium achieved between the solid and the solid. The second hypothesis is based on the formation of an alteration layer with protective properties (passivation layer). Radiation damage effects studies reported in the literature are performed by introducing short-lived actinides in a ceramic matrix (self irradiation) or by external irradiation by charged particles. The ceramic structure alterations were used to model long-term resistance to self-irradiation. [22] The combination of chemical durability and radiation tolerance studies reinforce the potential of ceramics as wasteforms.

Ceramics could also potentially be used as Inert Matrix Fuels (IMF). U-238 in this case would be replaced by an Inert Matrix (IM). This would effectively reduce the production of fission products as the new materials would be uranium free, notably yttria stabilised zirconia (YSZ). [23] The resulting lower level of actinides would also be an important advantage for a non-proliferation point of view. IMF could be used in fuels for the already existing reactors or in targets, for transmutation in future industrial installations. Moreover, the use of IMF could instigate a reduction of the spent fuel requiring a geological disposal by a factor of 10. Those materials would need to be fully characterised and be extremely reliable (thermally, thermodynamically, and mechanically) at high temperature and also be particularly resistant towards radiation damage. [24,25]

3.1. Oxide pyrochlores

Metal oxides with a pyrochlore structure ($A_2B_2O_7$) have generated interest for application as actinide host phases for radioactive waste immobilisation, and, more widely, for application in fuel cells and catalysis. Pyrochlore oxides are known to exhibit high ionic and electrical conductivity,[26] magnetic ordering, [27,28] as well as luminescence properties. [29,30] This diversity in application is associated with the chemical flexibility of the pyrochlore structure, which may accept substitution on both the A and B site, by cations of appropriate size and charge.

Pyrochlore ceramics tolerate both cation and anion disorder and are known for being chemically and radiation resistant which is the primary requirement for application as an actinide host, for instance Synroc. [31] Common pyrochlores usually approach the following stoechiometric form $(Na/\ Ca/\ REE/\ U)_2(Nb/\ Ta/\ Ti)_2O_6(F/\ OH/\ O)$. The structure is very flexible in terms of the sheer number of elements that can be incorporated and is amenable to actinide inclusion. Natural samples can contain up to 30 wt% of UO_2, 9 wt% of ThO_2 and 16 wt% REE_2O_3. This versatility in formulation is an important consideration for the nuclear criticality issue. However, the general formula is complicated and has the potential for vacancies and for insertion of water molecules in vacant tunnel sites (10-15 wt% as H_2O molecules and OH groups). In this work, natural samples were mainly used as inspiration for new synthesised pyrochlore formulations, which hopefully can be satisfactory actinide host phases. [14]

3.2. The pyrochlore structure

The ideal pyrochlore structure adopts the Fd-3m space group; with eight formula units per unit cell. The ideal $A_2B_2O_7$ pyrochlore structure is derived from fluorite (AO_2) via an ordered removal of one eighth of the oxygen atoms, combined with an ordered arrangement of A and B cations.

The ordered arrangement of cations and anion vacancies yields two distinct cation polyhedra: the A site (usually around 1 Å ionic radius) is 8-fold co-ordinated in the form of a distorted cube; whereas the B-site (usually around 0.6 Å ionic radius) is 6-fold co-ordinated in the shape of a distorted octahedron. [32] The A site is typically occupied by +2 and +3 cations, and the B site by +4 and +5 cations.

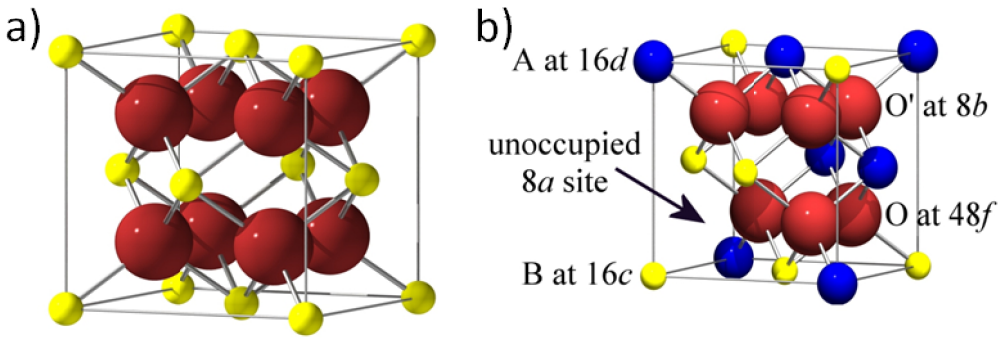

Figure 6: Simplified schemes of the fluorite a), and, pyrochlore b) structures. Yellow and blue atoms represent cations, red atoms represent anions (O^{2-}or F^- for example). [33]

These compounds are predominantly cubic and ionic in nature. A wide variety of chemical substitution at the A, B and O sites can be achieved, provided the ionic radius and charge neutrality criteria are satisfied.

There are three unique anion positions, in the pyrochlore structure: the 48 f (*x*, 1/8, 1/8), the 8b (3/8, 3/8, 3/8) and the vacant 8a (1/8, 1/8, 1/8). The structure can therefore be defined by two parameters: the 48f *x* (~ 3/8) anion position and the cubic unit cell parameter (*a*), which is usually ~10 Å and *x* is typically found around 0.309 to 0.355. [32]

The stability of the pyrochlore structure depends on the relative sizes of A and B cations. In general, the pyrochlore structure is stable for the radius ratio: $1.46 < r_A/r_B < 1.78$. [34] Below $r_A / r_B = 1.46$, we observe a defect fluorite structure with both anion and cation disorder. Above $r_A / r_B = 1.78$ a variety of phases can be formed. [27] Many of the pyrochlores known in the literature are of the $A_2^{3+}B_2^{4+}O_7$ type, simply because a larger number of A^{3+} and B^{4+} have suitable ionic radius for the formation of a pyrochlore structure.

3.3. Diversity of pyrochlore compositions

There are more than 500 synthetic formulations of the pyrochlore structure in the literature, predominantly niobates, zirconates and titanates. Titanate pyrochlores, $M_2Ti_2O_7$ (where M = Y and lanthanides from Sm to Yb), were first reported by Roth *et al.*[35] They are refractory materials with melting points around 1500 – 2000 °C and densities between 6 to 7 g/cc. When M belongs to the early lanthanide series (La, Ce, Pr and Nd) the material does not present a pyrochlore structure, as the radius ratio rule mentioned above is not respected.

As one would expect, a decrease in the lattice parameter, *a,* was observed when r^{3+} decreases. [36] Zirconate pyrochlores as $Ln_2Zr_2O_7$ are observed for lanthanides up to gadolinium, and, are stable until c.a. 1500°C. Above this value a transition towards a defect fluorite structure was reported [32] (2300 °C for Nd, 1530 °C for Gd for example).

3.4. The zirconolite structure

Zirconolite structures could be seen as a volumetrically condensed layered version of pyrochlore with a higher symmetry due to the presence of additional geometric sites such as 5-fold titanium sites. The structure is anion-deficient and also considered to be a derivative of the fluorite lattice. The general chemical composition of these complex oxides is $CaZrTi_2O_7$ which accepts several polytypic forms such as monoclinic 2M or 4M, orthorhombic 3O and hexagonal 3T. It can be described as an array of calcium and zirconium atoms inserted between planes of titanium atoms that are mainly within an octahedral site and a few 5 fold sites. The polytypic form of the structure is defined by the orientation of the successive titanium layers: the 2M and the 3T polytypes are described below.

3.5. Monoclinic (2M, 4M) and hexagonal (3T) zirconolite structures

Monoclinic Zirconolite (2M,4M)

The structure of zirconolite-2M, Figure 7, is related to pyrochlore by a compression of the cubic structure normal to one set of (111) planes, resulting in a condensed structure that is layered on (001), and has a reduced symmetry (C2/c). There are two distinct cation layers in zirconolite-2M: the HTB layer (i.e. hexagonal tungsten bronze type motif) and a layer of Ca and Zr atoms. The HTB layer is similar to that of pyrochlore, with the exception that the A-site located at the center of the six-membered polyhedra is replaced by a split Ti-site, coordinated by five anions, and statistically occupied.

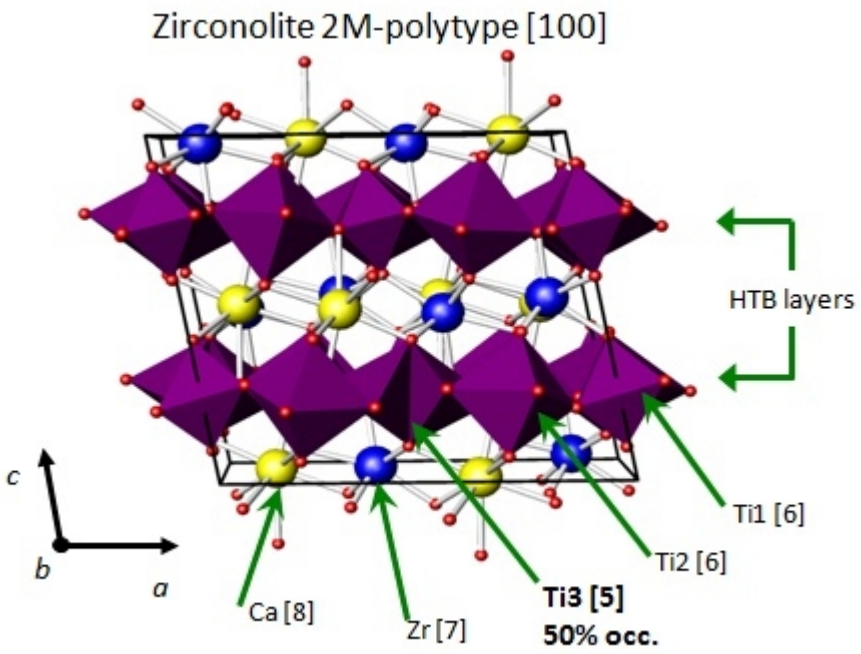

Figure 7: Schematic of a 2M polytype zirconolite structure ($CaZrTi_2O_7$) (Coordination number is shown next to the atoms and HTB i.e. hexagonal tungsten bronze type motif). [37]

Available refinements of zirconolite-4M indicate that the structure is based on a mixture of zirconolite and pyrochlore-like units. Thus, zirconolite-4M can be envisioned as a structural intermediate between zirconolite-2M and a pyrochlore structure. [38]

Usually 3T, 3O, and 4M structures occur with increasing levels of substitutions on the Ca- and Zr-sites of $CaZrTi_2O_7$. The type of the polytype was shown to be dependent on the type of substitution, temperature, and on the oxygen disorder and statistical occupancy. [37]

Hexagonal Zirconolite (3T)

The 3T zirconolite structure was first observed in a natural specimen [39] and is closely related to the 2M polytype. [40] Both polytypes have an alternation of Ti_4 and Ca_2Zr_2 layers. Figure 8 represents $Y_2Ti_{0.6}Fe_{0.7}Nb_{0.7}O_7$, which adopts the 3T polytype structure.

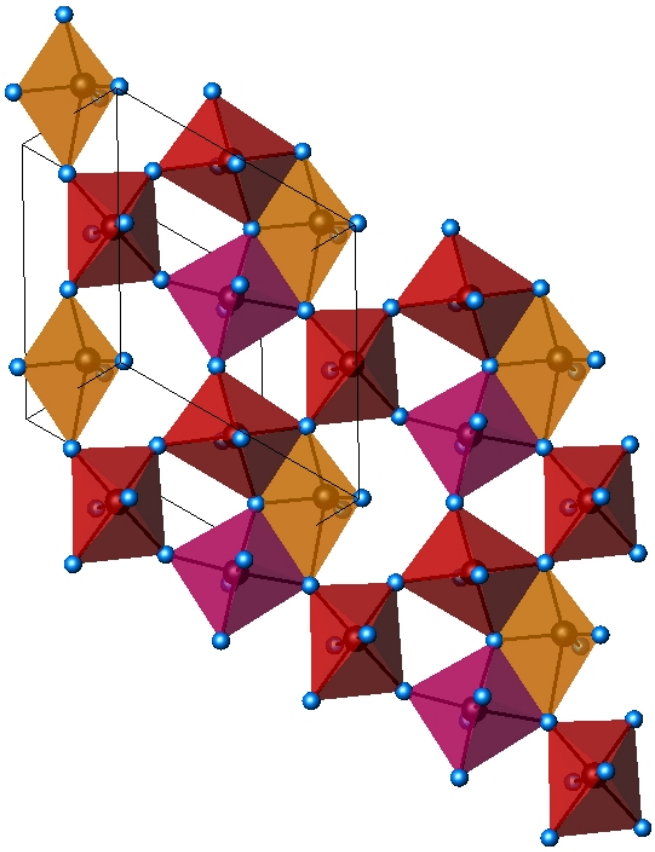

Figure 8: Structure of $Y_2Ti_{0.6}Fe_{0.7}Nb_{0.7}O_7$. Single hexagonal tungsten bronze layer projected down c-axis. Y sites (CN = 6) are shown by magenta, Ti/Fe (CN = 6) sites are shown in red, and Fe (CN = 5) sites are shown in orange. Oxygen anions are shown by blue spheres. (Fe (5) sites are shown at 50% occupancy).

In the 2M polytype there are only two orientations of the Ca_2/Zr_2 chains, 120 ° to one another. The 3T and 2M polytypes essentially differ in the disposition of small cations in the hexagonal rings in the HTB layers.

The 2M polytype has a Ti atom displaced from the centre of the ring to occupy a 5-coordinated site. The 3T polytype has partial occupancy of the same type of 5-coordinated site but in addition has partial occupancy of a 4-coordinated site with distorted tetrahedral coordination.

A similar situation was observed in 3O zirconolite where titanium is 5-coordinated and iron is a 4-coordinated metal ion. [39] All zirconolites have this statistical distribution feature of small cations displaced from the centre of the hexagonal ring.

Radioactive wasteforms immobilised in stable solid forms (ceramics, glasses for instance) possess a long term radiotoxic risk and need to be disposed of. Interim storage and geological disposal facilities are considered in order to prevent nuclear waste from contaminating the environment. The waste legacy will come into contact with water over a geological time, even though several barriers

have been engineered for geological disposal facilities. Our understanding of actinide hydrolysis is therefore fundamental.

4. ACTINIDE HYDROLYSIS

Hydrolysis of the actinides has been studied for decades and is known for its complexity. It is important to study the aqueous chemistry and geochemistry of the actinides to get a better knowledge of their fundamental behaviour in the environment, as a responsible management of nuclear waste relies on this.

Structural studies in solid and solution can give information such as coordination number, bond lengths and ligand exchange rate mechanisms, which are necessary to predict and understand chemical processes.

The model of partial charges [41] allows the prediction of the optimum theoretical conditions to obtain growing oxyhydroxide particles. This model allows the determination of the degree of hydrolysis (h) of a given metal ion (M):

$$[M(OH_2)_n]^{Z+} \overset{H_2O}{\Leftrightarrow} [M(OH)_h(OH_2)_{n-h}]^{(Z-h)+} + h\ H^+ \quad (1)$$

The principal hypothesis is that the electronegativity of each atom is equalized by electron transfer. This depends on the electronegativity as well as the size of the element (r, ionic radius) and its acidity (dependent on Z, the charge of the given metal ion). The quotient Z^2/r defines the reactivity of an element towards hydrolysis. Hydroxyl functional groups seem to be essential in the metal inner sphere if aggregation reactions are to be observed. The process is also pH dependent, Figure 9.

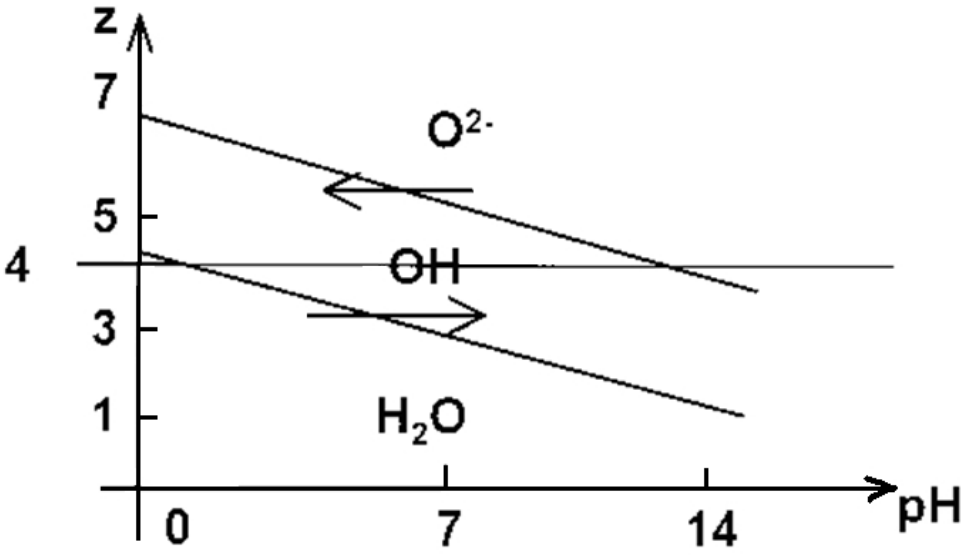

Figure 9: Nature of ligand (H_2O) in the coordination sphere depending on ion charge (Z) and pH. [41]

These polynuclearisation reactions are known as olation and oxolation mechanisms: [41]

***Olation*:** M-OH + M-OH_2 → M-OH-M + H_2O (2)

Oxolation: M-OH + M-OH → M-OH-M-OH → M-O-M(OH_2) → M-O-M + H_2O (3)

The elimination of water is irreversible. The system is driven by entropy towards the formation of oxides and oxohydroxides. In order to promote polymerisation, one has to keep the complex in the hydroxyl pH region and acid/base reactions can be used: [41]

$[M(O)]^- + H_3O^+ \rightarrow [M(OH)] + H_2O \leftarrow [M(OH_2)]^+ + HO^-$ (4)

4.1. Actinide metal ions in aqueous media

The actinide oxides readily dissolve in mineral acids to generate solutions of aqua ions. The 5f, 6d, 7s, and 7p orbitals have similar energies, and for elements up to americium, greater variations in oxidation state are observed as compared to the lanthanides. Thus, the actinides exist in several oxidation states: AnO_2^{2+} (aq), AnO_2^+ (aq), An^{4+} (aq), and An^{3+} (aq). For uranium the most stable form is the trans-dioxo ion, UO_2^{2+} (aq), whereas for americium it is Am^{3+} (aq), Figure 4.

Actinides, such as neptunium and plutonium, have a complex aqueous chemistry. The reasons for this being that they form highly charged ions and that they have several oxidation states that can coexist. In their tetravalent state they tend to precipitate at low pH and concentration.

Plutonium hydrolysis is often used to illustrate the assumption that the start of hydrolysis relies closely on the cation charge and is very pH dependent. The coloured bands in Figure 10 indicate the pH range where hydrolysis occurs.

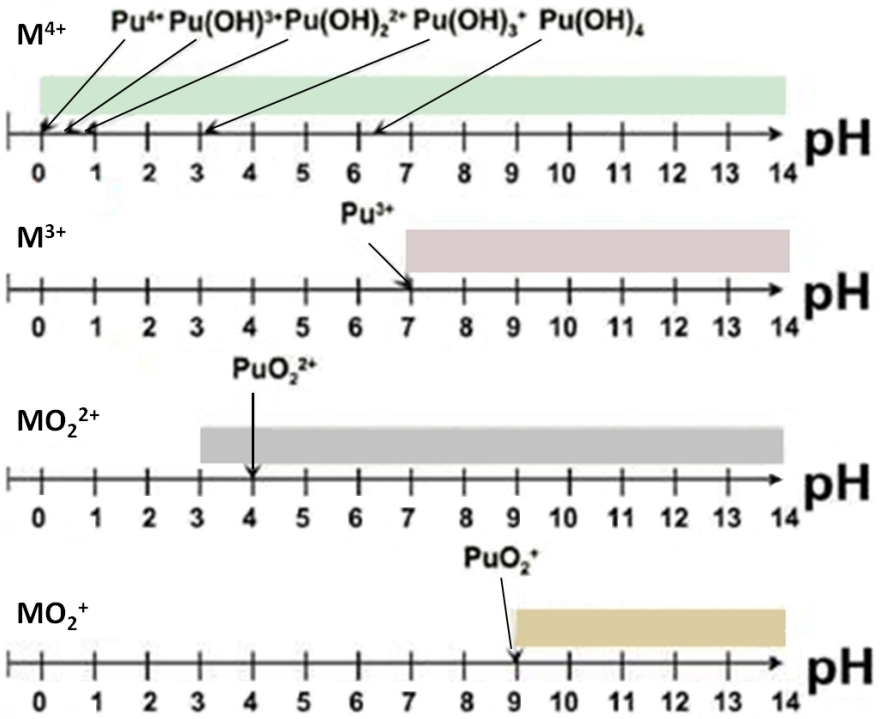

Figure 10: Schematic of the start of hydrolysis for plutonium (III), (IV), (V), and (VI) over the whole pH range.

4.2. Hydrolysis of tetravalent actinides

Tetravalent actinide behaviour is vital to understand for environmental studies [42,43] because they are very reactive towards water. They have low solubility and tend to precipitate as oxides and oxyhydroxides (Figure 11).

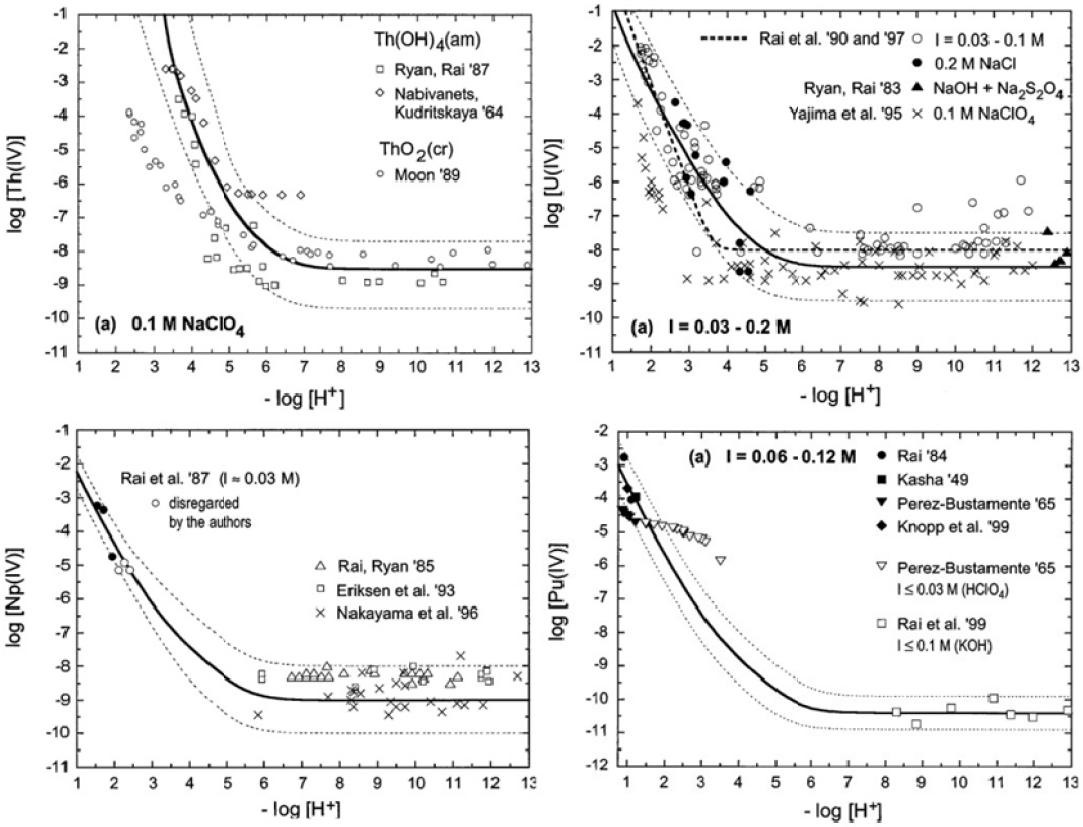

Figure 11: Solubility of tetravalent actinides (Th, U, Np and Pu) at ionic strengths < 0.12 M. [44]

The reported solid lines, [44] shown in Figure 11, confirm the low solubility even at low pH values. At higher ionic strengths, the solubility of thorium and uranium (IV) increases drastically, but this has little effect on plutonium and neptunium solubilities.

Reports on amorphous or crystalline An(IV) hydrolysis products show a lot of discrepancies. Solids do not have a unique defined solid phase; their particle size, water content, and other properties are very dependent on the experimental protocol, especially temperature.

The speciation of tetravalent actinides is often simplified by postulating that the species which form first in solution are mononuclear ($An(OH)_2^{2+}$, $An(OH)_3^{+}$, $An(OH)^{3+}$), [42,43,44] thus neglecting polynuclear species. However, this approach has a tendency to overestimate An(IV) species concentrations and their solubilities. Despite this estimation such models are still useful for the early stages of hydrolysis studies at low pH and metal concentration. Lanthanides can sometimes be used as actinide surrogates and their study could help the understanding of the behaviour of the actinides towards hydrolysis.

Most of the hydrolysis data reported in the literature derive from spectrophotometric (UV-vis) and solubility studies. New techniques could provide a better understanding of actinide hydrolysis. For instance, EXAFS showed that the coordination numbers of actinide aqua ions are not always well established. Measurements are consistent with coordination numbers 9–11 for Th^{4+}, U^{4+}, and Np^{4+}. [45] EXAFS studies also showed that the uranyl aquo ion was found as $[UO_2(H_2O)_5]^{2+}$ in solution. [46]

The literature shows some inconsistency in analytical results, which are highly dependent on the experimental procedure and on the underestimation of colloid formation. Unfortunately, some spectroscopic studies have included oversaturated solutions. Most of the time, colloid formation is avoided by working at low concentration (~10^{-4}-10^{-5} M) and low pH (< 2 - 3); or using solvent extraction techniques. The use of new techniques, such as laser induced breakdown detection (LIBD), could help to reveal actinide colloid sizes and their formation. Such techniques were used with Np(IV) and Pu (IV) when their concentration exceeded the solubility product at low pH. [44]

Thermodynamic data on polynuclear colloid formation cannot be easily obtained or compared. It is not surprising that different authors working in different media, with different ionic strengths, temperature and concentration suggested different sets of species.

4.2.1. Thorium hydrolysis

In general, the use of thorium simplified the study of actinide hydrolysis, in terms of experimental protocol, due to the fact that it has just one stable oxidation state in aqueous media (Th(IV)) and its lower radiotoxicity in comparison to other actinides (2.61 x 10^7 $Bq.g^{-1}$ for Np-237, 4.06 x10^3 $Bq.g^{-1}$for Th-232). Moreover, thorium is the largest tetravalent ion in the periodic table, based on Shannon ionic radii, [47] and should be the least susceptible tetravalent actinide to hydrolysis if the Z^2/r rule is used as a model.

Nevertheless, thorium hydrolysis is a very complex reaction where several species (mono- and polynuclear) exist simultaneously in solution, even at low pH and even around milimolar concentrations, as can be seen in Figure 12.

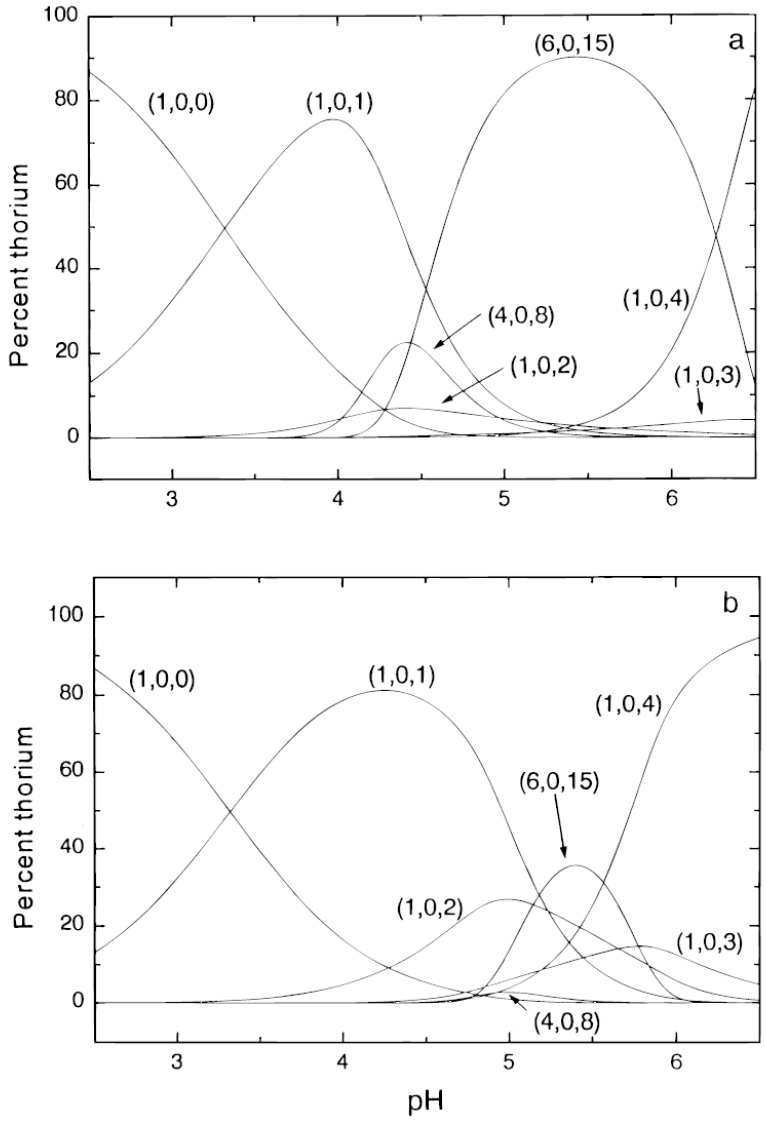

Figure 12: Percentage distribution of Th(IV) at r.t and 1M $NaClO_4$. Cth: a) 0.12 mM, b) 0.01 mM. Numbers in brackets correspond to the stoichiometry of the compound. The first number correspond to the number of metal centres: Th^{4+} in the coumpund, the second number correspond to the number of ligands: A^- and the last to the number of hydroxyls: HO^- [48]

The species proposed in the literature were deduced from titration experiments and the polynuclear species were the result of curve fitting procedures. Most of them are not yet confirmed by spectroscopic methods or other analytical techniques.

Coordination studies reported by Soderholm et al. showed that mononuclear and polynuclear structures could be obtained using water molecules as ligands when thorium compounds were dissolved in several acid media such as HBr [49] and HCl. [50]

4.2.2. Uranium (IV) hydrolysis

Uranium (IV) should be more susceptible to hydrolysis than thorium (IV) due to the Z^2/r rule. This probably contributes to the lack of structural data for U(IV) aqua complexes in the literature. The only available data for polynuclear species are based on a potentiometric titration, in 3M $NaClO_4$, which was interpreted with the formation of $U_6(OH)_{15}^{9+}$. [51] The U^{4+} (aq) ion is estimated to have a pKa of 0.7 (when I = 0 M).

4.2.3. Neptunium (IV) and plutonium (IV) hydrolysis

Neptunium (IV) and plutonium (IV) hydrolysis gets even more complex than uranium hydrolysis. For tetravalent actinides, *Z* is constant, but the ionic radius, *r*, decreases along the actinide series. Therefore, Np (IV) and Pu (IV) cations have a higher positively charged density, causing hydrolysis to occur at lower pH and, on a technical level, the toxicity/activity is much higher. Neptunium (IV) hydrolysis seems to be similar to plutonium (IV) as the first mono nuclear hydroxo species obtained are comparable (Table 2).

	$\log\beta^{o}_{11}$	$\log\beta^{o}_{12}$	$\log\beta^{o}_{13}$	$\log\beta^{o}_{14}$
Np(IV)	14.5 ± 0.2	28.3 ± 0.3	39.2 ± 1	47.1 ± 1
Pu(IV)	14.6 ± 0.2	28.6 ± 0.3	39.7 ± 0.4	47.5 ± 0.5

Table 2: Formation constants of mononuclear species for plutonium (IV) and neptunium (IV) at 25°C. [44]

As described above, actinide hydrolysis is complex, very dependant on the experimental conditions. Therefore, new routes to explore actinide oxide species were designed. In this specific project, it was decided to study the synthesis of actinide alkoxides.

4.3. Metal alkoxides

Bradley *et al.* [52] developed most of the reactions towards metal alkoxides and covered a very broad number of elements from group III to VIII, as well as a few actinides and lanthanides. The study of their solution molecular weights combined with homologues for several metals allowed a description of the aggregation of metal alkoxides, [53] which are usually used as precursors. Bradley *et al.* tried to define the degree of polymerisation of metal alkoxides and tried to predict their

structure. The degree of polymerisation is small compared to organic polymers and surprisingly tends to be the lowest possible. [53] It would mainly depend on the geometry of the compound, the size of the metal and on its ability to expand its coordination number. Unfortunately, it is difficult to prove the predicted degree of polymerisation.

4.3.1. Actinide alkoxides

Actinide alkoxides were first synthesised in the 50's during the Manhattan Project. Gilman *et al.* studied the uranium alkoxides and their derivatives in a search for volatile complexes for isotope separation. [54] Most of the work was then focussed on uranium and was pioneered by Bradley *et al.* [52] and Gilman *et al.* [55] At the time, elementary characterisation such as sublimation temperatures and solution molecular weights of the products were recorded. Since, little work has been done on the synthesis of actinide alkoxides. The synthetic routes are illustrated in Figure 13. [54, 56, 57, 58, 59, 60]

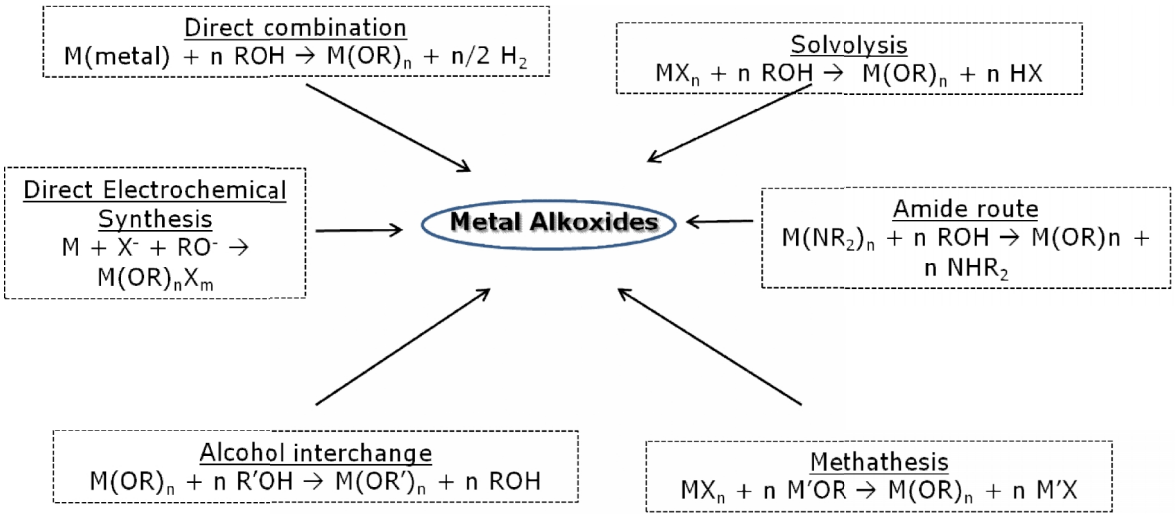

Figure 13: Schematic of the main synthetic routes leading to metal alkoxide complexes (-X= halide and -R= alkyl, aryl groups).

Some of the synthetic reactions mentioned above are not considered as main routes for producing metal alkoxides as the resultant compounds are difficult to separate from the by-products, which is the case for the reaction between alcohols and metal dialkylamides. The metal alkoxide and the dialkylamine by-product are both highly hydrolysable. [52]

It was reported that direct electrochemical methods to synthesise metal alkoxides should be considered for metals having normal hydrogen potentials in the range of 0.1 to 2 V and the alkoxohalide intermediates have to be soluble in the electrolyte. Therefore, most electrochemical

syntheses only allow the formation of metal alkoxohalides. [57] The key reactions for metal alkoxides syntheses are discussed below.

Actinide alkoxides preparation via the reaction between actinide halides and alcohols (solvolysis)

It has been claimed that some metal halide compounds such as zirconium, thorium and uranium chlorides undergo a partial solvolysis when reacted in boiling alcohols. $UCl_4.HOC(CH_3)_3$, [61] $ZrCl_3(C_2OH_5).C_2H_5OH$ and $ThCl_4.C_2H_5OH$ [52] were obtained by Bradley *et al.* instead of the respective metal alkoxides. Ammonia was introduced in this system as an attempt to drive the reaction towards the desired products. This alternative route should activate the alcohol as alcoholate species and drive the metathesis reaction. Several authors published or patented this route describing it as an easy and clean way to obtain metal alkoxides. [52, 62, 63] The ammonia route has not yet not been reported for alcoholysis of the actinide halides.

Reaction between actinide halides and metal alkoxides (methathesis reaction)

It is reported that metal alkoxides were used as a hard base in order to displace the halide groups from the metal ions coordination sphere. Hayton *et al.* [64] reported the preparation of a few compounds using this route, such as: $[Li(THF)]_2[U(OtBu)_6]$ and $[Li(THF)][U_2(OtBu)_9]$.

Direct combination

One of the most convenient routes to obtain an actinide alkoxide is the direct combination of a metal in its metallic state and the respective alcohol. However, a catalyst is needed to penetrate the oxide layer and activate the metal; iodine, Hg and $HgCl_2$ have been used by Bradley *et al*. [52] Barium alkoxides were obtained this way by the reaction of the metal with an excess of isopropanol. The reaction was done under an inert atmosphere, at reflux for 20h. The solvent was retrieved under reduced pressure. In a previous Manchester UMIST thesis, the yields obtained were very low, and the metals studied were Ti, V, Cr and Zr in the presence of ethanol. [56] The iodine route was also reported by Barnhart *et al.* [65] and Van Der Sluys *et al.*[66] for actinides such as thorium and uranium, where dimeric species were successfully synthesised and characterised by XRD.

These reactions and their products, utilising modern spectroscopic and structural techniques, are shedding new light on the stoichiometries and structures of actinide alkoxides and the mechanisms

of their formation. However, much work remains to be done on the synthesis, characterisation, and especially the reaction chemistry of these compounds.

5. PROJECT AIMS

This research project can be segregated in two key components: Solid State Chemistry and Analytical/Solution Chemistry. Nevertheless, both types of project aspire to the same aim which is to advance the knowledge on actinide oxide materials. This section will outline the specific objectives for each project as well as explaining how these studies can be combined.

5.1. Solid state project aim

There is a lack of data on actinide immobilisation within fluorite related structures (pyrochlores, zirconolites) in comparison to other minerals such as zircon, monazite and apatite (Table 3). The table does not present an extensive list of possible hosts for actinide immobilisation. For instance, minerals such as thorite or titanite, are not listed. Nevertheless, Table 3 reflects the amount of work needed for some formulations.

Mineral	Ideal Formula	GeoRef citations in 1998	Durable heavy mineral
Pyrochlore	$(Ca,REE)Ti_2O_7$	494	-
Zirconolite	$CaZrTi_2O_7$	62	-
Apatite	$Ca_{4-x}REE_{6+x}(SiO_4)_{6-y}(PO_4)_y(O,F)_2$	5 098	Yes
Zircon	$ZrSiO_4$	8 055	Yes
Monazite	$CePO_4$	1 711	Yes

Table 3: Mineral phases under investigation for plutonium disposal. [13]

Their synthesis conditions and capability to incorporate actinides and actinide surrogates are well documented, but little is known on their optimisation and its effect on the final ceramic. This was one of the motivations in studying double substitutions within pyrochlore systems, like $Y_2Ti_2O_7$ and their suitability as host for actinide elements.

The $Y_2Ti_2O_7$ system can accommodate tetravalent and trivalent actinides in the yttrium site. Moreover, the titanium site can also endure substitutions, which also allows $Y_2Ti_2O_7$ to host

transition metals that are common contaminants in nuclear waste streams due to the corrosion and dissolution of steel containers. This structural flexibility allowed the study of co-substitutions in $Y_2Ti_2O_7$.

In chapter 3, the Y^{3+} substitution (A site) by Ce^{4+} is reported, as well as the Ti^{4+} substitution by Fe^{3+} in the $Y_{2-x}Ce_xTi_{2-x}Fe_xO_7$ system. The latter substitution was mainly used to compensate the charge balance of the compound. In chapter 4, $Y_2Ti_{2-2x}Fe_xNb_xO_7$ is reported; Fe^{3+} could be potentially accommodated on the Ti^{4+} site, with charge compensation by Nb^{5+}. Co-substitution studied in both chapters could offer a route to improve the radiation tolerance of titanate pyrochlores. This is knwn to be sensitive to composition. Thus, the synthesis of $Y_{2-x}Ce_xTi_{2-x}Fe_xO_7$ and $Y_2Ti_{2-2x}Fe_xNb_xO_7$ are attempts to determine the potential existence of new pyrochlore families. Their structural study will define if they could be potential actinide hosts.

5.2. Solution Chemistry Project Objectives

The strict investigation of An (IV) *via* spectroscopic methods would not bring much more to the already extensive reported literature. As described previously, there are a significant amount of results for hydrolysis product formation in the literature, and their discrepancies are mainly due to differences in experimental conditions. Another similar study might only produce another set of data to add to the extensive literature reports. In this PhD project, two approaches were used in order to reduce the extent of hydrolysis. In aqueous media, the metal cations were capped by the introduction of an organic ligand. In dry media, novel metal alkoxides were hydrolysed with a known amount of water. Both routes could lead to the synthesis of new materials, while studying their growth in solution.

5.2.1. Controlled hydrolysis using a caping ligand in aqueous solution

Decommissioning active sites is an important aspect of the nuclear industry. A requirement for this portion of the nuclear industry is to find new waste decontamination techniques using physical or chemical methods [67] that would be efficient to treat the contaminated material. Among the chemical methods, decontamination can be achieved using organic ligands, which are similar to amino acids, as they contain the same chemical groups ($-NH_2$, -OH, and –COOH). Carboxylic acids are among the chemicals frequently used. [68] Among those, nitriloacetic acid (NTA) and ethylenediaminetetraacetic acid (EDTA) [69, 70, 71, 72, 73, 74] were widely studied in the past and are similar to the organic ligand used in this thesis.

In this study, N-(2-hydroxyethyl)iminodiacetic acid ($HOCH_2CH_2N(CH_2COOH)_2$, also called heidi, was used in order to restrict the number of free sites in the coordination environment of the metal ion, which would be available for aqua molecules; in an attempt to control hydrolysis. A schematic is shown in Figure 14.

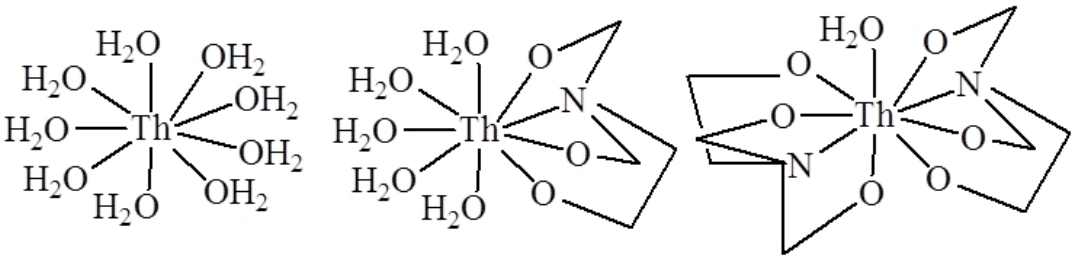

Figure 14: Schematic possible structures of $[Th(H_2O)_9]$, $[Th(H_2O)_5(heidi)]^+$and $[Th(H_2O)(heidi)_2]^{4-}$.

Previous work with heidi, reported by Heath *et al.*, shows the formation of clusters with many Lewis acidic metal ions such as iron, [75] aluminium [76] and gallium [77] *via* controlled hydrolysis. The aim of this study was to obtain polyoxoclusters, like those obtained with the p elements and 3d metal ions, but with actinide metal ions. The existence of uranium polymers [78], Figure 15, and the plutonium oxide nanocluster [79] $[Pu_{38}O_{56}(H_2O)_8]^{14-}$, Figure 16, shows that a good understanding of controlled hydrolysis can result in cluster production for actinide cations. However, d and p elements are not necessarily good surrogates for actinide ions due to large differences in physical properties (ionic radius, number of coordination sites, f-orbitals…) and chemical properties (several polynuclear species simultaneously present, oxidation state, electronegativity, geometry…).

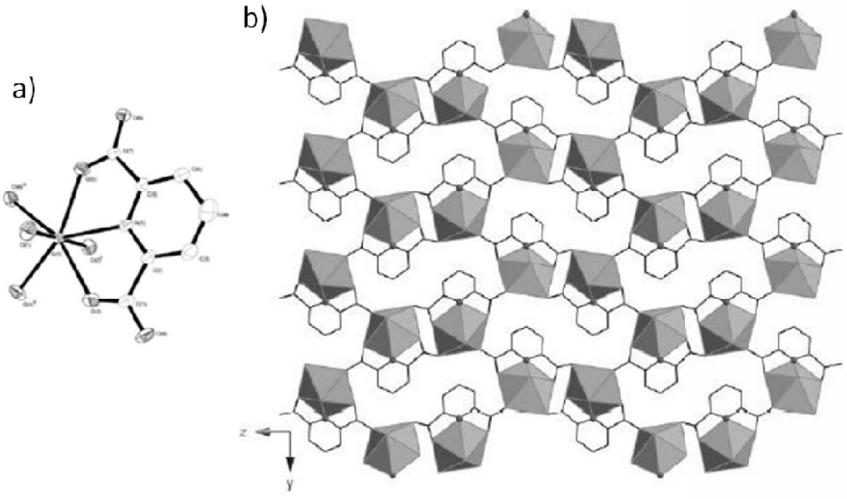

Figure 15: a) $[(UO_2)(C_7H_3NO_4)]$ cluster and b) three-dimensional sheet of $[(UO_2)(C_7H_3NO_4)]$. Black lines are the 2,6-pyridinecarboxylic acid and the polyhedra are the uranium pentagonal bipyramids.

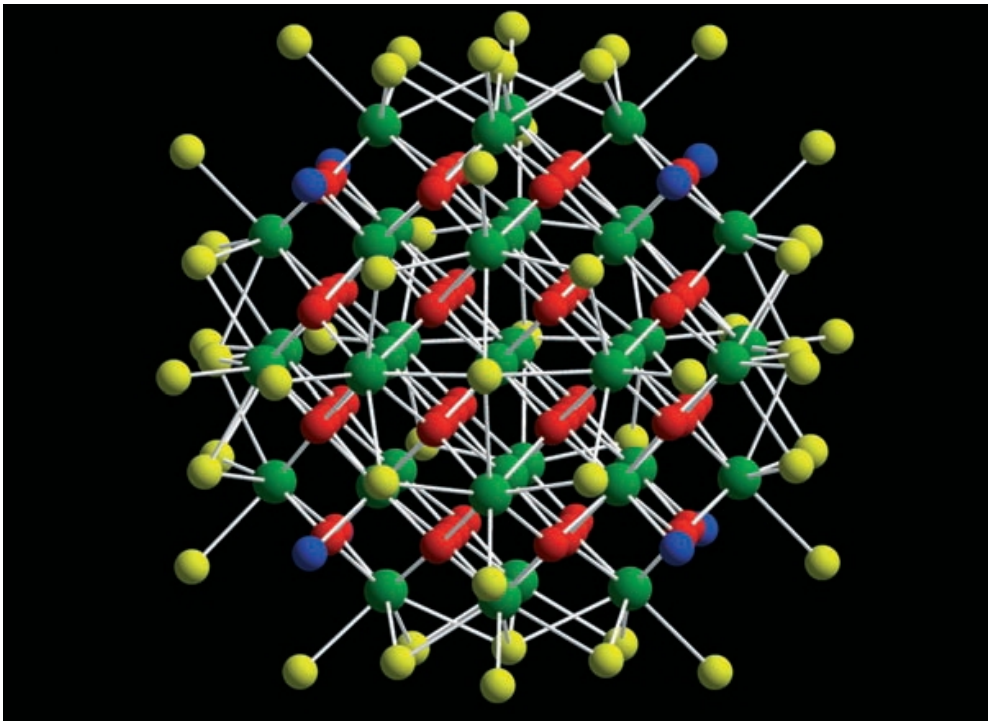

Figure 16: $[Pu_{38}O_{56}Cl_{54}(H_2O)_8]^{14-}$ cluster, where Pu(IV) (green), O_2^- (red), O from water (blue), Cl^- (yellow).

5.2.2. Controlled hydrolysis from metal organic compounds

Anhydrous precursors are also utilised to produce and study novel actinide oxide compounds, which can be produced by condensation reactions. This can be induced by their chemical instability, the introduction of water in trace levels or by their reaction with organic acids (methacrylates acids and aminopolicarboxylates acids for example). Several types of organometallics would be suitable for this kind of study, such as metal alkoxides.

Once actinide alkoxides are completely characterised, attempts to synthesise actinide clusters will be made by mixing the alkoxide compounds with methacrylates and aminopolicarboxylates used as a capping ligand, just as Kicklebick *et al.* did with zirconium alkoxides, [80] Figure 17, or as Sattelberger *et al.* who introduced a known amount of water to a dry system. [81] There is a choice between two different routes in order to form inorganic compounds *via* a sol-gel approach.

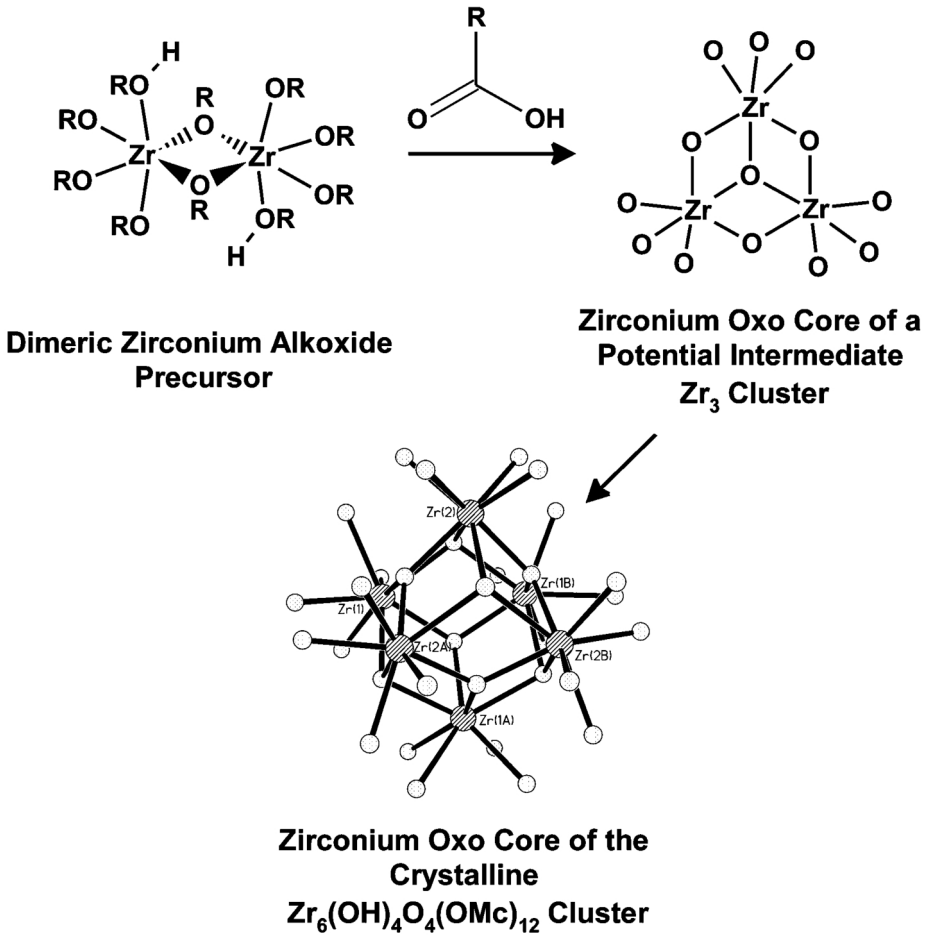

Figure 17: Scheme of the hydrolysis of a dimeric zirconium alkoxide *via* controlled hydrolysis.

6. ACTINIDE ALKOXIDES AS PRECURSORS FOR CERAMICS

High temperatures are needed for conventional powder synthesis of ceramics and glasses. This is due to the low reactivity of the initial substances, oxides, carbonates and nitrates, for instance. On the other hand, organometallic products are extremely reactive. Therefore, their use as precursors in a homogenous liquid phase for the synthesis of high density materials is appealing. Most common organometallics used for this purpose are metal alkyls and metal alkoxides. However, alkoxides are easier to handle, as metal alkyls can be extremely pyrophoric. They also react easily with one another, which is a benefit in a chemical process promoted by condensation reactions. Metal alkoxides are versatile compounds, and the functional group, -OR, can be saturated or unsaturated organic groups. Metal alkoxides are very reactive towards nucleophilic reagents, such as water, which induces their polymerisation. This process is now known as the Sol-Gel process. Most of the

early research by Stöber *et al.* was based on the study of the growth of silicon oxides from silicon organic precursors. [82] Nowadays, this approach is used for a large number of elements, and metal alkoxides are known for a large variety of metal ions, including the lanthanides and a few actinides.

6.1. Sol-Gel Process [83]

The sol-gel process provides a new way to synthesise a macromolecular product from molecular precursors where a network is built through oxygen bonds (oxo or hydroxyl bridges). When an inorganic or organometallic precursor monomer undergoes hydrolysis *via* a polymerisation reaction, they form a colloidal suspension called sol. The colloid can then aggregate and form a solid like state, which interconnects creating a rigid network whose average length is greater than a micrometer: *i.e.* a gel. The term has four categories denoted by Flory (well ordered lamellar structures, covalent polymeric networks completely disordered, polymer networks formed through physical or chemical aggregation, particular disordered structures). During the process, Figure 18, the sol is subjected to a series of operations: gelling, drying, pressing and casting which results in several phase and structural transformations.

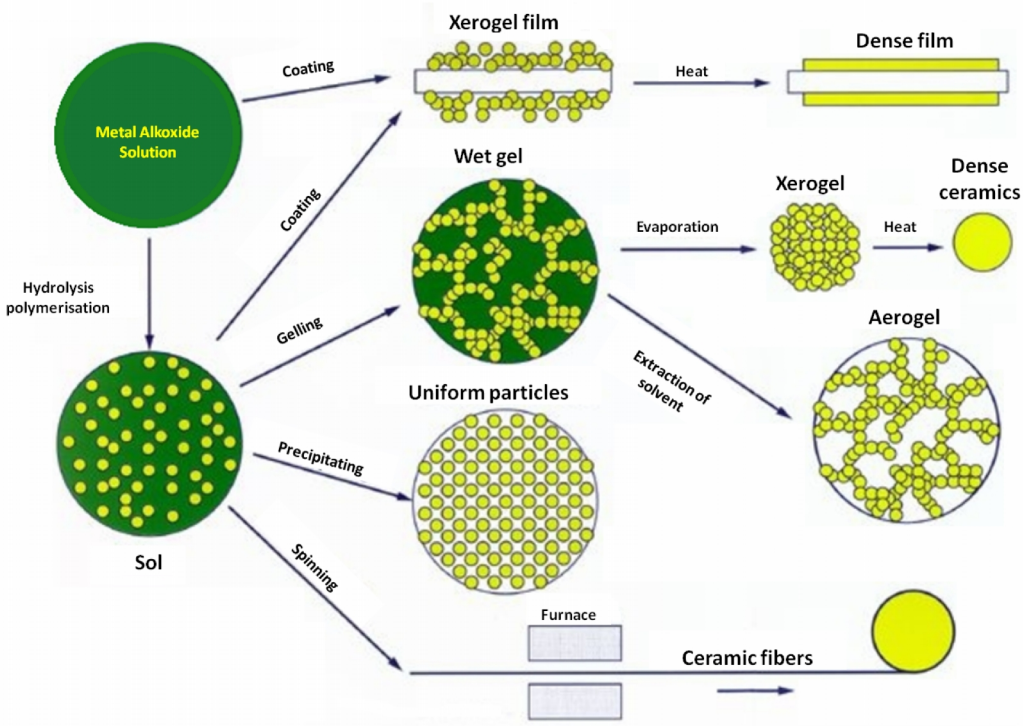

Figure 18: Scheme for a possible sol-gel process. [84]

Many advantages are offered by this type of procedure in comparison with a conventional powder method. More homogeneous mixed compounds can be obtained. The rheological properties of sols and gels allow the formation of fibers, composites and films (such as MOCVD and ALD) and the temperature needed is much lower, which makes the process economically interesting and can lead to the synthesis of unusual materials. [85,86,87] However, precursors such as metal alkoxides are expensive compounds; ageing and drying steps have to be thoroughly monitored as they are crucial in order to obtain high end materials without cracks, moreover organic residues can be present. [83]

This research project also aimed to use metal alkoxides, as well as their potential derivatives hydrolysed compounds, as precursors to produce ceramics *via* an alkoxide/wet route. This method should improve the homogeneity within the microstructure of the targeted ceramics, an example of a material obtained via the alkoxide route is shown in Figure 19. [88] The procedure could provide remarkable new materials.

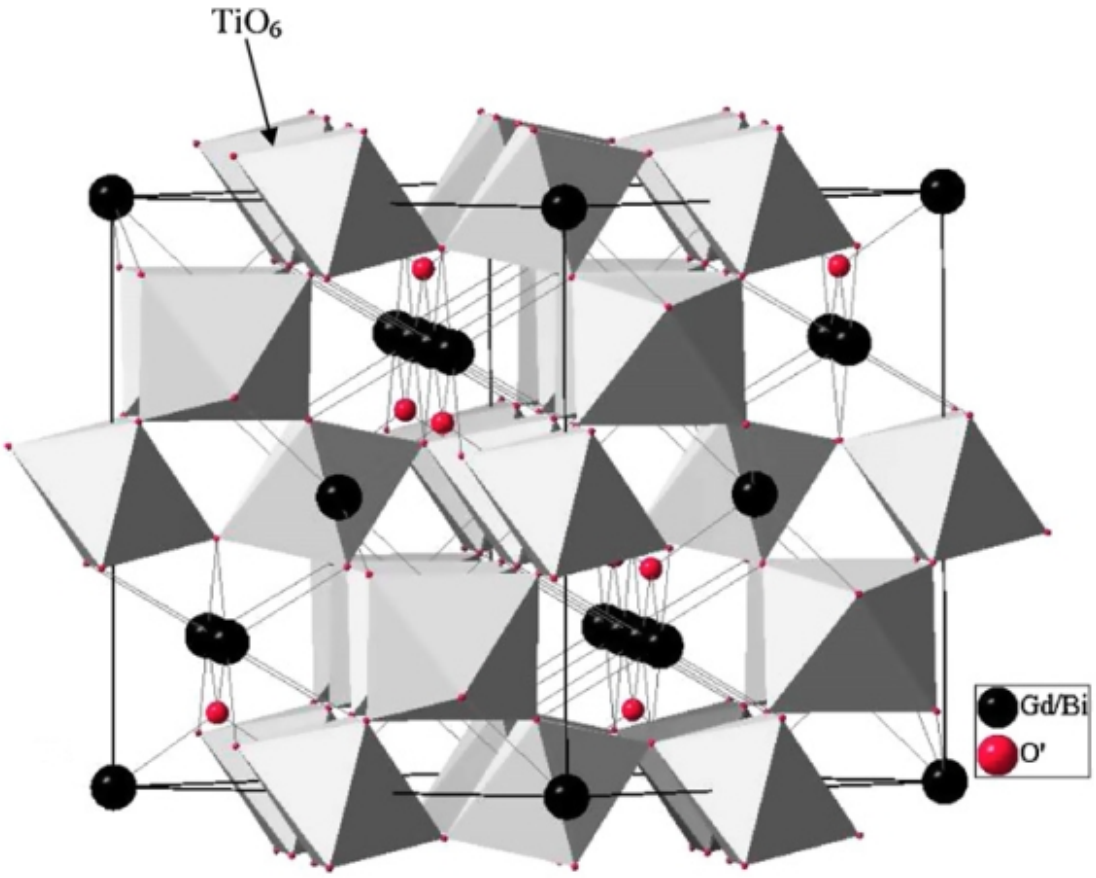

Figure 19: Cubic pyrochlore structure for $Gd_{2-2x}Bi_{2x}Ti_2O_7$ showing Ti octahedral sites and Gd/Bi cations channels. Material obtained via a sol-gel route.

The collaboration between the University of Sheffield (Immobilisation Science Laboratory) and the University of Manchester (Centre for Radiochemistry Research) allowed a broad scope to this PhD study. The following chapters will detail each different project that contributed to this thesis.

The candidate wrote all the chapters within this document. There were a few contributions to the work reported in this PhD thesis. The structural refinements of neutron and single crystal diffraction were produced with the help of Prof. Neil Hyatt and Dr. Sarah Heath, respectively. Magnetic susceptibility measurements were run by Dr Floriana Tuna, the transmission electron microscopy and SEM results were produced with the help of Dr. Martin Stennet.

7. REFERENCES

[1] P.D. Wilson, *The nuclear fuel cycle: from ore to wastes*, 1996, Oxford University Press, ISBN: 0198565402.

[2] A. P. Paiva, P. Malik, *Journal of Radioanalytical and Nuclear Chemistry*, 2004, **261**, N^{o} 2, 485-496.

[3] Nuclear National Lab, *Introduction to the nuclear industry course*, 2009, DIAMOND consortium.

[4] H. C. Aspinall, *Chemistry of the f-block elements*, advanced chemistry texts volume 5, 2001, Gordon and Breach Science Publishers, Amsterdam, ISBN: 905699333X.

[5] J. J. Katz, G. T. Seaborg, L. R. Morss, *The Chemistry of the Actinide Elements Second Edition*, 1986, J. W. Arrowsmith Ltd, Bristol, UK.

[6] G.R. Choppin, J-O. Liljenzin and J. Rydberg, *Radiochemistry and Nuclear Chemistry 3rd Edition*, 2002, Butterworth-Heinemann publishers, ISBN: 0750674636.

[7] C. E. Housecroft, E. Catherine and A. G. Sharpe, *Inorganic Chemistry*, 2001, Ashford Colour Press Ltd, Gosport, ISBN: 0582310806.

[8] D. L. Clark, *The Chemical Complexities of Plutonium, Los Alamos Science,* 2000, **26**, 364-381.

[9] N.Kaltsoyannis and P. Scott, *The f Elements*, 1999, Oxford University Press: Oxford, ISBN 0198504675.

[10] R. Telchadder, *Spectroscopic Studies of Uranyl Solution Phase Complexation by Short Chain β-Hydroxy Carboxylic Acids,* thesis from the University of Manchester, 2010.

[11] J. Bendix and A. Bøgevig, *Inorganic Chemistry*, 1998, **37**, 5992-6001.

[12] T. Gosh, C. Bandyopadhyay, *Transition Metal Chemistry*, 2004, **29**, 444-450.

[13] R.C. Ewing, *Proceedings of National Academy of Sciences*, 1999, **96**, 3432-3439.

[14] G.R Lumpkin, K. L. Smith, R. Giere and C. T. Williams, *Geological Society, London, special publications*, 2004, **236**, 89-111.

[15] R.C. Belin, P.M. Martin, P.J. Valenza and A.C. Scheinost, *Inorganic Chemistry*, 2009, **48**, 5376-5381.

[16] R.E. Sykora, P.E. Raison and R.G. Haire, *Journal of Solid State Chemistry*, 2005, **178**, 578-583.

[17] I.W. Donald, B.L. Metcalfe and R.N.J. Taylor, *Journal of Material Sciences*, 1997, **32**, 5851-5887.

[18] C.Fillet, T. Advocat, F. Bart, G. Leturcq, and H. Rabiller, *Comptes Rendus Chimie*, 2004, **7**, 1165-1172.

[19] Y. Zhang, M.W.A. Stewart, H. Li, M.L. Carter, E.R. Vance and S. Moricca, *Journal of Nuclear Materials*, 2009, **395**, 69-74.

[20] R.C. Ewing, W.J. Weber and J. Lian, *Journal of Applied Physics*, 2004, **95**, 5949-5971.

[21] W. Lutze and R.C. Ewing, *Radioactive Waste forms for the future*, Elsevier Science, Amsterdam, 1988, 233-334.

[22] A.E. Ringwood, S.E. Kesson, N.G. Ware, W. Hibberson and A. Major, *Nature*, 1979, **278**, 219-223.

[23] R. Restani, M. Martin, N. Kivel and D. Gavillet, *Journal of Nuclear Materials*, 2009, **385**, 435–442.

[24] S. Lutique, R.J.M. Konings, V.V. Rondinella, J. Somers and T. Wiss, *Journal of Alloys and compounds*, 2003, **352**, 1-5.

[25] V.M. Oversby, C.C. McPheeters, C.Degueldre and J.M. Paratte, *Journal of Nuclear Materials*, 1997, **245**, 17-26, **1997**

[26] E.N.S Muccillo, *Cerâmica*, 2008, **54**, 129-144.

[27] M.A. Subramanian, J.E. Greedan, N.P. Raju, A.P. Ramirez and A.W. Sleight, *Journal de Physique IV*, 1997, **7**, C1, 625-628.

[28] J.E. Greedan, N.P. Raju, A. Maignan, Ch. Simon,, J.S. Pedersen, A.M. Niraimathi, E. Gmelin and M.A. Subramanian, *Physical review B – Condensed Matter and Materials Physics*, 1996, **54**, Issue 10, 7189 – 7200.

[29] L.K. Joseph, K.R. Dayas, S. Damodar, B. Krishnan, K. Krishnankutty, V.P.N. Nampoori and P. Radhakrishnan, *Spectrochimica Acta – Part A: Molecular and Biomolecular Spectroscopy*, 2008, **71**, Issue 4, 1281-1285.

[30] J. Yang and Y. Su, *Materials Letters*, 2010, **64**, Issue 3, 313-316.

[31] A.E. Ringwood. *Fortschritt in Mineralogie,* 1980, **58**, 149-168.

[32] M.A. Subramian, G. Aravamudan and G.V. Subba Rao, *Progress in Solid State Chemistry*, 1983, **15**, 55-143.

[33] C.R. Stanek, *Atomic Scale Disorder in Fluorite and Fluorite Related Oxides*, Thesis of Imperial College of London, 2003.

[34] B.C. Chakoumakos, *Journal of Solid State Chemistry,* 1984, **53**, 120-129.

[35] R.S. Roth, *Journal of Research of the National Bureau of Standards*, 1956, **56**

[36] G.C. Lau, B.D. Muegge, T.M. McQueen, E.L. Duncan and R.J. Cava, *Journal of Solid State Chemistry*, 2006, **179**, 3126-3135.

[37] M.R. Gilbert, *Zirconolite waste-forms for plutonium disposition*, Thesis of the University of Manchester, 2009.

[38] A. A. Coehlo, R.W. Cheary, and K.L. Smith, Journal of Solid State Chemistry, 1997, **129**, 346–359.

[39] F. Mazzi and R. Munno, American Mineralogist, 1983, **68**, 262-276.

[40] B.M. Gatehouse, I.E. Grey, R.J. Hill, and H.J. Russell, *Acta Crystallographica Section B*, 1981, **37**, 306-312.

[41] J-P. Jolivet, J. Livage and H. Marc, *Metal oxide chemistry and synthesis: from solution to solid state*, John Wiley, ISBN: 0471970565, 2000.

[42] J.J. Harrison and G.D. Thyne, *Geochimica et Cosmochimimica Acta*, 1992, **56**, 565−586.

[43] A. Kremleva, S. Krueger and N. Roesch, *Inorganica Chimica Acta*, 2009, **362**, 2542−2550.

[44] V.Neck, J.I. Kim, B.S. Seidel, C.M. Marquant, K. Dardenne, M.P. Jensen and W. Hauser, *Radiochimica Acta*, 2001, **89**, 439-446.

[45] H. Moll, M.A. Denecke, F. Jalilehvand, M. Sandstrom, I. Grenthe, *Inorganic Chemistry*, 1999, **38**, 1795–1799.

[46] C. Henning, J. Tutschku, A. Rossberg, G. Bernhard and A.C. Scheinost, *Inorganic Chemistry*, 2005, **44**, 6655-6661.

[47] R.D. Shannon, *Acta Crystallographica Section A*, 1976, **32**, 751-926.

[48] C. Ekberg, Y. Albinsson, M.J. Comarmond and P.L. Brown, *Journal of Solution Chemistry*, 2000, **29**, Issue 1, 63-86.

[49] R.E. Wilson, S. Skanthakumar, P.C. Burns and L. Soderholm, Angewandte Chemie International Edition, 2007, **46**, 8043-8045.

[50] R.E. Wilson, S. Skanthakumar, G. Sigmon, P.C. Burns and L. Soderholm, *Inorganic Chemistry*, 2007, **46**, 2368-2372.

[51] S. Hietanen, *Acta Chemica Scandinavica*, 1956, **10**, 1531-1546.

[52] D.C. Bradley, R.C Mehrotra, and D.P. Gaur, *Metal Alkoxides*, London Academic Press, 1978.

[53] D.C. Bradley, *Nature*, 1958, **182**, 1211-1214.

[54] D.L. Clark, A.P. Sattelberger, W.G. Van Der Sluys and J.G. Watkin, *Journal of Alloys and Compounds*, 1992, **180**, 303-315.

[55] W. G. Van der Sluys, and A. P. Sattelberger, *Chemical Reviews*, 1990, **90**, 1027-1040.

[56] Alan Matear, *The synthesis of metal alkoxides*, Thesis of the University of Manchester, 1992.

[57] V.A Shreider, E.P. Turevskaya, N.I. Koslova and N.Ya Turova, *Inorganica Chimica Acta*, 1981, **53**, 73-76.

[58] S. Fortier, G. Wu and T. Hayton, *Inorganic Chemistry*, 2008, **47**, 4752 – 4761.

[59] D.M. Barnhart, T.M. Frankcom, P.L. Gordon, N.N. Sauer, J.A. Thompson and J.G. Watkin, 1995, *Inorganic Chemistry*, **34**, 4862-4867.

[60] W.G Van Der Sluys, J.C. Huffman, D.S. Ehler and N.N. Sauer, *Inorganic Chemistry*, 1992, **31**, 1316-1318.

[61] D.C. Bradley, R.N. Kapoor and B.C. Smith, *Journal of Inorganic and Nuclear Chemistry*, 1962, **24**, 863-867.

[62] D.C. Bradley and W. Wardlaw, *Journal of the Chemical Society*, 1951, 280-285.

[63] US Patent 3 754 011

[64] S. Fortier, G. Wu and T. Hayton, *Inorganic Chemistry*, 2008, **47**, 4752 – 4761.

[65] D.M. Barnhart, T.M. Frankcom, P.L. Gordon, N.N. Sauer, J.A. Thompson and J.G. Watkin, Inorganic Chemistry, 1995, **34**, 4862-4867.

[66] W.G Van Der Sluys, J.C. Huffman, D.S. Ehler and N.N. Sauer, *Inorganic Chemistry*, 1992, **31**, 1316-1318.

[67] International Atomic Energy Agency, *Technical reports series*, ISBN 92–0–104605–7, 2006.

[68] P. Thuery, *Inorganic Chemistry*, 2011, **50**, 1898–1904.

[69] E. Reinoso-Maset, P.J. Worsfold and M.J. Keith-Roach, *Environmental Pollution*, 2012, **1 62**, 399-405.

[70] M.J. Cabell, *Analyst*, 1952, **77**, 859-866.

[71] J. Starý and J. Prášilová*, Journal of Inorganic and Nuclear Chemistry*, 1961, **17**, 361-365.

[72] G. Gopala Rao and G. Somidevamma, *Fresenius' Journal of Analytical Chemistry*, 1957, **157**, 27-32.

[73] K. Doi, *Talanta*, 1980, **27**, 859-865.

[74] U.C. Maiwal and K. Srinivasulu, *Mikrochimica Acta*, 1983, **79**, 329-332.

[75] J.C. Goodwin, R.Sessoli, D. Gatteschi, W. Wernsdorfer, A.K. Powell and S.L. Heath, *Journal of the Chemical Society*, *Dalton Transactions*, 2000, **12**, 1835-1840.

[76] S.L. Heath, P.A. Jordan, I.D. Johnson, G.R. Moore, A.K. Powell, M. Helliwell, *Journal of Inorganic Biochemistry*, 1995, **59**, 785-794.

[77] J.C. Goodwin, S.J. Teat and S.L. Heath, *Angewandte Chemie International Edition*, 2004, **43**, 4037-4041.

[78] M. Frisch, C.L. Cahill, *Dalton Transctions*, 2006, 4679-4690.

[79] L. Soderholm, P.M. Almond, S.Skanthakumar, R.E. Wilson and P.C. Burns, *Angewandte Chemie International Edition*, 2007, **47**, 298-302.

[80] G. Kickelbick, M. Puchberger, *J. Chem. Soc., Dalton Trans.*, pp.3892-3899, **2002**

[81] W.G. Van Der Sluys and A.P. Sattelberger, *Polyhedron*, 1990, **9**, 1843-1848.

[82] W. Stöber, A. Fink and E. Bohn, *Journal of Colloid and Interface Science*, 1968, **26**, 62-69.

[83] L. L. Hench and J.K. West, *Chemical Reviews*, 1990, **90**, 33-72.

[84] C.J. Brinker and G.W. Scherer, *Sol-Gel Science - The Physics and Chemistry of Sol-Gel Processing*, 1990, New York, Academic Press.

[85] J. Livage, M. Henry and C. Sanchez, *Progress in Solid State Chemistry*, 1988, **18**, 258-341.

[86] G.I. Spijksma, L. Kloo, H.J.M. Bouwmeester, D.H.A. Blank, V.G. Kessler, *Inorganica Chimica Acta*, 2007, **360**, 2045-2065.

[87] J.D. Mackenzie, *Journal of Non-Crystalline Solids*, 1985, **73**, 631-637.

[88] A. Garbout, S. Bouattour, A.W. Kolsi, *Journal of Alloys and Compounds*, 2009, **469**, 229-236.

Chapter 2:

EXPERIMENTAL TECHNIQUES AND METHODS

This chapter contains theoretical details of the main experimental techniques and methods used during this PhD project. Experimental specifications of the apparatus and details of sample preparation will be presented in the experimental sections of the following relevant chapters.

1. DIFFRACTION TECHNIQUES

1.1. Production of X-rays

The production of X-rays was originally discovered by Roentgen, in 1895, using a Crooke tube. [1] The device consisted of a glass envelope under high vacuum, with a wire element at one end forming the cathode, and a metal target at the other end forming the anode. When a high voltage was applied to the electrodes, electrons formed at the cathode would travel towards the anode and hit the metal target with a high energy. The impact slows the electrons which dissipate energy by emitting X-rays in all directions. X-rays can be directionally focussed by the use of a monochromator, which is a crystal placed to the incident beam, active for a chosen wavelength. The filament is commonly made of tungsten and the choice of the metal target (anode) will depend on the application needs. The wavelength of the X-rays produced differs depending on the element from which the anode is constructed (commonly copper, iron, chromium or molybdenum). The device components are kept under a reduced atmosphere in order to cool the anode.

1.2. X-ray diffraction (XRD)

Figure 1 is an illustration of the diffraction of an X-ray by a crystal with planar crystal lattice (dark green lines in Fig. 1) distances equal to d. The travel path length is illustrated by the ray paths ABC and A'B'C'. When a crystal is irradiated with X-rays of a fixed wavelength, λ, at a certain incident angle, θ, diffracted X-rays are obtained. Intense X-ray reflections are produced when scattered X-rays interfere constructively. This occurs when the wavelength is equal to a combination of the crystal lattice planar spacing and the incident angle, which is expressed by the Bragg law:

$$n\,\lambda = 2\,d\sin\theta \qquad (1)$$

Where n is the order of reflection of the X-rays, λ (nm) is the fixed wavelength of the incident X-rays, d (nm) is the interplanar spacing of the crystal and θ (^{o}) is the angle of incidence.

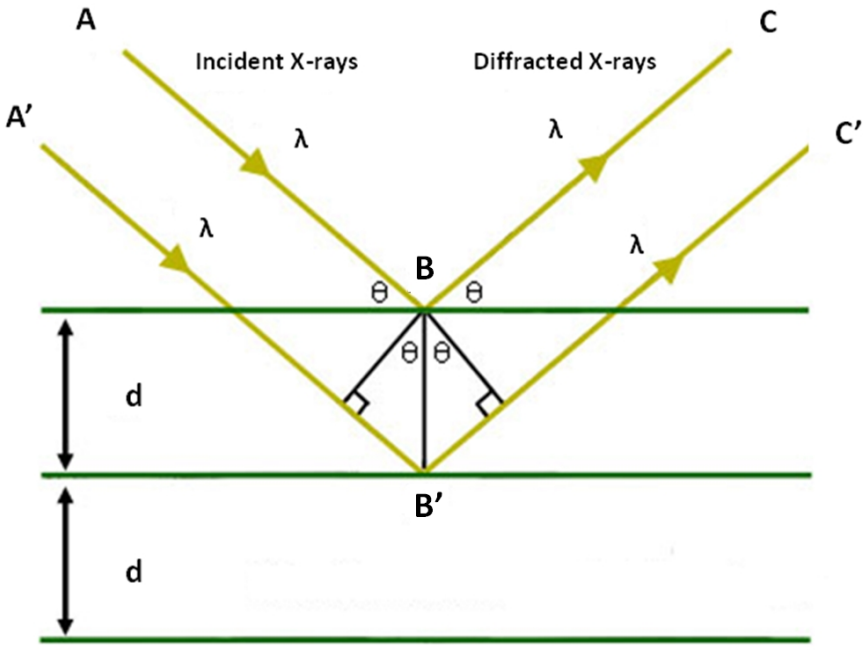

Figure 1: Illustration of the Bragg law.

Any plane can also be characterised by a vector perpendicular to it. Therefore, the projection of a position vector of any point belonging to the plane is constant and independent of the point. The projection is also called reciprocal lattice. The collection of the distances of the planes to the origin, the d-spacing, is used in X-ray diffraction (XRD) to identify and characterise samples independently of a specific point. Solving Bragg's equation gives the d-spacing between the crystal lattice planes of atoms. The structural identification of an unknown sample is based on the collection of the reciprocal lattice of all the planes.

A key component of all XRD methods is the angle between the incident and diffracted rays. Powder and single crystal diffraction vary in instrumentation beyond this.

1.3. Powder XRD [2]

Max von Laue discovered in 1912 that crystalline substances act as three-dimensional crystals for X-ray wavelengths similar to the spacing of planes in their crystal lattice. Therefore X-ray diffraction is used as a common technique for the study of crystal structures and atomic spacing.

As described above, the X-rays are generated by a X-ray tube, filtered to produce monochromatic radiation, collimated to concentrate, and directed toward the sample. The interaction of the incident rays with the sample produces constructive interference (and a diffracted ray) when the conditions satisfy Bragg's Law. By scanning the powdered sample through a range of 2θ angles, all possible diffraction directions of the lattice should be attained due to the random orientation of the

powdered material. The identification of the sample is typically achieved by comparison of the d-spacing data with standard reference patterns.

1.4. Neutron Diffraction (ND) [3]

Neutron diffraction is a technique that uses neutrons to determine the atomic structure of a material. Similarly to XRD, Bragg's law predicts the direction of the diffracted beam. Their intensity is predicted by the structure factor.

Unlike X-rays, neutrons are scattered by the nucleus of an atom and not by electron clouds. Therefore, ND can determine the 'true' atomic positions and magnetic moments in solids. Also, light elements, such as hydrogen and oxygen, can be accurately located because there is no dependence of neutron diffraction lengths on atomic weights (Z). Moreover, elements with similar Z values may also be distinguished. The efficiency of scattering is independent of the scattering angle, the wavelength of neutrons is much larger than the size of an atom, and therefore there are no interference effects.

There are generally two types of neutron sources. The first are spallation sources, where neutrons are generated by striking pulses of highly accelerated protons onto a heavy metal target. This kind of source can be pulsed or continuous depending on the application requirement. The other type of neutron source is a reactor source, where neutrons are directly generated from a nuclear reactor in which the core is specifically designed to maximise neutron flux. The neutron data in this PhD project were collected from a spallation neutron source located at the Paul Scherrer Institute (PSI), in Switzerland.

1.5. Data Processing

Powder XRD [2]

As previously mentioned, a typical powder diffraction pattern is a plot of scattered intensities versus 2θ. Software packages, such as WinXpow, include several analysis tools that can extract crystallographic information (unit cell dimensions and symmetry) from raw diffraction data.

Peak search functions are commonly combined with patterns search and match tools. This produces a pattern suitable for the identification of phases. However, the accuracy of the generated pattern depends on the raw data quality and on the algorithm employed.

Automatically or manually marked peaks can also be fitted to experimental data by a profile fitting function which usually uses peak positions, their intensities and other relevant variables that describe peak shape. This approach may be difficult to employ if diffraction patterns are complex and contain overlapping reflections.

Full pattern decomposition methods can be applied if some information on the unit cell is known. This method is often used to obtain accurate lattice parameters when a pattern has been indexed but its crystal structure remains unknown.

Structural Refinements [4,5]

The structural refinements present in the following chapters will refer to R_p, R_{wp}, R_{exp} and χ^2 parameters, which are given by on the following equations:

R-pattern $$R_p = \frac{\sum |y_i(obs) - y_i(calc)|}{\sum y_i(obs)} \quad (2)$$

R-weighed profile $$R_{wp} = \left[\frac{\sum w_i (y_i(obs) - y_i(calc)^2}{\sum w_i (y_i(obs))^2}\right]^{1/2} \quad (3)$$

R-expected $$R_{exp} = \left[\frac{(N-P)}{\sum w_i (y_i(obs))^2}\right]^{1/2} \quad (4)$$

Indicator of goodness-of-fit $$\chi^2 = \left(\frac{R_{wp}}{R_{exp}}\right)^2 \quad (5)$$

Where y_i is the intensity at the i^{th} step, $y_i(obs)$ is the intensity of the observed data, $y_i(calc)$ the intensity of the calculated data, w_i is the weighing factor of the observed data, N is the number of steps and P is the number of parameters in the model. The R-pattern is also commonly called R-value.

Different procedures are applied in order to solve single crystal and neutron diffraction data. Currently direct and Rietveld methods are most widely used.

Single Crystal Refinement [6]

During this PhD project, single crystal crystallographic data were processed by direct methods. These procedures derive diffraction phases directly from experimentally measured diffraction amplitudes.

After the data have been collected, corrections for instrumental factors (polarisation effects, X-ray absorption and crystal decomposition) must be applied to the entire data set. This integration

process reduces the raw data to a smaller set of individual integrated intensities. These corrections and processing procedures are typically part of the software package that runs the data collection.

Once an initial crystal structure is obtained, various steps follow to attain the best possible fit between the observed and calculated crystal structure. The results of the structure refinement yield a list of atom assignments in the unit cell, shape of the anisotropic intensity centre for each atom (thermal parameters), and the distance of the nearest atomic neighbours (angles between nearest neighbours are also given). The quality of a solution is assessed by the values of the R-value and goodness-of-fit (GooF).

R1, also called R-value, is the percentage difference between the calculated and observed models. Ideal solutions would have R-values of 0, but R-values below 5% are considered adequate.

GooF refers to the "goodness of fit" of the calculated crystal structure and takes into account the number of observed reflections and the parameters used. At the end of refinement, the GooF value should approach 1.

ND Refinement method

The ND data were refined by a Rietveld method. [5] The position and intensity of Bragg peaks are used in a least squares approach to refine the theoretical profile until it matches with the measured profile. The steps in Figure 2 are performed to accomplish a Rietveld refinement.

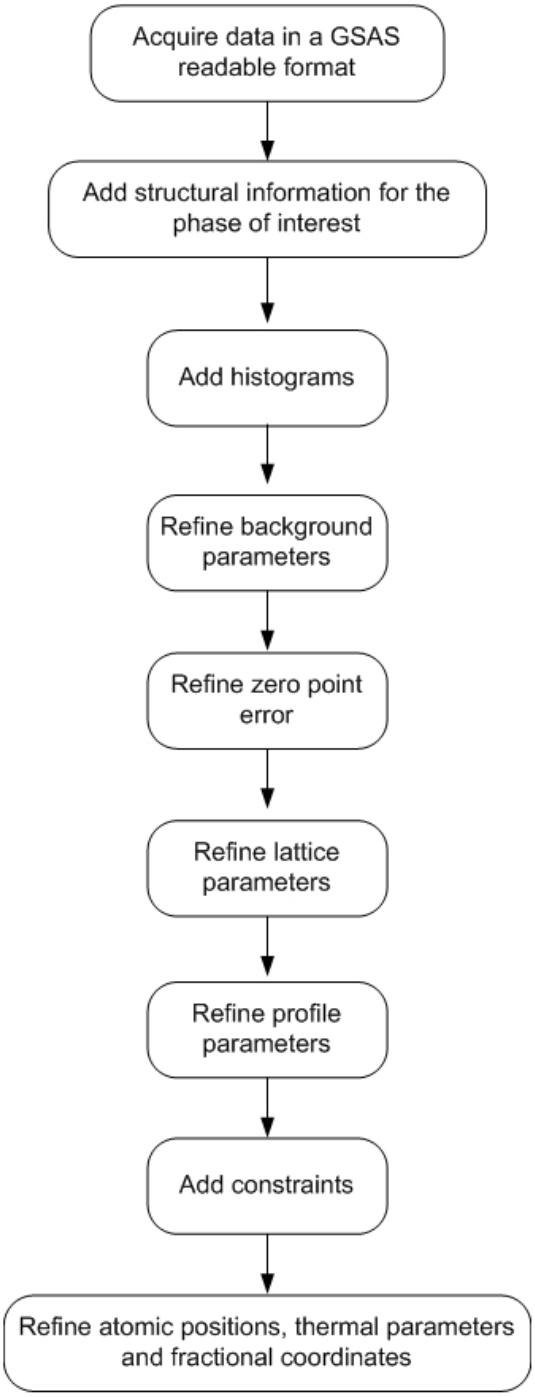

Figure 2: Steps followed to perform Rietveld analysis. [5]

Difference profile plots and goodness of fit parameters were used to measure the reliability of the Rietveld refinement. A difference profile plot is a graphical representation of the difference between the empirical and the calculated data. This graphical representation is a very effective tool to guide the user through a refinement if combined with the examination of R_p, R_{wp}, R_{exp} and χ^2.

The magnitudes of the values indicate how well the observed data fit the structural model. A value of $\chi^2 \sim 1$ indicates an ideal fit. If data are over-collected χ^2 values can be greater than 1. R_p and R_{wp} values of 10 % or less are likely to indicate that the chosen model is correct.

Moreover, the chemical sense of a structural model is an important criterion for direct or Rietveld methods. A good model is also characterised by sensible interatomic distances, valence bond sums, bond angles and stoichiometry.

2. TRANSMISSION ELECTRON MICROSCOPY (TEM)

TEM is a versatile technique which can be used to obtain crystallographic and morphological information as patterns can reveal subgrain defects. In this project this technique was used to confirm structural data analysis obtained from other techniques.

A transmission electron microscope has a source at the top of the microscope which emits electrons that travel through a vacuum in the column of the microscope. Electrons are negatively charged particles incapable of passing through glass. Therefore, the lenses used to focus the beam are electromagnetic. The electron beam produced then travels through the studied specimen. Depending on the density of the material present, some of the electrons are scattered. The unscattered electrons hit a fluorescent screen, and create an image of the specimen structure with its different parts displayed according to their density. The image can be studied directly by the operator or photographed with a camera.

3. X-RAY ABSORPTION SPECTROSCOPY (XAS) [7]

XAS or XAFS (X-ray Absorption Fine Structure) covers X-ray absorption near edge structure (XANES) and extended X-ray absorption fine structure (EXAFS) spectroscopies. XANES can be used to determine the valence state and coordination geometry, while EXAFS is used to determine the local molecular structure of a particular element within a sample.

3.1. Principles of X-ray absorption spectroscopy

The principles and terminology used in XAS are based on the interactions of X-rays with matter. Atoms have sets of orbitals that can be populated with electrons, which occupy the orbital closest to the nucleus first, because this orbital has the lowest energy. Then the other orbitals are populated in order of increasing energy. The energy required to remove an electron from an atom is the electron binding energy. This energy is lowerer for higher-energy orbitals, located further from the

nucleus than for lower-energy orbitals (closer to the nucleus). This difference occurs because the inner electrons screen the positively charged nucleus from the outer electrons. There are generally two groups of electrons associated with an atom. The bound electrons which occupy the outermost orbitals and participate in chemical bonding (valence electrons) and the electrons that occupy the inner orbitals and are an integral part of the atom (core electrons). Different oxidation states of an atom are determined by charge imbalances caused by the removal of the valence electrons.

3.2. X-ray Absorption

X-ray absorption occurs when an atom acquires all the energy of an X-ray, which is used to excite electrons into higher energy electron orbitals that are unoccupied, or into the continuum (where the electron is no longer associated with the atom). A relaxation process occurs with the release of energy as an electron transitions from a higher-energy electron orbital to fill the empty electron orbital (excitation of core electrons creates core holes). The promotion of an electron into a higher energy state by X-ray absorption takes approximately a femto second (10^{-15} s). The core hole is filled by an electron that transitions from a higher energy orbital. The transition is accompanied by a release of energy. The energy released can be in the form of fluorescence radiation, Auger electron production, secondary electron or photon production.

The absorption of X-rays by a material is designated by the percentage decrease in the incident X-ray intensity (*Io*) or by the energy-dependent absorption length of the material that is the exponential factor, μx. The X-ray absorption coefficient (μ) is the probability for an X-ray to be absorbed by a sample. X-ray absorption spectroscopy involves measuring the absorption coefficient as a function of X-ray energy.

The X-rays go through an ionization chamber to measure the number of incident X-rays (I_o), then through the sample, and then through another ionization chamber to measure the number of transmitted X-rays (I_t). The absorption coefficient (μ) is a function of the incident X-ray energy. The probability for absorption increases sharply when the incident X-ray energy equals the energy required to excite an electron to an unoccupied electron orbital. These steps in the absorption coefficient are also called absorption edges. This results when a core electron absorbs energy equal to or greater than its binding energy. Edges are labelled according to the shell that the core electron originates from. The K-shell electrons are closest to the atom's nucleus, Fig. 3, and therefore they have greater binding energy than the L-shell electrons.

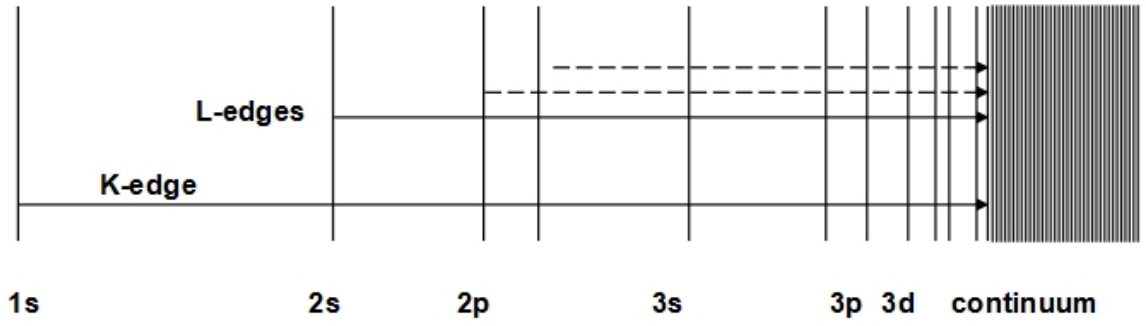

Figure 3: Illustration of the absorption edge labelling according to the electron shell.

Elements with greater atomic numbers, Z, have more positively charged nuclei and a greater number of protons, and therefore, greater binding energy of an electron in a given atomic orbital.

An XAS spectrum can be divided in two main areas, the XANES and the EXAFS region. Typical examples of X-ray absorption spectra are shown in Figure 4.

XANES is the part of the absorption spectrum near an absorption edge, and is found approximately −50 to +200 eV from the edge energy. The shape of the absorption edge can be related to the density of states available for the excitation of the photoelectron. Therefore, the binding geometry and the oxidation state of the atom affect the XANES part of the spectrum. For most elements, the absorption edge looks mostly like a step. The main step feature of the absorption edge is due to the excitation of the photoelectron into the continuum.

The EXAFS part of the spectrum is the normalized oscillatory part of the absorption coefficient. It is commonly found approximately + 1000 eV above the absorption edge. The EXAFS spectral region is used to determine local molecular bonding environments. The EXAFS spectrum reflects the back-scattering data; therefore it contains information on the type and number of atoms in coordination with absorber atoms, interatomic distances, and the degree of local molecular bonding disorder.

Pre-edge and rising edge regions can also be used to characterise a sample. Pre-edge features contain information about centrosymmetry, ligand field and spin-state. Rising edge traits can be used to estimate the charge of metal ions and the local coordination of a given type of atom.

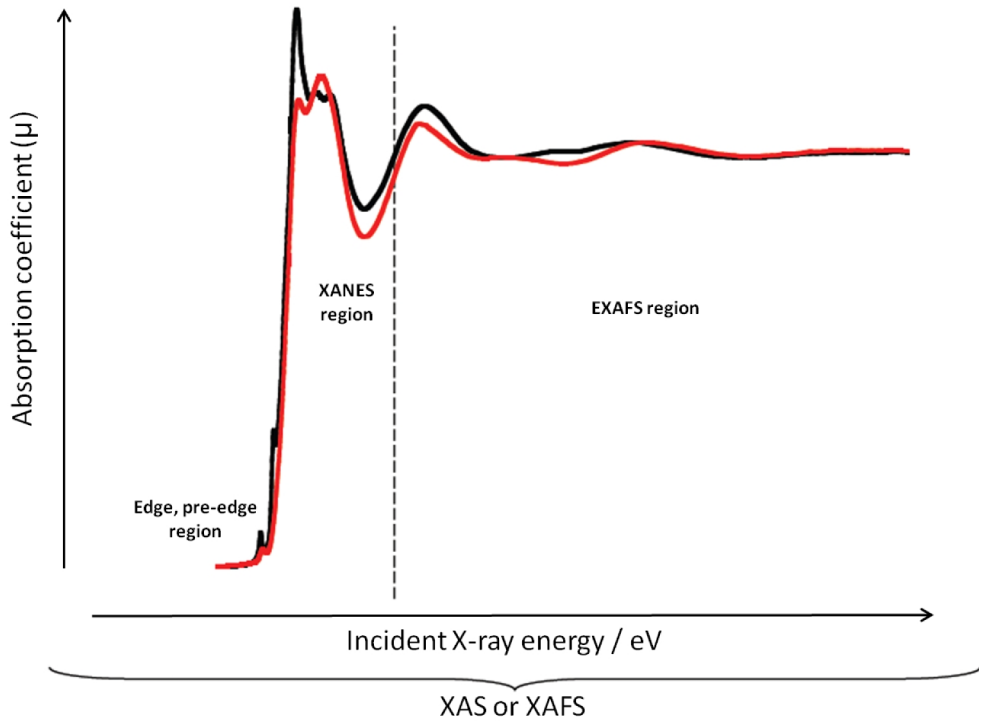

Figure 4: Schematics of typical XAS absorption profiles.

4. Scanning Electron Microscopy (SEM) [8]

The scanning electron microscope uses a focused beam of high-energy electrons to generate a variety of signals at the surface of solid specimens. The signals that derive from the interaction between the sample and the electrons reveal information about the sample, including texture and chemical composition. Areas ranging from approximately from 1 cm to 5 microns in width can be imaged.

The SEM is capable of performing analyses of selected point locations on the sample; this approach is especially useful in determining chemical compositions, using Energy Dispersive X-ray spectroscopy (EDX) qualitatively or semi-quantitatively.

4.1. Principles of SEM

Accelerated electrons in an SEM carry significant amounts of energy, dissipated in a variety of signals when the incident electrons are decelerated in the solid sample. These signals include secondary electrons, backscattered electrons and photons. Secondary and backscattered electrons are commonly used for imaging. Secondary electrons show morphology and topography in

samples. Backscattered electrons illustrate contrasts in composition, which is used to delineate different phases within a sample.

X-ray generation is produced by inelastic collisions of the incident electrons with electrons in the atoms orbitals within the sample. As the excited electrons return to lower energy states, they yield X-rays that are of a fixed wavelength (that is related to the difference in energy levels of electrons in different shells for a given element). Thus, characteristic X-rays are produced for each element in a mineral that is excited by the electron beam. These data are used to determine the composition of the phase of interest.

5. MÖSSBAUER SPECTROSCOPY

Initial attempts to detect resonant processes when radioactive nuclei excite other stable nuclei, by gamma radiation for example, were unsuccessful. To obtain resonance the energy of the emitted gamma ray needs to be greater than the absorption energy. However, the energy due to nuclear recoil prevents resonant absorption of gamma rays. [9]

In 1957, Mössbauer discovered that a nucleus within a solid matrix can sometimes emit and absorb gamma rays without recoil and consequently the energy may be emitted without loss due to recoil and may be greater than the absorption energy of a different atom of the same element in a sample.

Nuclei in atoms may undergo a variety of energy level transitions, often associated with the emission or absorption of a gamma ray. These energy levels are influenced by their chemical environment, and can change or split. These small changes in energy levels can provide means to use the nuclear transitions as a probe of its local chemical environment. The radioactive source nuclei are usually within a solid that provides the simplest possible interaction between the nuclei and their environment. In order to investigate the energy levels in the absorber nucleus, it is necessary to modify the energy of the emitted gamma rays. This is typically accomplished by moving the source to a fixed absorber, Figure 5, or to move the absorber close to a stationary source. This provides an energy shift to the gamma rays due to the Doppler effect (Figure 6). To produce a resonant signal the emitted and absorbed energies need to overlap (illustrated by the red-shaded area in Figure 6).

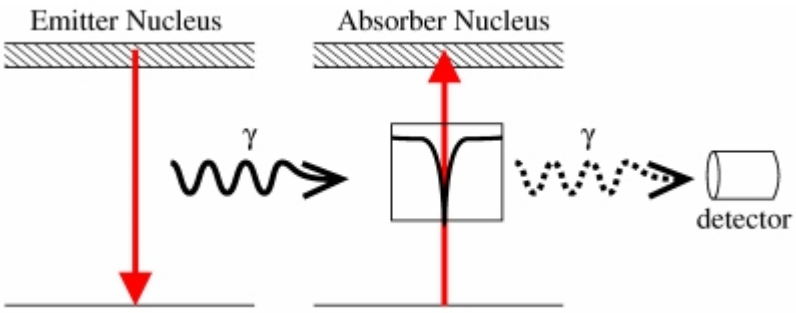

Figure 5: Simple Mössbauer spectrum from identical source and absorber.

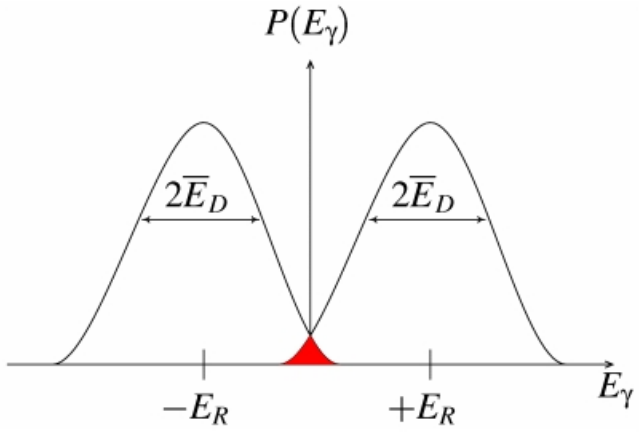

Figure 6: Resonant overlap, E_R represents the recoil energy, E_D illustrate the spread of values due to the Doppler Effect.

The limiting resolution, once recoil and Doppler broadening have been eliminated, is the natural linewidth of the excited nuclear state. This is related to the average lifetime of the excited state before it decays by emitting the gamma-ray. For the most common Mössbauer isotope, ^{57}Fe, an exceptional resolution of about 1 in 10^{12} is reported. This characteristic shows why Mössbauer spectroscopy is particularly useful in detecting hyperfine interactions.

However, resonance only occurs when the transition energy of the emitting and absorbing nucleus match exactly and so the effect is isotope specific. The relative number of recoil-free events (and hence the strength of the signal) is strongly dependent upon the gamma-ray energy and so the Mössbauer effect is only detected in isotopes with very low lying excited states. Similarly the resolution is dependent upon the lifetime of the excited state. These two factors limit the number of isotopes that can be used successfully for Mössbauer spectroscopy. The most used is ^{57}Fe, because it has both characteristics: a very low energy gamma-ray and a long-lived excited state.

Isomer shift: δ (mm.s^{-1})

The isomer shift, or centre shift, is a result of the difference between the electron densities in different materials, *i.e.* the absorber and the source. Any difference in the s-electron environment between the source and absorber produces a shift in the resonance energy (Fig. 6). This shifts the whole spectrum positively or negatively depending upon the s-electron density, and sets the centroid of the spectrum (Fig. 7). Therefore, isomer shifts do not have absolute values and are usually expressed relative to a standard absorber.

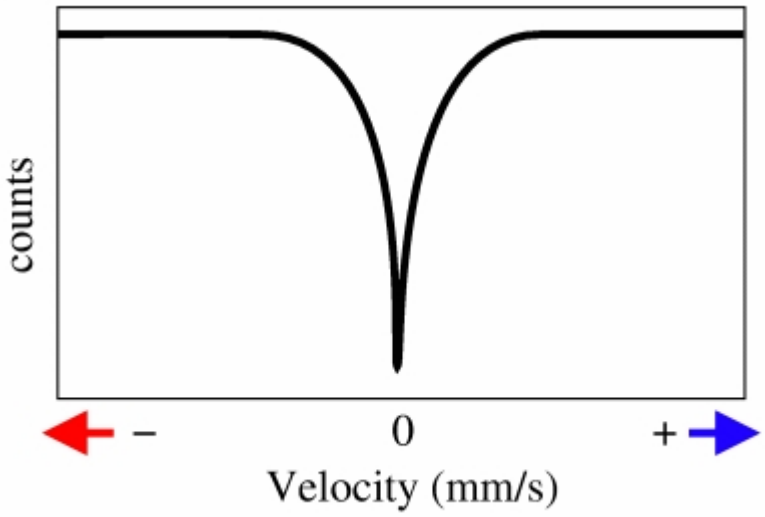

Figure 7: Absorption peak where source and absorber are identical.

Quadrupole shift: Δ (mm.s^{-1})

The charge distribution is often assumed as spherical. However, nuclei in states with an angular momentum quantum number I >1/2 have a non-spherical charge distribution. This produces a nuclear quadrupole moment. In the presence of an asymmetrical electric field (produced by an asymmetric electronic charge distribution or ligand arrangement) this splits the nuclear energy levels. The difference in energy between the two levels is known as quadrupole shift. In the case of an isotope with a I=3/2 excited state, such as ^{57}Fe or ^{119}Sn, the excited level is split into two substates $m_I=\pm 1/2$ and $m_I=\pm 3/2$, Figure 8, and generates a doublet.

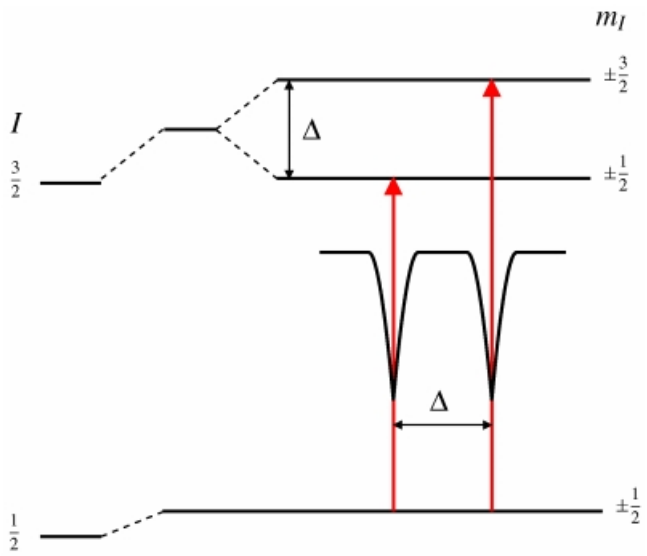

Figure 8: Quadrupole splitting for I = 3/2.

6. NUCLEAR MAGNETIC RESONANCE (NMR)

Nuclear magnetic resonance, NMR, [10] is a phenomenon which occurs when the nuclei of certain atoms in a static magnetic field are exposed to a second magnetic field. Some nuclei respond to this interaction when they possess a property called spin. The nuclei of many elemental isotopes have a characteristic spin, I, that can be integral (*i.e.* I = 1, 2, 3 ...), fractional (I = 1/2, 3/2, 5/2 ...) or zero, I = 0 (^{12}C, ^{16}O, ^{32}S, for instance).

6.1. Spin

Spin is a fundamental property of nature, like electrical charge or mass and comes in multiples of ± 1/2. Protons, electrons, and neutrons possess spin and each possesses a spin of 1/2. The spin of a proton can be seen as a magnetic moment vector, causing the proton to behave like a magnet. When the proton is placed in an external magnetic field, the spin vector of the particle aligns itself with the external field, just like a magnet would. The external magnetic field is generally called *B*. Particles with a net spin may absorb a photon, of frequency ν, which depends on the gyromagnetic ratio, γ of the particle.

$$\nu = \gamma B$$

6.2. Nuclei with Spin

The shell model for the nucleus tells us that nucleons, just like electrons, fill orbitals. When the number of protons or neutrons equals 2, 8, 20, 28, 50, 82, and 126, orbital shells are filled. Because

nucleons have spin, just like electrons, their spin can pair up when the orbitals are being filled and cancel out. NMR spectroscopy can only be performed on isotopes whose natural abundance is detectable. Some of the nuclei routinely used in NMR are listed below in Table 1.

Nuclei	Unpaired Protons	Unpaired Neutrons	Net Spin	γ (MHz/T)
^{1}H	1	0	1/2	42.58
^{13}C	0	1	1/2	10.71
^{19}F	1	0	1/2	40.08
^{31}P	1	0	1/2	17.25

Table 1: Properties of NMR-active nuclei.

6.3. Transitions

A particle can undergo a transition between the two energy states by the absorption of a photon. The energy of this photon must exactly match the energy difference between the two states. The energy, *E*, of a photon is related to its frequency, *ν*, by Planck's constant ($h = 6.626 \times 10^{-34}$ J.s).

$$E = h \nu$$

From $\nu = \gamma B$ and $E = h \nu$, the energy of the photon needed to cause a transition between the two spin states is:

$$E = h \gamma B$$

6.4. Chemical Shift

When an atom is placed in a magnetic field, its electrons circulate about the direction of the applied magnetic field. This circulation causes a small magnetic field at the nucleus, which opposes the externally applied field. The magnetic field at the nucleus, also called the effective field, is therefore smaller than the applied field by a fraction, σ. This phenomenon is called deshielding. The effective field is given by:

$$B = B_o (1-\sigma)$$

Where Bo is the strength of the external magnetic field in the absence of chemical effects.

The electron density around each nucleus in a molecule varies according to the types of nuclei and bonds in the molecule. The opposing field and therefore the effective field at each nucleus will vary. This phenomenon is referred to as the chemical shift.

The chemical shift of a nucleus is the difference between the resonance frequency of the nucleus and a standard, relative to the standard. This quantity is reported in ppm and given the symbol delta, δ.

$$\delta = (n - n_{REF}) \times 10^6 / n_{REF}$$

In NMR spectroscopy, the standard is often tetramethylsilane, $Si(CH_3)_4$, abbreviated TMS.

6.5. Spin-Spin Coupling

Nuclei experiencing the same chemical environment or chemical shift are called equivalent. Those nuclei experiencing different environments or having different chemical shifts are non-equivalent. Nuclei which are close to one another exert an influence on each other's effective magnetic field. This effect shows up in the NMR spectrum when the nuclei are nonequivalent. If the distance between non-equivalent nuclei is less than or equal to three bond lengths, this effect is observable. This effect is called spin-spin coupling or *J*-coupling.

The NMR spectrum for adjacent nuclei A and B, each with spin I = ½, will show splitting due to the interaction of the different nuclear spins. Considering a molecule with one atom of A and one atom of B, the A absorption line is split into 2 absorption lines centred on δ_A, and the B absorption line is split into 2 lines centred on δ_B. The distance between two split absorption lines is called the J coupling and is a measure of the magnetic interaction between two nuclei.

The complexity of the splitting pattern in a spectrum increases as the number of B nuclei increases. Table 2 contains a few examples.

Configuration	Peak Ratios
A	1
AB	1:1
AB_2	1:2:1
AB_3	1:3:3:1
AB_4	1:4:6:4:1
AB_5	1:5:10:10:5:1
AB_6	1:6:15:20:15:6:1

Table 2: Splitting pattern predicted by Pascal's triangle.

When there are two different types of nuclei three bonds or less away, there will be two values of J, one for each pair of nuclei.

7. ULTRAVIOLET – VISIBLE SPECTROSCOPY [11]

An obvious difference between certain compounds is their colour. Although, colours are seen as uniform, they are actually composed of a broad range of radiation wavelengths from different portions of the electromagnetic spectrum. Electromagnetic radiation such as visible light is commonly treated as a wave phenomenon, characterised by a wavelength or frequency.

When molecules are exposed to light some of the energy is absorbed as the electrons are promoted to a higher energy orbital. An optical spectrometer records the wavelengths at which absorption occurs, together with the degree of absorption at each wavelength. The absorbance of a sample is proportional to the number of absorbing molecules in the sample (*e.g.* molar concentration), and to the pathway that the light has to travel across the sample. Therefore, it is necessary to provide a way to compare absorptions in a meaningful way. The Beer-Lambert law states that the absorption of a sample depends on the absorptivity of the studied molecule (also called extinction coefficient), on the molar concentration and on the path length that the incident light source has to travel through the sample:

$$A = l \varepsilon c$$

Where: ε is the extinction coefficient ($mol^{-1}.dm^3.cm^{-1}$); l is the path length (cm); c is the concentration ($mol.dm^{-3}$); A is the absorption, which has no units.

A molecule can be excited by absorbing a photon, and consequently raise its energy from a ground state to an excited state.

8. RAMAN SPECTROSCOPY [12]

Raman spectroscopy is a spectroscopic technique based on the inelastic scattering of monochromatic light, usually from a laser source. Inelastic scattering means that the frequency of photons in monochromatic light changes upon interaction with a sample. Photons of the laser light are absorbed by the sample and then re-emitted. The frequency of the reemitted photons is shifted up or down in comparison with the original monochromatic frequency, and this is called the Raman effect. This shift provides information about vibrational, rotational and other low frequency transitions in the sample molecules.

The Raman effect is based on molecular deformations in an electric field, *E*, determined by the molecular polarisability (α). The laser beam can be considered as an oscillating electromagnetic wave with an electrical vector. Upon interaction with the sample, it induces an oscillating electric dipole moment.

When they de-excite, these oscillating dipoles emit light by three mechanisms.

- A molecule can absorb a photon, which will lead it to an unstable excited state. When the molecule returns back to its original vibrational state it emits light. This type of interaction is called elastic or Rayleigh scattering.

- If a photon is absorbed by Raman-active molecule in its lowest vibrational state, part of the photon's energy is transferred to the Raman active mode. The resulting energy of scattered light is reduced. This type of interaction is called Stokes scattering.

- If a photon is absorbed by a Raman active molecule, which, at the time of interaction, is already in an excited vibrational state, then the excess energy can be released, and the molecule returns to the ground vibrational state. The resulting scattered light is called Anti-Stokes.

These phenomena are illustrated in Figure 9:

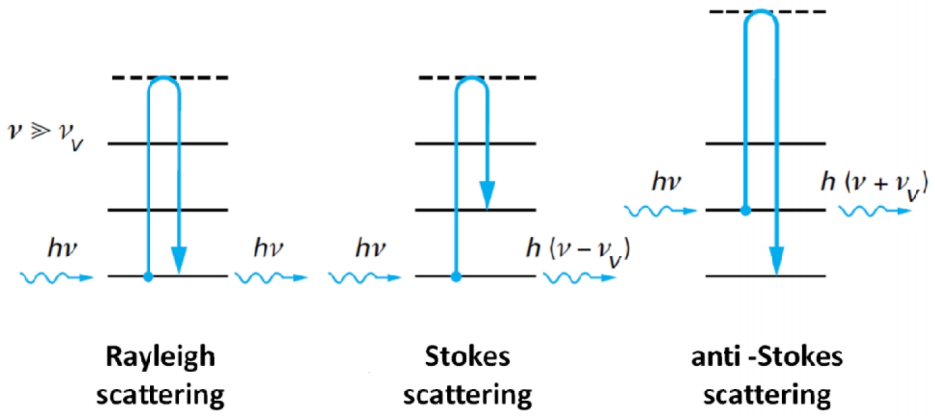

Figure 9: Schematic of the interaction of a photon with matter. [13]

A Raman system typically consists of four major components: an excitation source (laser), a sample illumination system, wavelength selector (filter or spectrophotometer) and a detector. A sample is normally irradiated with a laser beam in the ultraviolet (UV), visible (Vis) or near infrared (NIR) range. The scattered light is collected with a lens and is sent through an interference filter, or spectrophotometer, to obtain a Raman spectrum of the sample.

9. ERROR ESTIMATION

9.1. Gaussian distribution

Generally as the number of measurements increases their distribution approaches a specific curve profile (Fig. 10). This continuous curve is called the limiting distribution. The width of the limiting distribution curve, σ, is the uncertainty of a set of measurements and its value decreases as the number of measurements increase. The mathematical curve that describes such distribution is known as a Gaussian function.

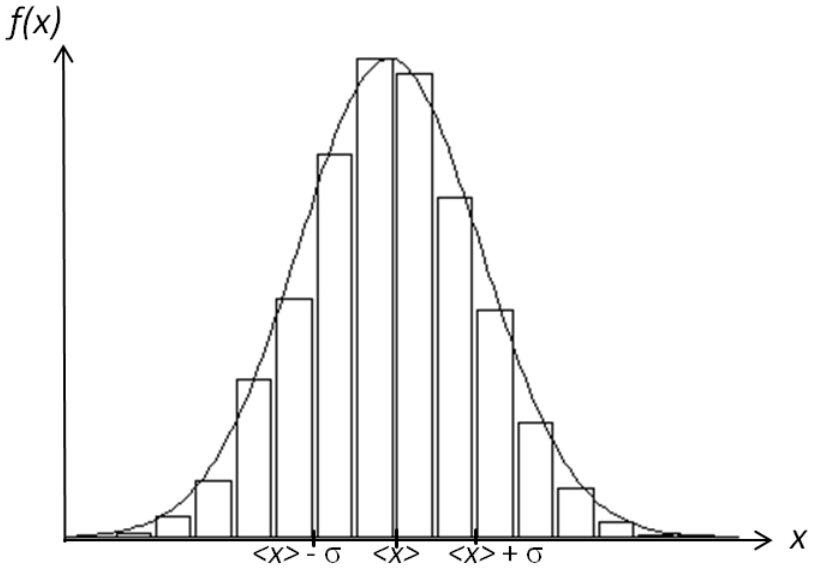

Figure 10: Histogram for measurements of the same quantity. The curve is the data Gaussian distribution.

The standard deviation, σ, allow the calculation of the probability that the true value falls within a given distance from a measured value, *i.e.* it is a measure of experimental error.

9.2. Weighted averages

Assuming N separate measurements of a quantity x, with their corresponding uncertainties σ,

$$x_1 \pm \sigma_1, x_2 \pm \sigma_2, \ldots, x_N \pm \sigma_N$$

The best estimate based on their measurements is expressed by:

$$x_{best} = \frac{\sum w_i x_i}{\sum w_i}$$

Where w_i are the inverse squares of the corresponding uncertainties:

$$w_i = 1 / \sigma_i^2 \qquad \text{for } i = 1, 2, \ldots, N$$

Since the weight attached to each measurement involves the square of the corresponding uncertainty, any measurement which is less precise contributes less to the final answer.

If the experiment involves the measurement of two different physical variables, the statistical analysis of data use a different approach known as least square-fitting.

9.3. Least-squares fitting

If two physical variables x and y linearly related, such as: $y = a\,x + b$, then a graph of y against x should be a straight line and the data set (x_i, y_i) would lie exactly on the line. In practice, uncertainties cause the points to be away from the line, hopefully at a reasonable distance. Usually, finding the best line that fit the data set is equivalent to finding the best estimates of the constants a and b. This can be done graphically or by the least-squares fit for a line (also called linear regression). This mathematical method is not only applied to variables linearly related. Many other types of data (such as polynomial, exponential, for instance) can be solved in a similar way.

9.3.1. Simple guideline to evaluate measurement results

In many practical measurement situations the probability distribution, characterised by the measurement result, y, is combined to a standard uncertainty. When this is the case, y can be defined within an interval from $y - \Delta y$ to $y + \Delta y$. The measurement result then lies within a high level of confidence. For instance if the parameter a equals 7.23245 (5) Å, its values fall between 7.23240 and 7.23250 Å. Values outside this bracket would not be retained.

10. REFERENCES

[1] B.E. Warren, *X-ray diffraction*, 1990, New York : Dover, ISBN: 0486663175.

[2] H.P. Klug and L. E. Alexander, *X-ray diffraction procedures for polycrystalline and amorphous materials*, 2nd ed. Wiley-Interscience, 1974, ISBN: 0471493694.

D.M. Moore and R. C. Reynolds, *X-Ray diffraction and the identification and analysis of clay minerals*, 1997, 2nd Ed. Oxford University Press, ISBN: 0195087135.

[3] C.C. Wilson, *Single crystal neutron diffraction from molecular materials*, 2000, London, World Scientific, ISBN: 9789810237769, 2000.

[4] J.R. Taylor, *An introduction to error analysis: the study of uncertainties in physical measurements*, 1997, University Science Books, ISBN: 093570275X.

[5] R.A. Young, *The Rietveld Method*, 1993, Oxford Univeristy Press, ISBN: 0198555776.

[6] D.W. Bennett, *Understanding single crystal X-ray crystallography*, 2010, John Wiley, ISBN: 3527327940.

[7] S.D. Kelly, B.Ravel, D. Hesterberg, *Methods of soils analysis: Analysis of Soils and MineralsUsing X-ray Absorption Spectroscopy*, 2008, Soil Science Society of America, Mineralogical Methods, SSSA Book Series, no. 5, ISBN: 978-0-89118-846-9.

[8] L. Reimer, *Scanning electron microscopy : physics of image formation and microanalysis*, 1998, Springer, ISBN: 3540639764

[9] D.P.E. Dickson and F.J. Berry, *Mössbauer Spectroscopy*, 1986, Cambridge University Press, ISBN: 0521261015.

[10] P.J. Hore, S. Wimperis and J. Jones, *NMR: the toolkit*, 2000, Oxford University Press, ISBN: 0198504152.

[11] H-H. Perkampus, *UV-Vis spectroscopy and its applications*, 1992, London Springer-Verlag, ISBN: 9780387554211.

[12] N.B. Colthup, *Introduction to Infrared and Raman spectroscopy*, 1964, New York : Academic Press.

[13] J. Barbillat, D.Bougeard, G. Buntinx, M. Delhaye, P. Dhamelincourt, F. Fillaux, *Techniques de l'ingénieur Spectrométries, Spectrométrie Raman*, 1999, 2865-2896.

Chapter 3:

SYNTHESIS AND CHARACTERISATION OF A POSSIBLE HOST FOR TETRAVALENT ACTINIDES: $Y_{2-x}Ce_xTi_{2-x}Fe_xO_7$

Carlos De La Fontaine [a], M.C. Stennett [b], Sarah L. Heath [a] and N.C. Hyatt [b]*

Centre for Radiochemistry Research, School of Chemistry, University of Manchester, Oxford Road, Manchester M13 9PL, United Kingdom [a]

Department of Engineering Materials, University of Sheffield, Mappin Street, Sheffield, S1 3JD, United Kingdom [b]

(Correspondence: N.C.Hyatt@sheffield.ac.uk)

ABSTRACT

The synthesis and structure of a novel waste form suitable to host Pu(IV) is reported here. The $Y_{2-x}Ce_xTi_{2-x}Fe_xO_7$ system is a potential model host for tetravalent actinide (Act) species by substitution of Act^{4+} at the Y^{3+} site with substitution of Fe^{3+} on the Ti^{4+} site to maintain charge balance. Compositions in this system were prepared by consecutive solid state reaction of intimately mixed oxide powder precursors. Dense ceramic specimens (ca. 95% theoretical density) were prepared by sintering. XRD patterns combined with Mössbauer spectroscopy confirmed that compositions $x \leq 0.1$ adopt the pyrochlore structure. In contrast, compositions with $0.5 \leq x \leq 0.6$ adopt the unusual zirconolite 3T structure which appears to be stabilised by Fe^{3+} in 5-fold co-ordination, as demonstrated by Mössbauer spectroscopy. Compositions where $x \geq 0.7$ were found to comprise a mixture of zirconolite 3T and a fluorite phase (CeO_2).

1. INTRODUCTION

Zirconolite ($CaZrTi_2O_7$) and pyrochlore structured ($A_2B_2O_7$) materials have attracted interest as radioactive waste immobilisation matrices, and, more widely, for application in fuel cells and catalysis. Pyrochlore oxides are known to exhibit high ionic and electrical conductivity, [1] magnetic ordering, [2,3] as well as luminescence properties. [4,5] This diversity in application is associated with the chemical flexibility of the pyrochlore structure, which may accept substitution on both the A and B site, by cations of appropriate size and charge. Zirconolite and pyrochlore ceramics tolerate both cation and anion disorder and are known for their resistance to chemical corrosion and radiation damage, [6] which is the primary requirement for application as an actinide host, e.g. as within Synroc (SYNthetic ROCk). [7] Immobilised High Level Waste (HLW) from a nuclear plant undergoes decay events to produce many atomic defects in the solid matrix. In highly crystalline material the crystallinity can be significantly affected by the direct irradiation as well as the chemical changes due to decay in the ceramic and void swelling leading to amorphisation. Many naturally occurring minerals contain actinides and rare earth elements and have inspired the choice of synthetic ceramic formulations for High Level Waste (HLW) immobilisation, as an alternative to vitrification. The choice of synthetic pyrochlore and zirconolites as actinide hosts was inspired by the existence of naturally occurring actinide rich minerals with these structure types.

1.1. The pyrochlore structure

The ideal pyrochlore structure adopts the Fd-3m space group; with eight formula units per unit cell. The ideal $A_2B_2O_7$ pyrochlore structure is derived from the fluorite structure (AO_2) via an ordered removal of one eighth of the oxygen atoms, combined with an ordered arrangement of A and B cations. The ordered arrangement of anion vacancies yields two distinct cation polyhedra: the A site is 8-fold coordinated, which takes the form of a distorted cube; whereas the B-site is 6-fold co-ordinate, and is a distorted octahedron. [8] The A site is typically occupied by +2 and +3 cations, and the B site by +4 and +5 cations.

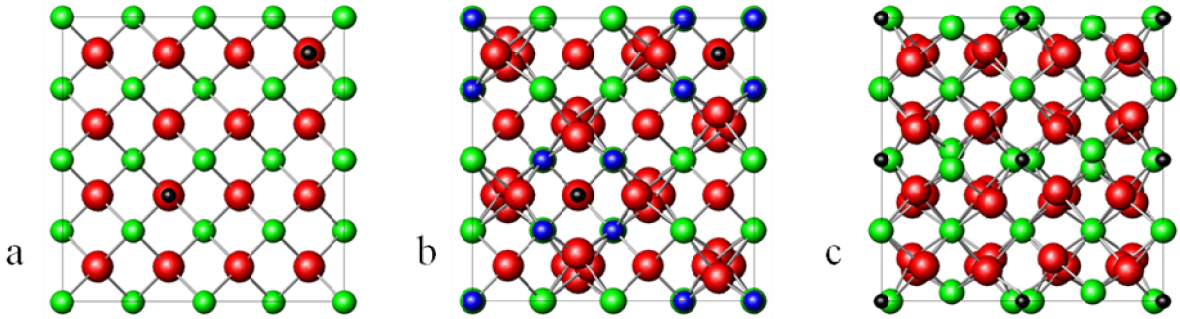

Figure 1: Schematic representations of the crystal structures of (a) $AX_{1.75}$ defect fluorite, (b) $A_2B_2X_7$ pyrochlore, and (c) A_2X_3 C-type structures, projected along the [100] direction. Red spheres represent X anions, green spheres represent A cations, blue spheres represent B cations, and small black spheres represent anion vacancies.

There are three unique oxygen positions, in the pyrochlore structure: the 48f position (x, 1/8, 1/8), the 8b position (3/8, 3/8, 3/8) and the 8a position (1/8, 1/8, 1/8) which is vacant. The pyrochlore structure can then therefore be defined by two parameters: the 48f x oxygen position and the cubic unit cell parameter (*a*). All atoms, except the 48f oxygen, adopt special symmetry defined positions. The stability of the pyrochlore structure depends on the relative sizes of A and B cations. In general, the pyrochlore structure is stable for the radius ratio: $1.46 < r_A/r_B < 1.78$. [9] Below $r_A / r_B = 1.46$ we observe a defect fluorite structure (space group Fm-3m) with both anion and cation disorder. Above $r_A / r_B = 1.78$, a more complex monoclinic phase is formed.

1.2. The zirconolite structure

Zirconolite is a derivative of the fluorite structure. The generalised chemical composition of zirconolite is $CaZrTi_2O_7$ although zirconolite can adopt several different polytypic structures with monoclinic (2M or 4M), orthorhombic (3O) and hexagonal (3T) symmetry. The structure can be described as consisting of layers of calcium and zirconium atoms situated between planes of titanium polyhedra arranged in hexagonal tungsten bronze (HTB) arrays. The polyhedra in the HTB arrays are both octahedral (6-fold) and square pyramidal (5-fold), as indicated in Figure 2.

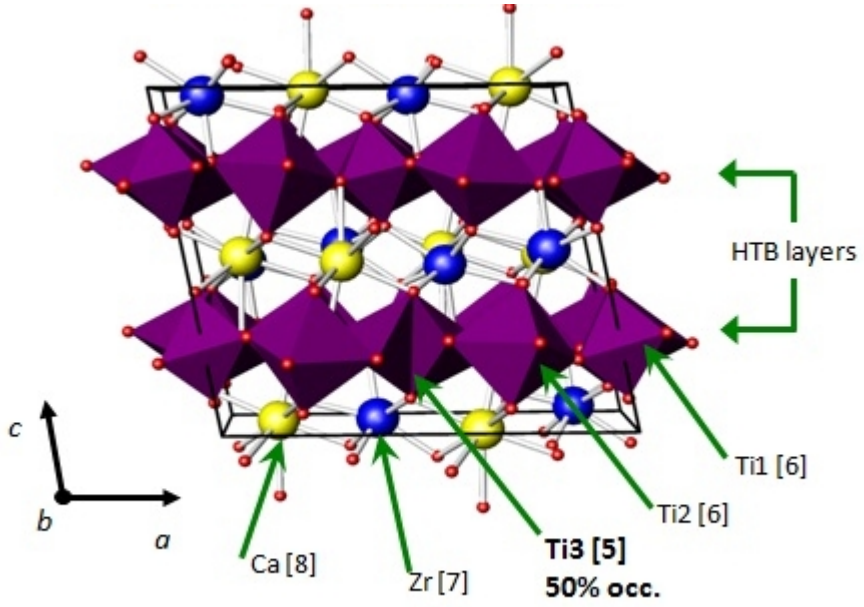

Figure 2: Schematic of a 2M polytype zirconolite structure ($CaZrTi_2O_7$). Coordination number of cation site is showed next to the atoms. [10]

In nature, the zirconium chemical composition differs from the generalised one due to extensive cation substitution. Some natural samples have been found to incorporate up to 24 wt% UO_2, 22 wt% ThO_2 and 32 wt% REE_2O_3.[11]

1.3. $Y_{2-x}Ce_xTi_{2-x}Fe_xO_7$

Handling plutonium or other transuranium elements requires special facilities; therefore, many ceramic studies use non radioactive surrogates during the early stages of wasteform development. A number of different surrogates have been used in order to mimic actinide behaviour for both glass and ceramic studies. When choosing a suitable surrogate one has to consider several properties such as, valence, electronic configuration, ionic radius, redox potentials, and melting temperatures. Hence a multi-surrogate approach may be chosen, where the choice of surrogate depends on the properties being studied. The most useful redox and ionic radii surrogate for plutonium, is cerium. [12] Ce^{4+} has been chosen for this study as it has an ionic radius in eight-fold coordination (111 pm) that is very similar to that of Pu^{4+} (110 pm). [13] In additional to size, one also needs to consider chemical and physical behaviour. Marra *et al*. [14] demonstrated Ce to be a suitable surrogate from a process development standpoint although differences in the redox potentials between Ce and Pu cations mean processing conditions, such as atmosphere, need to be considered. Both cerium and plutonium generally exhibit the tetravalent oxidation state in titanate and zirconate based ceramics processed under oxidising conditions. Cerium is however more easily reduced to its trivalent oxidation state under reducing processing, or melting, conditions.

Here we report the study of the $Y_{2-x}Ce_xTi_{2-x}Fe_xO_7$ system, a possible host for tetravalent actinides where Ce (IV) is added as a Pu (IV) surrogate. The effect of rare earth doping on the microstructure $Y_2Ti_2O_7$ was previously studied in order to improve the dielectric properties, [15] where the cubic pyrochlore structure was stable for all elements in the lanthanide series. Due to criticality concerns, most studies related to nuclear wasteforms tend to choose a highly efficient neutron absorber element such as Gd^{3+} instead of Y^{3+}. [10,16] The presence of a neutron absorbing species however precludes the use of neutron diffraction as a structural probe and it has been reported in the literature that rare earth pyrochlores are more easily amorphised than Y-pyrochlores. [17] Structural stability and radiation damage of fluorite related structures depends on the bond types, relative cationic sizes of A and B sites and the structure deviation from the ideal structure and only a few studies of Y^{3+} and Ln^{3+}/An^{4+}-doped matrices have been reported.[18] Yttrium also allows the use of solid state NMR for further characterisations. [19] Titanium can adopt different oxidation states, coordination geometry (square pyramidal for Gd_2TiO_5 and Eu_2TiO_5, [20] trigonal bipyramidal within Dy_2TiO_5 and octahedral in Er_2TiO_5). Thus, incorporation of relatively high levels of impurities, such as derived waste from the steel containers, could be facilitated by the geometry flexibility of Ti^{4+}. Fe^{3+} is a common contaminant in nuclear waste streams (steel containers) [21] and acted as a charge balance on the Y^{3+} substitution by Ce^{4+} in $Y_{2-x}Ce_xTi_{2-x}Fe_xO_7$. Moreover, double substitutions concerning actinides and iron are poorly reported in the literature and could offer a route to improve the radiation tolerance of titanate pyrochlores, which is known to be sensitive to composition. Thus, the synthesis of $Y_{2-x}Ce_xTi_{2-x}Fe_xO_7$ was an attempt to determine the potential existence of a new family of pyrochlore compositions suitable as a Pu (IV) wasteform.

2. EXPERIMENTAL PROCEDURE

Synthesis of $Y_{2-x}Ce_xTi_{2-x}Fe_xO_7$ was achieved by several consecutive solid state reactions of the stoechiometric amount of the respective oxide precursors: Y_2O_3, CeO_2, TiO_2 and Fe_2O_3. The substitution limits were investigated for $0 \leq x \leq 1.0$ in intervals of 0.1. The different compositions were mixed in a rotary ball mill for 16 h in high density polyethylene (HDPE) pots containing yttria stabilised ZrO_2 media and isopropanol as a carrier solvent. The resulting mixed powder slurries were separated from the milling media, dried at 100 °C overnight, and reacted in alumina crucibles. Several heat treatments were carried out with intermittent regrinding, to ensure complete reaction. The first reaction was at 1573 K for 8 h followed by two additional reactions at 1673 K for 8 h. In all cases a ramp of 5 K min^{-1} was used. The reactions were carried out in air, under atmospheric pressure. After heating, the products were removed from the crucibles, broken down and planetary milled for 2 minutes at 300 rpm in sialon pots containing sialon milling media. The

powders were then sieved through a 250 μm mesh. The reaction process was monitored by XRD and the reaction was assumed to have gone to completion when no further changes were observed in the XRD patterns. Ceramic bodies were prepared by pressing approx. 1 g of material in a 10 mm diameter die at ~ 1 ton for 2 minutes. Sintering was performed for 8 hours at temperatures up to 1898 K. Final sintered densities of > 95% theoretical were achieved.

Raman spectra were acquired using a Bruker Senterra Microscope Spectrometer at 534 nm excitation. The laser intensity was set to 50%. Each pellet was irradiated at several different surface areas; three iterations were done for every measurement.

Microstructural analysis of sintered pellets was performed using a JEOL JSM6400 scanning electron microscope (SEM) equipped with an energy dispersive spectrometer (EDX). Prior to analysis the sintered specimens were sectioned using a slow speed diamond bladed saw and then ground parallel using SiC grinding paper. Once the samples had been ground to a 1200 grit finish, they were polished to an optical finish (1 micron) using diamond paste. Each specimen was then thermally etched for 1 hour at 90 % of its sintering temperature, mounted on an aluminium sample stub and carbon coated to prevent charging in the microscope (Edwards 'Speedivac').

X-ray diffraction patterns were acquired on a Bruker D8 Advance Powder diffractometer. Samples were prepared from planetary milled powder and mounted in transmission geometry. The diffractometer utilised a copper radiation source ($K_{\alpha 1}$, λ= 0.15406 nm and $K_{\alpha 2}$, λ= 1.5444 nm) and was equipped with a standard scintillation detector operating at 40 kV and 30 mA. Diffraction patterns were recorded between 10 and 70° 2theta using a scan step of ~ 0.02°. The analysis of the data was performed using WinXPow or Xpert Highscore Plus.

Specimens for Mössbauer spectroscopy were prepared by dilution of 50 - 100 mg of finely powdered sample in 100 mg of graphite. Data were acquired in transmission at room temperature using a WissEL Mössbauer Spectrometer with a ^{57}Co:Rh source. Data analysis was performed using the RECOIL software package. [22]

Neutron diffraction data for x = 0,1 and 0.6, were collected at room temperature using the HRPT diffractometer at the pulsed spallation neutron source of the SINQ spallation neutron source at the Paul Scherrer Institute. A vertically focused beam of wavelength λ=1.4940(1) Å was selected using the (5 3 3) reflection of the Ge monochromator. For each composition studied, around 3 g of finely powdered sample was loaded into a cylindrical vanadium can. Diffraction data were collected over the angular range $5 \leq 2\theta \leq 165°$ with a step size of 0.05. Data refinement was performed using the GSAS software. [23]

3. RESULTS AND DISCUSSION

3.1. X-ray diffraction data

The stacked X-ray diffraction (XRD) patterns are shown in Figure 3. The XRD patterns show that several different structures are stabilised across the solution range. Compositions where $0.0 \leq x \leq 0.1$, could be indexed on a pyrochlore cell (Fd-3m, space group 227) based on that of $Y_2Ti_2O_7$. [24] The diffraction pattern for $x = 0.1$ is shown in Figure 4 as an example. In the diffraction pattern for composition $x = 0.2$, extra reflections were observed that could not be attributed to a pyrochlore pattern. These extra reflections indicated the presence of an additional phase which was confirmed by micro-structural and micro-chemical analysis to be different in composition and co-exist alongside the pyrochlore structured phase. With increasing Ce^{4+} and Fe^{3+} content the pyrochlore $(111)_P$ and $(222)_p$ reflections reduced in intensity and new reflections were observed. These additional reflections were attributed to a an unusual hexagonal polytype of the zirconolite structure, [25,26] with space group $P3_121$ (152) (see Figure 4). For $0.5 \leq x \leq 0.6$ all the reflections could be attributed to the hexagonal zirconolite phase. Extra reflections were again observed (consistent with the presence of a fluorite structured phase) for compositions where $x \geq 0.7$, and the presence of a Ce rich phase was confirmed by scanning electron microscopy (Figure 5). Comparison of the unit cell a-parameter for $Y_{2-x}Ce_xTi_{2-x}Fe_xO_7$ with $x = 0.0$ and $x = 0.1$, Table 1, shows that the unit cell expanded slightly with substitution of Ce^{4+} and Fe^{3+}. This is consistent with a small decrease in the overall ratio of A site to B site ionic radii: $r_A / r_B = 1.69$ ($x = 0.0$) compared to $r_A / r_B = 1.67$ ($x = 0.1$). The observed increase in the unit cell parameter thus appears to be driven by substitution of the Ti^{4+} cations (0.605 Å) for Fe^{3+} (0.645 Å) rather than the substitution of Y^{3+} (1.159 Å, CN = 8) with Ce^{4+} (1.110 Å, CN = 8). [13]

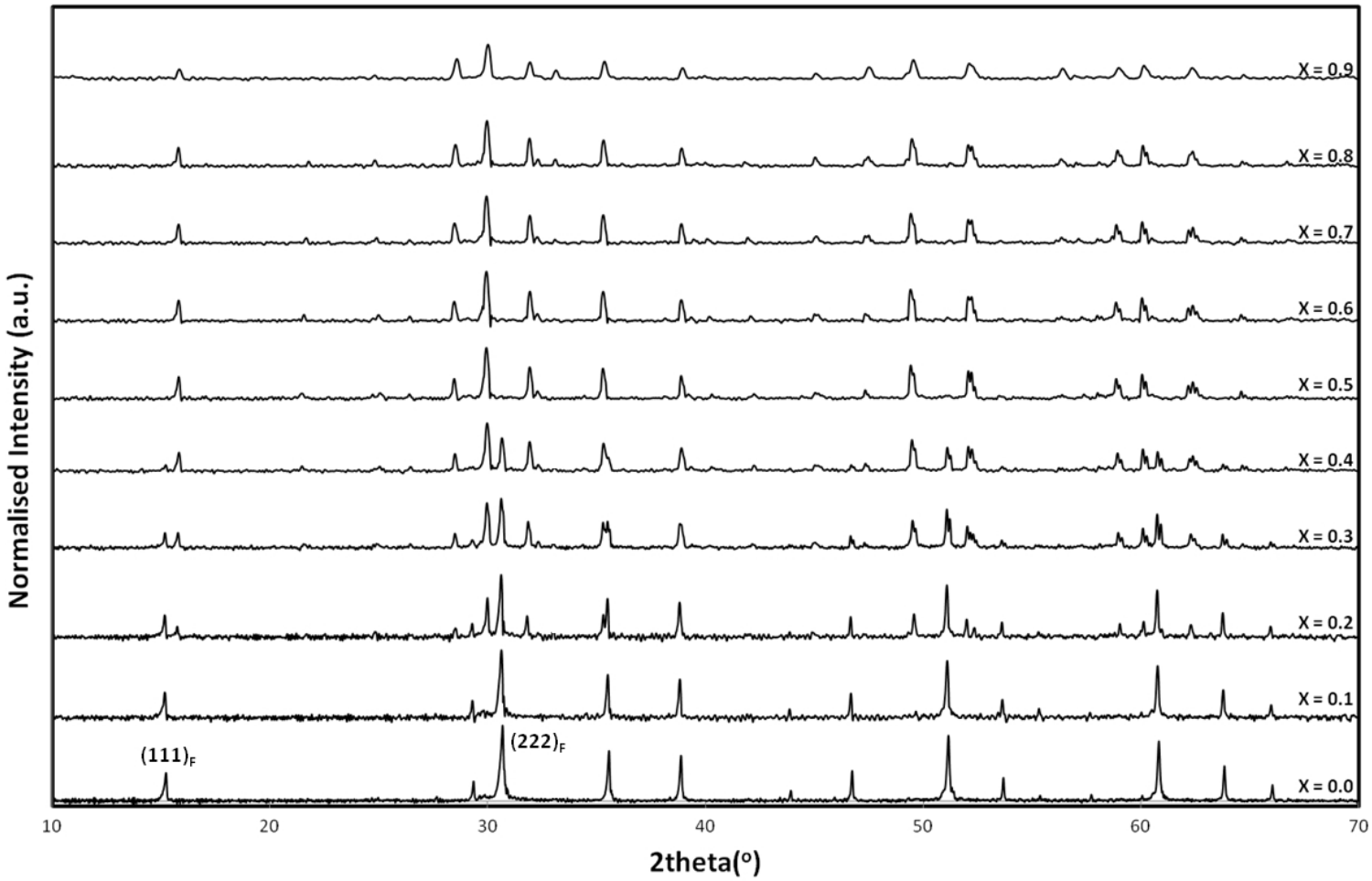

Figure 3: Normalised X-Ray diffraction data of $Y_{2-x}Ce_xTi_{2-x}Fe_xO_{7.}$

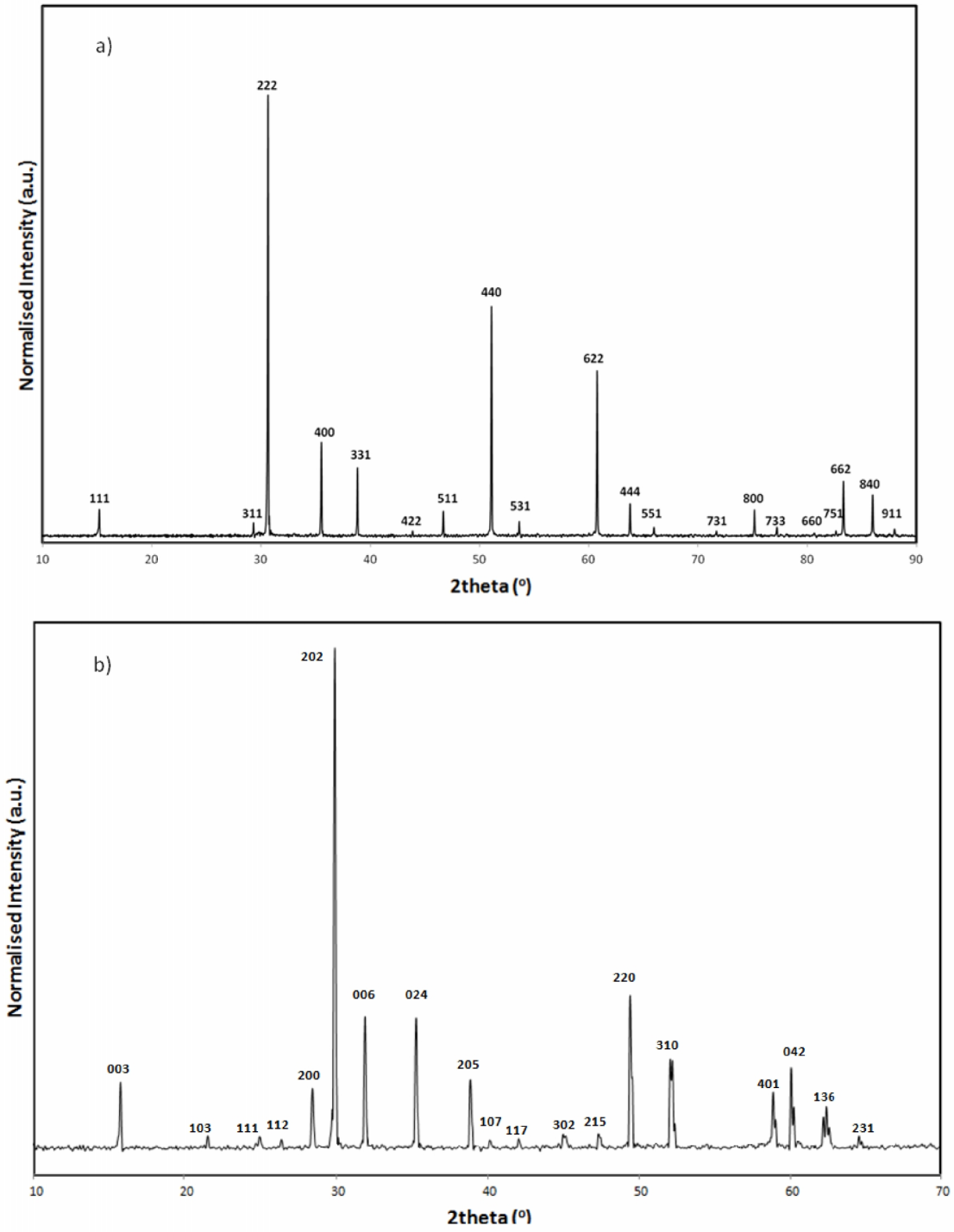

Figure 4: Indexed XRD patterns of $Y_{2-x}Ce_xTi_{2-x}Fe_xO_7$, a) x = 0.1 (pyrochlore) and b) x = 0.6 (zirconolite-3T).

3.2. Scanning electron microscopy (SEM)

Electron microscopy was used to determine the assemblage, morphology and chemistry of the phases present. SEM combined with quantitative EDX analysis confirmed the formation of single phase ceramic specimens (when $x \leq 0.1$ and $0.5 \leq x \leq 0.6$) consistent with the observations from the XRD data. Figure 5 shows representative electron micrographs from a range of $Y_{2-x}Ce_xTi_{2-x}Fe_xO_{7,}$ specimens. All the secondary electron images showed a small volume fraction of porosity, consistent with the average sintered density of 95 ± 2 % of theoretical. This porosity appears as black circular features. All the grains are uniform in contrast demonstrating compositional homogeneity. The presence of a secondary phase was indicated by XRD (Figure 3) in samples where $0.2 \leq x \leq 0.4$. These samples were a mixture of a pyrochlore and a zirconolite phase. This observation was confirmed by electron microscopy as different contrast grains were observed. When $0.5 \leq x \leq 0.6$, a single phase material was observed, which is consistent with the XRD analysis. Another secondary phase was observed when $x > 0.7$, which was shown by energy dispersive spectroscopy to consist almost entirely of CeO_2, which is consistent with the presence of reflections consistent with a fluorite structured phase in the XRD patterns. The compositions of all specimens are reported on Table 1.

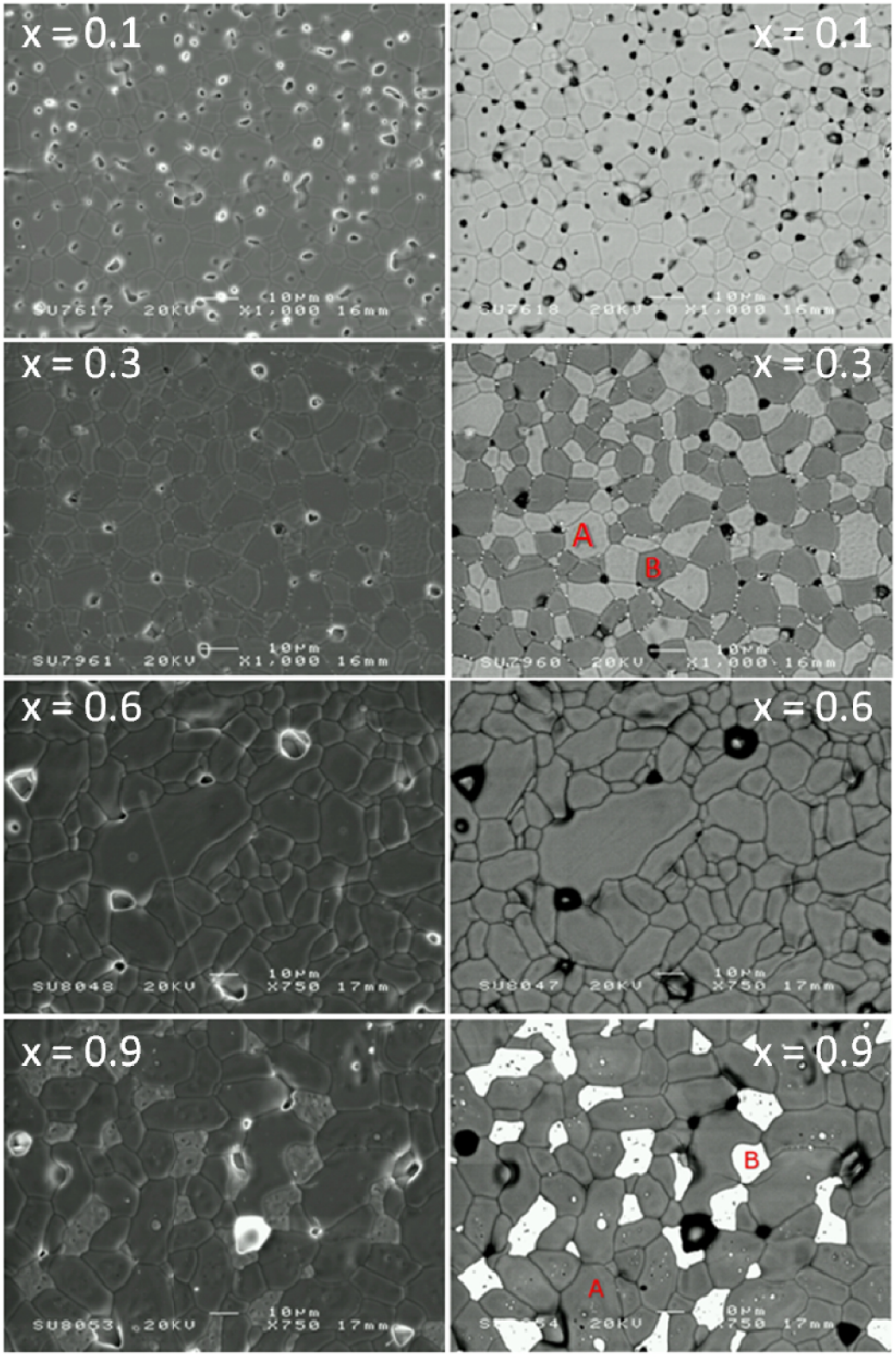

Figure 5: Secondary (left) and backscattered (right) electron micrographs representative of all specimen.

Nominal Composition (x)	Measured composition (± 0.01)	Structure assignment
0.0	$Y_{2.13}Ti_{1.92}O_7$	Pyrochlore
0.1	$Y_{1.96}Ce_{0.11}Ti_{1.85}Fe_{0.1}O_7$	Pyrochlore
0.2	$Y_{1.86}Ce_{0.18}Ti_{1.8}Fe_{0.16}O_7$	Pyrochlore
	$Y_{1.72}Ce_{0.39}Ti_{1.46}Fe_{0.47}O_7$	Zirconolite
0.3	$Y_{1.83}Ce_{0.21}Ti_{1.79}Fe_{0.17}O_7$	Pyrochlore
	$Y_{1.64}Ce_{0.45}Ti_{1.46}Fe_{0.48}O_7$	Zirconolite
0.4	$Y_{1.79}Ce_{0.24}Ti_{1.79}Fe_{0.18}O_7$	Pyrochlore
	$Y_{1.6}Ce_{0.48}Ti_{1.46}Fe_{0.48}O_7$	Zirconolite
0.5	$Y_{1.5}Ce_{0.53}Ti_{1.47}Fe_{0.5}O_7$	Zirconolite
0.6	$Y_{1.43}Ce_{0.62}Ti_{1.35}Fe_{0.61}O_7$	Zirconolite
0.7	$Y_{1.33}Ce_{0.69}Ti_{1.3}Fe_{0.68}O_7$	Zirconolite
	$Y_{0.3}Ce_{3.06}Ti_{0.05}Fe_{0.02}O_7$	Fluorite
0.8	$Y_{1.37}Ce_{0.66}Ti_{1.29}Fe_{0.69}O_7$	Zirconolite
	$Y_{0.28}Ce_{3.22}Ti_{0.02}Fe_{0.01}O_7$	Fluorite
0.9	$Y_{1.38}Ce_{0.67}Ti_{1.28}Fe_{0.68}O_7$	Zirconolite
	$Y_{0.35}Ce_{3.17}Ti_{0.06}Fe_{0.01}O_7$	Fluorite

Table 1: Quantitative elemental analysis of $Y_{2-x}Ce_xTi_{2-x}Fe_xO_7$ specimen.

3.3. Mössbauer data

Mössbauer spectroscopy was used to determine both the valence state and coordination geometry of the Fe cations within the samples. Spectra from samples with the cubic pyrochlore structure were successfully fitted with a single Lorentzian doublet, indicative of the presence of only one geometrically distinct iron site. The isomer shift, 0.34(2) mm s^{-1}, and quadrupole splitting, 0.92(2) mm s^{-1}, indicate that the iron is trivalent, and in six-fold coordination, consistent with the targeted substitution of iron on to the titanium site in the pyrochlore structure. [27] Figure 6 a) shows the ^{57}Fe Mössbauer spectrum acquired from the x = 0.1 sample, which is representative of $Y_{2-x}Ce_xTi_{2-x}Fe_xO_7$ compositions where $x \leq 0.1$. There was no indication of any divalent iron in the samples which would be associated with a doublet that exhibits a considerably larger isomer shift.

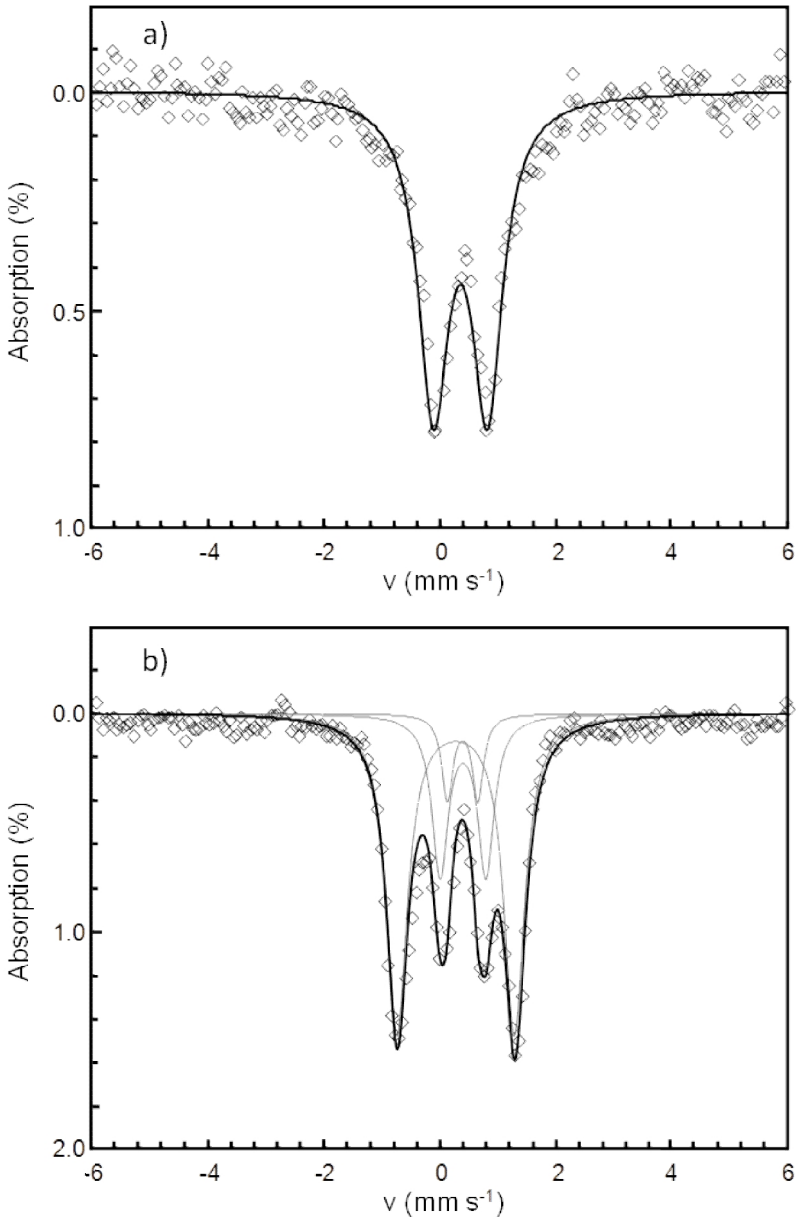

Figure 6: Room temperature ^{57}Fe Mössbauer spectrum of a) x = 0.1 sample (cubic pyrochlore) and b) x = 0.6 sample (hexagonal 3T-zirconolite).

Figure 6 b) shows the spectrum acquired from the x = 0.6 sample which is typical of the higher iron content single phase compositions in the $Y_{2-x}Ce_xTi_{2-x}Fe_xO_7$ system ($0.4 < x < 0.7$). For these samples the spectra were fitted with three separate Lorentzian doublets which indicated three geometrically distinct iron sites in the structure. Grey lines show the individual Lorentzian doublets whilst the black line represents the total fit. There was no evidence of any divalent iron with the isomer shifts of all three doublets being consistent with Fe^{3+}. The zirconolite-3T structure contains three distinct titanium coordination environments. One is five-fold coordinated and the other two

are six-fold coordinated. [26] The doublet with the large quadrupole splitting of 2.01(2) mm s^{-1} can be attributed to five-fold coordinated iron; the Mössbauer parameters are consistent with those previously reported in $CaZrTi_{2-2x}Nb_xFe_xO_7$ which are monoclinic zirconolite structured materials (space group C2/c) which also contain one five- and two six-fold coordinated titanium sites. [28,29] The two remaining doublets [IS = 0.36(2) mm s^{-1}, QS = 0.52(2) mm s^{-1} and IS = 0.37(2), QS = 0.79(2)] are consistent with the other two sites being six fold coordinated with one having a slightly larger quadrupole splitting which can be a measure of the degree of distortion when considering two sites with the same nominal coordination environment. The doublet with the large quadrupole splitting was therefore attributed to Fe residing in the more distorted octahedral site within the structure. [26,30]. Analysis of the area of each doublet indicated that 65% of the total iron in the sample was situated on the five-fold coordinated site, 8% on the less distorted six-fold coordinated site, and 27% on the more distorted six-fold site.

3.4. Raman Spectroscopy

Structural transformations of the pyrochlore structure under the effects of doping can be followed by spectroscopy. XRD combined with SEM/EDX showed that three types of structures were present within the $Y_{2-x}Ce_xTi_{2-x}Fe_xO_7$ system. Even if elemental analyses show an average of seven oxygen atoms, sometimes not all cations will have the same environment, due to site defects. Raman data for $Y_2Ti_2O_7$ [31] were previously published and were used as a reference for our titanate pyrochlore samples. If a molecular approach is used to determine the number of active Raman modes, 23 bands would be expected for a $A_2B_2O_6O'$ pyrochlore with a 13 atom unit. The observed experimental results show fewer bands, and it has been previously shown through theoretical studies that a site symmetry approximation is more appropriate to pyrochlore and fluorite structures. [32,33] The approach is summarised below.

Cubic pyrochlores, such as $A_2B_2O_6O'$, belong to the space group number 227 (Fd-3m, Z = 8). A and B cations are within a D_{3d} symmetry site. Oxygen, labelled O, is within a C_{2v} site while the O' is in a T_d site. [34] The vibrational normal modes were then predicted as being: [35]

$$\Gamma = A_g^{(R)} + 3A_{2u}^{(in.)} + E_g^{(R)} + 3E_u^{(in.)} + 2F_{1g}^{(in.)} + 7F_{1u}^{(IR)} + 4F_{2g}^{(R)} + 4F_{2u}^{(in.)} \qquad (1)$$

where (R) denotes Raman active, (in.) inactive and (IR) Infrared active bands. No active Raman band is expected for the A and B symmetry sites. Possible oxygen active bands were the following: A_g, E_g and $3F_{2g}$ and F_{2g} for O' sites.

The fluorite structure, AO_2, belongs to the space group no. 225 (Fm3m, Z = 4). The A type cation sits within an octahedral symmetry site and the oxygen is on a tetrahedral symmetry site. The reduction of the vibrational formula is given by the following equation: [36]

$$\Gamma = F_{1u}^{(IR)} + F_{2g}^{(R)} \qquad (2)$$

Raman spectra obtained from zirconolite structures have not been widely reported and no vibrational model was found in the literature due to the complexity of the reported natural samples. As a consequence the band assignments could not be made in the Raman spectra; the spectra were simply used as a fingerprinting technique.

The number of experimentally observed Raman bands does not always equal the number of predicted by theory. This could be due to a change in local symmetry, for example a change in coordination number, or the incorporated atoms could allow silent IR modes to appear in the Raman data. In addition some bands could be a combination of several modes which require deconvolution.

Figure 7 illustrates the results for pyrochlore phases obtained within specimens where x = 0.1 to 0.3. The intensity of some bands decreased when the dopant concentration increased, however, no internal standard was used during the experiments. Therefore, the intensity from different samples cannot be directly compared. On the other hand, results showed in Table 2, relate to the peak positions and can ultimately give information about the bonding energies and the geometry of the samples.

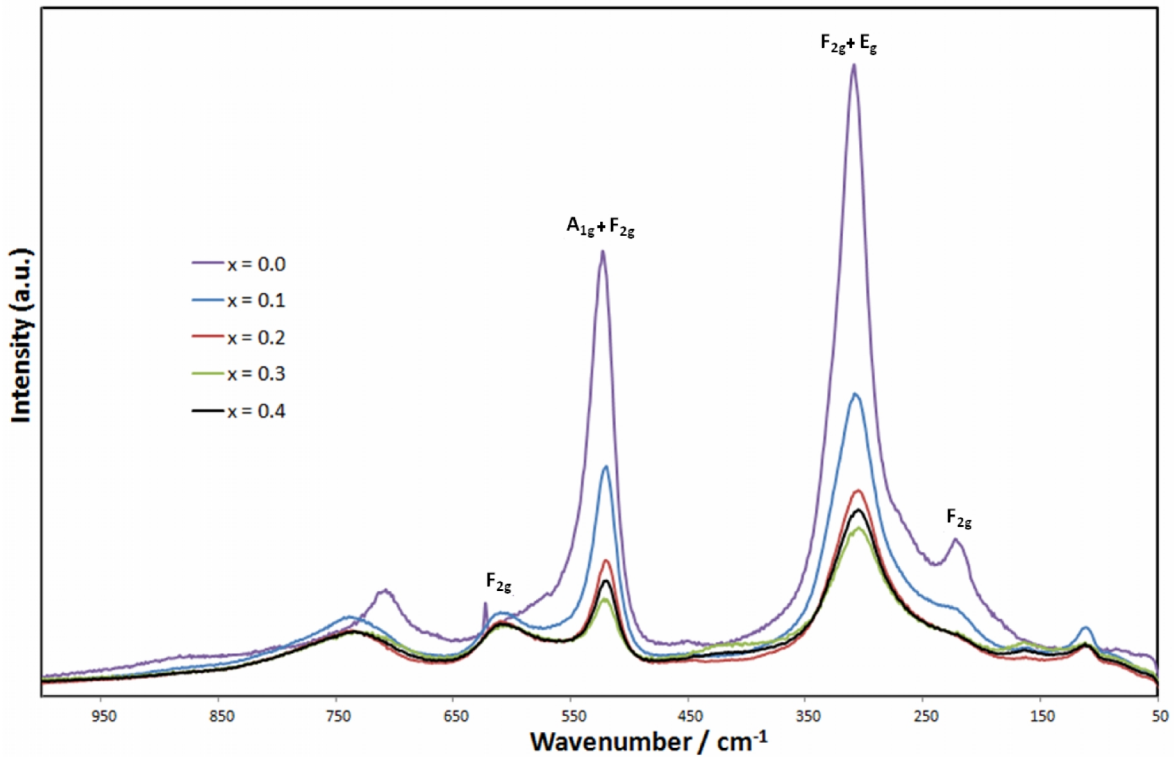

Figure 7: Raman spectra of $Y_{2-x}Ce_xTi_{2-x}Fe_xO_7$ for x = 0 (violet), x = 0.1 (blue), x = 0.2 (red) and x = 0.3 (green).

Broadening of most of the peaks (an increase in FWHM) was observed with an increase in dopant concentration. The incorporation of new atoms into the system may introduce some disorder into the system and disrupt the local symmetry. This is one possible reason for the broadening observed in some peaks. This was prominent with bands at ca. ~220, 300 and 700-750 cm^{-1}.

According to group theory, only six Raman signals are expected and have been assigned for $Y_2Ti_2O_7$ using polarised Raman spectra. [37] The same assignment was then used with the $Y_{2-x}Ce_xTi_{2-x}Fe_xO_7$ system, as the reported spectra and peak positions were close to our experimental results. Several signals (low frequencies and frequencies above 700 cm^{-1}) were not labelled as they might be due to structural distortion, displacement of atoms from their ideal positions or harmonic effects. Most of the Raman signals observed tend to slightly shift towards higher wavenumber values or lower energies (Table 3). The band at 750 cm^{-1} were assigned to an oxygen atom within $Ti\text{-}O_7$ coordinated species as it appeared within a pyrochlore yttria stabilised zirconia sample doped with titanium. The decrease in energy indicates that the Ti – O bonds would be weakened when ***x*** increases and some titanium sites might be distorted.

$Y_2Ti_2O_7$ (cm^{-1})	$Y_{1.9}Ce_{0.1}Ti_{1.9}Fe_{0.1}O_7$ (cm^{-1})	$Y_{1.8}Ce_{0.2}Ti_{1.8}Fe_{0.2}O_7$ (cm^{-1})	$Y_{1.7}Ce_{0.3}Ti_{1.7}Fe_{0.3}O_7$ (cm^{-1})	$Y_{1.6}Ce_{0.4}Ti_{1.6}Fe_{0.4}O_7$ (cm^{-1})	Raman band [32, 33]
-	107	111	111	116	-
-	-	-	165	166	-
220	227	221	221	221	F_{2g}
307	306	304	303	304	$F_{2g} + E_g$
522	520	518	517	518	$A_{1g} + F_{2g}$
-	609	609	609	609	F_{2g}
708	738	742	732	740	-

Table 2: Observed bands in the Raman spectra at room temperature of pyrochlore structures from $Y_{2-x}Ce_xTi_{2-x}Fe_xO_7$

Raman scattering bands can be a contribution of several vibrational modes (equation (1)); a shift on the position of a specific Raman active mode could be the origin of the observed broadening. This hypothesis is supported by previous studies [38] and by the fact that the band at ca. 550 cm^{-1} has split in two. This signal was formerly reported to be a contribution of the A_{1g} and F_{2g} normal modes (equation (1)). The splitting was formerly observed when $Y_2Ti_2O_7$ was doped with Zr (IV) into the Ti (IV) site. [39]

For higher compositions, such as x = 0.8, Figure 9, the distinction of two different phases was clear; while for x = 0.4, Figure 8, the two different phases could not be differentiated by Raman spectroscopy.

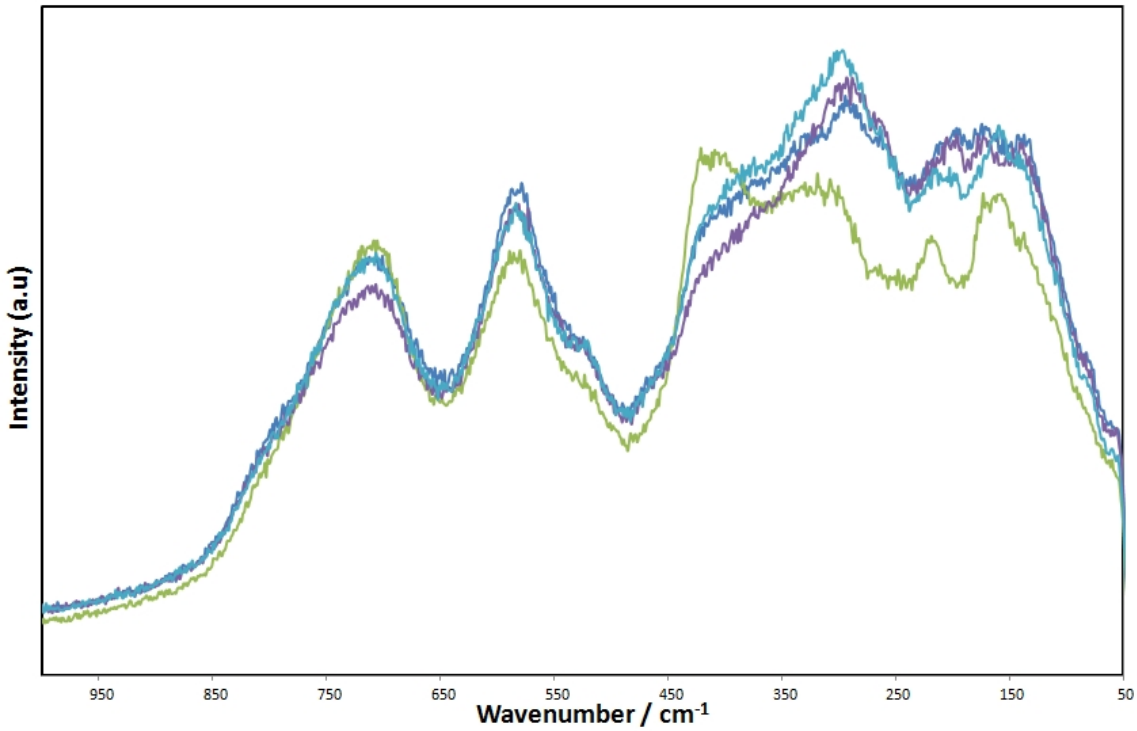

Figure 8: Raman spectra of $Y_{1.6}Ce_{0.4}Ti_{1.6}Fe_{0.4}O_7$.

Above $x = 0.7$ the fluorite phase could be monitored (Fig. 9). It was deduced that the peak observed around 450 cm^{-1} (blue line) was the only predicted Raman active band ($F_{2g}^{(R)}$) for a fluorite structure. This hypothesis would be consistent with the results from other characterisation techniques.

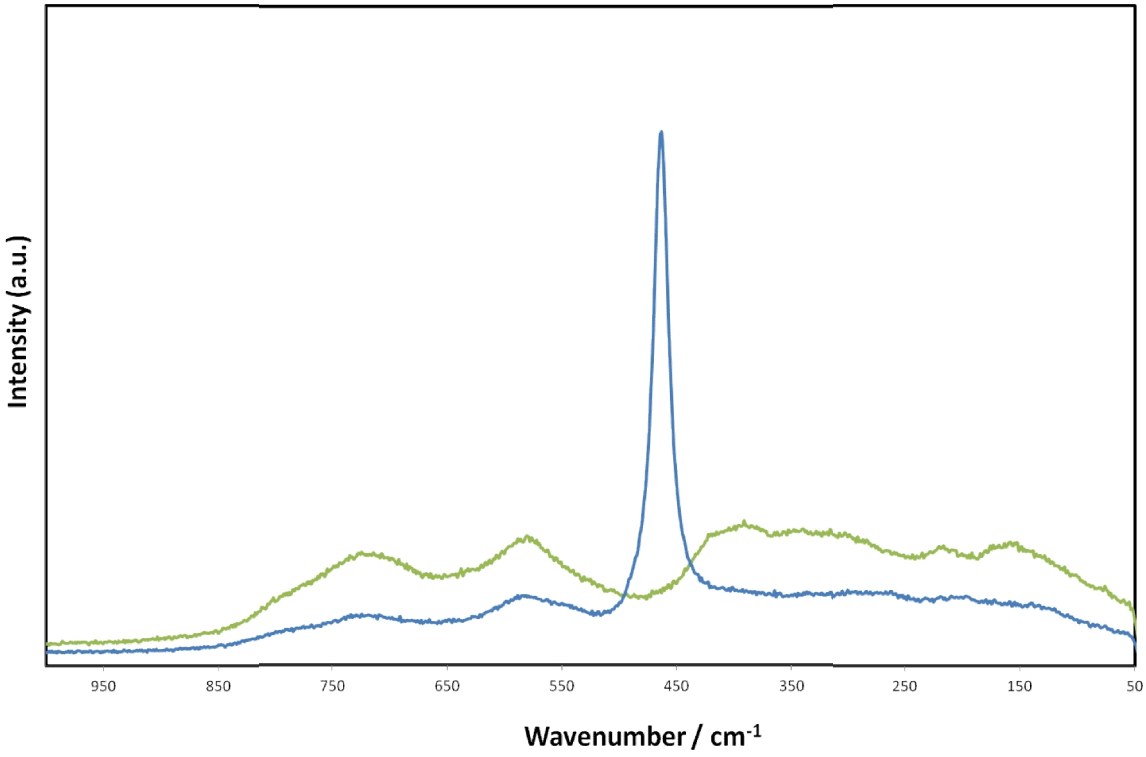

Figure 9: Raman spectra of x=0.8 where the blue line represents a fluorite structure (CeO_2) and the green a zirconolite lattice (yttria-titanate-oxide).

The band at ca. 750 cm^{-1} was previously observed in highly Ti-doped YSZ [39] (cubic yttria-stabilised-zirconia) which is a similar system to $Y_{2-x}Ce_xTi_{2-x}Fe_xO_7$. The intensity of the band usually depends on the Ti concentration. However, such an assumption cannot be made from our results.

3.5. Structural refinement

3.5.1. Pyrochlore solid solution: $Y_{1-x}Ce_xTi_{1-x}Fe_xO_7$ with x = 0.1

Consideration of X-ray diffraction data suggested the formation of a single phase pyrochlore solid solution in the range $0.0 \leq x \leq 0.1$. The compositions with x = 0.1 were selected for further

investigation by neutron powder diffraction for the purpose of structure refinement. The neutron powder diffraction data for the x = 0.1 composition were successfully indexed in space group Fd-3m. Structure refinement used the structure model for the $Y_2Ti_2O_7$, published by Harvey *et al*., as the starting point. [24] This model places the B site cation at the origin (16c position), with Y located at (0.5, 0.5, 0.5); O2 at (3/8, 3/8, 3/8), and O1 at (x, 1/8, 1/8) with x ≈ 3/8 (corresponding to the 8a, 8b and 48f positions, respectively). Ce^{4+} was assumed to substitute for Y^{3+} at the larger 8-fold co-ordinate site, and Fe^{3+} was assumed to substitute for Ti^{4+} at the smaller 6-fold co-ordinate site. The isotropic thermal displacement parameters of atoms occupying the same site were constrained to be equal. The structure refinement converged quickly affording the refined parameters reported in Table 3. The goodness of fit indicators, R_{wp} = 5.60 % and χ^2 = 3.91 %, together with the graphical fit, Figure 10, demonstrate a good fit to the diffraction data confirming the pyrochlore structure model.

a = 10.10087(21) (Å)					
Name	x	y	z	U_{iso} (x 100 Å^2)	Frac.
Y1	0.5	0.5	0.5	1.28(3)	0.95
Ce1	0	0	0	1.28(3)	0.05
Ti1	0	0	0	0.60(7)	0.95
Fe1	0	0	0	0.60(7)	0.05
O1	0.3293(1)	0	0	1.29(2)	1
O2	0.375	0.375	0.375	1.02(5)	1

Table 3: Refined structural parameters for $Y_{1.9}Ce_{0.1}Ti_{1.9}Fe_{0.1}Nb_xO_7$ (x = 0.1), determined from Rietveld analysis of neutron powder diffraction data.

x	Bond lengths (Å)			Bond Valence Sums (v.u)			
	Y/Ce-O1 x 6	Y/Ce-O2 x 2	Ti/Fe-O1 x 6	Y	Ce	Ti	Fe
0.0 [24]	2.4827(5)	2.1861(1)	1.9555(3)	2.99	-	4.1	-
0.1	2.4816(7)	2.18690(3)	1.9574(4)	2.98	3.7	4.08	3.37

Table 4: Key bond lengths for $Y_{2-x}Ce_xTi_{2-x}Fe_xO_7$ determined from Rietveld analysis of neutron powder diffraction data and resulting cation bond valence sums.

The lattice parameter increase is a consequence of the fact that the mean ionic radius of the 6-fold co-ordinate B-site increases, as a consequence of Fe^{3+} (0.645 Å) substitution for Ti^{4+} (0.605 Å); whereas, the mean ionic radius of the 8-fold co-ordinate A-site decreases, as a consequence of Ce^{4+} (1.110 Å, N.C = 8) substitution for Y^{3+} (1.159 Å, N.C = 8). [13] The observed increase in the unit cell parameter thus appears to be driven by substitution of the larger Fe^{3+} cation for Ti^{4+} within an effectively rigid B_2O_6 network of corner sharing octahedra, forming channels which encapsulate the A cations (in an anti-cristobalite A_2O array), as described by Subramanian *et al.* [2] The bond valence sums of the $Fe^{3+}$and Ce^{4+} substituents deviate significantly from the formal valence states. However, as discussed in the case of the $Y_2Ti_{2-2x}Fe_xNb_xO_7$ pyrochlore solid solution, [40] this is to be expected at the dilute limit of substitution where the Y/Ce-O and Ti/Fe-O bond lengths will be effectively imposed by the rigid B_2O_6 network of corner-sharing octahedra. Further expansion of the unit cell as a function of composition, coupled with an increase in the average Ti/Fe-O bond length and decrease in average Y/Ce-O bond length, as suggested by Table 4, would be expected to lead to more optimal bond valence sums for the substituent species.

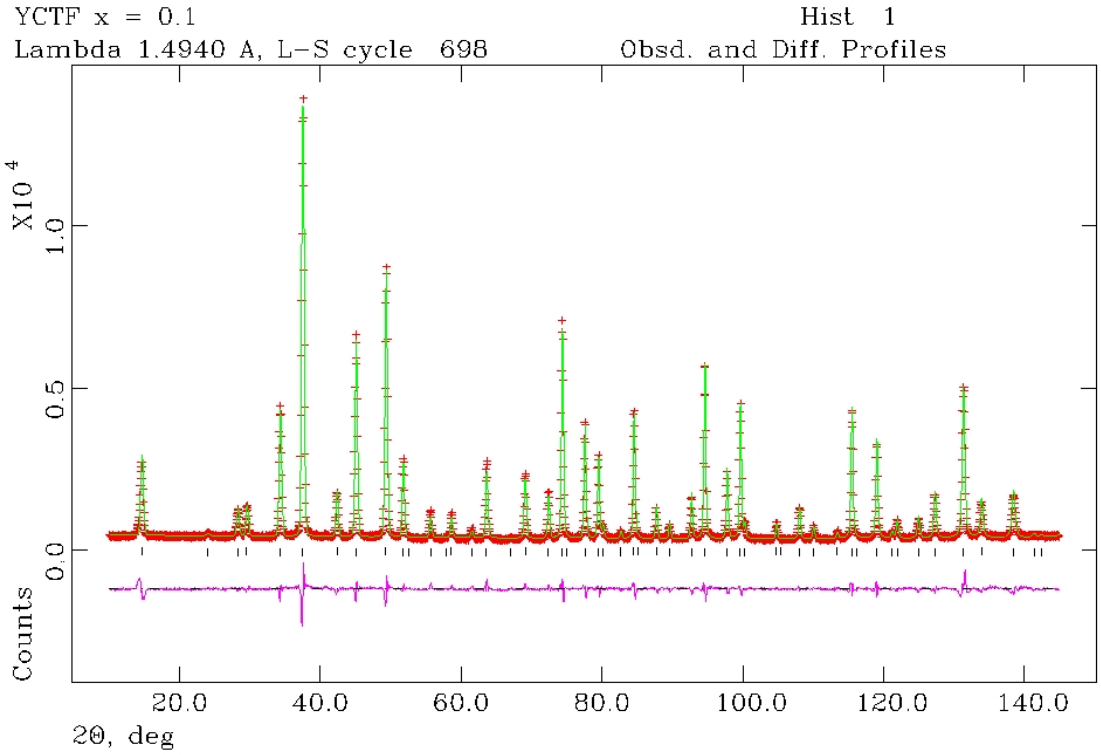

Figure 10: Showing fit (solid line) to high resolution neutron diffraction data (points) for $Y_{1.9}Ce_{0.1}Ti_{1.9}Fe_{0.3}Nb_{0.1}O_7$ (x = 0.1) at 25 °C in space group Fd-3m; tick marks show allowed reflections, the difference profile (lower solid line) demonstrates a good fit to the data, R_{wp} = 5.60% and χ^2 = 3.91 %.

3.5.2. Zirconolite-3T structure: $Y_{2-x}Ce_xTi_{2-x}Fe_xO_7$ with x = 0.6

Consideration of X-ray diffraction data, as described above, suggested the formation of a single phase zirconolite structure for the composition with x = 0.6, which was selected for further investigation by neutron powder diffraction for the purpose of structure refinement. The initial attempt to fit the acquired diffraction assumed the material to be isostructural with $Y_2Ti_{0.6}Fe_{0.7}Nb_{0.7}O_7$, adopting the zirconolite-3T structure in space group $P3_121$. [40] This model provided an adequate fit to the data, but additional unindexed reflections were apparent which could be attributed to the presence of an additional pyrochlore phase. Since electron microprobe and back scattered electron microscopy analyses provided no evidence for the formation of two phases with significantly different composition, it was assumed for the subsequent analysis that both the zirconolite-3T and pyrochlore phases were of identical composition. An attempt to fit the neutron diffraction data using models based on the closely related zirconolite 2M (C2/c [41,42]) was unsuccessful, affording a significantly poorer fit. The refined zirconolite-3T structure model for

$Y_{1.4}Ce_{0.6}Ti_{1.4}Fe_{0.6}O_7$ was therefore considered a good approximation of the structure. The zirconolite 3T structure contains 6 distinct cation sites: two 8-fold co-ordinate sites (Ln1(8) and Ln2(8)), one 7-fold co-ordinate site (Ln3(7)), two 6-fold co-ordinate sites (of different distortion, M1(6) and M2 (6)) and a single 5- fold co-ordinate site which is 50% occupied (M3(5)). It was assumed that the larger Y^{3+}/Ce^{4+} cations occupied, exclusively, the larger 8- and 7-fold co-ordinate sites, with the transition metal cations confined to the smaller 6- and 5-fold co-ordinate sites. The co-ordinates and thermal parameters of atoms occupying the same crystallographic site were constrained to be equal. The Ti / Fe site distribution was fixed in accordance with the results of ^{57}Fe Mössbauer analysis. Note that fitting of the Mössbauer spectra of the x = 0.6 sample required three Fe environments, as discussed above: one environment with quadrupole splitting typical of 5-fold co-ordinate Fe^{3+}, and two environments with similar but significantly different quadrupole splitting characteristic of 6-fold co-ordinate Fe^{3+} with different site distortion. In general, a larger quadrupole splitting implies a greater site distortion, all other factors remaining constant, allowing us to assign 27 % of total Fe to the more distorted M2(6) site, 8 % of total Fe to the less distorted M1(6) site, and 65 % of total Fe is located at the M3(5) site. The Y / Ce distribution was initially assumed to be random, but later refined under chemical constraint of overall unit cell electro-neutrality. This led to the conclusion that the Ln1(8) and Ln2(8) sites were occupied exclusively by Y, with Ce partitioned exclusively to the Ln3(7) site, and this site distribution was fixed for the final stages of the refinement.. The Y and Ce neutron scattering lengths of 7.75 and 4.84 fm, respectively, afford reasonable contrast in this respect.

The refinement converged to yield the refined structural parameters in Table 5. The final goodness of fit parameters were R_{wp} = 8.81% and χ^2 = 9.35 %, which combined with the graphical fit shown in Figure 11, demonstrate an adequate overall fit to the acquired data. A schematic representation of the refined crystal structure is shown in Figure 12.

The refined metal-oxygen bond lengths and occupancy of the Ln and M sites are reported in Tables 6 and 7. Occupancies and bond valence sums for the Ln and M sites are reported in Tables 8 and 9. Consideration of bond valence sums reported for the Ln1(8), Ln2(8) and Ln3(7) sites, given in Table 9, show that Y prefers the Ln1(8) and Ln2(8) sites compared to the Ln3(7) site in which it is substantially over bonded. The Ce bond valence sums deviate significantly from the formal tetravalent oxidation state in all sites. This suggests that the preferential occupancy of Ce in the Ln3(7) site is a consequence of this being the least favoured site for Y. Inspection of the bond lengths for the M3(5) site show that the cation within this interstice has one non-bonding contact distance of 2.96 Å, with the remaining four bond lengths distributed about a mean of 1.91 Å. Consequently, this site should more properly be described as a distorted tetrahedron and will be referred, to herein as the M3(4) site. The Shannon polyhedral distortion index, Δ_n, is a useful

indicator of polyhedron bond length distortion, *viz.* $\Delta_n = 1/n\ [\sum(r_i - r_m) / r_m)^2] \times 10^3$, where r_i and r_m are the individual and mean metal-oxygen bond lengths respectively. Calculation of the distortion index for the M sites shows that the M2(6) site is considerably more distorted than the M1(6) site, consistent with the assignment of Fe occupancy from ^{57}Fe Mössbauer analysis. The Ti and Fe bond valence sums indicate no significant preference of either cation for the M1(6), M2(6) or M3(4) sites: the Ti bond valence sum is close to 4.0 v.u. in all sites, whereas that of Fe, 3.3 v.u., demonstrates significant over bonding of this cation. Clearly, the preferential occupancy of the M3(4) site by Fe cannot be explained on the grounds of ionic size. The M3(4) site shares a common edge with the M1(6) and M2(6) sites, within the hexagonal tungsten bronze layer, as discussed for the case of $Y_2Ti_{0.6}Fe_{0.7}Nb_{0.7}O_7$. The metal-metal distance between the M1(6)-M3(4) sites is 3.20 Å and 3.09 Å for the M2(6)-M3(4) sites. Unfavourable electrostatic interactions across the shared polyhedral edges of these sites would be minimised by selective occupation of the M3(4) site by Fe^{3+}, reducing the number of Ti^{4+} cations sharing a common polyhedral edge. This would explain the Fe distribution observed by ^{57}Fe Mössbauer spectroscopy.

Overall, it may be argued that the refined model is a plausible but approximate description of the crystal structure of $Y_{1.4}Ce_{0.6}Ti_{1.4}Fe_{0.6}O_7$. It is possible that this structure adopts a symmetry lower than $P3_121$, which may account for the residual intensity mismatch across the diffraction pattern in Figure 11, but further investigation by transmission electron microscopy and electron diffraction, on single grains, is required to resolve this issue. The bond valence sums for Y^{3+} and Ti^{4+} occupancy of the Ln and M sites are generally acceptable, but those of the lower concentration substituent species, $Ce^{4+}$and Fe^{3+}, show more significant deviation from the formal oxidation state. These bond valence sums may point to an underlying instability of the zirconolite-3T structure over the $Y_{2-x}Ce_xTi_{1-x}Fe_xO_7$ composition range.

Space group: $P3_121$		a = 7.3774(3) (Å)		c = 16.817(22) (Å)	
Name	Site	x	y	z	U_{iso} (x 100 Å^2)
Y/Ce1(8)	3a	0.8766(31)	0	0.3333	1.1(3)
Y/Ce2(8)	3a	0.3482(33)	0	0.3333	1.1(3)
Y/Ce3(7)	6c	0.162(4)	0.659(4)	0.0142(8)	1.5(3)
Ti/Fe1(6)	3a	0.310(11)	0	0.8333	1.7(5)
Ti/Fe2(6)	6c	0.516(16)	0.334(19)	0.164(5)	1.9(3)
Ti/Fe3(4)	6c	0.092(6)	0.933(6)	0.1880(20)	1.8(3)
O1	6c	0.6397(34)	0.656(4)	0.1575(10)	1.9(4)
O2	6c	0.012(5)	0.838(5)	0.0640(10)	1.6(3)
O3	6c	0.504(4)	0.338(5)	0.0433(10)	2.1(3)
O4	6c	0.209(4)	0.2347(33)	0.1410(12)	1.6(3)
O5	6c	0.523(4)	0.876(4)	0.0504(13)	1.2(2)
O6	6c	0.931(4)	0.340(5)	0.0606(12)	0.7(2)
O7	6c	0.235(4)	0.615(4)	0.1484(13)	1.6(3)

Table 5: Refined structural parameters for $Y_{1.4}Ce_{0.6}Ti_{1.4}Fe_{0.6}O_7$ (x = 0.6) determined from Rietveld analysis of neutron powder diffraction data, occupancies for M sites are reported in Table 8. The goodness of fit parameters were R_{wp} = 8.81 % and χ^2 = 9.35.

Bond	Length (Å)	Bond	Length (Å)	Bond	Length (Å)
Ln1(8)-O2	2.131(32)	Ln2(8)-O1	2.651(17)	Ln3(7)-O2	2.27(4)
Ln1(8)-O2	2.130(32)	Ln2(8)-O1	2.650(17)	Ln3(7)-O3	2.324(34)
Ln1(8)-O3	2.545(31)	Ln2(8)-O2	2.538(31)	Ln3(7)-O5	2.397(30)
Ln1(8)-O3	2.545(31)	Ln2(8)-O2	2.538(31)	Ln3(7)-O5	2.130(29)
Ln1(8)-O4	2.486(22)	Ln2(8)-O3	2.135(35)	Ln3(7)-O6	2.245(35)
Ln1(8)-O4	2.485(22)	Ln2(8)-O3	2.134(35)	Ln3(7)-O6	2.166(32)
Ln1(8)-O6	2.809(30)	Ln2(8)-O5	2.434(31)	Ln3(7)-O7	2.378(26)
Ln1(8)-O6	2.809(30)	Ln2(8)-O5	2.434(31)		
$\Delta_{Ln1(8)} = 0.709$		$\Delta_{Ln2(8)} = 0.306$		$\Delta_{Ln3(7)} = 0.020$	
Expected BVS (v.u.) = 3.0		Expected BVS (v.u.) = 3.0		Expected BVS (v.u.) = 3.4	
Mean BVS (v.u.) = 2.8		Mean BVS (v.u.) = 3.0		Mean BVS (v.u.) = 4.0	

Table 6: Key bond lengths for Ln sites in $Y_{1.4}Ce_{0.6}Ti_{1.4}Fe_{0.6}O_7$ (x = 0.6) determined from Rietveld analysis of neutron powder diffraction data and resulting cation bond valence sums. The expected bond valence sum assumes the nominal cation oxidation state given in Table 8. The mean bond valence sum is the weighted mean calculated bond valence sum derived from the refined site occupancies and bond valence sums determined from bond length data, given in Table 9.

Bond	Length (Å)	Bond	Length (Å)	Bond	Length (Å)
M1(6)-O4	1.93(6)	M2(6)-O1	2.08(12)	M3(4)-O1	2.96(5)
M1(6)-O4	1.94(6)	M2(6)-O1	2.04(12)	M3(4)-O2	1.77(4)
M1(6)-O6	1.899(31)	M2(6)-O3	2.02(8)	M3(4)-O2	2.19(4)
M1(6)-O6	1.900(31)	M2(6)-O4	2.04(10)	M3(4)-O4	1.57(4)
M1(6)-O7	2.06(6)	M2(6)-O5	2.04(8)	M3(4)-O4	2.10(4)
M1(6)-O7	2.06(6)	M2(6)-O7	1.73(10)		
$\Delta_{M1(6)} = 1.230$		$\Delta_{M2(6)} = 3.533$		$\Delta_{M3(5)} = 31.694$	
Expected BVS (v.u.) = 3.9		Expected BVS (v.u.) = 3.8		Expected BVS (v.u.) = 3.2	
Mean BVS (v.u.) = 4.0		Mean BVS (v.u.) = 4.2		Mean BVS (v.u.) = 3.5	

Table 7: Key bond lengths for M in sites $Y_{1.4}Ce_{0.6}Ti_{1.4}Fe_{0.6}O_7$ (x = 0.6) determined from Rietveld analysis of neutron powder diffraction data. M site occupancies are given in Table 8. The expected bond valence sum assumes the nominal cation oxidation state together with occupancies given in Table 9. The mean bond valence sum is the weighted mean calculated bond valence sum derived from the refined site occupancies and bond valence sums determined from bond length data.

Cation	Site			Site		
	Ln1(8) 3a	Ln2(8) 3a	Ln3(7) 6c	M1(6) 3a	M2(6) 6c	M3(4) 6c
Y	1.00	1.00	0.60	-	-	-
Ce	0.00	0.00	0.40	-	-	-
Ti	-	-	-	0.90	0.84	0.11
Fe	-	-	-	0.10	0.16	0.39

Table 8: Occupancies for Ln and M sites in $Y_{1.4}Ce_{0.6}Ti_{1.4}Fe_{0.6}O_7$ (x = 0.6) determined from ^{57}Fe Mössbauer spectroscopy and Rietveld analysis of neutron powder diffraction data.

Cation	Site			Site		
	Ln1(8) 3a	Ln2(8) 3a	Ln3(7) 6c	M1(6) 3a	M2(6) 6c	M3(4) 6c
Y	2.8	3.0	3.6	-	-	-
Ce	3.4	3.7	4.5	-	-	-
Ti	-	-	-	4.1	4.0	4.0
Fe	-	-	-	3.4	3.3	3.3

Table 9: Bond valence sums for Ln and M sites in $Y_{1.4}Ce_{0.6}Ti_{1.4}Fe_{0.6}O_7$ (x = 0.6) determined from bond length data reported in Tables 6 and 7.

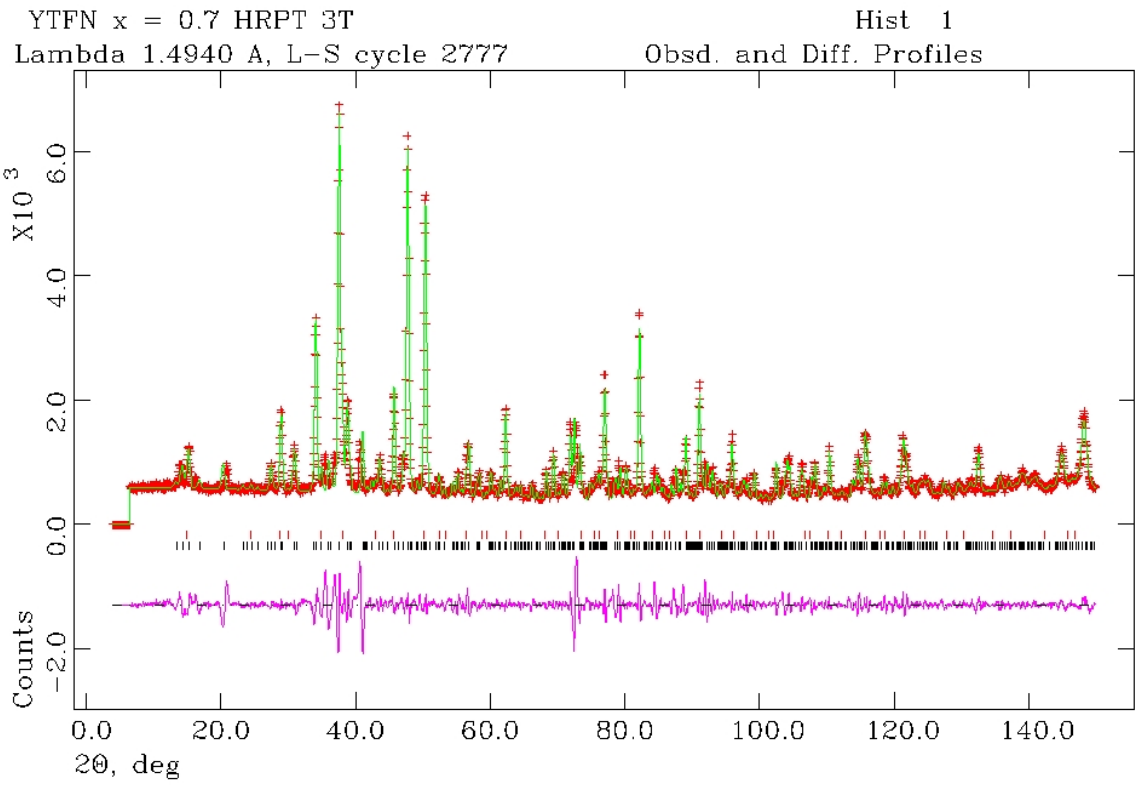

Figure 11: Showing fit (solid line) to high resolution neutron diffraction data (points) for $Y_{1.4}Ce_{0.6}Ti_{1.4}Fe_{0.6}O_7$ (x = 0.6) at 25 °C in space group $P3_121$; tick marks show allowed reflections, for pyrochlore (red markers) and zirconolite 3T (black markers), the difference profile (lower solid line) demonstrates an adequate fit to the data.

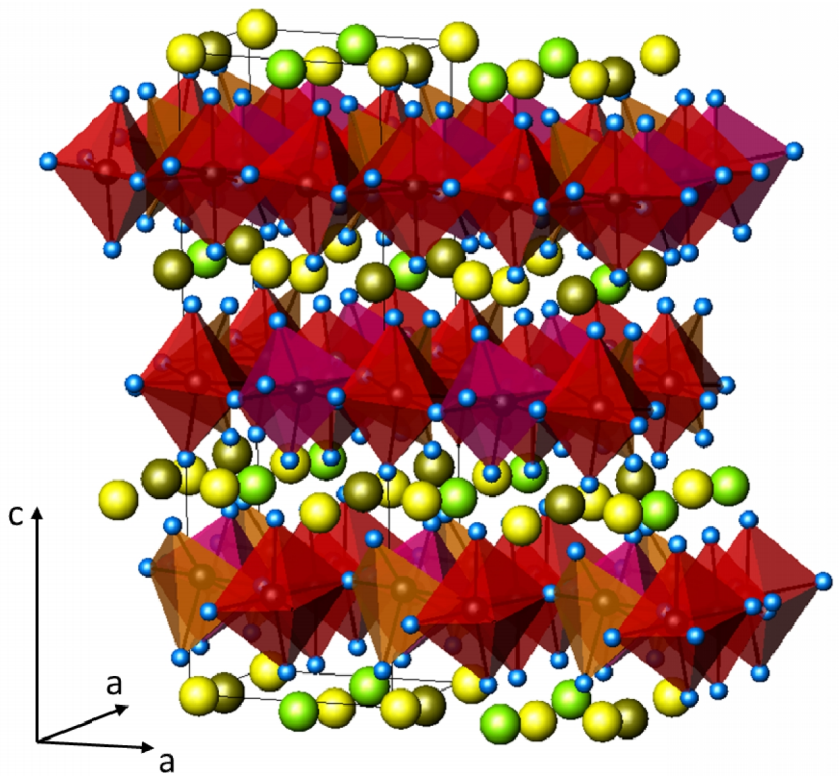

Figure 12: Schematic representation of refined structural model for: Ln1(8), Ln2(8) and Ln3(7) sites are denoted by gold, green and yellow spheres, respectively; M1(6), M2(6) and M3(4) sites are shown by magenta, red and orange polyhedra, respectively; oxygen anions are shown by blue spheres. Note M3(4) sites are shown at 50% occupancy.

4. CONCLUSION

The $Y_{2-x}Ce_xTi_{2-x}Fe_xO_7$ system undergoes several phase transitions when x increases from 0 to 1.0. It first accepts a cubic structure within the pyrochlore family for formulations where $x < 0.1$. Mixed phased samples are observed until $x = 0.4$ and a zirconolite-3T phase is obtained when the sample compositions are in between $0.5 < x < 0.6$. The system then contains an additional phase as a fluorite material was detected as well as a zirconolite-3T phase, for compositions above 0.7.

5. FUTURE WORK

X-ray absorption spectroscopy (XAS) is a sensitive measure of oxidation state in redox active elements, and the study of the Ce edge could confirm that Ce is found as Ce^{4+}.

Further investigation is necessary to confirm whether Fe^{3+} cations, from $Y_{2-x}Ce_xTi_{2-x}Fe_xO_7$ specimen, can also be found in other phases than pyrochlore or zirconolite.

Solid state ^{89}Y NMR and EXAFS data could elucidate the structure on an atomic scale, such as for the oxygen sites, the x parameter could also be obtained by such a method.

All the structures obtained in the study of this system (pyrochlore, zirconolite, fluorite) are known to be resistant chemically and to radiation damage. Nevertheless, these features are very dependent on the ceramic formulation. The co-substitution could improve or diminish the radiation resistance, as well as the chemical resistance of this titanate based system.

Chemical and physical resistance properties of this double substituted system would need to be studied, and if conclusive, actinide substitution experiments (U (IV), Pu (IV) and Np (IV) instead of Ce (IV) incorporation) should go ahead.

Seeing that multiple phases are obtained, the proportion of actinide substitution should not exceed $x=0.6$ if this system is retained as a wasteform. Above this proportion, CeO_2 was obtained and AnO_2 might be synthesised if transactinides are incorporated at such a percentage.

6. REFERENCES

[1] E.N.S Muccillo, *Cerâmica*, 2008, **54**, 129-144.

[2] M.A. Subramanian, J.E. Greedan, N.P. Raju, A.P. Ramirez and A.W. Sleight, *Journal de Physique IV*, 1997, **7**, C1-625C1-628.

[3] J.E. Greedan, N.P. Raju, A. Maignan, Ch. Simon,, J.S. Pedersen, A.M. Niraimathi, E. Gmelin and M.A. Subramanian, *Physical review B – Condensed Matter and Materials Physics*, 1996, **54**, Issue 10, 7189 – 7200.

[4] L.K. Joseph, K.R. Dayas, S. Damodar, B. Krishnan, K. Krishnankutty, V.P.N. Nampoori and P. Radhakrishnan, *Spectrochimica Acta – Part A: Molecular and Biomolecular Spectroscopy*, 2008, **71**, Issue 4, 1281-1285.

[5] J. Yang and Y. Su, *Materials Letters*, 2010, **64**, Issue 3, 313-316.

[6] W. Lutze and R.C. Ewing, *Radioactive Waste forms for the future*, Elsevier Science, Amsterdam, 1988, 233-334.

[7] A.E. Ringwood. *Fortschritt in Mineralogie,* 1980, **58**, 149-168.

[8] M.A. Subramian, G. Aravamudan and G.V. Subba Rao, *Progress in Solid State Chemistry*, 1983, **15**, 55-143.

[9] B.C. Chakoumakos, *Journal of Solid State Chemistry*, 1984, **53**, 120-129.

[10] M.R. Gilbert, *Zirconolite waste-forms for plutonium disposition*, Thesis of the University of Manchester, 2009.

[11] G.R Lumpkin, K. L. Smith, R. Giere and C. T. Williams, Geological Society, London, special publications, 2004, **236**, 89-111.

[12] P.A. Bingham. R.J. Hand, M.C. Stenett, N.C. Hyatt and M.T. Harrison, 2008, Materials Research Society Symposium Proceedings, **1107**, 421-428.

[13] R.D. Shannon, *Acta Crystallographica*, 1976, **A32**, 751.

[14] J.C. Marra, A.D. Cozzi, R.A. Pierce, J.M. Pareizs, A.R. Jurgensen and D.M. Missimer, *Ceramic Transactions*, 2002**, 132**, 381.

[15] J. Ding, Y. Xiao, P. Han and Q. Zhang, *Journal of Rare Earths*, 2010, **28**, No. 5, 765-768.

[16] S.X. Wang, B.D. Begg, L.M. Wang, R.C. Ewing, W.J. Weber and K.V. Govindan Kutty, *Journal of Materials Research*, 1999, **14**, 4470-4473.

[17] S.X. Wang, L.M. Wang, R.C. Ewing and K.V. Govindan Kutty, *Physics Research Section B*, 2000, **169**, Issues 1-4, 135-140.

[18] J. Lian, F.X. Zhang, M.T. Peters, L.M. Wang and R.C. Ewing, *Journal of Nuclear Materials*, 2007, **362**, 438-444.

[19] S.E. Ashbrook, KR. Whittle, G.R. Lumpkin and I. Farnan, *The Journal of Physical Chemistry B*, 2006, **110**, 10358-10364.

[20] Hk. Muller-Buschbaum and J.-P. Werner, *Journal of Alloys and Compounds*, 1994, **206**, L11-L13.

[21] P.D. Wilson, *The Nuclear Fuel Cycle: From Ore to Wastes*, Oxford University Press, ISBN: 0198565402, 1996.

[22] K. Legarec, D.G. Rancourt, *Recoil: Mössbauer Spectral Analysis Software for Windows*, v. 1.0, 1998.

[23] A.C. Larson and R.B. Von Dreele, *General Structural Analysis System (GSAS)*, University of California: Los Alamos, 1998.

[24] E.J. Harvey, S.E. Ashbrook, G.R. Lumpkin, S.A.T Redfern, *Journal of Materials Chemistry*, 2006, **16**, 4665–4674.

[25] L. Borodin, I. Nazarenko, T. Richter, *Doklady Academy Sciences USSR, Earth Science Section (English. Translation)*, 1960, **134**, 1022.

P. Bayliss, F. Mazzi, R. Munno and T. White, *Mineralogical Magazine*, 1989, **53**, 565.

[26] F. Mazzi and R. Munno, *American Mineralogist*, 1983, **68**, 262-276.

[27] M.D. Dyar, D.G. Agresti, M.W. Schaefer, C.A. Grant and E.C. Sklute, *Annual Review Earth Planetary Sciences*, 2006, **34**, 83-125.

[28] F.J. Berry, G.R. Lumpkin, G.Oates and K.R. Whittle, *Hyperfine Interactions*, 2006, **106**, 363-366.

[29] G.R. Lumpkin, K.R. Whittle, C.J. Howard, Z. Zhang, F.J. Berry, G. Oats, C.T. Williams and A.N. Zaitsev, *Materials Research Society Symposium Proceedings*, 2006, **932**.

[30] I.E. Grey, W.G. Mumme, T.J. Ness, R.S. Roth and K.L. Smith, *Journal of Solid State Chemistry*, 2003, **174**, 285-295.

[31] A.F. Fuentes, K. Boulahya, M. Maczka, J. Hanuza and U. Amador, *Solid State Sciences*, 2005, **7**, 343-353.

[32] R. A. McCauley, *Journal of Applied Physics*, 1980, **51**, 290-294.

[33] H.C. Gupta, S. Brown, N. Rani and V.B. Gohel, *Journal of Physics and Chemistry of Solids*, 2002, **63**, 535-538.

[34] R.A. McCauley, *Journal of Applied Physics*, 1980, **51**, 290-294.

[35] F.W. Poulsen, M. Glerup and P. Holtappels, *Solid State Ionics*, 2000, **135**, 595-602.

[36] N. Kjerulf-Jensen, R.W. Berg and F.W. Poulsen, *2nd European Solid oxide fuel cell forum,* Norway, 1996, Vol.2, Edited by Bernt Thorstensen, 647-656.

[37] M.T. Vandenborre, E.Husson, J.P. Chatry and D. Michel, *Journal of Raman Spectroscopy*, 1983, **14**, No. 2, 63-71.

[38] W.J. Chung, B.J. Park, H.S. Seo, J.T. Ahn and Y.G. Choi, *Chemical Physics Letters*, 2006, **419**, 400-404.

[39] M . Glerup, O.F. Nielsen and F.W. Poulsen, *Journal of Solid State Chemistry*, 2001, **160**, 25-32.

[40] C. De La Fontaine, M.C. Stennett, S.L. Heath and N.C. Hyatt, *in this volume*, 2013, **4,** 116-157.

[41] K.R. Whittle, N.C. Hyatt, K.L. Smith, I. Margiolaki, F.J. Berry, K.S. Knight, G.R. Lumpkin, *American Mineralogist*, 2012, **97**, 291-298.

[42] B. Gatehouse, I. Grey, R. Hill, H. Rossell, *Acta Crystallographica*, 1981, **B37**, 306-312.

Chapter 4:

SYNTHESIS AND CHARACTERISATION OF NEW PYROCHLORE ZIRCONOLITE SOLID SOLUTIONS FOR ACTINIDE IMMOBILISATION: $Y_2Ti_{2-2x}Fe_xNb_xO_7$

Carlos De La Fontaine[1], M.C. Stennett[2], Sarah L. Heath[1] and N.C. Hyatt [2]*

[1]Centre for Radiochemistry Research, School of Chemistry, University of Manchester, Oxford Road, Manchester M13 9PL, United Kingdom.

[2]Department of Engineering Materials, University of Sheffield, Mappin Street, Sheffield, S1 3JD, United Kingdom.

(Correspondence: N.C.Hyatt@sheffield.ac.uk)

ABSTRACT

The synthesis and structure of a new pyrochlore $Y_2T_{i2-2x}Fe_xNb_xO_7$ (where x = 0.0 to 1.0) is reported. This is a model host for trivalent actinide species which may be substituted at the Y^{3+} site. The compositions were prepared by a solid state reaction and sintering method, affording ceramic specimens of > 95% theoretical density. Compositions with $0.0 < x < 0.5$ adopt the pyrochlore structure with substitution of Fe^{3+} on the octahedral Ti site confirmed by Mössbauer spectroscopy. In contrast, compositions with $0.7 < x < 0.9$ adopt an unusual zirconolite-3T structure which appears to be stabilised by Fe^{3+} in 5-fold co-ordination, as demonstrated by Mössbauer spectroscopy. Compositions $0.4 < x < 0.7$ were found to comprise a mixture of both pyrochlore and zirconolite and $x > 0.9$ consist of a zirconolite-3T and a fluorite phase.

1. INTRODUCTION

Zirconolite ($CaZrTi_2O_7$) and pyrochlore structured ($A_2B_2O_7$) materials have generated interest for application as actinide host phases for radioactive waste immobilisation, and, more widely, for application in fuel cells and catalysis. Pyrochlore oxides are known to exhibit high ionic and electrical conductivity, [1] magnetic ordering,[2, 3] as well as luminescence properties. [4,5] This diversity in application is associated with the chemical flexibility of the pyrochlore structure, which may accept substitution on both the A and B sites, by cations of appropriate size and charge. Zirconolite and pyrochlore ceramics tolerate both cation and anion disorder and are known for their resistance to chemical corrosion and radiation damage, [6] which is the primary requirement for application as an actinide host, and can be used either as single phase hosts or as part of a multiphase assemblage, as in Synroc (SYNthetic ROCk). [7] Radiation damage occurs due to radioactive decay events which produce atomic defects. The crystallinity of ceramic materials will be modified by these radiactive decay events leading to disruption of long range order, creation of void space and ultimately amorphisation of the crystal lattice. The choice of synthetic zirconolite and pyrochlores as actinide hosts was inspired by the existence of naturally occurring actinide rich minerals with these structure types.

1.1. The zirconolite structure

Zirconolite is a derivative of the fluorite structure. The generalised chemical composition of zirconolite is $CaZrTi_2O_7$, although zirconolite can adopt several different polytypic structures with monoclinic (2M or 4M), orthorhombic (3O) and hexagonal (3T) symmetry. The structure can be described as consisting of layers of calcium and zirconium atoms situated between planes of titanium polyhedra arranged in hexagonal tungsten bronze (HTB) arrays. The polyhedra in the HTB arrays are both octahedral (6-fold) and square pyramidal (5-fold), as indicated in Figure 1.

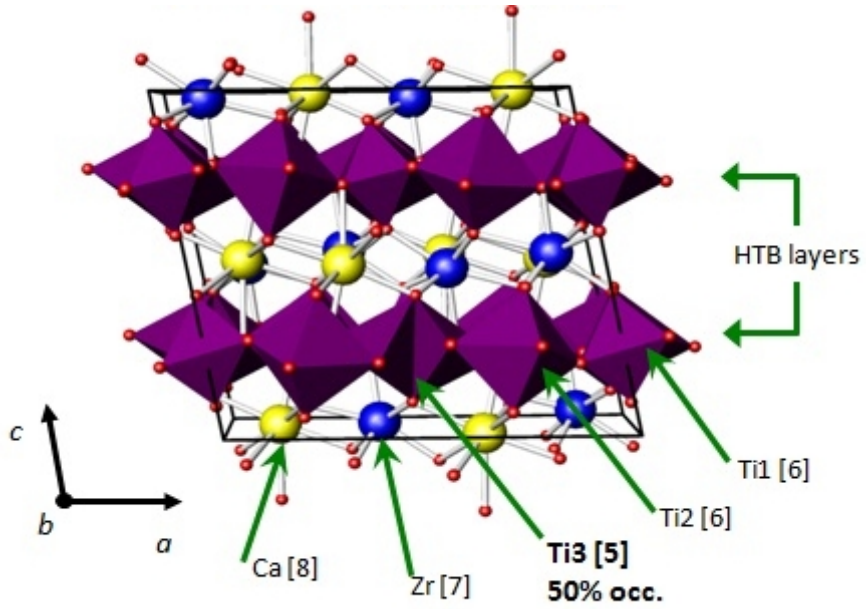

Figure 1: Schematic of a 2M polytype zirconolite structure ($CaZrTi_2O_7$) (Coordination number of cation site is showed next to the atoms). [8]

In nature, the zirconium chemical composition differs from the generalised one due to extensive cation substitution. Some natural samples have been found to incorporate up to 24 wt% UO_2, 22 wt% ThO_2 and 32 wt% REE_2O_3. [9]

1.2. The pyrochlore structure

The ideal pyrochlore structure adopts the Fd-3m space group; with eight formula units per unit cell. The ideal $A_2B_2O_7$ pyrochlore structure is derived from fluorite (AO_2) via an ordered removal of one eighth of the oxygen atoms, combined with an ordered arrangement of A and B cations. The ordered arrangement of anion vacancies yields two distinct cation polyhedra: the A site is 8-fold coordinated, and takes the form of a distorted cube; whereas the B-site is 6-fold co-ordinate, and is a distorted octahedron. [10] The A site is typically occupied by +2 and +3 cations, and the B site by +4 and +5 cations.

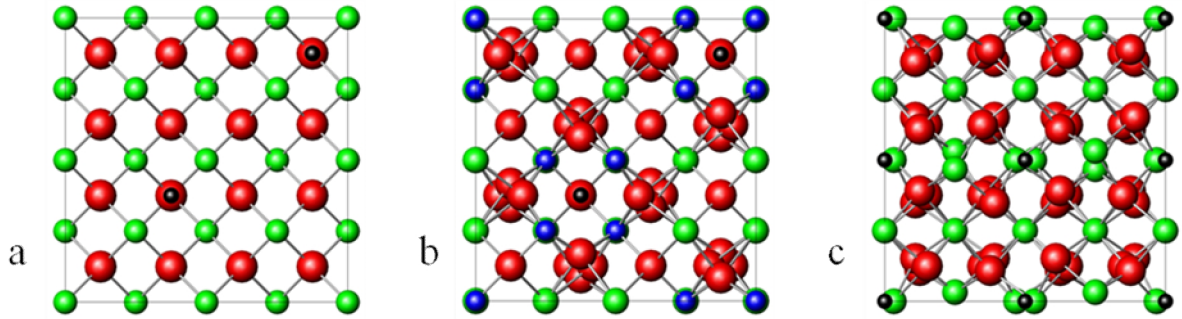

Figure 2: Schematic representations of the crystal structures of (a) $AX_{1.75}$ defect fluorite, (b) $A_2B_2X_7$ pyrochlore, and (c) A_2X_3 C-type structures, projected along the [100] direction. Red spheres represent X anions, green spheres represent A cations, blue spheres represent B cations, and small black spheres represent anion vacancies.

There are three unique oxygen positions, in the pyrochlore structure: the 48f position (x, 1/8, 1/8), the 8b position (3/8, 3/8, 3/8) and the 8a position (1/8, 1/8, 1/8) which is vacant. The pyrochlore structure can then therefore be defined by two parameters: the 48f x oxygen position and the cubic unit cell parameter (*a*). All atoms, except the 48f oxygen, adopt special symmetry defined positions. The stability of the pyrochlore structure depends on the relative sizes of A and B cations. In general, the pyrochlore structure is stable for the radius ratio: $1.46 < r_A/r_B < 1.78$. [11] Below $r_A / r_B = 1.46$ we observe a defect fluorite structure (space group Fm-3m) with both anion and cation disorder. Above $r_A / r_B = 1.78$, a more complex monoclinic phase is formed.

1.3. $Y_2Ti_{2-2x}Fe_xNb_xO_7$

The $Y_2Ti_{2-2x}Fe_xNb_xO_7$ is a model host for trivalent actinides which may be incorporated by substitution at the Y^{3+} site. Transition metals such as Fe^{3+} are common contaminants in nuclear waste streams (arising from corrosion of steel containment vessels) [12, 13] and could be potentially accommodated on the pyrochlore B-site, because of its flexibility in accepting different oxidation state cations, and ability to adopt different geometries (square pyramidal in Dy_2TiO_5, [14] trigonal bipyramidal in Gd_2TiO_5 [15] and octahedral in $(Gd/Cs)_2Ti_2O_{7-y}$. [16] Titanate pyrochlores have been widely studied, [2] however $Y_2Ti_{2-2x}Fe_xNb_xO_7$ have not been previously investigated. Iron containing niobates such as $(CdLn)(Fe_{1/2}^{3+}Nb_{3/2}^{5+})O_7$ were investigated by Fedorov *et al.* in the 70's and were found to crystallise with the pyrochlore structure. [17] Introducing multivalent oxidation state elements (Fe, Nb) could potentially lead to the distortion of the cubic structure and/or affect the stochiometry. Moreover, the co-substitution of Fe and Nb for Ti, could offer a route to improving the radiation tolerance of titanate pyrochlores, which are known to be sensitive to composition.

Thus, the synthesis of $Y_2Ti_{2-2x}Fe_xNb_xO_7$ was attempted to determine the potential existence of a new family of pyrochlore compositions of this type.

2. EXPERIMENTAL PROCEDURE

Synthesis of $Y_2Ti_{2-2x}Fe_xNb_xO_7$ was achieved by several consecutive solid state reactions of the stochiometric amount of the respective oxide precursors: Y_2O_3, TiO_2, Fe_2O_3 and Nb_2O_5. The substitution limits were investigated for $0 \leq x \leq 0.5$, in intervals of 0.05 and for $0.5 < x \leq 1.0$ in intervals of 0.1. The different compositions were mixed in a rotary ball mill for 16 h in high density polyethylene (HDPE) pots containing yttria stabilised ZrO_2 media and isopropanol as a carrier solvent. The resulting mixed powder slurries were separated from the milling media, dried at 100 °C overnight, and reacted in alumina crucibles. Several heat treatments were carried out with intermittent regrinding, to ensure complete reaction. The first reaction was at 1573 K for 8 h followed by two additional reactions at 1673 K for 8 h. In all cases a ramp of 5 K min^{-1} was used. The reactions were carried out in air, under atmospheric pressure. After heating the products were removed from the crucibles, broken down and planetary milled for 2 minutes at 300 rpm in sialon pots containing sialon milling media. The powders were then sieved through a 250 μm mesh. The reaction process was monitored by XRD and the reaction was assumed to have gone to completion when no further changes were observed in the XRD patterns. Ceramic bodies were prepared by pressing approximately 1 g of material in a 10 mm diameter die at ~ 1 ton for 2 minutes. Sintering was performed for 8 hours at temperatures up to 1898 K. Compositions were observed to be less refractory with increasing Fe / Nb substitution. Final sintered densities of > 95% theoretical were achieved.

X-ray diffraction patterns were acquired on a Bruker D8 Advance Powder diffractometer. Samples were prepared from planetary milled powder and mounted for measurement in transmission geometry. The diffractometer utilised a copper radiation source ($K_{\alpha1}$, λ= 0.15406 nm and $K_{\alpha2}$, λ= 1.5444 nm) and was equipped with a standard scintillation detector operating at 40 kV and 30 mA. Diffraction patterns were recorded between 10 and 70° 2theta using a scan step of ~ 0.02 °. The analysis of the data was performed using WinXPow or Xpert Highscore Plus.

Microstructural analysis of sintered pellets was performed using a JEOL JSM6400 scanning electron microscope (SEM) equipped with an energy dispersive spectrometer (EDX). Prior to analysis, the sintered specimens were sectioned using a slow speed diamond bladed saw and then ground parallel using SiC grinding paper. Once the samples had been ground to a 1200 grit finish they were polished to an optical finish (1 micron) using diamond paste. Each specimen was then

thermally etched for 1 hour at 90 % of its sintering temperature, mounted on an aluminium sample stub and carbon coated to prevent charging in the microscope (Edwards 'Speedivac').

Selected area diffraction patterns (SADP's) were obtained using a Philips EM420 transmission electron microscope (TEM), operating with a working voltage of 120 keV. The samples were prepared from sintered specimens by conventional mechanical thinning followed by ion beam milling to electron transparency, using a Gatan Duomill. Zone axis diffraction patterns (ZADP's) were collected from several different grains using a double tilt holder to facilitate collection of a number of ZADP's from each individual single grain. Simulated diffraction patterns were created using the space group and atomic positions determination by Reitveld refinement of the neutron diffraction data and qualitatively compared with the experimentally observed SADP's using CaRIne Crystallography 3.1.

For analysis by X-ray absorption spectroscopy (XAS), ~10 mg of finely powdered sample was ground with ~100 mg of polyethylene glycol (PEG) and pressed to form pellets for analysis in transmission mode at the Fe K-edge. The exact amount of sample used for each composition was calculated so as to give an absorption edge step of approximately one. The energy scale was calibrated by reference to an Fe foil with E_0 = 7112 eV. Experiments were undertaken at beamline BL11.1 at the ELETTRA light source. Data reduction and analysis was performed using the programs Athena, Artemis and Hephaestus. [18]

Specimens for Mössbauer spectroscopy were prepared by dilution of 50 - 100 mg of finely powdered sample in 100 mg of graphite. Data were acquired in transmission at room temperature using a WissEL Mössbauer Spectrometer with a ^{57}Co:Rh source. Data analysis was performed using the RECOIL software package. [19]

Raman spectra were acquired using a Bruker Senterra Microscope Spectrometer at 534 nm excitation. The laser intensity was set to 50%. Each pellet was irradiated at several different surface areas; three iterations were done for every measurement.

Powder neutron diffraction data were collected for samples x = 0, 0.1, 0.2, 0.3, 0.4, 0.7 and 0.8 using the HRPT diffractometer of the SINQ spallation neutron source at the Paul Scherrer Institute. A vertically focused beam of wavelength λ=1.4940(1) Å was selected using the (5 3 3) reflection of the Ge monochromator. Diffraction data were collected over the angular range $5 \leq 2\theta \leq 165°$ with a step size of 0.05. The overall data collection time was 2 h using a finely powdered sample of around 3 g contained in a 5 mm diameter vanadium can. The data refinement was performed using the GSAS software package. [20]

Magnetic susceptibility measurements were performed at the Photon Science Institute (The University of Manchester). Data sets were collected using a Quantum Design MPMS-XL SQUID magnetometer equipped with a 7-T magnet, within a temperature range of 0 to 300 K.

3. RESULTS AND DISCUSSION

3.1. Powder X-ray diffraction

The stacked X-ray diffraction (XRD) patterns are shown in Figure 3. The XRD patterns showed two distinctly different structures to be stabilised across the $Y_2Ti_{2-2x}Fe_xNb_xO_7$ composition range, where $0.0 \leq x \leq 0.5$ could be indexed on a pyrochlore cell (Fd-3m, space group 227) based on that of $Y_2Ti_2O_7$., [21] The diffraction pattern for x = 0.2 is shown in Figure 4 as an example. In the diffraction pattern for x = 0.6, extra reflections were observed that could not be attributed to a pyrochlore structured material. These extra reflections indicated the presence of an additional phase which was confirmed by micro-structural and micro-chemical analysis. For compositions in the range $0.7 \leq x \leq 0.8$ all the reflections attributed to the pyrochlore structured phase were absent and the remaining reflections were consistent with the formation of an unusual hexagonal polytype of the zirconolite structure, [22,23] with space group $P3_121$ (152), see Figure 4. Extra reflections were again observed for compositions where $x > 0.8$ and the presence of a number of additional phases were confirmed by scanning electron microscopy (Figure 5).

Close inspection of the XRD patterns for compositions between $0.0 < x < 0.5$ revealed subtle changes in the pyrochlore $(111)_P$ reflection at c.a. $2\theta = 15^{o}$. This and other reflections such as the $(311)_P$ at $2\theta = 29^{o}$ and the $(511)_P$ reflection at $2\theta = 46^{o}$, gradually diminished in intensity, relative to the $(222)_P$, as *x* increased and these changes could be related to the ordering of the structure. Further investigation will be implemented by other characterisation methods in this paper.

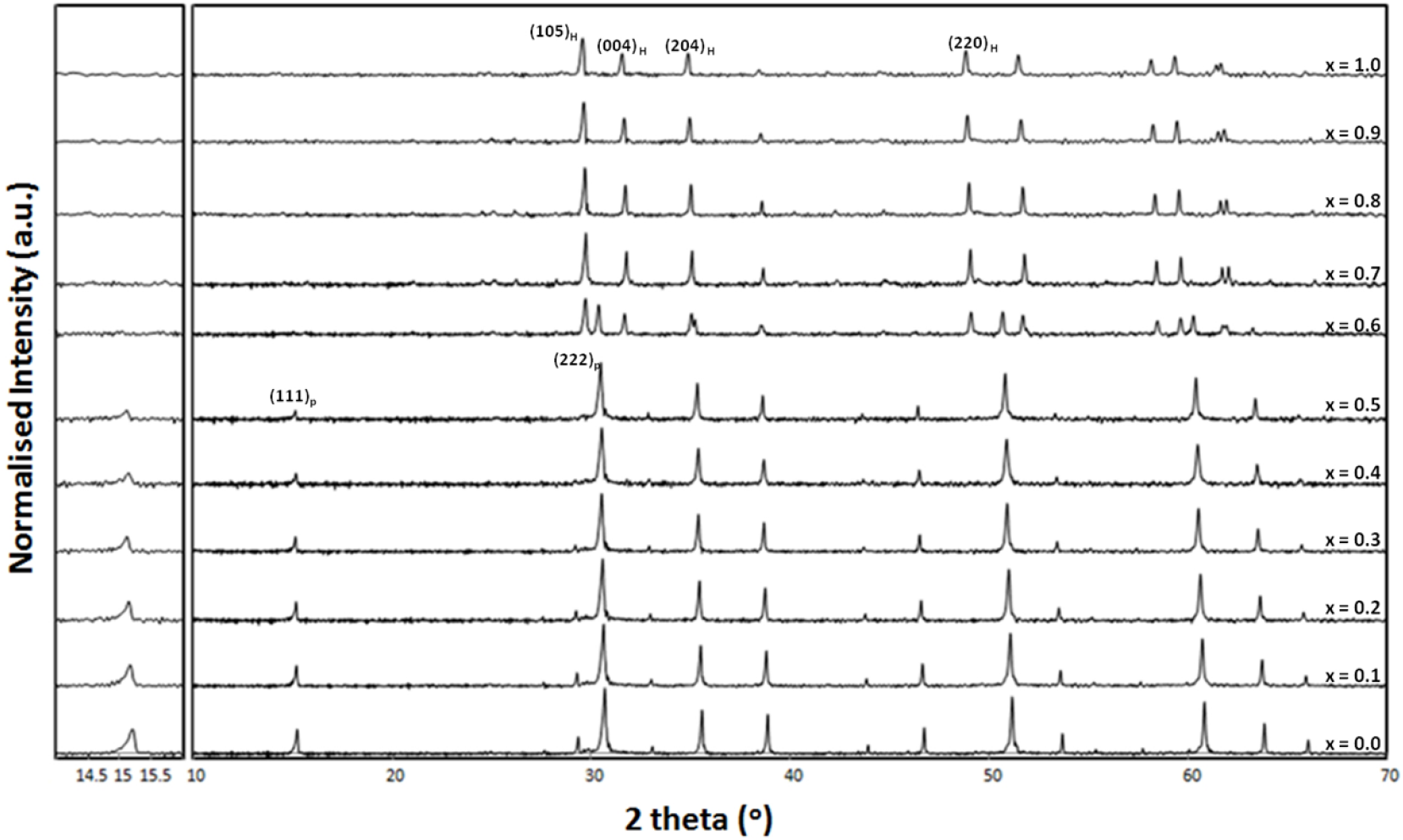

Figure 3: Normalised X-Ray diffraction data of $Y_2Ti_{2-2x}Fe_xNb_xO_7$.

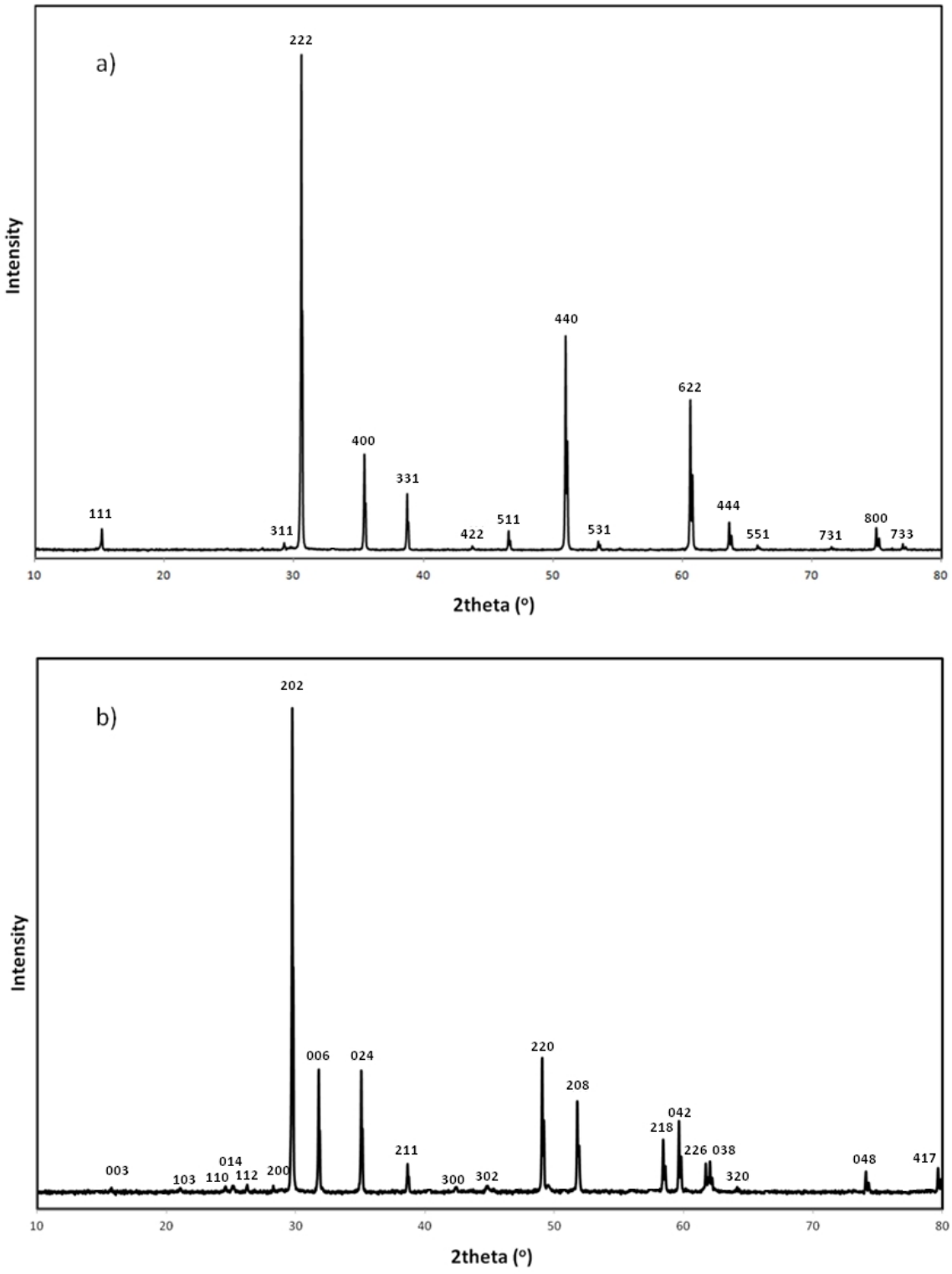

Figure 4: Indexed XRD patterns of $Y_2Ti_{2-2x}Fe_xNb_xO_7$, a) x = 0.2 (pyrochlore) a) and b) x = 0.7 (zirconolite-3T).

3.2. Scanning electron microscopy (SEM)

Electron microscopy was used to determine the assemblage, morphology and chemistry of the phases present. SEM combined with quantitative EDX analysis confirmed the formation of single phase ceramic specimens (when $x \leq 0.5$ and $x = 0.7$ and 0.8) consistent with the observations from the XRD data.

Figure 5 shows electron micrographs of $Y_2Ti_{2-2x}Fe_xNb_xO_{7,}$ samples. All the secondary electron images showed a small volume fraction of porosity, consistent with the average sintered density of 95 ± 2 % of theoretical. The porosity appears as black circular features. The back-scattered electron micrograph showed grains with uniform contrast demonstrating the compositional homogeneity. The possibility of a phase transition above compositions where $x = 0.5$ was raised by XRD data analysis and was confirmed by electron micrographs from $x = 0.6$. During the transition, different types of grains were observed. Unfortunately, the second phase grains were too small and their specific chemical composition was not obtained. However, the XRD data (Figure 3) showed those samples have a mixture of a pyrochlore and a zirconolite phase. When $x = 1.0$, secondary phases were observed in the electron micrographs which is consistent with the assumption made during the fitting of the XRD data. However, the presence of secondary phases was not conclusive by XRD for $x = 1.0$. A fluorite-type structure, rich in yttrium and niobium atoms, was detected.

Figure 5 shows a bi-modal grain size distribution along the whole *x* compositions. The size distribution mainly showed grains between 5-6 μm and c.a. 10 μm. A closer look at the microstructure determined grain growth size when $x= 0.3$ and 0.4. At higher compositions the size distribution became more homogenous at c.a. 7-8 μm.

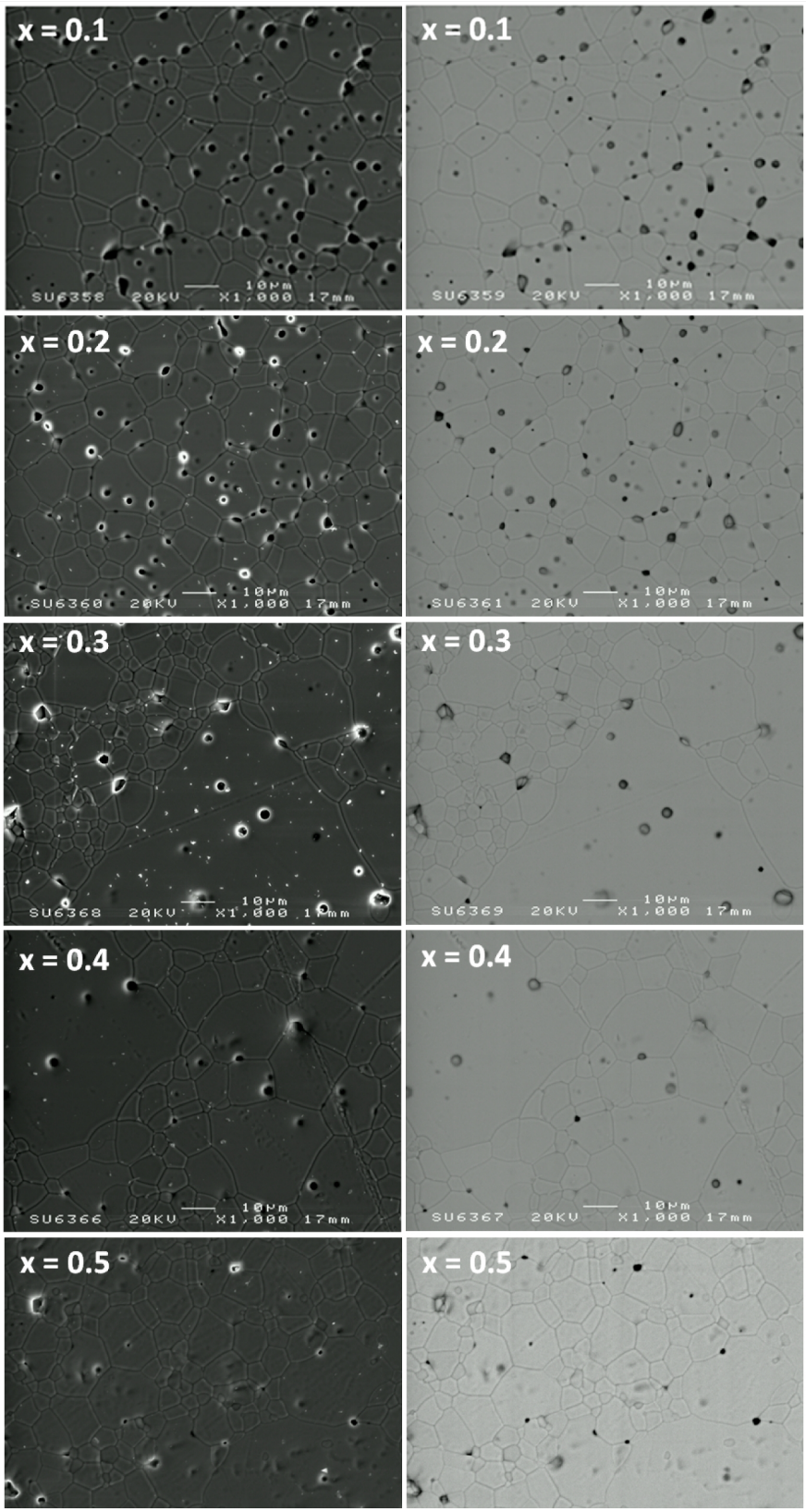
x = 0.1
SU6358 20KV X1,000 17mm
10μm
x = 0.1
SU6359 20KV X1,000 17mm
10μm
x = 0.2
SU6360 20KV X1,000 17mm
10μm
x = 0.2
SU6361 20KV X1,000 17mm
10μm
x = 0.3
SU6368 20KV X1,000 17mm
10μm
x = 0.3
SU6369 20KV X1,000 17mm
10μm
x = 0.4
SU6366 20KV X1,000 17mm
10μm
x = 0.4
SU6367 20KV X1,000 17mm
10μm
x = 0.5
x = 0.5

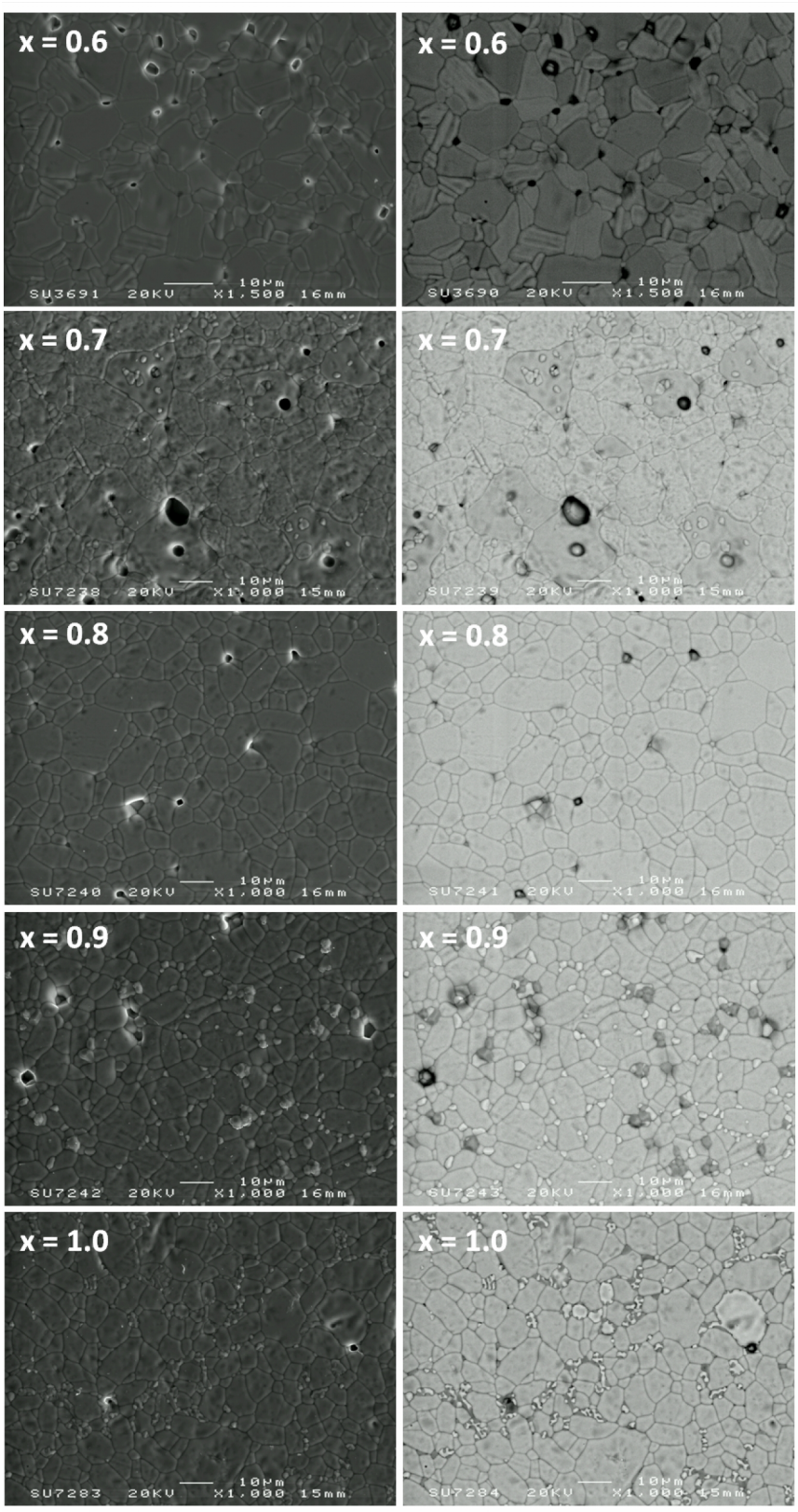

Figure 5: Secondary (left) and backscattered (right) electron micrographs representative of all specimens. From top to bottom: pyrochlore compositions $Y_2Ti_{1.8}Fe_{0.1}Nb_{0.1}O_7$ and $Y_2Ti_{1.2}Fe_{0.4}Nb_{0.4}O_7$, a biphasic composition $Y_2Ti_{0.8}Fe_{0.6}Nb_{0.6}O_7$, a zirconolite-3T sample $Y_2Ti_{0.4}Fe_{0.8}Nb_{0.8}O_7$ and Y_2FeNbO_7.

The actual bulk compositions of the specimens are reported on Table 1.

Nominal Composition (x)	Bulk measured composition (± 0.01)	Structure assignment
0.0	$Y_{2.14}Ti_{1.90}O_7$	Pyrochlore
0.1	$Y_{2.06}Ti_{1.76}Fe_{0.10}Nb_{0.09}O_7$	Pyrochlore
0.2	$Y_{2.06}Ti_{1.56}Fe_{0.20}Nb_{0.19}O_7$	Pyrochlore
0.3	$Y_{2.06}Ti_{1.36}Fe_{0.29}Nb_{0.30}O_7$	Pyrochlore
0.4	$Y_{2.05}Ti_{1.17}Fe_{0.39}Nb_{0.40}O_7$	Pyrochlore
0.5	$Y_{2.03}Ti_{0.97}Fe_{0.5}Nb_{0.51}O_7$	Pyrochlore
0.6	$Y_{2.03}Ti_{0.78}Fe_{0.59}Nb_{0.60}O_7$	Multiphase
0.7	$Y_{2.05}Ti_{0.57}Fe_{0.66}Nb_{0.72}O_7$	Zirconolite
0.8	$Y_{2.05}Ti_{0.38}Fe_{0.76}Nb_{0.82}O_7$	Zirconolite
0.9	$Y_{2.03}Ti_{0.19}Fe_{0.85}Nb_{0.92}O_7$	Multiphase
1.0	$Y_{2.05}Fe_{0.93}Nb_{1.01}O_7$	Multiphase

Table 1: Quantitative elemental analysis of $Y_2T_{i2-2x}Fe_xNb_xO_7$ compositions.

3.3. Transmission electron microscopy (TEM)

Electron diffraction is very sensitive to subtle structural modulations and was used to corroborate the space group and structures proposed based on the X-ray diffraction data. These were subsequently confirmed by refinement of neutron diffraction data (see section 3.7). Figure 6 shows typical zone axis diffraction patterns obtained from $Y_2Ti_{1.4}Fe_{0.3}Nb_{0.3}O_7$ (x = 0.3).

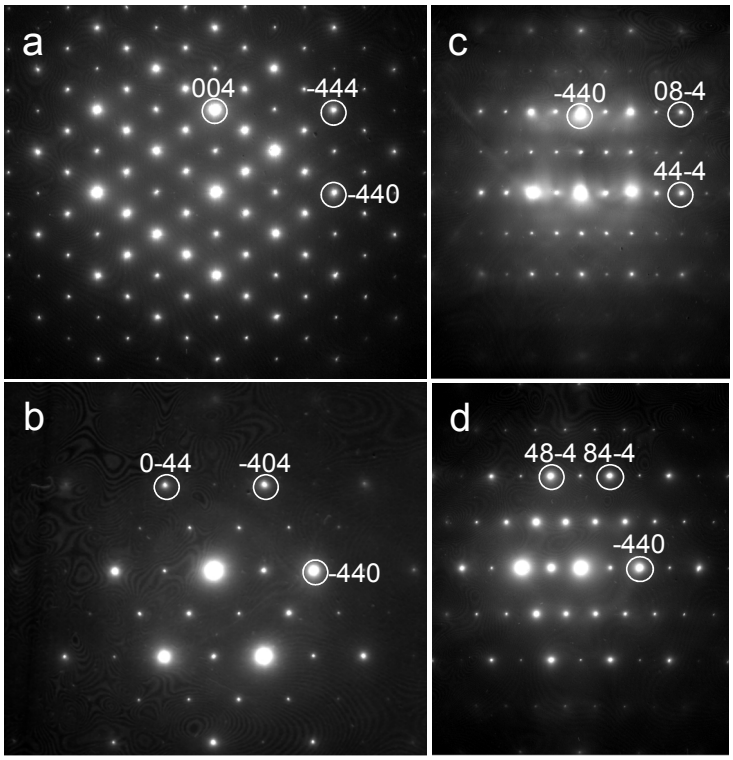

Figure 6: Selected a) [110], b) [111], c) [112], and d) [113] zone axis diffraction patterns for $Y_2Ti_{1.4}Fe_{0.3}Nb_{0.3}O_7$ (x = 0.3). Patterns indexed assuming the space group and atomic positions from Harvey *et.al.* [23]

The diffraction patterns were successfully indexed assuming the cubic pyrochlore structure proposed from refinement of the neutron data. The diffraction patterns show sharp reflections with an absence of any un-indexed reflections or streaking. The diffuse scatter around some of the brighter reflections (particularly prominent in Figure 6c) is a result of the long exposure times required to check for the presence of additional weak reflections. Streaking of diffraction spots has been shown to indicate disorder in cubic pyrochlore structured materials, usually driven by size mismatch between the A and B cation sites. [24] The absence of any streaking indicates that these materials are well ordered.

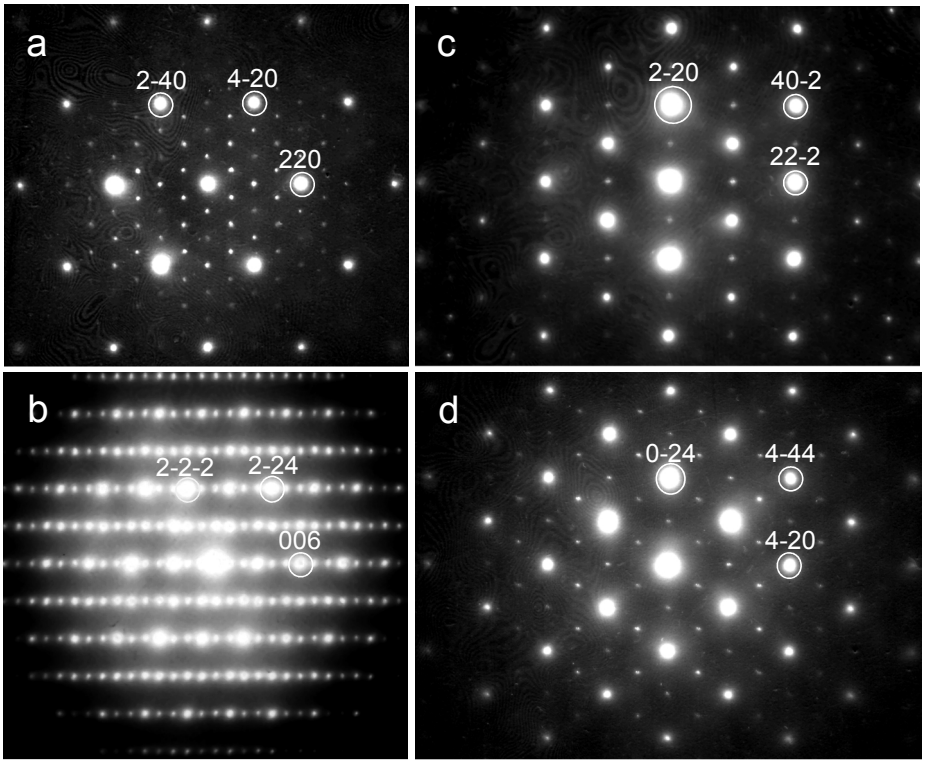

Figure 7: Selected a) [001], b) [110], c) [112], and d) [121] zone axis diffraction patterns for $Y_2Ti_{0.8}Fe_{0.7}Nb_{0.7}O_7$ (x = 0.7). Patterns indexed assuming the space group and atomic positions from Mazzi and Munno. [23]

Typical zone axis diffraction patterns (ZADP's) from $Y_2Ti_{0.8}Fe_{0.7}Nb_{0.7}O_7$ (x = 0.7) are shown in Figure 7. The ZADP's show sharp reflections which could be indexed by quantitative comparison with simulated diffraction patterns created using the space group and the atomic positions obtained from refinement of the neutron data. A number of different polytypes of zirconolite have been reported to occur in natural mineral specimens where they typically exist as intergrowth structures. [25] Synthetic zirconolite samples containing rare earth species and uranium have also been shown to adopt different structures, as a function of dopant content, often displaying significant twinning, intergrowth and stacking disorder. [25,26,27] It is important to verify the structural quality of samples by electron diffraction as many of the subtle structural features in zirconolites are not readily apparent by X-ray diffraction analysis alone. The absence of any extra reflections, diffuse scatter or streaking in the ZADP's, Figure 7, indicate the sample to be a fully ordered zirconolite-3T free from any intergrowths or structural defects.

3.4. ^{57}Fe Mössbauer spectroscopy

Mössbauer spectroscopy was used to determine both the Fe valence state and coordination geometry of the iron in the samples. Spectra from samples with the cubic pyrochlore structure could be successfully fitted with a single Lorentzian doublet indicative of the presence of only one geometrically distinct iron site in the structure. The isomer shift and quadrupole splitting indicate that the iron is trivalent and in six-fold coordination consistent with the targeted substitution of iron on to the titanium site in the pyrochlore structure. [28]

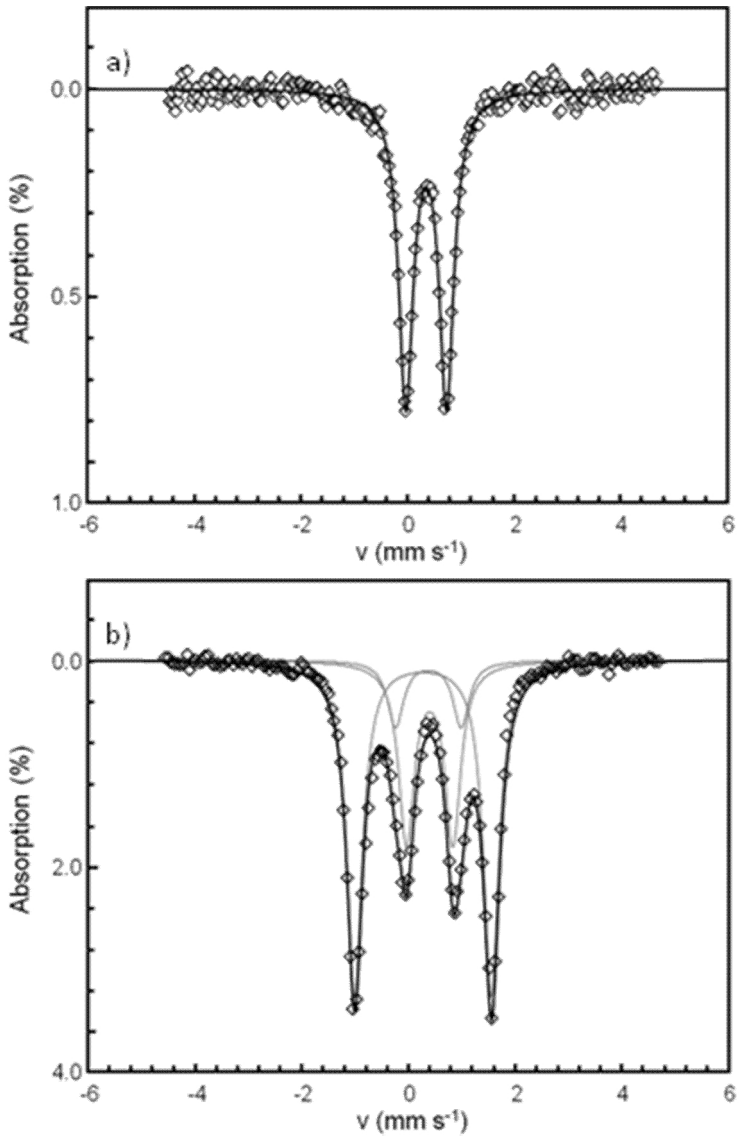

Figure 8: Room temperature ^{57}Fe Mössbauer spectrum of a) x = 0.3 sample (cubic pyrochlore) and b) x = 0.7 sample (hexagonal 3T-zirconolite).

Figure 8 a) shows the ^{57}Fe Mössbauer spectrum acquired from the x = 0.3 sample, which is representative of compositions $Y_2Ti_{2-2x}Fe_xNb_xO_7$ where $0.1 \leq x \leq 0.5$. There was no indication of any divalent iron in the samples which would be associated with a doublet which exhibits a considerable larger isomer shift. Figure 8 b) shows the spectrum acquired from the x = 0.7 sample which is typical of the higher iron (and niobium) content single phase compositions in the $Y_2Ti_{2-2x}Fe_xNb_xO_7$ system ($0.7 \leq x \leq 0.8$). For these samples the spectra were fitted with three separate Lorentzian doublets which indicated three geometrically distinct iron sites in the structure. Grey lines show the individual Lorentzian doublets in Figure 8 b) whilst the black line represents the total fit. As for the previously discussed samples there was no evidence of any divalent iron with the isomer shifts of all three doublets being consistent with Fe^{3+}. The 3T-zirconolite structure contains three distinct Ti coordination environments; one is five-fold coordinated and the other two are six-fold coordinated. [23] The doublet with the large quadrupole splitting of 2.56(2) mm s^{-1} can be attributed to five-fold coordinated iron; the Mössbauer parameters are consistent with those previously reported in $CaZrTi_{2-2x}Nb_xFe_xO_7$ which are monoclinic zirconolite structured materials (space group C2/c) and also contain one five- and two six-fold coordinated titanium sites. [29,30] The two remaining doublets are consistent with the other two sites being six fold coordinated with one having a slightly larger quadrupole splitting. Quadrupole splitting can be a measure of the degree of distortion, away from ideal geometry, when considering two sites with the same nominal coordination environment. The large quadrupole splitting measured here can therefore be attributed to the more disorted octahedral site in the structure. [23,31] The isomer shifts, quadrupole splittings and linewidths for the single phase samples are summarised in Table 2 along with the percentage of the total iron content on each site.

Compound	Specimen structure	Fe site geometry	$\delta \pm 0.02$ / mm s^{-1}	$\Delta \pm 0.02$ / mm s^{-1}	FWHM $\pm$ 0.02 / mm s^{-1}	Area (%)
$Y_2Ti_{1.8}Fe_{0.1}Nb_{0.1}O_7$	Pyrochlore	O_h	0.35	0.88	0.26	100
$Y_2Ti_{1.6}Fe_{0.2}Nb_{0.2}O_7$	Pyrochlore	O_h	0.35	0.88	0.18	100
$Y_2Ti_{1.4}Fe_{0.3}Nb_{0.3}O_7$	Pyrochlore	O_h	0.36	0.90	0.16	100
$Y_2Ti_{1.2}Fe_{0.4}Nb_{0.4}O_7$	Pyrochlore	O_h	0.34	0.88	0.16	100
$Y_2Ti_{0.6}Fe_{0.7}Nb_{0.7}O_7$	Zirconolite 3T	O_h	0.37	0.87	0.18	31
		Distorted O_h	0.34	1.23	0.18	12
		5-fold	0.24	2.56	0.18	57
$Y_2Ti_{0.4}Fe_{0.8}Nb_{0.8}O_7$	Zirconolite 3T	O_h	0.36	0.80	0.15	26
		Distorted O_h	0.35	1.15	0.19	24
		5-fold	0.24	2.49	0.18	50

Table 2: ^{57}Fe Mössbauer parameters for single phase compositions in $Y_2Ti_{2-2x}Fe_xNb_xO_7$ system.

3.5. X-ray absorption spectroscopy (XAS)

X-ray absorption spectroscopy is a sensitive measure of oxidation state in redox active elements such as transition metals. A typical X-ray absorption spectrum for a transition metal consists of three regions: a pre edge region which is located approximately 15-20 eV in-front of the main absorption edge, the absorption edge and features approximately 40 eV past the edge, and the oscillations in the absorption above the edge. The first two region are commonly refered to as the X-ray absorption near edge structure (XANES) and the third region as the the extended X-ray absorption fine structure (EXAFS). The intensity and absolute energy of the pre edge feature gives information on the site geometry and oxidation state of the element being probed. There are many examples in the literature of Fe K-edge XAS studies on minerals, natural sediments, glasses and ceramics. [32,33,34,35,36,37] There are large increases in pre-edge intensity for tetrahedrally coordinated Fe^{2+} and Fe^{3+} with respect to that observed for their octahedrally coordinated counterparts. Non-centrosymmetry intensifies the absorption at the pre-edge and therefore the pre-edge intensity varies according to the degree of distortion from centrosymmetry in octahedrally coordinated compounds. [34] The position of the pre-edge shifts to higher energy with increasing oxidation state due to an increase in the binding energy of core electrons. Wilke et. al. reported a separation of approximately 1.4 ± 0.01 eV between the average pre-edge positions for Fe^{2+} and Fe^{3+}. [33] A corresponding shift in the position of the absorption edge is also observed although extraction of the edge position and hence the oxidation state is often complicated by large variations in the features in the edge and the edge crest for compounds with the same nominal oxidation state. These differences arise from constructive and destructive interference between the central core atom and more distant neighbouring atoms. Therefore, correlation of the edge position and oxidation state is often only possible for model compounds with closely related structures. [38]

The comparison of the Fe K-edge XANES spectra of the x = 0.3 composition with those of a suite of well characterised standard samples is shown in Figure 9. The standards contain Fe^{3+} (Fe-berlinite and aegerine) and Fe^{2+} (siderite and staurolite) in four-fold (Fe-berlinite and siderite) and six-fold coordination (aegerine and staurolite). As can be seen from the right hand side of Figure 9, the differences in shape and features on the absorption edge, as a function of structure, makes quantification of the oxidation state from the edge position difficult. The position of the pre-edge peak however offers a convenient way of quantifying oxidation state (shown in the left hand side of Figure 9.

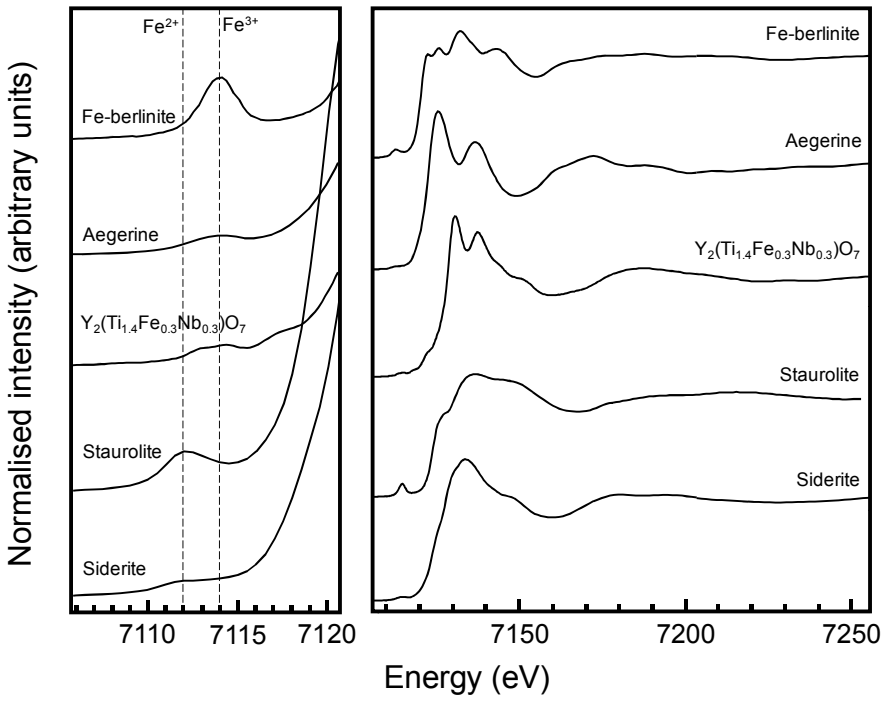

Figure 9: Fe K-edge XANES spectra of FeO, Fe_2O_3 and x = 0.3 composition.

For analysis of the pre-edge position and intensity the contribution of the edge step to the pre-edge was modelled using a spline function and fitted as a background several eV before and after the pre-edge feature The background subtracted pre-edge was then fitted using Gaussian components by varying the normalised height, position, half-width, and integrated intensity of each component. The Gaussian functions were modelled assuming the same width for each pre-peak feature.

Characterisation by XANES then showed that iron was present in the pyrochlore samples ($x \leq 0.4$) as a ferric ion within an octahedral geometry.

3.6. Raman spectroscopy

Raman spectroscopy has previously been used to follow structural phase transformation in pyrochlore and fluorite systems. [39] With this characterisation method it was possible to extract information about symmetry and also relative degrees of disorder for phases in the $Y_2Ti_{2-x}Fe_xNb_xO_7$ system. Figure 10 illustrates the results for pyrochlore samples obtained where x = 0.0 to 0.5. The data are very similar to the spectra for $Y_{2-x}Ce_xTi_{2-x}Fe_xO_7$ pyrochlores. [40]

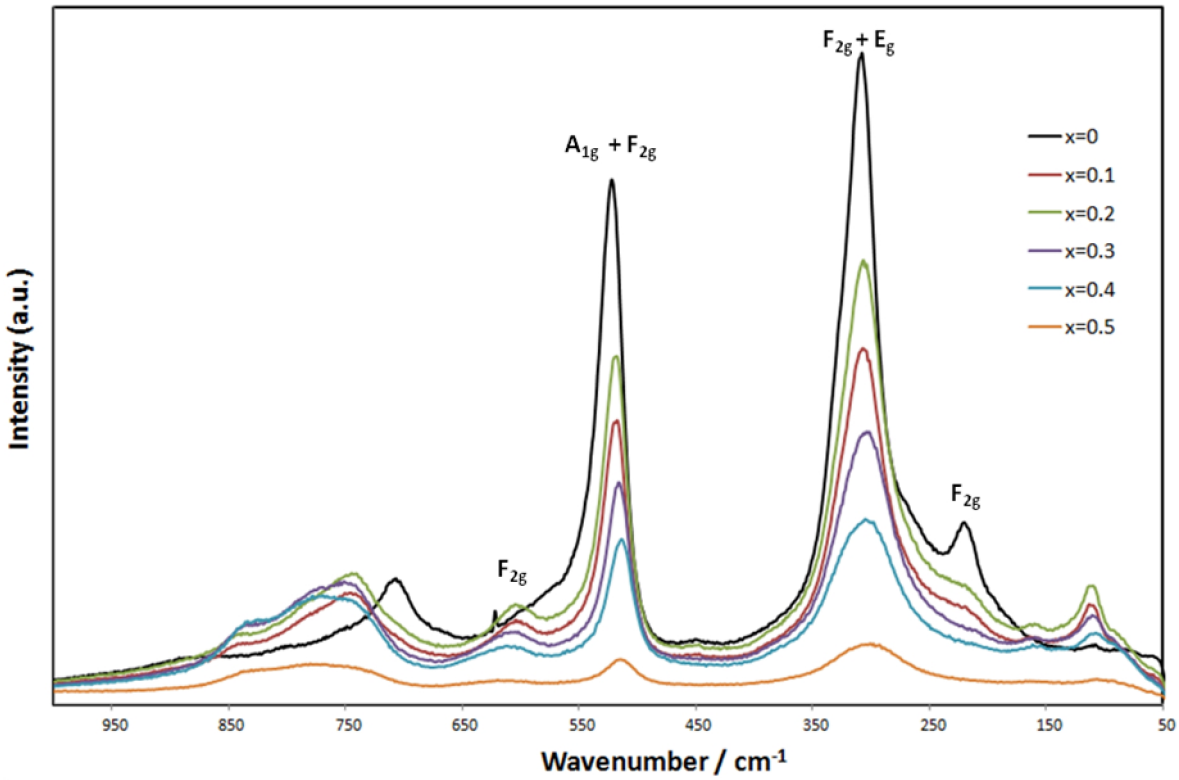

Figure 10: Raman spectra of the pyrochlore samples.

If a molecular approach is used to determine the number of active Raman modes 23 bands would be expected for a $A_2B_2O_6O'$ pyrochlore with a 13 atom unit. The observed experimental results show fewer bands and it has been previously shown through theoretical studies that a site symmetry approximation is more appropriate to pyrochlore and fluorite structures. [41,42] The approach is summarised below. Cubic pyrochlores, such as $A_2B_2O_6O'$, belong to the space group number 227 (Fd-3m, Z=8). The A and B cation sites have D_{3d} symmetry, the oxygen site, labelled O, has C_{2v} symmetry whilst the O' site has T_d symmetry. The vibrational normal modes are predicted as being: [43]

$$\Gamma = A_g^{(R)} + 3A_{2u}^{(in.)} + E_g^{(R)} + 3E_u^{(in.)} + 2F_{1g}^{(in.)} + 7F_{1u}^{(IR)} + 4F_{2g}^{(R)} + 4F_{2u}^{(in.)} \qquad (1)$$

Where (R) denotes Raman active, (in.) denotes inactive and (IR) denotes infrared active bands. Possible oxygen active bands are therefore A_g, E_g and $3F_{2g}$ and F_{2g} for the O' site. The intensity of some bands decreased with increasing dopant concentration; however, since no internal standard was used during the experiments the absolute intensity from different samples cannot be directly compared. It is however possible to relate changes in band position to changes in bonding energy and the geometry of the samples.

Broadening of most of the peaks was observed with increasing dopant concentration. The addition of different cations into the structure system causes some defect, which is probably the reason that we observed the broadening of some peaks, such as the ones observed at ~220, 300 and 750 cm^{-1}. Intensity in individual Raman scattering bands can arise due to contributions from several different vibrational modes. Therefore, a shift in the position of these individual bands relative to one another could be the origin of the observed line broadening. This hypothesis is supported by previous reported literature. [44] On doping, the band at c.a. 550 cm^{-1} is observed to split into two discrete bands. This signal is reported to be a contribution of the A_{1g} and F_{2g} normal modes (equation (1)). This type of splitting has been previously observed when $Y_2Ti_2O_7$ was doped with Zr^{4+} into the Ti^{4+} site. [39]

$Y_2Ti_2O_7$ (cm^{-1})	$Y_2Ti_{1.8}Fe_{0.1}Nb_{0.1}O_7$ (cm^{-1})	$Y_2Ti_{1.6}Fe_{0.2}Nb_{0.2}O_7$ (cm^{-1})	$Y_2Ti_{1.4}Fe_{0.3}Nb_{0.3}O_7$ (cm^{-1})	$Y_2Ti_{1.2}Fe_{0.4}Nb_{0.4}O_7$ (cm^{-1})	$Y_2Ti_{1.0}Fe_{0.5}Nb_{0.5}O_7$ (cm^{-1})
106	112	111	112	111	105
-	162	162	163	162	163
222	219	220	-	-	-
309	307	308	304	305	300
522	517	517	516	515	515
-	610	604	612	615	618
709	747	746	762	769	777

Table 3: Observed bands in the Raman spectra for pyrochlore structures of $Y_2Ti_{2-x}Fe_xNb_xO_7$

The signal obtained at c.a. 750 cm^{-1} shifts towards higher wavenumbers which equates to a decrease in bond energy. These broad bands have previously been assigned to oxygen atoms within Ti-O_7 coordinated polyhedra in pyrochlore structured yttria stabilised zirconia samples doped with titanium. [39] Therefore, the Ti – O bonds would be weakened when *x* increases and could be indicating that some titanium sites are distorted. For the x = 0.6 composition, the distinction of two different phases was not clear; above x = 0.6 a new phase was detected by Raman spectroscopy. When x > 0.9, the distinction between several phases was not apparent.

Figure 11 confirms the presence of a zirconolite phase. The sample where x = 0.8 is representative of a previously reported synthetic zirconolite 3T specimen. [8]

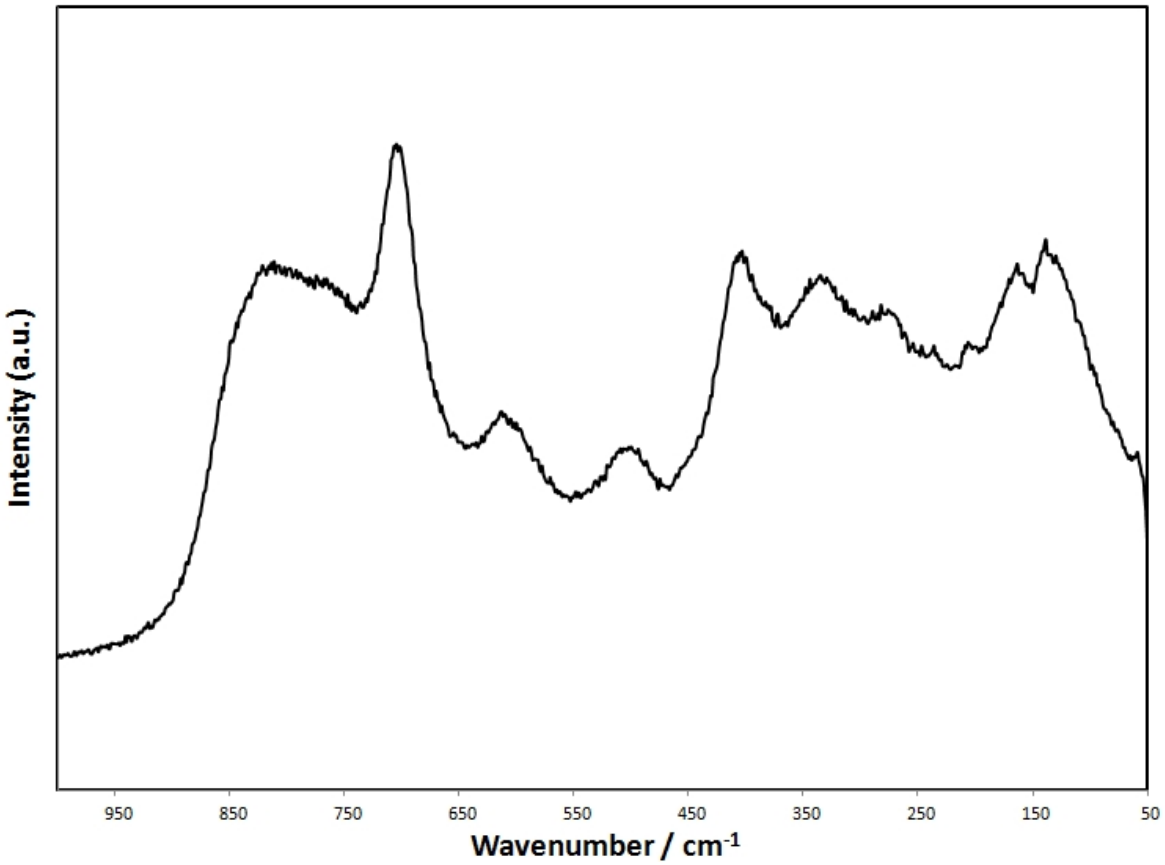

Figure 11: Raman spectrum of $Y_2Ti_{0.4}Fe_{0.8}Nb_{0.8}O_7$.

Little is known on the assignment of Raman bands for zirconolite phases as they have several different geometry sites; making indexing of signals difficult. Moreover, the zirconolite 3T type was rarely obtained via synthetic routes; natural samples are so far the most studied examples of this structure. Nevertheless, this spectroscopic method allowed the changes in the microstructure to be followed and the determination of the limit of the pyrochlore solid solution.

3.7 Structural refinement

3.7.1. Pyrochlore solid solution: $Y_2Ti_{2-2x}Fe_xNb_xO_7$ with $0.0 < x < 0.5$

Neutron powder diffraction data from samples in the composition range $0.0 < x < 0.5$ were successfully indexed in space group Fd-3m. The presence of reflections indicating cell doubling, with respect to the underlying fluorite cell, such as the strong (331) reflection at $2\theta \approx 38^o$ in Figure 12, confirmed the retention of the pyrochlore structure over this composition range. This is consistent with the analysis of electron diffraction patterns, reported above, which could be fully indexed assuming the Fd-3m space group characteristic of the pyrochlore structure. The diffraction pattern in Figure 12 is representative of all pyrochlore samples of $Y_2Ti_{2-2x}Fe_xNb_xO_7$ and shows a clear shift to lower two theta, indicating an increase in unit cell size with increasing substitution of Fe^{3+} and Nb^{5+}. This is consistent with the larger ionic radii of these species (0.645 Å and 0.64 Å, respectively) compared to Ti^{4+} (0.605 Å), in six fold co-ordination. [45]

The compositional change across the solid solution has a noticeable impact on the reflection intensities, associated with the change in scattering factor associated with the pyrochlore B-site, as Fe^{3+} and Nb^{5+} (coherent bound scattering lengths of 9.45 fm and 7.054 fm) respectively, substitute for Ti^{4+} (-3.438 fm); based on the data of Sears *et al.* [46]

Structure refinement used the structure model for $Y_2Ti_2O_7$, published by Harvey *et al*., as a starting point. [21] This model places the B site cation at the origin (16c position), with the Y atoms located at (0.5, 0.5, 0.5); O2 at (3/8, 3/8, 3/8), and O1 at (*x*, 1/8, 1/8) with $x \approx 3/8$ (corresponding to the 8a, 8b and 48f positions, respectively). The occupancy of the B site was fixed at the nominal composition in each case and the isotropic thermal displacement factors of Ti, Fe and Nb constrained to be equal. Structure refinements converged quickly affording the refined parameters reported in Table 4. The goodness of fit indicators (Table 4) and graphical fits, see for example Figure 12, demonstrated a good fit to the diffraction data in each case, confirming the pyrochlore structure model.

x	a (Å)	x_{O1}	U_{iso} (x 100 Å^2)				R_{wp} (%)	χ^2
			Y	M	O1	O2		
0.0	10.09730(4)	0.32910(8)	0.667(2)	0.66(2)	0.68(1)	0.38(3)	6.44	4.50
0.1	10.11162(4)	0.32950(8)	0.671(2)	0.70(2)	0.72(1)	0.39(3)	7.18	5.12
0.2	10.12594(4)	0.33048(8)	0.672(2)	0.76(2)	0.75(1)	0.38(3)	7.33	4.87
0.3	10.14063(4)	0.33211(8)	0.675(2)	0.84(2)	0.77(1)	0.35(3)	7.22	5.22
0.4	10.15521(5)	0.33360(8)	0.679(2)	0.81(2)	0.81(1)	0.34(3)	6.65	5.34
0.5	10.17081(5)	0.33507(8)	0.702(2)	0.83(2)	0.82(1)	0.34(3)	6.88	5.54

Table 4: Refined structural parameters $Y_2Ti_{2-2x}Fe_xNb_xO_7$ pyrochlore solid solution, in space group Fd-3m, determined from Rietveld analysis of neutron powder diffraction data. M site occupancies are in accordance with the nominal stoichiometry x. M located at (0,0,0), Y at (0.5, 0.5, 0.5), O2 at (3/8, 3/8, 3/8), and O1 at (x, 1/8, 1/8) (corresponding to the 8a, 8b and 48f positions, respectively).

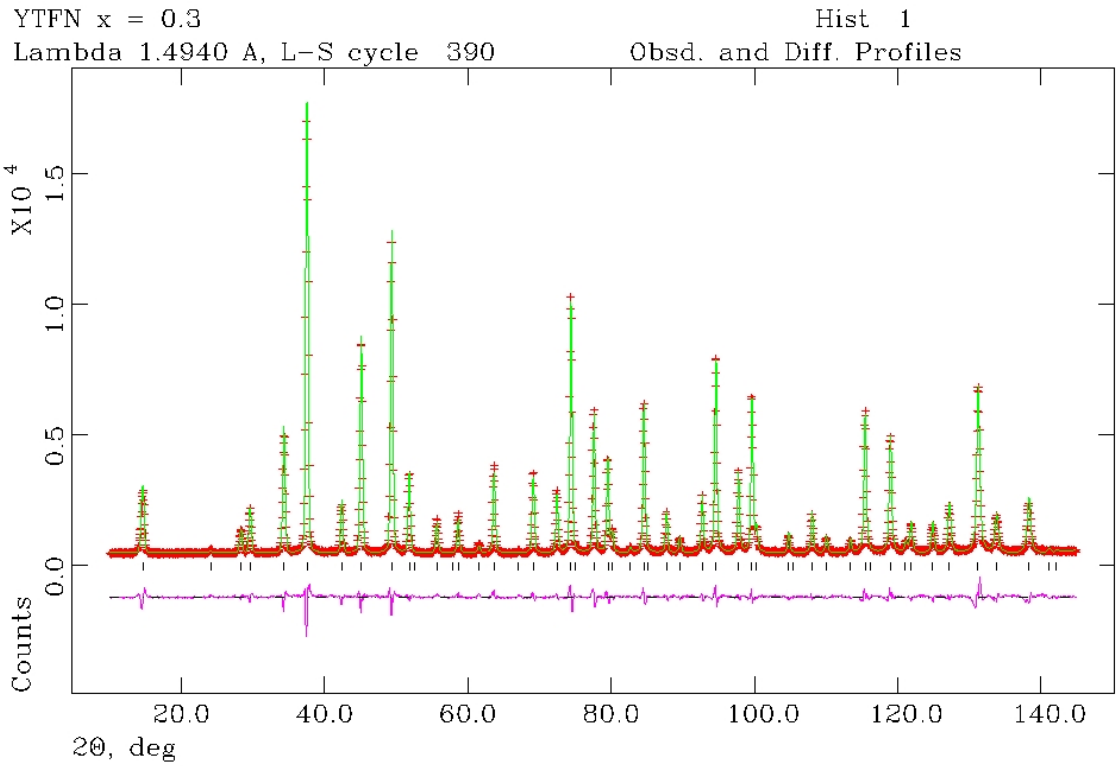

Figure 12: Showing fit (solid line) to high resolution neutron diffraction data (points) for $Y_2Ti_{1.4}Fe_{0.3}Nb_{0.3}O_7$ (x = 0.3) at 25 °C in space group Fd-3m; tick marks show allowed reflections, the difference profile (lower solid line) demonstrates a good fit to the data.

The unit cell a-parameter increases with increasing substitution of Fe^{3+} and Nb^{5+} in the $Y_2Ti_{2-2x}Fe_xNb_xO_7$ solid solution ($0 < x < 0.5$), consistent with the larger ionic radii of these species (0.645 Å and 0.64 Å, respectively) compared to Ti^{4+} (0.605 Å), in six fold co-ordination. [45] This is shown clearly by Figure 13, in which a linear dependence of the unit cell a-parameter as a function of composition is apparent, demonstrating ideal mixing of Ti, Fe, and Nb, on the B-site, in accordance with Vegard's Law.

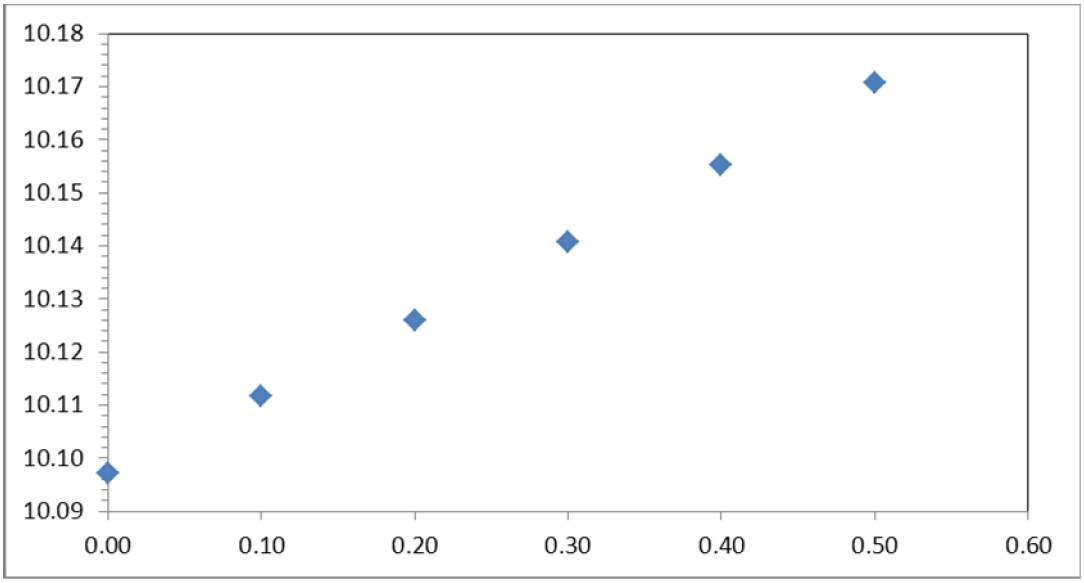

Figure 13: Variation of unit cell a-parameter with nominal composition (x) in the $Y_2Ti_{2-2x}Fe_xNb_xO_7$ pyrochlore solid solution (space group Fd-3m) determined from Rietveld analysis of neutron powder diffraction data. Error bars represent 3 esds and are smaller than the data points.

In the case of the $Y_2Ti_2O_7$ end member, the refined structure agrees very well with that reported previously on the basis of neutron diffraction data, with a = 10.09397(3) Å and x_{O1} = 0.32913(3) according to Harvey *et al.*, [21] and a = 10.0986(5) Å and x_{O1} = 0.3253(4) according to Chtoun *et al.* [47] Substitution of Ti^{4+} by Fe^{3+} and Nb^{5+} results in an increase in the x co-ordinate of the O1 atom located on the 48f position, as shown graphically in Figure 14. The observed increase in the x co-ordinate of the O1 atom reflects the larger ionic radii of the Fe^{3+} and Nb^{5+} cations in comparison with Ti^{4+} in six-fold co-ordination, resulting in an increase in the average M-O1 bond length: see Table 5 and Figure 15. The increase in the x co-ordinate of the O1 atom and, by definition, the M-O1 bond length, seem to show a linear increase as a function of composition as might be expected on the basis of ideal mixing and ionic size effects. This is addressed in more detail below.

The increase in O1 x co-ordinate, as a consequence of expansion of the octahedral M-site, results in an effective compression of the Y-O1 bond length, as shown in Table 5 and Figure 15. However, there is only a small 0.6% increase of the weighted mean Y-O distance over the solid solution range, due expansion of the Y-O2 bond length as a consequence of the increase in unit cell volume. This invariance of the weighted mean Y-O bond length is reflected in the bond valence sum of the Y site which increases only marginally over the solid solution range, and is always within 2% of the expected value of 3.00 v.u. The bond valence sums for M site cations show an interesting trend over the solid solution range, as shown in Table 5. The Ti cation is slightly over bonded (4.10 v.u.) in the $Y_2Ti_2O_7$ end member, which suggests a slight mismatch of the Y^{3+} and Ti^{4+} ionic radii. In effect, the Y^{3+} cation appears to be slightly too large for the 8-fold co-ordinate A site causing the 6-fold co-ordinate B site to be compressed. At low levels of substitution, the larger Fe^{3+} and Nb^{5+} species relieve the apparent bond length mismatch by expanding the unit cell volume and hence the octahedral B site. This reduces the over-bonding of the Ti^{4+} cation without significantly impacting on the Y site. The Fe^{3+} and Nb^{5+} cations are markedly overbonded at low concentration, but with increasing unit cell volume, the bond valence sums decrease to more optimal values toward the upper limit of the solid solution range. However, the consequence of this trend, at higher concentration of substituent species, is a rapid decrease in the bond valence sum of the Ti^{4+} cation.

These trends may be understood by considering the pyrochlore structure as a rigid B_2O_6 network of corner sharing octahedra, forming channels which encapsulate the A cations (in an anti-cristobalite A_2O array), after Subramanian *et al*. [2] At low concentrations of dopants, the stiffness of the network, and B-O bond length, would be expected to be determined by the elasticity of Ti-O bonds. However, when the concentration of the substituent species can no longer be considered to be dilute, the network stiffness, and B-O bond length, are expected to be dependent on the elasticity of Fe-O and Nb-O bonds. Since each BO_6 octahedron is corner linked to six neighbouring BO_6 octahedra in the AB_2O_6 network, we can expect the stiffness of the B_2O_6 network to become significantly influenced by the substituent species when nearest-neighbour interactions become significant. That is, when the concentration where each Ti^{4+} cation has a non identical nearest neighbour, above ~17% occupancy of the B site by Fe^{3+} and Nb^{5+}. This corresponds to the change in gradient of the value of the x-parameter as function of composition shown in Figure 14.

The composition dependence of the weighted mean bond valence sum is also of interest. As shown in Table 5, the weighted mean bond valence sum is within 3% of the weighted mean formal oxidation state over the range $0 < x < 0.4$, but for $x = 0.5$, the variation increases to 5% and both the Ti^{4+} cation and Nb^{5+} cation are significantly under bonded. At lower concentrations, therefore, it is apparent that positive and negative deviations from ideal bond valence sum values, indicative of ionic size mismatch, effectively cancel and stabilise the structure. However, at $x = 0.5$, the trend

of decreasing bond valence sums for all B site cations, together with significant underbonding of Ti^{4+} and Nb^{5+} cations, point to an increasingly strained structure. The limit of at x = 0.5 can therefore be interpreted as a result of an initial stabilisation but progressive destabilisation of the rigid B_2O_6 network as a function of composition.

Finally, the refined isotropic thermal parameters in Table 4 deserve comment. The thermal parameter for the Y, M and O1 sites show a general increase as a function of composition. This can be interpreted as a signature of increased local positional disorder of M site cations with increasing variance in ionic radii, as could be expected. In contrast, the thermal parameter of the O2 anion is essentially invariant as a function of composition, within precision, in accordance with the fact that this anion is located at the centre of a tetrahedron formed by only Y cations.

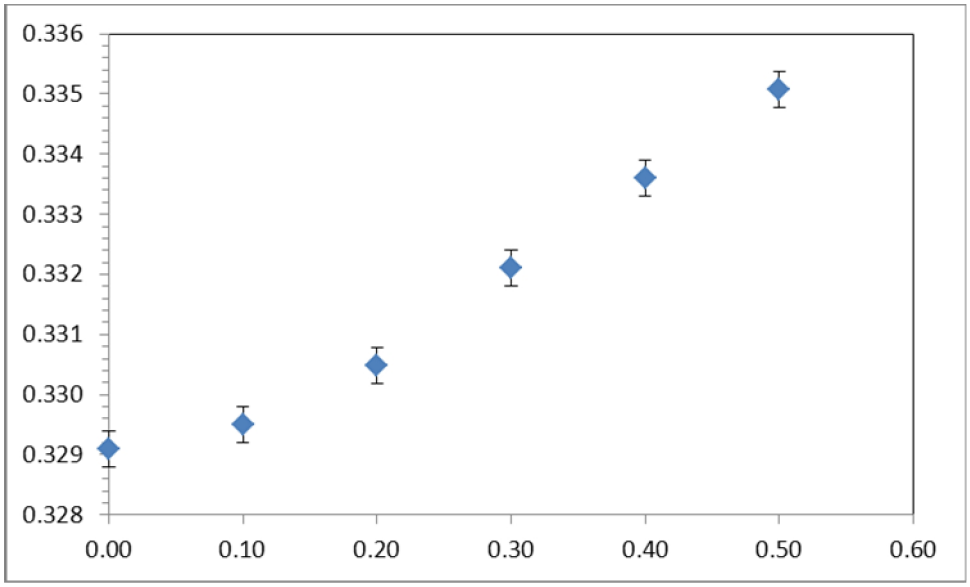

Figure 14: Variation of unit cell x- co-ordinate of O1 atom (at the 48f oxygen position) with nominal composition (x) in the $Y_2Ti_{2-2x}Fe_xNb_xO_7$ pyrochlore solid solution (space group Fd-3m) determined from Rietveld analysis of neutron powder diffraction data. Error bars represent 3 esds.

x	Bond lengths (Å)			Bond Valence Sums (v.u)				
	Y-O1 x 6	Y-O2 x2	M-O1 x 6	Y	Ti	Fe	Nb	Mean
0.0	2.4827(5)	2.1861(1)	1.9555(3)	2.99	4.10	-	-	4.10
0.1	2.4830(5)	2.1890(1)	1.9600(3)	2.98	4.05	3.35	5.26	4.08
0.2	2.4801(5)	2.1923(1)	1.9668(5)	2.98	3.98	3.29	5.16	4.03
0.3	2.4723(5)	2.1955(1)	1.9766(5)	3.00	3.88	3.20	5.03	3.95
0.4	2.4654(6)	2.1987(1)	1.9858(4)	3.03	3.78	3.12	4.90	3.87
0.5	2.4590(6)	2.2020(1)	1.9953(4)	3.05	3.69	3.04	4.78	3.80

Table 5: Key bond lengths for $Y_2Ti_{2-2x}Fe_xNb_xO_7$ determined from Rietveld analysis of neutron powder diffraction data and resulting cation bond valence sums.

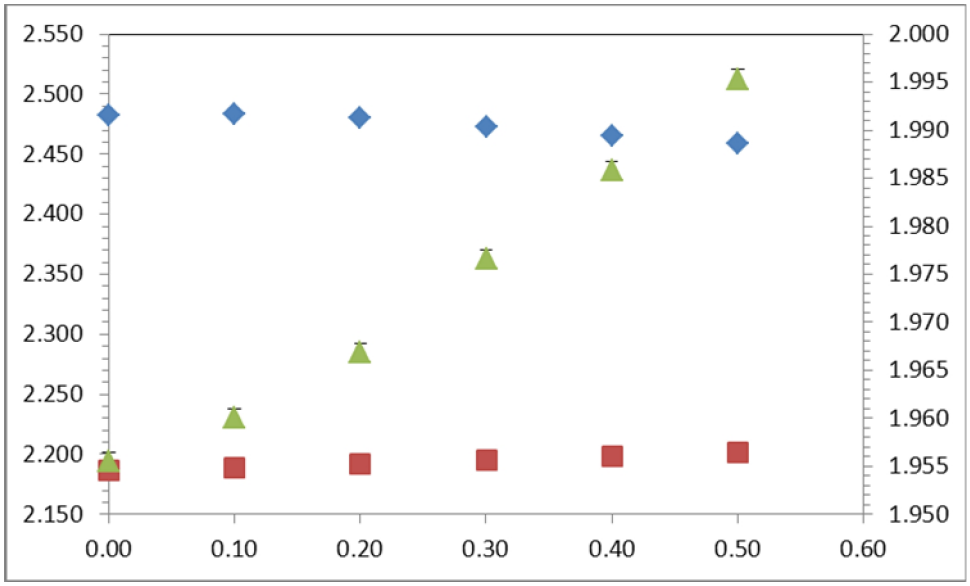

Figure 15: Variation of key metal – oxygen bond lengths with nominal composition (x) in the $Y_2Ti_{2-2x}Fe_xNb_xO_7$ pyrochlore solid solution (space group Fd-3m) determined from Rietveld analysis of neutron powder diffraction data. Y-O1 and Y-O2 bonds are denoted by blue diamonds and red squares respectively (left hand axis); M-O1 bonds are denoted by green triangles (right hand axis). Error bars represent 3 esds and are smaller than the data point where not visible.

3.7.2. Zirconolite-3T structure: $Y_2Ti_{2-2x}Fe_xNb_xO_7$ with x = 0.7

Consideration of X-ray and electron diffraction data, as described above, pointed to the formation of a zirconolite-3T structure in space group $P3_121$ for x = 0.7 and 0.8 (coexisting with other phases for x = 0.6 and x = 0.9). Attempted structure refinement of the x = 0.8 composition was hindered by the presence of reflections attributed to impurity phases not obviously apparent in the X-ray diffraction pattern. Therefore, only structure refinement against the data set for the x = 0.7 composition will be reported here. The initial model for Rietveld analysis of neutron diffraction data was derived from that reported by Mazzi and Munno for a natural specimen of zirkelite (zirconolite-3T). This crystal structure contains 6 distinct cation sites: two 8-fold co-ordinate sites (A1(8) and A2(8)), one 7-fold co-ordinate site (A3(7)), two 6-fold co-ordinate sites (of different distortion, M1(6) and M2 (6)) and a single 5- fold co-ordinate site which is 50% occupied (M3(5)). It was assumed that the larger Y^{3+} cation occupied, exclusively, the larger 8- and 7-fold co-ordinate sites, with the transition metal cations confined to the smaller 6- and 5-fold co-ordinate sites. The presence of three chemically unique species over three crystallographic sites requires at least three independent measurements of structure factors (i.e. reflection intensities) in order to determine unambiguously the pattern of cation ordering. In general, this demands the application of synchrotron resonant X-ray scattering methods, where diffraction data are acquired near the X-ray absorption edge of the elements of interest and the non-negligible imaginary part of the X-ray scattering factor leads to measurably different structure factors. Unfortunately, within the limits of the current study, the acquisition of such diffraction data was not possible. Furthermore, given the fact that the zirconolite-3T structure contains seven oxygen anions, all on general positions, and consideration of resonant X-ray diffraction data would require simultaneous refinement against one neutron and at least 3 X-ray powder diffraction data sets, presumably all equally weighted, the precision in locating the oxygen anions could be expected to be significantly degraded.

Nevertheless, it is possible to make progress in resolving the site occupancy conundrum by incorporating the results from ^{57}Fe Mössbauer spectroscopy and applying crystal chemistry arguments. ^{57}Fe Mössbauer data permit calculation of the fraction of Fe atoms located on each of the M sites. If we *assume* the 5-fold co-ordinate M site to be occupied exclusively by Fe and Ti (i.e. Nb is *excluded*), the problem becomes the simple determination of Ti and Nb distribution over two crystallographic sites which can be resolved by refinement against a single neutron powder diffraction data set (since the Fe distribution is fixed by Mössbauer analysis). Is it reasonable to assume Nb is excluded from the 5-fold co-ordinate M site? NbO_5 species are rare in solid state chemistry and generally adopt square pyramidal co-ordination, with a short "niobyl" Nb=O bond, as in Nb doped $CaTiSiO_5$. [48] However, the 5-fold M site in the zirconolite-3T structure is essentially a distorted trigonal bipyramid which is inconsistent with the formation of such "niobyl"

bonds. Furthermore, consideration of dual Fe and Nb substitution in $CaZrTi_{2-2x}Fe_xNb_xO_7$, which adopts the zirconolite-2M structure, failed to find evidence of Nb substitution at a similar trigonal bipyramidal cation site on the basis of combined neutron and synchrotron resonant X-ray scattering methods. The assumption of Nb exclusion from the M3(5) site is therefore considered chemically plausible and, moreover, could be validated by bond valence sum calculations using the refined structural model. Thus, in the initial structural model, the M3(5) site was assumed to be occupied only by Fe and Ti, with the remaining Ti and Nb distributed statistically over the M6(1) and M6(2) sites, subject to the Fe occupancy determined by ^{57}Fe Mössbauer spectroscopy.

Note that fitting of the Mössbauer spectra of the x = 0.7 sample required three Fe environments, as discussed above: one environment with quadrupole splitting typical of 5-fold co-ordinate Fe^{3+}, and two environments with similar but significantly different quadrupole splitting characteristic of 6-fold co-ordinate Fe^{3+} with different site distortion. In general, a larger quadrupole splitting implies a greater site distortion, all other factors remaining constant, allowing us to assign 12 % of total Fe to the more distorted M2(6) site and 31% of total Fe to the less distorted M1(6) site. Thus, 57 % of total Fe is located at the M3(5) site.

Refinement of the zirconolite-3T structure against the neutron diffraction data employed constraints to require multiple cations occupying the M1(6), M2(6) and M3(5) sites to adopt the same co-ordinates and isotropic thermal parameters. In the latter stage of the refinement, Ti and Nb occupancy of the M1(6) and M2(6) sites was accomplished subject to the constraint of full site occupancy with due regard to different site multiplicities. The refinement converged satisfactorily to yield the refined structural parameters in Table 6. The final goodness of fit parameters were R_{wp} = 7.92% and χ^2 = 3.67 %, which combined with the graphical fit shown in Figure 16, demonstrate good agreement between calculated and observed diffraction patterns. A schematic representation of the refined structure model is shown in Figure 17.

Space group: $P3_121$		a = 7.42050(16) (Å)		c = 16.8953(7) (Å)	
Name	**Site**	**x**	**y**	**z**	**U_{iso} (x 100 Å^2)**
Y1(8)	3a	0.829(2)	0	0.3333	1.1(2)
Y2(8)	3a	0.332(2)	0	0.3333	0.6(2)
Y3(7)	6c	0.172(1)	0.669(2)	0.0172(4)	1.1(1)
M1(6)	3a	0.326(5)	0	0.8333	1.7(4)
M2(6)	6c	0.494(5)	0.315(4)	0.1639(8)	0.4(1)
M3(5)	6c	0.081(5)	0.940(3)	0.167(1)	1.3(2)
O1	6c	0.623(3)	0.643(3)	0.154(1)	1.4(3)
O2	6c	0.000(3)	0.827(2)	0.0636(5)	1.0(2)
O3	6c	0.504(3)	0.325(4)	0.0464(6)	1.8(2)
O4	6c	0.203(2)	0.225(1)	0.1451(6)	1.1(2)
O5	6c	0.528(2)	0.867(2)	0.0542(6)	0.9(2)
O6	6c	0.972(2)	0.307(2)	0.0525(7)	0.2(1)
O7	6c	0.214(2)	0.614(2)	0.1501(6)	0.9(2)

Table 6: Refined structural parameters for $Y_2Ti_{0.6}Fe_{0.7}Nb_{0.7}O_7$ determined from Rietveld analysis of neutron powder diffraction data, occupancies for M sites are reported in Table 9. The goodness of fit parameters were R_{wp} = 7.92 % and χ^2 = 3.67.

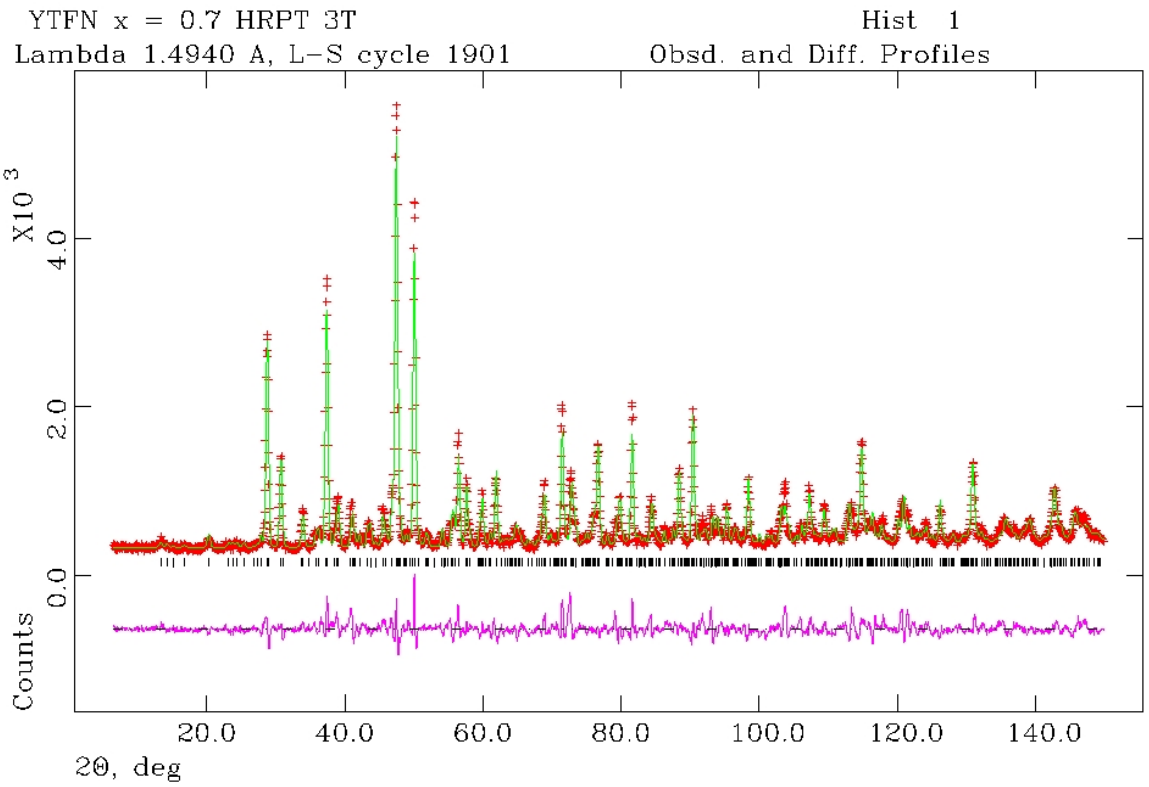

Figure 16: Showing fit (solid line) to high resolution neutron diffraction data (points) for $Y_2Ti_{0.6}Fe_{0.7}Nb_{0.7}O_7$ (x = 0.7) at 25 °C in space group $P3_121$; tick marks show allowed reflections, the difference profile (lower solid line) demonstrates a good fit to the data.

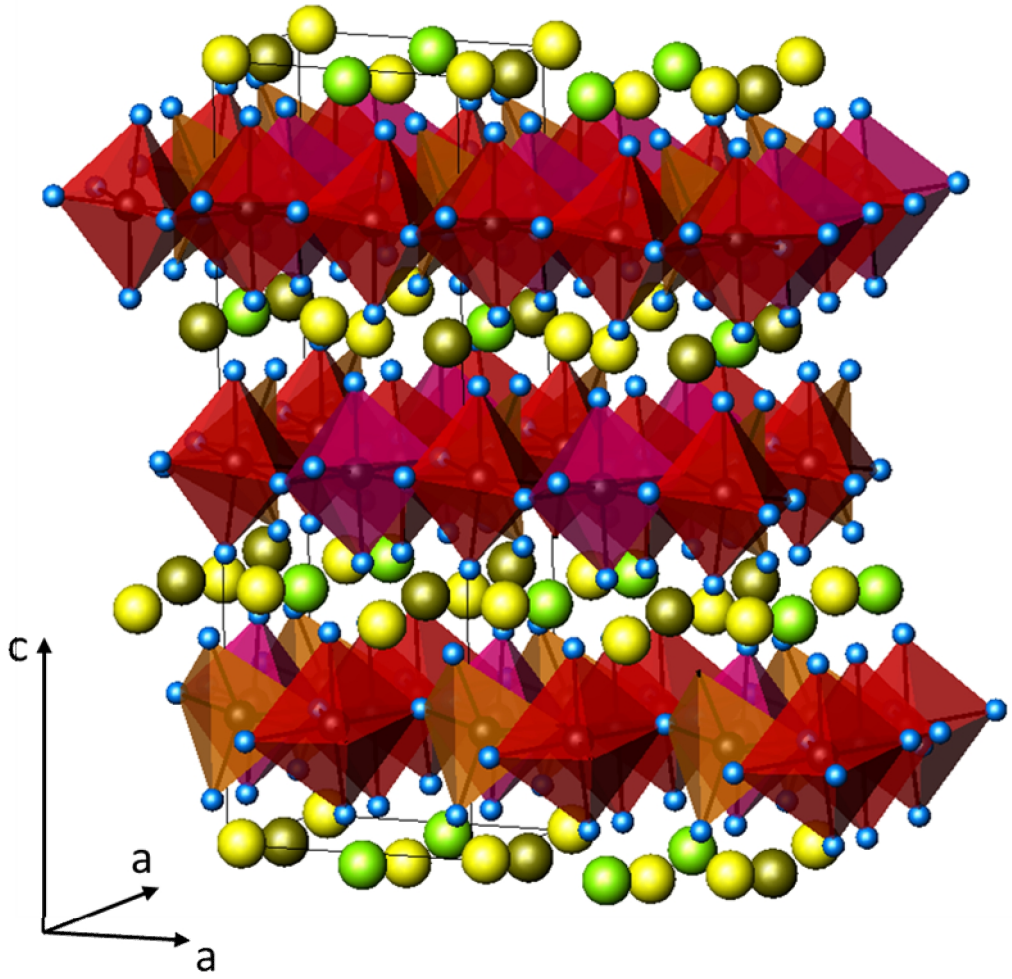

Figure 17: Schematic representation of refined structural model for : Y1(8), Y2(8) and Y3(7) sites are denoted by gold, green and yellow spheres, respectively; M1(6), M2(6) and M3(5) sites are shown by magenta, red and orange polyhedra, respectively; oxygen anions are shown by blue spheres. Note M3(5) sites are shown at 50% occupancy.

The refined metal-oxygen bond lengths and occupancy of the M sites are reported in Tables 7 -9. Bond valence sums reported for the Y1(8) and Y3(7) site, given Table 7, are close to the formal oxidation state, whereas that for the Y2(8) site is significantly lower than expected by ~10%. The Shannon polyhedral distortion index, Δ_n, is a useful indicator of polyhedron bond length distortion, *viz.* $\Delta_n = 1/n\ [\sum(r_i - r_m) / r_m)^2] \times 10^3$, where r_i and r_m are the individual and mean metal-oxygen bond lengths, respectively. Calculation of the distortion index for the Y sites shows that the Y2(8) site is considerably more distorted than the Y1(8) and Y3(7) sites. Inspection of Table 7 shows that the low bond valence sum and distortion of the Y2(8) site is due, primarily, to the Y2(8)-O1 contacts which are much longer than the average Y-O bond lengths in this structure. The O1 anion also

forms part of the co-ordination polyhedron of the M2(6) and M3(5) sites (the latter of which is 50% occupied). The isotropic thermal parameter of the O1 anion is noticeably larger than those of the other oxygen anions, which may be due to positional disorder associated with random occupancy of the M3(5) site. The distortion of the Y2(8) site, resulting in a lower than expected, but not implausible, bond valence sum, is therefore considered a consequence of the distortion of neighbouring M2(6) and M3(5) polyhedra, combined with the effects of cation occupancy disorder.

The refined metal oxygen bond lengths for the M site, combined with application of the Shannon site distortion index, demonstrate that the M3(5) and M1(6) sites are considerably more distorted than the M2(6) sites, as shown in Table 8. Consideration of bond valence sums for the M3(5) site, based on the refined M-O bond lengths, Table 8, demonstrates that the bond valence sums for all cations are significantly below the formal oxidation state. However, the deviation is considerably smaller for Fe^{3+}, ~10%, compared to that for Ti^{4+}, ~17%, and Nb^{5+} ~15%. These bond valence sums indicate that Fe is a better fit to the M3(5) site than Nb and Ti, consistent with the analysis of ^{57}Fe Mössbauer data which show that 80% of the occupied M3(5) sites are populated by Fe (corresponding to 55% of total Fe). Considering the M1(6) and M2(6) sites, Fe is found to preferentially occupy the less distorted M1(6) site, see Tables 8 and 9. The Fe bond valence sums calculated for these sites are essentially identical, indicating that the different site occupancies cannot be explained by ionic size effects. The higher Ti and Nb occupancy of the more distorted M2(6) site may be a consequence of the second order Jahn Teller effect, commonly observed for d^0 cations. Donation of electron density from filled oxygen 2*p* states into empty transition metal d^0 states, for cations such as Nb^{5+} and Ti^{4+}, triggers a distortion of the co-ordination environment (a second order Jahn Teller distortion) leading to a lower energy state. [49,50] The lower Fe occupancy of the more distorted M2(6) site determined from ^{57}Fe Mössbauer spectroscopy is thus considered a consequence of the preferential occupancy of this site by Ti and Nb, stabilised by the second order Jahn Teller distortion. Consideration of the Nb and Ti distribution over the M1(6) and M2(6) sites, shows a preference of Nb for the less distorted M1(6) site, although the bond valence sum is closer to optimal for the more distorted M2(6) site (and vice versa for Ti). The M3(5) site shares a common edge with the M1(6) and M2(6) sites, within the hexagonal tungsten bronze layer, as shown in Figure 18, however, the metal-metal distance between the M1(6)-M3(5) sites is only 2.93 Å compared to 3.20 Å for the M2(6)-M3(5) sites. The longer metal-metal contact distance across the shared polyhedral edge for the M2(6)-M3(5) sites may favour occupancy of this site by Nb on electrostatic grounds.

Although we cannot claim the refined cation distribution and structure model for $Y_2Ti_{0.6}Fe_{0.7}Nb_{0.7}O_7$ to be unique, it is certainly a plausible model based on consideration of bond valence sums and crystal chemistry. Comparison of the expected and calculated weighted mean

bond valence sums based on the final site occupancy, Tables 7-9, show reasonable agreement, except in the case of the 50% occupied and highly distorted M3(5) site. The key uncertainty is the assumption that the M3(5) site is occupied exclusively by Fe and Ti, with Nb occupying only the octahedral sites. Note that such a distribution was found to be the case of $CaZrTi_{2-2x}Fe_xNb_xO_7$, which adopts the zirconolite-2M structure. [30] Bond valence sums do not provide clear cut evidence that Nb occupancy of the M3(5) site is strongly disfavoured on grounds of ionic size, in comparison to Ti occupancy. However, restricting Nb occupancy to the octahedral sites would clearly minimise unfavourable coulombic interactions across the shared edge of the M1(6)-M3(5) and M2(6)-M3(5) polyhedra, because this precludes Nb^{5+} cations sharing a common polyhedral edge. In summary, the refined structural model is plausible and based on reasonable assumptions, in terms of crystal chemistry, but it cannot be considered to be a unique description of the crystal structure.

It is worthwhile commenting on the stability of the zirconolite 3T structure in the $Y_2Ti_{2-2x}Fe_xNb_xO_7$ solid solution, which is stabilised only over a narrow composition range near x = 0.7. As described above, substitution of the larger Fe^{3+} and Nb^{5+} cations for Ti^{4+} eventually destabilises the octahedral B_2O_6 network of the pyrochlore structure at x = 0.5. However, from the above analysis it may be appreciated that the stability of the zirconolite-3T structure may be sensitive to small variations in composition. In particular, for x = 0.7 there is sufficient Fe^{3+} available such as to fill 80% of the occupied M3(5) sites, minimising coulombic interactions across the shared edge of the M1(6)-M3(5) and M2(6)-M3(5) polyhedra. At lower Fe^{3+} / Nb^{5+} concentration, a greater proportion of the occupied M3(5) sites would be occupied by Ti^{4+} species, potentially destabilising the structure. At higher Fe^{3+} / Nb^{5+} concentrations, the interaction between Nb^{5+} species on adjacent M1(6) and M2(6) sites would become more significant, again potentially destabilising the structure. Consequently, the stability of the zirconolite 3T structure may be considered to arise from a delicate balance of ionic size, charge, and electronic effects, leading to a narrow solid solution range. This is consistent with the fact that there are only two other well characterised examples of materials adopting the zirconolite-3T structure: a natural specimen of the mineral zirkelite and $Ca_{0.8}Ti_{1.35}Zr_{1.3}Th_{0.5}Al_{0.4}O_7$. [51,23] However, the current study points to a potentially larger family of titanate zirconolites, formulated $A_2B_2O_7$, where the r_A/r_B size ratio is increased above the stability limit for the pyrochlore structure, using suitable chemical substitution. For example, Al^{3+} is well known to adopt 5-fold co-ordination in crystalline and amorphous metal oxides, thus, as yet unknown zirconolite phases could exist in the $Ln_2Ti_{2-2x}Al_xNb_xO_7$ solid solution.

Bond	Length (Å)	Bond	Length (Å)	Bond	Length (Å)
Y1(8)-O2	2.450(23)	Y2(8)-O1	2.619(17)	Y3(7)-O2	2.267(21)
Y1(8)-O2	2.450(23)	Y2(8)-O1	2.618(17)	Y3(7)-O3	2.304(19)
Y1(8)-O3	2.287(22)	Y2(8)-O2	2.396(27)	Y3(7)-O5	2.374(20)
Y1(8)-O3	2.286(22)	Y2(8)-O2	2.396(27)	Y3(7)-O5	2.305(18)
Y1(8)-O4	2.477(11)	Y2(8)-O3	2.335(30)	Y3(7)-O6	2.404(21)
Y1(8)-O4	2.476(11)	Y2(8)-O3	2.334(30)	Y3(7)-O6	2.282(20)
Y1(8)-O6	2.339(18)	Y2(8)-O5	2.375(20)	Y3(7)-O7	2.330(13)
Y1(8)-O6	2.339(18)	Y2(8)-O5	2.375(20)		
$\Delta_{Y1(8)}$ = 0.0091		$\Delta_{Y2(8)}$ = 0.0341		$\Delta_{Y3(7)}$ = 0.0011	
BVS (v.u) = 3.02		BVS (v.u) = 2.73		BVS (v.u) = 3.10	

Table 7: Key bond lengths for Y sites in $Y_2Ti_{0.6}Fe_{0.7}Nb_{0.7}O_7$ (x = 0.7) determined from Rietveld analysis of neutron powder diffraction data and resulting cation bond valence sums.

Bond	Length (Å)	Bond	Length (Å)	Bond	Length (Å)
M1(6)-O4	2.028(33)	M2(6)-O1	2.13(4)	M3(5)-O1	1.97(4)
M1(6)-O4	2.028(33)	M2(6)-O1	1.93(4)	M3(5)-O2	1.903(30)
M1(6)-O6	1.936(12)	M2(6)-O3	1.988(18)	M3(5)-O2	1.890(28)
M1(6)-O6	1.937(12)	M2(6)-O4	1.932(32)	M3(5)-O4	1.873(23)
M1(6)-O7	1.947(34)	M2(6)-O5	1.969(17)	M3(5)-O4	2.50(4)
M1(6)-O7	1.947(34)	M2(6)-O7	1.96(4)		
$\Delta_{M1(6)}$ = 0.4305		$\Delta_{M2(6)}$ = 1.1739		$\Delta_{M3(5)}$ = 13.8623	
Expected BVS (v.u.) = 3.92		Expected BVS (v.u.) = 4.44		Expected BVS (v.u.) = 3.20	
Mean BVS (v.u.) = 4.03		Mean BVS (v.u.) = 4.39		Mean BVS (v.u.) = 2.82	

Table 8: Key bond lengths for M in sites $Y_2Ti_{0.6}Fe_{0.7}Nb_{0.7}O_7$ (x = 0.7) determined from Rietveld analysis of neutron powder diffraction data. The expected bond valence sum assumes the nominal cation oxidation state together with occupancies, given in Table 9. The mean bond valence sum is the weighted mean calculated bond valence sum derived from the refined site occupancies and bond valence sums determined from bond length data, given in Table 10.

Cation	Site		
	M1(6)	M2(6)	M3(5)
Ti	0.216(20)	0.391(10)	0.101
Fe	0.434	0.084	0.399
Nb	0.350(20)	0.525(10)	0

Table 9: Cation occupancies of M sites in $Y_2Ti_{0.6}Fe_{0.7}Nb_{0.7}O_7$ (x = 0.7) determined from Rietveld analysis of neutron powder diffraction data and ^{57}Fe Mössbauer spectroscopy. Errors are reported for cation occupancies refined in Rietveld analysis. Nb is assumed to be excluded from the M3 site.

Cation	Site		
	M1(6)	M2(6)	M3(5)
Ti	3.96	3.85	3.27
Fe	3.18	3.18	2.70
Nb	5.14	4.99	4.24

Table 10: Bond valence sums for M sites in $Y_2Ti_{0.6}Fe_{0.7}Nb_{0.7}O_7$ (x = 0.7) determined from bond length data reported in Table 8.

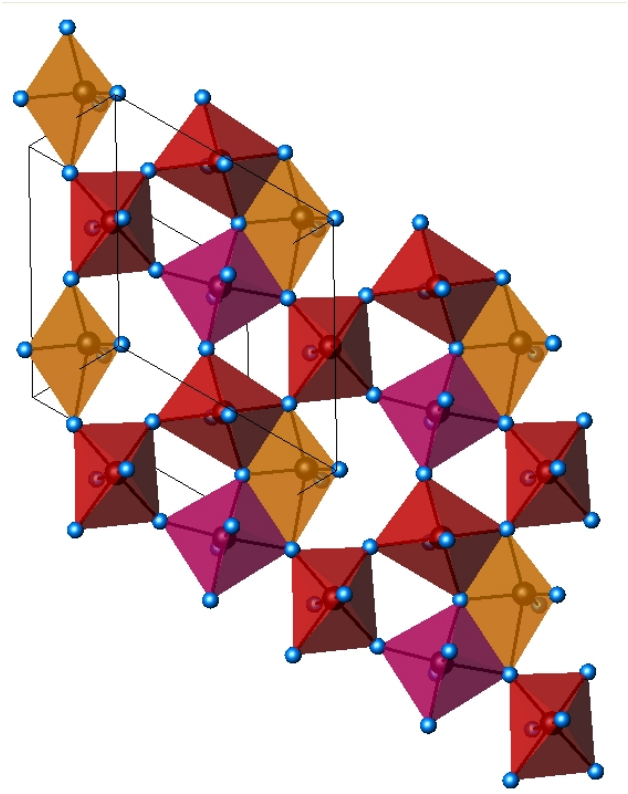

Figure 18: Single hexagonal tungsten bronze layer in $Y_2Ti_{0.6}Fe_{0.7}Nb_{0.7}O_7$, projected down c-axis.; M1(6), M2(6) and M3(5) sites are shown by magenta, red, and orange polyhedra, respectively; oxygen anions are shown by blue spheres. Note M3(5) sites are shown at 50% occupancy.

3.8. Magnetic properties

Magnetic properties have been reported for pyrochlore $A_2B_2O_7$, [52] in these systems the tendency to form a long-range ordered ground state is frustrated. Antiferromagnetic M-M interactions would be expected via M-O-M superexchange, however, B cations are clustered into tetrahedral units which share corners forming intersecting chains which tend to frustrate the M-M interactions. Spins at two points of the tetrahedron may couple in an antiparallel way and it might be impossible for the remaining atoms to align their spins in an antiparallel fashion as the other two. Therefore, materials adopt novel short range ordered arrangements such as spin glasses, spin ices and spin liquids.

$Y_2Ti_{2-2x}Fe_xNb_xO_7$ provides a system where the amount of iron (III) increases in composition, creating a possibility of a magnetic interaction. The B site also adopted different geometries, octahedral for lower x compositions (cubic structure) and settled as a mixed 5-fold – 6-fold geometry for higher compositions (proved by Mössbauer, Fig. 8). The magnetic susceptibility at

different temperatures was then recorded, at a constant magnetic field. The magnetic results were plotted on Figure 19.

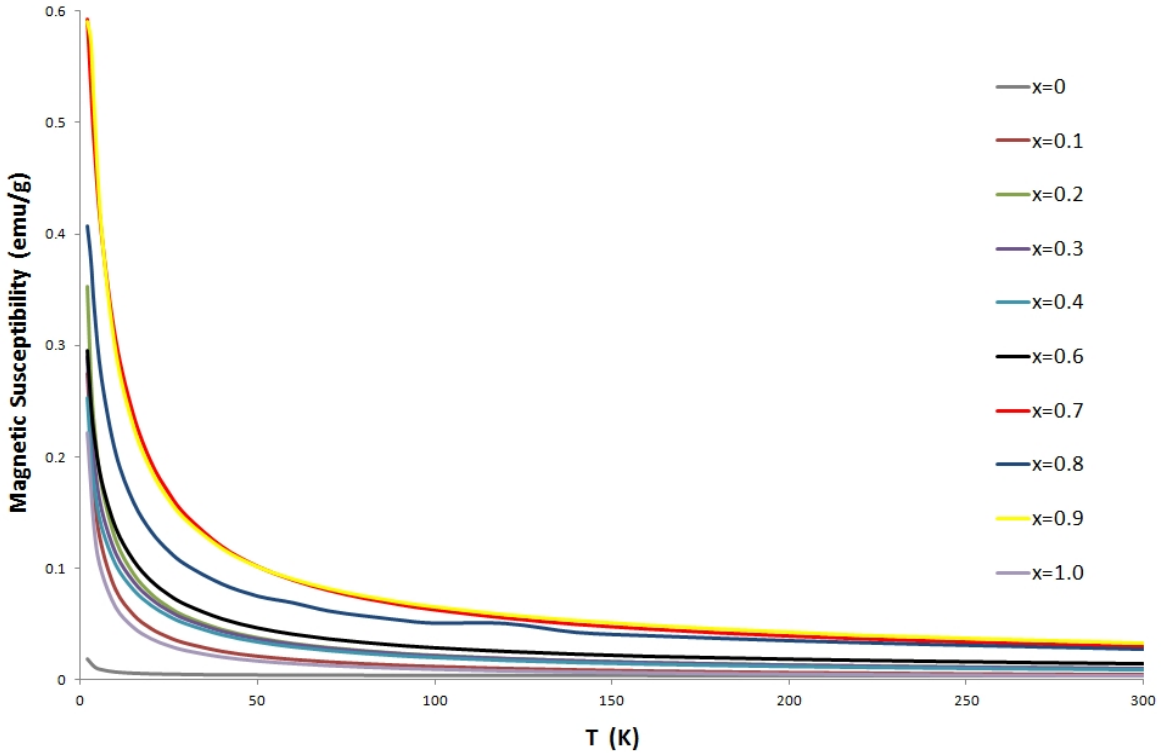

Figure 19: Magnetic susceptibility of $Y_2Ti_{2-2x}Fe_xNb_xO_7$ compositions over $0 < T < 300$ K.

A paramagnetic behaviour was deduced from Figure 19; the x = 0.8 sample showed a different trend than the rest of the whole $Y_2Ti_{2-2x}Fe_xNb_xO_7$ compositions between 100 and 150 K, probably because of the presence of impurities. The magnetic frustration in this system was more prominent than in previously reported compounds as a paramagnetic behaviour was observed. Clustering of B cations in octahedral and 5-fold sites may be the reason for the lack of M-M interactions.

4. CONCLUSION

Powder X-ray diffraction and SEM / EDX data confirmed the synthesis of a new pyrochlore solid solution $Y_2Ti_{2-2x}Fe_xNbO_7$ with $0.0 < x \leq 0.4$. The unit cell parameters scale with the weighted mean radius of the B site cations, as expected. ^{57}Fe Mössbauer spectroscopy and Fe K-edge XANES data demonstrated the presence of only Fe^{3+} species, as targeted. Furthermore, Mössbauer spectroscopy demonstrated the presence of Fe^{3+} in an octahedral site, consistent with substitution at the pyrochlore B-site.

Investigation of $Y_2Ti_{2-2x}Fe_xNb_xO_7$, within $0.7 \leq x \leq 0.9$ by X-ray and neutron diffraction, revealed the synthesis of a new phase of an unusual zirconolite 3T structure. Sample characterisation by Mössbauer and XANES confirmed the presence of Fe^{3+} species, as targeted. Furthermore, Mössbauer spectroscopy presented both 6- and 5-fold co-ordination environments. Thus, it would appear that the new zirconolite 3T phase is stabilised by formation of FeO_5 species. The observation of a two phase region in the phase diagram of $Y_2Ti_{2-2x}Fe_xNb_xO_7$, between $0.5 < x < 0.7$, implies that the free energy of the pyrochlore and zirconolite phase must be similar.

The synthesis and characterisation of $Y_2Ti_{2-2x}Fe_xNb_xO_7$ was achieved. Pyrochlore structured materials were obtained for $0.0 < x \leq 0.4$, whereas a new zirconolite structure was obtained for $0.7 \leq x \leq 0.9$. The structure and suitability of this new structure as a potential actinide host is under further investigation.

5. FURTHER WORK

5-coordinated iron (III) ions are not commonly reported in the literature. More extensive data needs to be collected in order to extend our knowledge on such cations. XANES pre edge features, Mössbauer and Raman at variable temperature, on samples where $x \geq 0.7$, could give some more information about this kind of chemical environment. Incorporation of Ln and An (III) on the yttrium site, determination of radiation and corrosion tolerance, are currently underway.

6. REFERENCES

[1] E.N.S. Muccillo, *Cerâmica*, 2008, **54**, N° 330, 129-144.

[2] M.A. Subramanian, J.E. Greedan, N.P. Raju, A.P. Ramirez and A.W. Sleight, *Journal de Physique IV*, 1997, **7**, C1-625C1-628.

[3] J.E. Greedan, N.P. Raju, A. Maignan, Ch. Simon,, J.S. Pedersen, A.M. Niraimathi, E. Gmelin and M.A. Subramanian, *Physical review B – Condensed Matter and Materials Physics*, 1996, **54**, Issue 10, 7189 – 7200.

[4] L.K. Joseph, K.R. Dayas, S. Damodar, B. Krishnan, K. Krishnankutty, V.P.N. Nampoori and P. Radhakrishnan, *Spectrochimica Acta – Part A: Molecular and Biomolecular Spectroscopy*, 2008, **71**, Issue 4, 1281-1285.

[5] J. Yang and Y. Su, *Materials Letters*, 2010, **64**, Issue 3, 313-316.

[6] W. Lutze and R.C. Ewing, *Radioactive Waste forms for the future*, 1988, Elsevier Science, Amsterdam, 233-334.

[7] A.E. Ringwood. *Fortschritt in Mineralogie,* 1980, **58**, 149-168.

[8] M.R. Gilbert, *Zirconolite waste-forms for plutonium disposition*, Thesis of the University of Manchester, **2009.**

[9] G.R Lumpkin, K. L. Smith, R. Giere and C. T. Williams, *Geological Society, special publications*, 2004, London, **236**, 89-111.

[10] M.A. Subramian, G. Aravamudan and G.V. Subba Rao, *Progress in Solid State Chemistry*, 1983, **15**, 55-143.

[11] B.C. Chakoumakos, *Journal of Solid State Chemistry*,1984, **53**, 120-129.

[12] E.R. Maddrell, *Journal of the American Ceramic Society*, 2001, **84**, 1187-1189.

[13] P.E.D. Morgan, D.R. Clarke, C.M. Jantzen and A.B. Harker, *Journal of the American Ceramic Society*, 1981, **64**, 248-258.

[14] Hk. Muller-Buschbaum and J.-P. Werner, *Journal of Alloys and Compounds*, 1994, **206**, L11-L13.

[15] Yu. F. Shepelev and M. A. Petrova, *Inorganic Materials*, 2008, **44**, 1354–1361.

[16] A. Garbout, S. Bouattour, M. Ellouze and A.W. Kolsi, *Journal of Alloys and Compounds*, 2006, **425**, 88-95.

[17] K. A. Gschneidner, Jr. and L. Eyring, *Handbook on the Physics and Chemistry of Rare Earth*, 1993, **16**, Elsevier Science Publisher B.V.

[18] B. Ravel, and M. Newville, *Journal of Synchrotron Radiation*, 2005, **12**, 537-541.

[19] K. Legarec and D.G. Rancourt, *Recoil: Mössbauer Spectral Analysis Software for Windows, v. 1.0*, 1998.

[20] A.C. Larson and R.B. Von Dreele, *General Structural Analysis System (GSAS)*, University of California: Los Alamos, 1998.

[21] E.J. Harvey, S.E. Ashbrook, G.R. Lumpkin, S.A.T Redfern, *Journal of Materials Chemistry*, 2006, **16**, 4665–4674.

[22] L. Borodin, I. Nazarenko, T. Richter, *Doklady Academy Sciences USSR, Earth Science Section (English. Translation)*, 1960, **134**, 1022.

P. Bayliss, F. Mazzi, R. Munno and T. White, *Mineralogical Magazine*, 1989, **53**, 565.

[23] F. Mazzi and R. Munno, *American Mineralogist*, 1983, **68**, 262-276.

[24] D.P. Reid, M.C. Stennett and N.C. Hyatt, *Journal of Solid State Chemistry*, 2012, **191**, 2-9.

[25] K.L. Smith and G.R. Lumpkin, *Structural Features of Zirconolite, Hollandite and perovskite, the Major Waste-Bearing Phases in Synroc., in Defects and Processes in the Solid State: Geoscience Applications*, 1993, The McLaren Volume. Eds. J. N. Boland and J. D. Fitzgerald. Elsevier Science Publishers, 401-422.

[26] E.R. Vance, G.R. Lumpkin, M.L. Carter, D.J. Cassidy, C.J. Ball, R.A. Day, and B.D. Begg, *Journal of the American Ceramic Society*, 2002, **85**, 1853-1859.

[27] M. C. Stennett, N. C. Hyatt, E. R. Maddrell, F. G. F. Gibb, G. Moebus, and W. E. Lee, *Microchemical and crystallographic characterisation of fluorite-based ceramic wasteforms*, *Scientific Basis for Nuclear Waste Management XXIX*, 2006, Ed P. VanIseghem. Materials Research Society, 623-630.

[28] M.D. Dyar, D.G. Agresti, M.W. Schaefer, C.A. Grant and E.C. Sklute, *Annual Review Earth Planetary Sciences*, 2006, **34**, 83-125.

[29] F.J. Berry, G.R. Lumpkin, G.Oates and K.R. Whittle, *Hyperfine Interactions*, 2006, **106**, 363-366.

[30] G.R. Lumpkin, K.R. Whittle, C.J. Howard, Z. Zhang, F.J. Berry, G. Oats, C.T. Williams and A.N. Zaitsev, *Materials Research Society Symposium Proceedings*, 2006, **932**.

[31] I.E. Grey, W.G. Mumme, T.J. Ness, R.S. Roth and K.L. Smith, *Journal of Solid State Chemistry*, 2003, **174**, 285-295.

[32] P.E. Petit, F. Farges, M. Wilke and A. Solé, *Journal of Synchrotron Radiation*, 2001, **8**, 952-954.

[33] M. Wilke, F. Farges, P-E. Petit, G.E. Brown Jr and F. Martin, *American Mineralogist*, 2001, **86**, 714-730.

[34] G.A. Waychunas, M.J. Apted and G.E. Brown , *Physics and Chemistry of Minerals*, 1983, **10**, 1-9.

[35] P. A. O'Day, N. Rivera Jr, R. Root and S.A. Carroll, *American Mineralogist*, 2004, **89**, 572-585.

[36] M. Wilke, G.M. PArtzsch, R. Bernhardt and D. Lattard, *Chemical Geology*, 2004, **213**, 71-87.

[37] M. Wilke, C. Schmidt, F. Farges, V. Malavergne, L. Gautron, A. Simiovici, M. Hahn and P-E Petit, *Chemical Geology*, 2006, **229**, 144-161.

[38] F. Farges, *Physical Review B*, 2005, **71**, 155109-155123.

[39] M. Glerup, O.F. Nielsen and F.W. Poulsen, *Journal of Solid State Chemistry,* 2001, **160**, 25-32.

[40] C. De La Fontaine, M.C. Stennett, S.L. Heath and N.C. Hyatt, *in this volume*, 2013, **3**, 84-115.

[41] R. A. McCauley, *Journal of Applied Physics*, 1980, **51**, 290-294.

[42] H.C. Gupta, S. Brown, N. Rani and V.B. Gohel, *Journal of Physics and Chemistry of Solids*, 2002, **63**, 535-538.

[43] F.W. Poulsen, M. Glerup and P. Holtappels, *Solid State Ionics*, 2000, **135**, 595-602.

[44] W.J. Chung, B.J. Park, H.S. Seo, J.T. Ahn and Y.G. Choi, *Chemical Physics Letters*, 2006, **419**, 400-404.

[45] R.D. Shannon, *Acta Crystallographica*, 1976, **A32**, 751.

[46] V.F. Sears, *Neutron News*, 1992, **3**, No. 3, 29-37.

[47] E. Chtoun, L. Hanebali, P. Garnier and J. M. Kiat, *European Journal of Solid State and Inorganic Chemistry*, 1997, **34**, 553-561.

[48] R.P. Liferovich and R.H. Mitchell, *Canadian Mineralogist*, 2006, **44**, 1089-1098.

[49] N.S.P. Bhuvanesh and J. Gopalakrishnan, *Journal of Materials Chemistry*, 1997, **7,** 2297-2306.

[50] M.H. Wheeler, M.H. Whangbo, T. Hughbanks, R. Hoffmann, J.K. Burdett, and T.A. Albright, *Journal of the American Chemical Society*, 1986, **108**, 2222-2236.

[51] I.E. Grey, W.G. Mumme. T.J. Ness, R.S. Roth, K.L. Smith, *Journal of Solid State Chemistry*, 2003, **174**, 285-295.

[52] J.S. Gardner, M.J.P. Gingras and J.E. Greedan, *Review of Modern Physics*, 2010, **82**, 53-107.

Chapter 5:

OLIGOMERIC COMPLEXES OF ACTINIDES FORMED THROUGH LIGAND CONTROLLED HYDROLYSIS AND THE PREPARATION OF A NOVEL URANIUM (IV) IODO ISOPROPOXIDE ISOPROPANOL

Carlos De La Fontaine, Stéphanie M. Cornet, Tamara L. Griffiths and Sarah L. Heath*

Centre for Radiochemistry Research, School of Chemistry, The University of Manchester, Manchester M13 9PL

(Correspondence: sarah.l.heath@manchester.ac.uk)

ABSTRACT

A study of actinide hydrolysis in the presence of an organic ligand is presented, as well as the preparation of a novel uranium alkoxide, a possible precursor for a new controlled hydrolysis route. The polycarboxylate ligand, N-(2-hydroxyethyl)iminodiacetic acid (heidi), was chosen as part of a study that is developing models of environmentally mobile actinide colloids and cluster species. Metal to ligand ratios and the denticity of the ligand, under different pH regimes, are some of the parameters used to control the hydrolysis. Solid state data have been reported previously for the 1:2 metal to ligand ratio without any discussion of its solution chemistry. Analytical results for the same ratio are reported for Zr (IV), Th (IV), U (IV), U (VI), Np (IV) and Np (VI) in order to obtain a full insight of the chemical behaviour of this system.

The preparation of a new monomeric homoleptic U(IV) alkoxide by direct combination of uranium metal and isopropanol in the presence of iodine gave $[UI(O\text{-}i\text{-}Pr)_2.(HO\text{-}i\text{-}Pr)_4]I$, which crystallised in a triclinic P-1 space group with the following unit cell parameters a = 9.7633 Å, b = 11.4804 Å, c = 14.377 Å, $\alpha = 88.794^{o}$, $\beta = 79.142^{o}$, $\gamma = 68.017^{o}$.

1. INTRODUCTION

For decades, the complex nature of actinide hydrolysis has been studied. [1,2,3] Numerous species in several oxidation states can co-exist in solution.[4] It is important to study the aqueous chemistry and geochemistry of the actinides, and their surrogates, to gain a better understanding of their fundamental behaviour in the environment. [4] This knowledge will underpin the chemical treatment of nuclear waste and decommissioning management. [5]

Structural studies of the solid and solution states provide information on coordination number, bond lengths, ligand exchange rates and mechanisms, which are necessary to predict and understand chemical processes that will occur during the treatment and disposal of nuclear waste.

The literature shows many discrepancies in data due mainly to different experimental conditions (concentration, media, ionic strength etc...) [2]. An abundant number of contributions to actinide hydrolysis based on spectrometric [6] and potentiometric [3] studies have been reported with "bare" ions. Hydrolysis has often been modelled using 'the partial charge model', [7] which defines the reactivity of an element towards hydrolysis by its Z^2/r quotient (where Z is the charge of a given metal ion and r its ionic radii). Ions are more prone to hydrolysis for higher values of Z^2/r.

Our approach avoids working with "bare" cations by using capping ligands to control the hydrolysis and should allow the study of the hydrolysis process and the isolation of actinide cluster species which are the intermediates during the formation of insoluble oxides and hydroxides. This paper describes the study of the solution chemistry of zirconium, thorium, uranium and neptunium in the presence of two equivalents of a simple amino carboxylate ligand: $HOCH_2CH_2N(CH_2COOH)_2$ (heidi, Figure 1). This was undertaken alongside structural studies of solids obtained under similar conditions. [8]

Heidi is a relevant organic ligand for the environment; it contains several features found in amino acids (-NH_2, -OH, and –COOH) and similar chemicals (such as NTA, EDTA) are already used within decommissioning projects in the nuclear industry. [5]

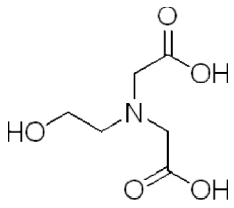

Figure 1: Schematic of N-(2-Hydroxyethyl)iminodiacetic acid (heidi).

Furthermore, amino acid-like ligands could help understand the exact role of humic and fulvic acid fractions (formed from decomposing natural organic matter) in the binding and migration of metals in soils and groundwater. [9]

Previous work with heidi reported by Heath *et al.* shows the formation of clusters with many Lewis acidic metal ions such as iron, [10] aluminium, [11] and gallium [12] *via* controlled hydrolysis. These systems may give information about the process of cluster growth and the role of the reactants.

However, d and p block elements are not a good model for the actinide series due to large differences in physical properties *e.g.* ionic radius, number of coordination sites and f-orbitals and chemical properties (speciation, oxidation state, electronegativity and geometry).

Hydrolysis of tetravalent elements was previously studied within the CRR by Christopher Mydlowski, [8] who was able to grow a few new d-metal and early actinide structures using aminocarboxylic acids such as heidi. A monomer was obtained with zirconium, as well as a dimer with thorium, which are shown in Figure 2.

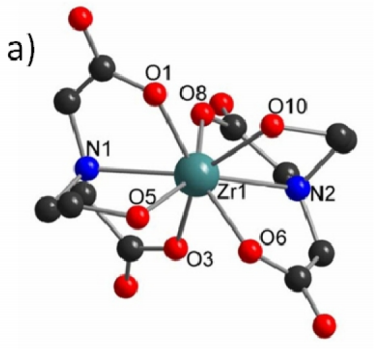

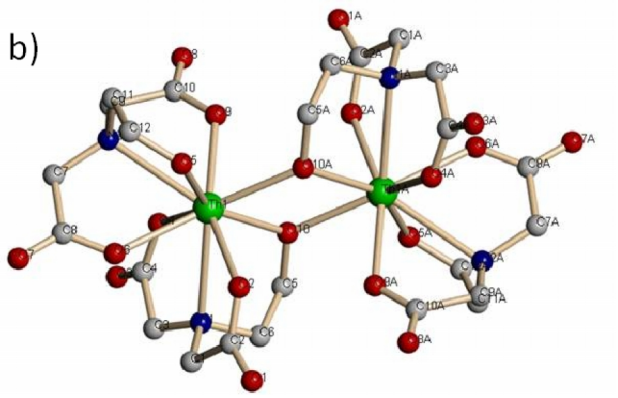

Figure 2: Ball and stick representations of a) $[Zr(heidi)_2].9H_2O$ and b) $[Th_2(heidi)_4]^{4-}$. [8]

The aim of this work is to understand the formation/growth of clusters, such as $[Pu_{38}O_{56}(H_2O)_8]^{14-}$, in aqueous media. [13] Typical titration experiments across the whole pH range have been conducted using a metal ion (Zr (IV), Th (IV), U(IV/VI) and Np(IV,V) and (VI)) and different ligand to metal ratios. NMR and UV-vis-nIR spectroscopy were also used to analyse samples when possible. This paper focusses on systems with a metal:ligand ratio of 1:2.

Another approach to study hydrolysis consisted of introducing a known amount of water to anhydrous metallic compounds, such as metal alkoxides, $M(OR)_n$. The preparation of a new U(IV) alkoxide is also reported.

During the 1950's Bradley and co-workers [14] developed most of the known reactions leading to the formation of metal alkoxides. They covered a broad number of elements from groups III to VIII, as well as a few actinides and lanthanides. These early studies mainly focussed on elementary characterisations of the products. Structural predictions of metal alkoxide compounds were established by analogy between similar metal ions chemical behaviour. Most of these cluster compounds have been obtained solvothermally by trial and error, lacking control of the crystallisation and the nature of the final product. The long-term goal of this study is to use actinide alkoxides as precursors in the synthesis of novel actinide oxo clusters, promoting cluster growth *via* controlled hydrolysis. Here, we report the synthesis of a novel U(IV) iodo alkoxide monomer.

2. EXPERIMENTAL PROCEDURE

UCl_4 was synthesised according to previous reported methods. [15] All the other chemicals were purchased from Sigma-Aldrich and used without further modification unless it is stated otherwise below.

Potentiometry

Potentiometric experiments were performed in D_2O or H_2O. Solutions were titrated with a 0.1 M NaOH or NaOD solution, prepared from NaOH pellets dissolved in distilled water or by diluting a 14.76 M NaOD solution in D_2O. The ionic strength of all solutions was adjusted to 0.5 M using $NaNO_3$ or NaCl, depending on the nature of the relevant metal salts. Four different experiments were run to obtain the reported graphs: a blank, free metal (5 mM), free ligand (10 mM) and metal (5 mM) with 2 equivalents of heidi. An automated apparatus, a 751 GPD Titrino Metrohm autotitrator, was used to perform the titrations. Nitrogen gas was bubbled through the bulk solution for 25 mins before the start of the titration and during the whole duration of the experiments.

U(IV) and Np(IV) experiments were run manually in a 1M HCl (or 1M DCl) solution under an inert atmosphere. A 0.1 M NaOH (and respectively NaOD) degassed solution was used as a base.

Preparation of a neptunium (IV) chloride solution

Np-237 (25 mg, 0.105 mmol) in 4M HNO_3 from a laboratory stock solution (5mg ^{237}Np/ml in 4M HNO_3) was precipitated as $NpO_2OH.xH_2O$ by the addition of a 6 M NaOH aqueous solution. In order to clean the $NpO_2OH.xH_2O$ precipitate, the sample was centrifuged, the supernatant removed and the precipitate was washed with distilled water (3 x 2 ml). This cleaning process was repeated three times. The $NpO_2OH.xH_2O$ precipitate was dissolved in 1 M HCl (1 ml) to form a Np (V) solution. The neptunium oxidation state at this stage was checked by UV-vis-nIR spectroscopy.

The volume of the sample was reduced using a heat lamp. Five drops of HI solution (*57 wt.%)* were added to the neptunium solution, which was then heated in order to reduce Np(V) to Np(IV). The reduction was confirmed by UV-vis-nIR spectroscopy. The solution was placed under vacuum and heated for several hours (around 2-4h) in order to eliminate the iodine from the solution.

Preparation of a neptunium (VI) nitrate solution

Np-237 (25 mg, 0.105 mmol) in a 4 M HNO_3 solution from a laboratory stock solution (5mg ^{237}Np/ml in 4M HNO_3) was heated to dryness using a heat lamp. Once cooled to room temperature, the dark brown residue was dissolved in 1 ml of a $HClO_4$ (70 %) solution. The sample was heated again, which caused the sample to produce white fumes and turn into a faint pink

solution. The volume was reduced by evaporation to almost dryness and the slurry obtained was dissolved in 1 M DNO_3 (1 ml).

The experiment detailed below was performed under a dry and inert atmosphere, either in an argon filled glovebox or using Schlenk techniques. Solvents were degassed and dried over CaH_2 or by sodium/ potassium metals prior to use.

[UI(O-i-Pr)$_2$.(HO-i-Pr)$_4$]I (1)

The pyrophoric U metal turnings (1.265 g, 5.315 mmol) were carefully broken down with tweezers and washed with concentrated HNO_3 (3 x 2ml) in order to remove the oxide layer from the surface of the metal. The shiny metal was then washed with water (5 x 2 ml) to remove the acid and with acetone (5 x 2ml). The metal was dried under vacuum.

Sublimed I_2 (2.01 g, 7.92 mmol) was dissolved in dry isopropanol (5 ml) and added to the uranium metal turnings via canula. The resulting red mixture was stirred for 24h in a water bath until it turned black. The viscous solution was then separated from the remaining uranium metal and left to crystallise in the freezer between -25 ^{o}C and -30 ^{o}C. Lavender crystals were obtained after 3-4 days. The reaction had a 52 % yield based on the weight of uranium. The excess isopropanol was removed whilst the sample was kept around -40 ^{o}C. This was done a few times and a more stable sample, in regard to temperature and solvation, was then obtained. IR (Nujol mull) υ/cm^{-1}, 3301 (brd), 3015 (s), 2948 (s), 2412 (s), 1680 (m), 1438 (s), 1267 (m). UV-vis, $\varepsilon_{\lambda(nm)}$ (mol^{-1}.dm^{-3}.cm^{1}), ε_{223}= 44.6, ε_{410}= 53.5, ε_{461}= 77.25, ε_{581}= 29.87, ε_{975}= 21.23. No elemental analysis can be presented as the crystals were too air sensitive. A summary of crystallographic data is presented in Table 1.

Empirical formula	C18 H40 I2 O6 U
Formula weight	844.33
Temperature	100(2) K
Wavelength	0.71073 Å
Crystal system	Triclinic
Space group	P-1
Unit cell dimensions	a = 9.8127(13) Å
	b = 11.4782(15) Å
	c = 14.3536(19) Å
	α = 89.032(2) °
	β = 79.076(2) °
	γ = 68.083(2) °
Volume	1470.1(3) $Å^3$
Z	2
Density (calculated)	1.907 Mg/m^3
Absorption coefficient	7.644 mm^{-1}
F(000)	788
Crystal size	0.25 x 0.10 x 0.10 mm^3
Theta range for data collection	1.45 to 26.42°.
Index ranges	-12 <= h<= 12, -14<= k <= 14,
	-17 <= l <= 17
Reflections collected	11435
Independent reflections	5862 [R(int) = 0.0256]
Completeness to theta = 26.42 °	97.1 %
Absorption correction	None
Max. and min. transmission	0.893 and 0.203
Refinement method	Full-matrix least-squares on F^2
Data / restraints / parameters	5862 / 12 / 286
Goodness-of-fit on F^2	1.278
Final R indices [I > 2sigma(I)]	R1 = 0.0678, wR2 = 0.1797
R indices (all data)	R1 = 0.0702, wR2 = 0.1805
Largest diff. peak and hole	5.033 and -2.937 $e.Å^{-3}$

Table 1: X-ray Crystallographic data for $C_{18}H_{40}I_2O_6U$ (1)

Instruments

NMR spectra were recorded using a Bruker Advance 400 MHz spectrometer. NMR spectra were measured at 400.13 MHz and 100.62 MHz for ^{1}H and ^{13}C, respectively.

UV-vis-n-IR data from samples containing uranium and neptunium were recorded in a double beam Cary Varian 500 scan UV-vis-nIR spectrophotometer.

Solids obtained throughout the experiments were analysed by elemental analysis. A Carlo ERBA instrument CHNS-O EA1108 elemental analyser was used for C, H and N analyses and a Fisions Horizon elemental analyser ICP-OES spectrophotometer was used for metal and halide analysis.

Elemental analysis

Elemental analysis was performed by the analytical services department of the School of Chemistry. Carbon, hydrogen and nitrogen composition were determined by combustion on a Carlo Erbra Instruments CHNS–O EA1108 Elemental Analyser. Halides analysis was undertaken by potentiometry and metals analysis by atomic emission spectra on a Fisons Horizon elemental analysis ICP–OED (AES) spectrometer.

Multinuclear NMR Spectroscopy

^{1}H and ^{13}C NMR experiments were recorded using a Bruker Advance 400 MHz spectrometer at the Centre for Radiochemistry Research (CRR), the University of Manchester. NMR spectra of ^{1}H were measured at 400.13 MHz and ^{13}C at 100.62 MHz. The chemical shifts were compared to previous published data. [16]

Single Crystal X-Ray Diffraction

Analysis of single crystals was carried out using a Bruker Apex platform CCD area diffractometer or an Oxford Diffraction Crysalis CCD diffractometer at 100 K with a Mo-K_{α} radiation source (λ = 0.71073 Å). Direct methods were used to solve the structures and were performed using the SHELX-97 program suite. [17]

3. RESULTS AND DISCUSSION

3.1. Potentiometric results

Figures 3, 4, 5 and 6 illustrate the potentiometric data collected for Zr (IV), Th (IV), U (IV) and U(VI), respectively, over the pH range 0 – 12. Heidi is sparingly soluble below pH 1.5 – 2 at a concentration of 10^{-2} M. The carboxylate groups are protonated below these pH values causing the ligand to remain as its solid form. It was also observed that the solubility of the ligand increased in the presence of metal ions. This was more prominent in the case of Th (IV) (Fig. 4). Once dissolved, heidi had an effect on hydrolysis for all metal ions (Fig. 3 – Fig. 6), as more base was needed to bring the solution to a given pH than for solutions with free metal ion only. The tendency to hydrolysis in the presence of heidi according to our experimental results, Fig. 3 – Fig. 6, showed the following trend: U(IV) > Zr (IV) > Th (IV) > U(VI). However, the Z^2/r rule should follow the order: Zr (IV) > U(IV) > Th (IV) > U(VI). Unsurprisingly, a higher affinity for hydrolysis was observed for tetravalent elements. [18]

Two inflections were observed in the thorium (IV) and uranyl metal ion titrations. The first inflection was observed at c.a. pH 3.33 for the thorium (IV) in the absence of heidi, and at pH 4.29 in the presence of heidi. The same trend was observed for uranyl ions with a first inflection detected at pH 3.78 for uranyl on its own and at pH 7.95 in the presence of heidi. This could suggest that the ligand is delaying hydrolysis. Above pH 10, the high concentration of HO^- ions leads actinide hydrolysis to produce insoluble actinide oxides *via* hydroxides precursors. [18,19]

The titration of the uranyl (VI) ion showed three pH inflections in presence of 2 equivalents of heidi (Fig. 6). The third inflection, in this case, may be masked for tetravalent elements as they are known to hydrolyse even at low pH, [2] for instance, the presence of polymeric plutonium (IV) should be expected whenever the acid concentration is below 0.5 M.[20]

On a closer look, the results for zirconium (IV): 2 heidi are very similar to the results of the ligand by itself. The zirconium (IV) does not seem to interact in the same way towards the ligand as the other tetravalent metal ions studied. Zirconium (IV) is often used as a non radioactive surrogate for tetravalent actinide hydrolysis [8]; however, in this specific case this assumption would be incorrect, as the actinide (IV) ions showed different trends from zirconium (IV).

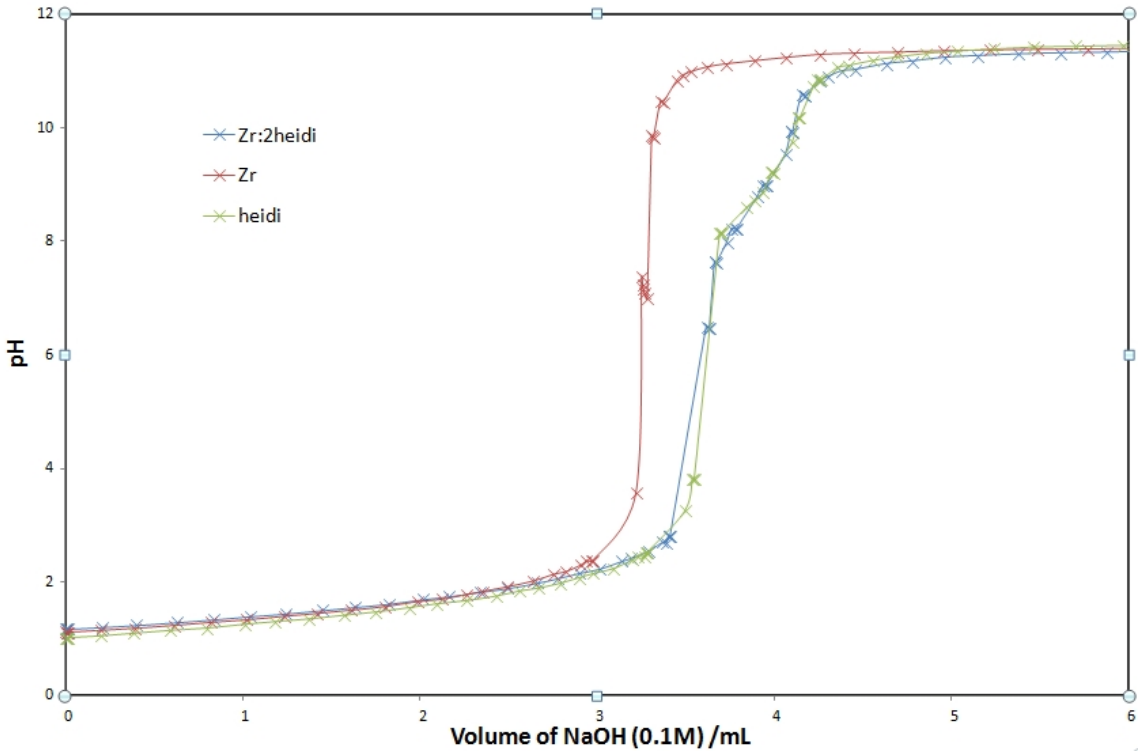

Figure 3: Titration of zirconium (IV) at 5.10^{-3} M (red line), in presence of 2 eq. of heidi (blue line) and heidi by itself (green line), I=0.5 M (NaCl).

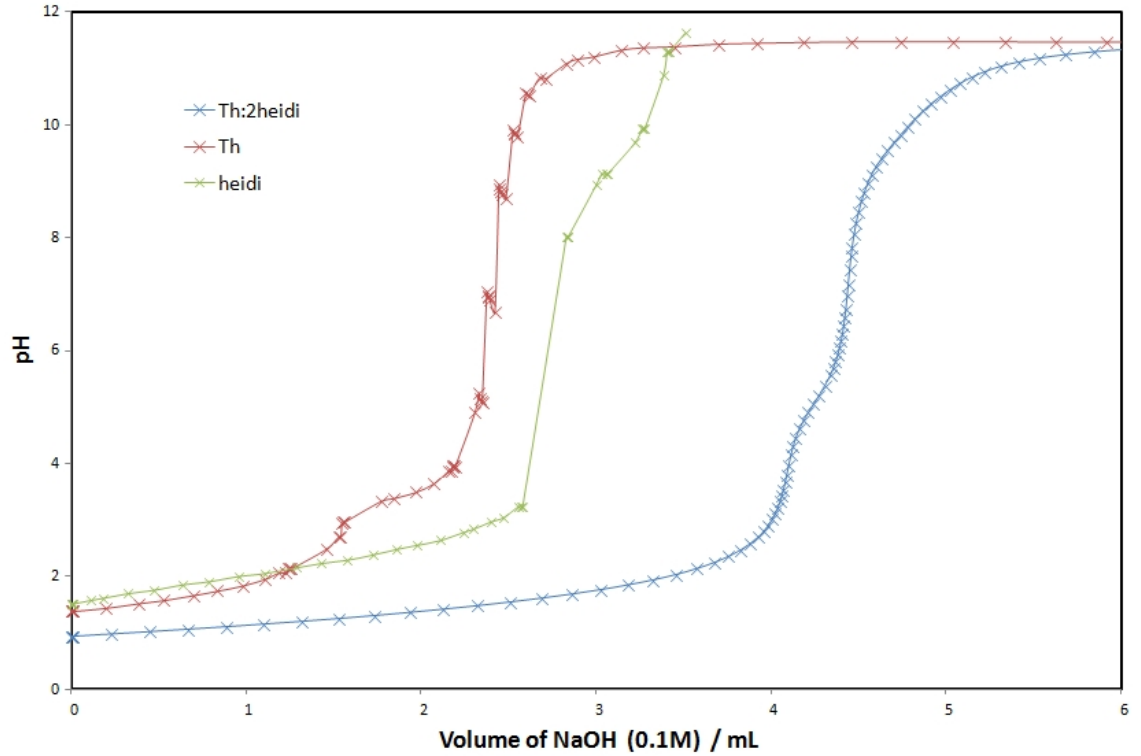

Figure 4: Titration of thorium (IV) at 5.10^{-3} M (red line), in presence of 2 eq. of heidi (blue line) and heidi by itself (green line), I=0.5 M ($NaNO_3$).

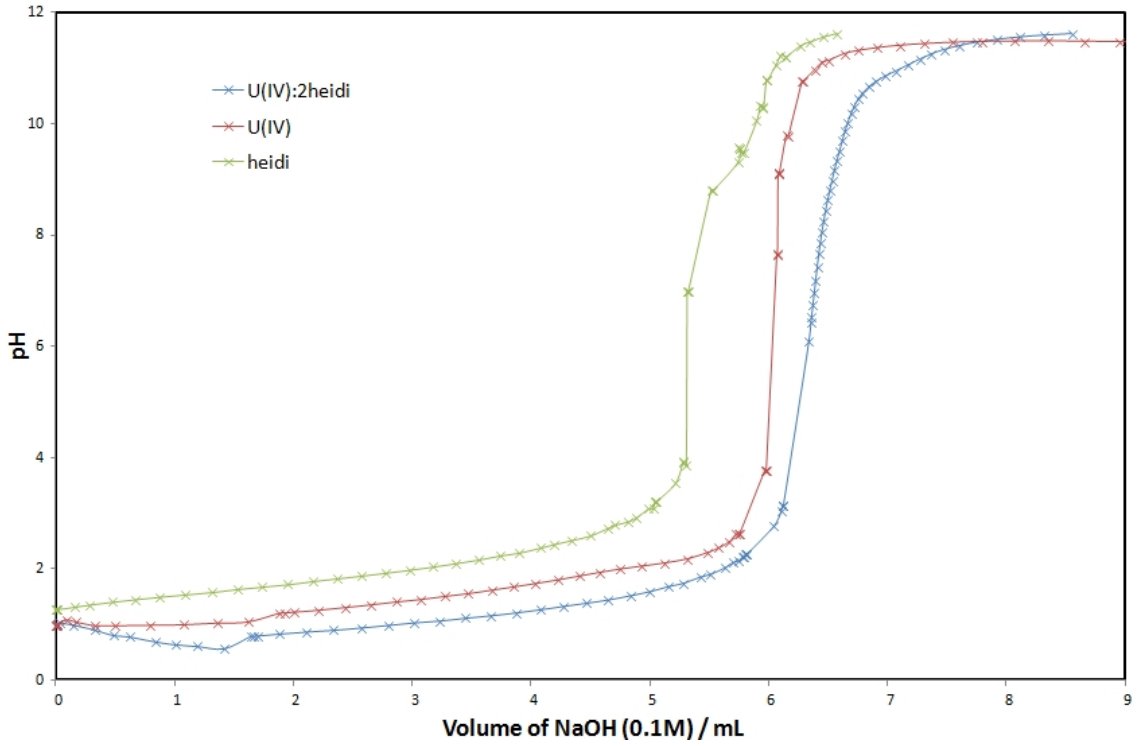

Figure 5: Titration of uranium (IV) at 5.10^{-3} M (red line) in a HCl (1M) solution, in presence of 2 eq. of heidi (blue line) and heidi by itself (green line), I=0.5 M (NaCl).

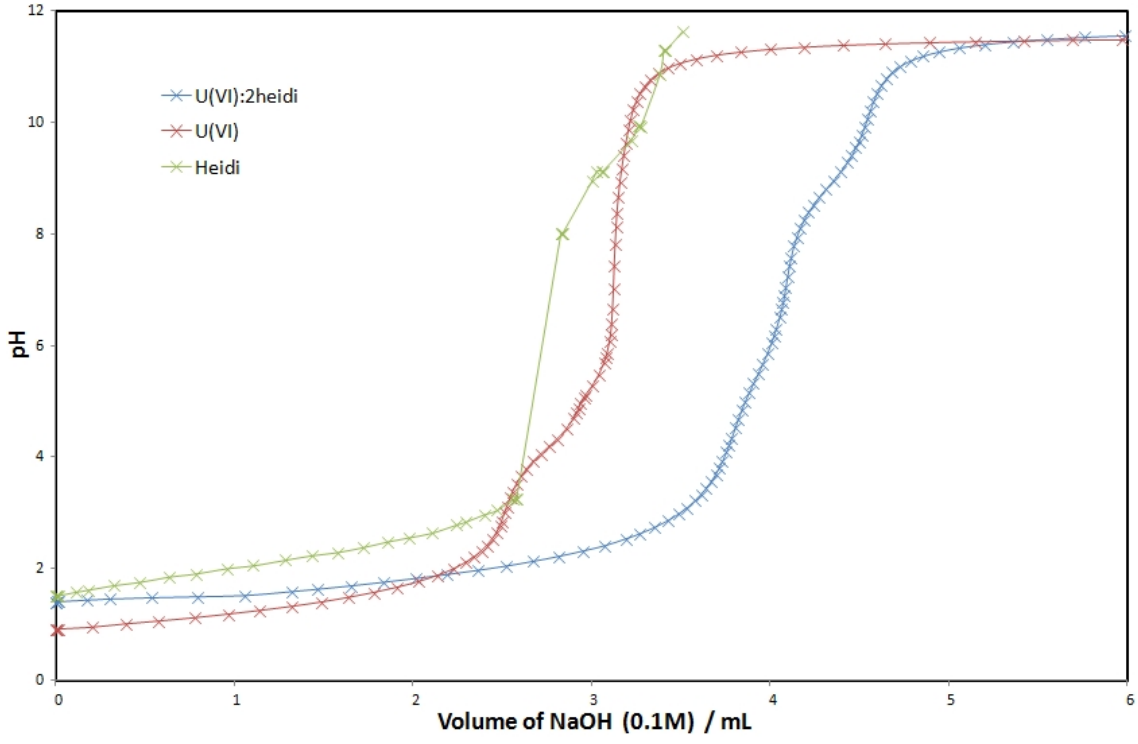

Figure 6: Titration of uranyl at 5.10^{-3}M (red line), in presence of 2 eq. of heidi (blue line) and heidi by itself (green line), I=0.5 M ($NaNO_3$).

Potentiometric raw data has the drawback that free hydrogen ions also contribute. It is therefore difficult to relate potentiometric results to their exact hydrogen ion source. The data are also dependent on concentration and on the background. A FORTRAN program was used to subtract the hydrogen ion background contribution from the titration data by comparing a blank titration to those with samples present.

Large changes in pH values between blank and experimental data (steps) could reveal pKa values. For instance, heidi pKa values derived from the potentiometric data, were found to be 2.2 for the carboxylate groups and 8.6 for the nitrogen (I = 0.5 M), Fig. 7, which was concordant with the literature (2.22 and 8.9 respectively). [21, 22]

In the presence of heidi, uranium (VI), thorium (IV) and zirconium (IV) ions, showed a step at c.a. pH 2, which is close to the pKa value of the carboxylate groups from the ligand. This result suggests that this first inflection does not correspond to the neutralisation of free H^+ ions, as reported in an early published study. [23] A slow build up was then observed from pH ~3 to 9-10. At high pH values, any small changes in slope between the blank and the experiment would give a strong step as the curves (from experiment and blank) are almost parallel (Figures 3 to 6). Therefore, inflections above pH 10 are difficult to interpret and can be artefacts.

Several different trends were observed. Results for metal ions such as uranium (VI) and zirconium (IV) in the presence of heidi, have a similar behaviour to free ligand experiments. This could be suggesting that little interaction occurs between Zr(IV) or U(IV) ions and the ligand, or that the ligand depronates and subsequently binds to the metal ions, preventing any other reaction to take place.

The data set for the thorium (IV) : 2 heidi system showed an additional inflection at c.a. pH 6 that did not correspond to the free ligand or free metal results. It could be that this is evidence of polycondensation reactions due to hydrolysis, which is sensible given the previously published speciation data for thorium (IV) hydrolysis, [2] and the single crystal obtained in a previous study (Fig. 2). [8] Alternatively, the step size observed at c.a. pH 6 for thorium (IV) : 2 heidi system was compared to the results of the ligand on its own and it could correspond to the deprotonation of the nitrogen group of the ligand as the step size is similar. This could be evidence of complexation between the metal and the ligand and might help understand how the dimer previously reported (Fig. 2) under similar experimental conditions was obtained. Metal ions tend to force deprotonation of organic ligands, which would explain the observation of a step below the expected pKa_2 value.

The uranium (IV) : 2 heidi data set was very similar to the uranium (IV) ion on its own, which indicates that this system is mainly governed by the metal ion behaviour and that no significant complexation take place. The data set showed evidence that the hydrolysis reaction started at c.a. pH 1 (c.a. pH 1.5 – 2). There was no real indication of complexation between heidi and uranium (IV) across the studied pH range.

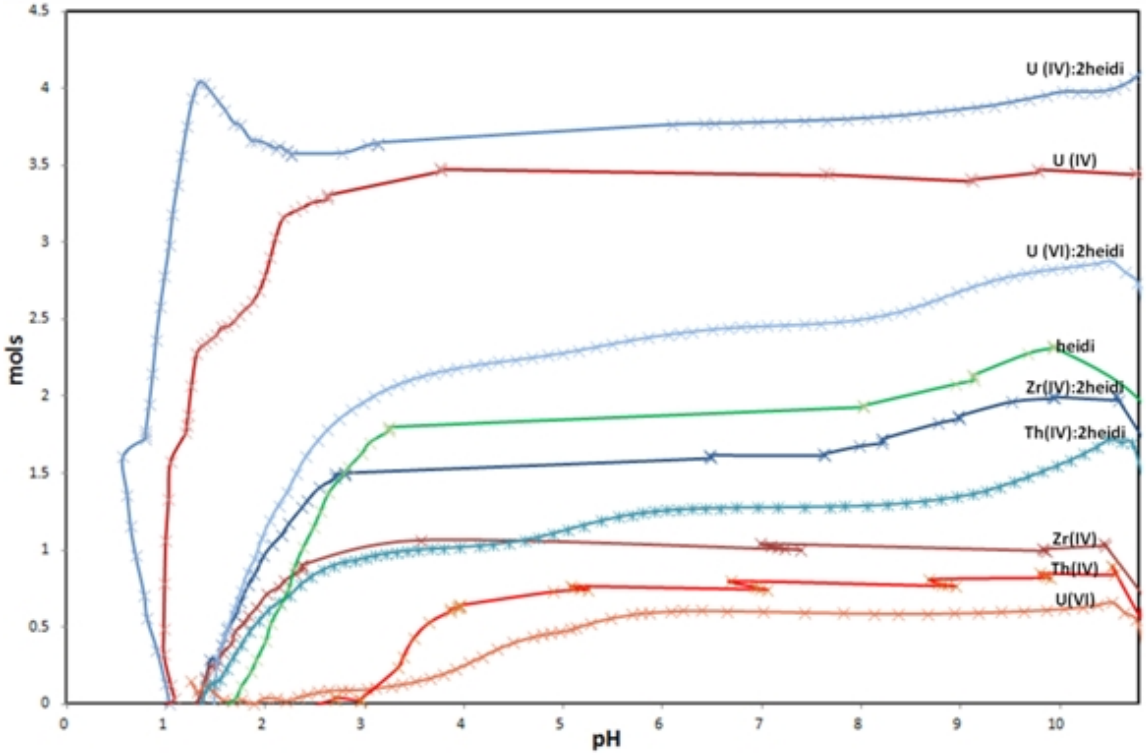

Figure 7: pH difference between blank and potentiometric data for M and 2 heidi solution at 10^{-3} M, I = 0.5 M, where M = Zr(IV), Th(IV), U(IV), U(VI).

3.2. NMR Spectroscopy

NMR spectra were measured for the previous titration experiments, so that the behaviour of heidi in the presence of diverse metal ions can be analysed and hence gain information on the speciation of these systems.

Heidi

^{1}H NMR

The NMR spectra of the heidi ligand shows three peaks: at pH 2 a singlet representing the protons next to the carboxylate groups (*Hc*) was detected at c.a. 4 ppm, and triplets representing the protons from the ethyl branch. The *Hb* protons appear at c.a. 3.8 ppm, shifted downfield from the *Ha* protons (c.a. 3.4 ppm), as they are closer to the hydroxyl group.

Following the ligand behaviour using NMR spectroscopy at different pH values, it was observed that the singlet shifted from a chemical shift at c.a. 4 ppm (at pH 2) to c.a. 3.2 ppm (pH 13). Triplets from the ethyl group hydrogens appeared at around 3.8 ppm (*Ha*) and 3.4 ppm for Hb at pH 2. They shifted to lower values when the pH increased from 2 to 13.

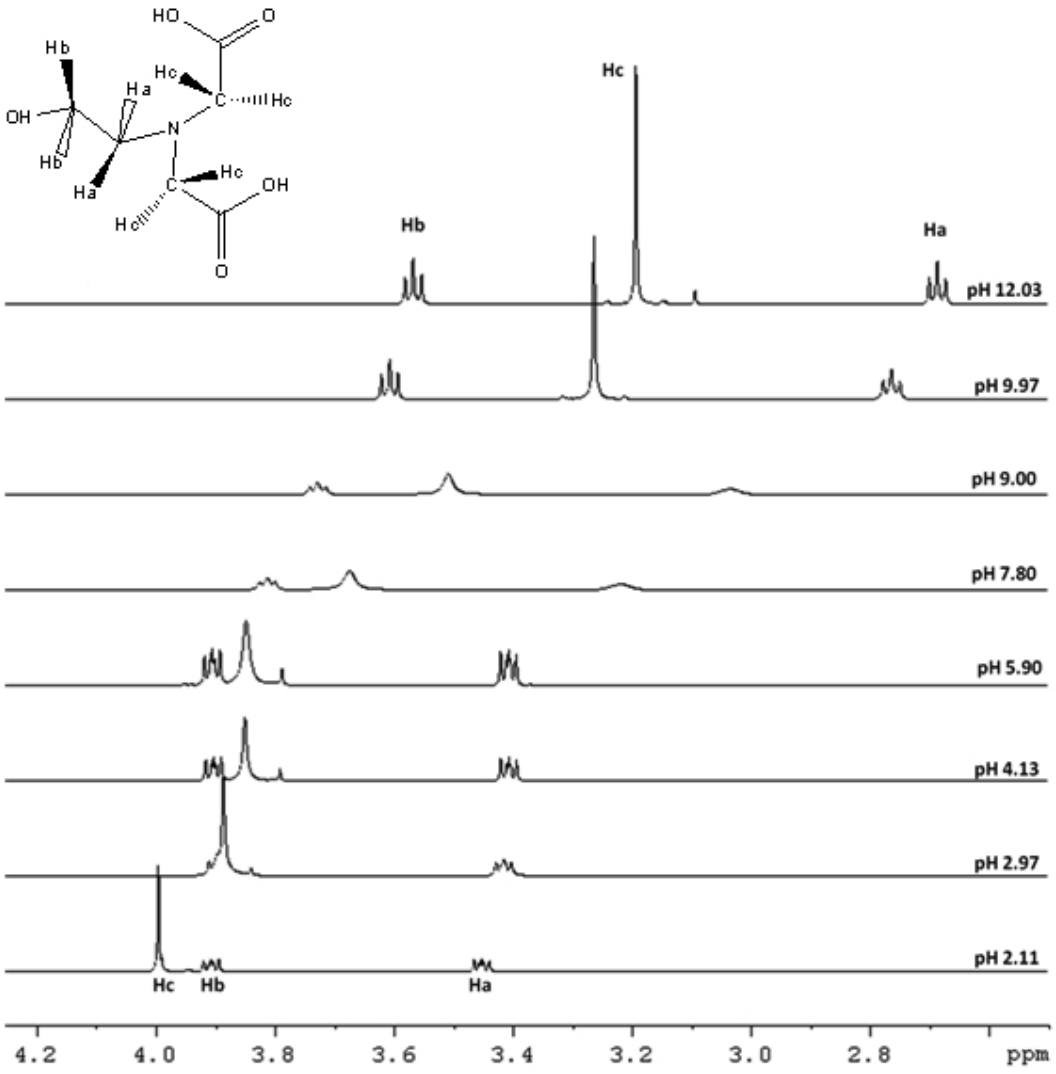

Figure 8: Labelled heidi (above) and ^{1}H NMR data for heidi in D_2O from pH 2 to 12.

Protonation/deprotononation of the ligand may be the cause of the observed broadening of the peaks. As the pH values increase, the deprotonation of the ligand gradually shifts the NMR signals towards upfield values.

^{13}C NMR

In order to assign the peaks in the ^{13}C NMR spectra of heidi, previous results obtained with 3-hydroxybutyric acid were used as a reference. [24] The carbon atoms attached to the carboxylate groups, C_1, were observed at δ = 169.53 ppm at pH 2.11, and gradually shifted to δ = 179.85 ppm at pH 12.03. The same trend was observed with the other different carbon environments present in heidi. Throughout the whole pH range studied, C_2 had δ values between 56.34 – 59.00 ppm, C_3 between 56.97 – 58.92 ppm and C_4 between 55.5 to 56.42 ppm. Figure 9 shows all of the ^{13}C NMR spectra recorded for heidi.

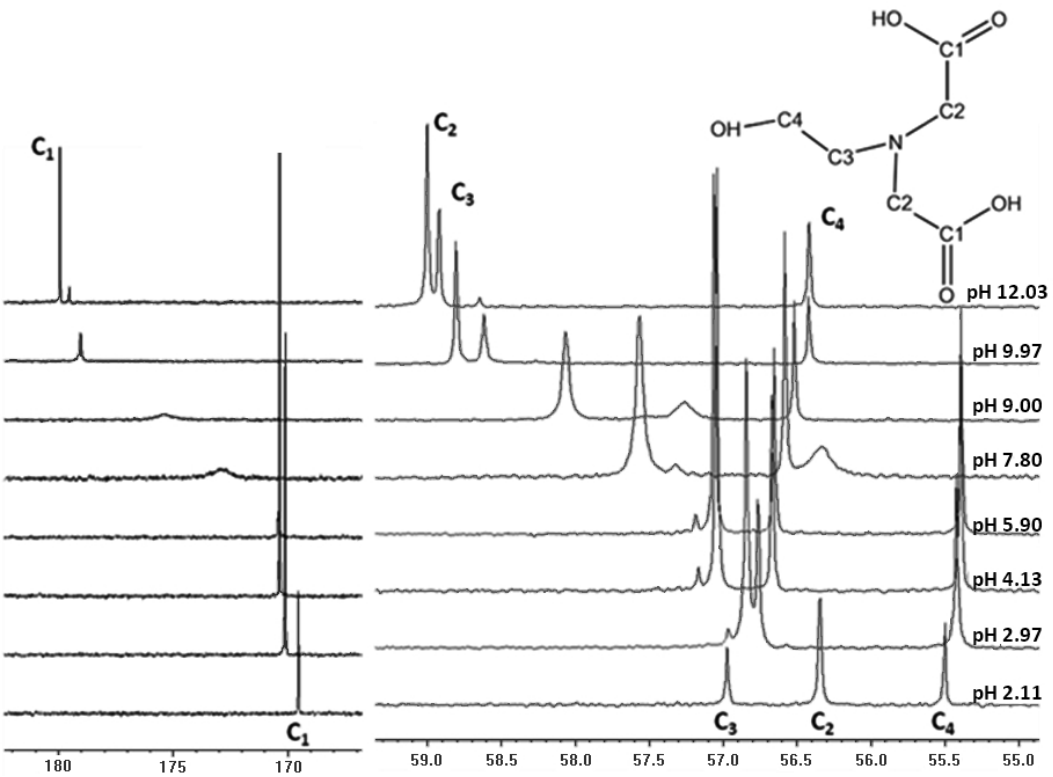

Figure 9: ^{13}C NMR data for heidi (1M, I = 0.5 M) in D_2O from pH 2 to 12.

At pH values 8 – 9, some of the ^{13}C NMR signals were broad, as was observed for ^{1}H NMR results. Protonation/deprotononation of the ligand may be the cause of the observed broadening and decrease in the intensity of the peaks.

Figure 10 shows the variation in chemical shift of the carbon atom from the carboxylate groups, C_1, with pH (Fig. 9). The Henderson Hasselbalch equation (1) was used to calculate the amount of each form of the carboxylate acid present at any point during the fitting.

$$pH = pKa + [\log_{10} \frac{[A^-]}{[HA]}] \qquad (1)$$

Where HA is the protonated acid form, and, A^- is the conjugate base form of the ligand.

Assuming that the peak position is the weighted average of the species in solution, the observed chemical shift will be given by:

$$\delta_C = \frac{(\delta_A 10^{(pH-pKa)} + \delta_{AH})}{1+10^{(pH-pKa)}} \qquad (2)$$

Where δ_c is the observed chemical shift at a given pH, δ_{AH} is the chemical shift for the acid form of heidi and δ_A is the chemical shift of the conjugate base form of heidi.

Values of δ_{AH}, δ_A and pKa were found by a process of trial and error, where calculated values of δ_C were compared with the real chemical shifts. Figure 10 shows the experimental data and model fit with the pKa and chemical shifts values as follows: $pKa_1 = 2.1$, $pKa_2 = 8.92$ and δ_{AH2}, δ_{AH} and δ_A were 168, 170 and 179.8 ppm, respectively (Fig. 10). The pKa values for heidi obtained *via* this method are consistent with literature values, [21, 22] and with our potentiometric experimental data.

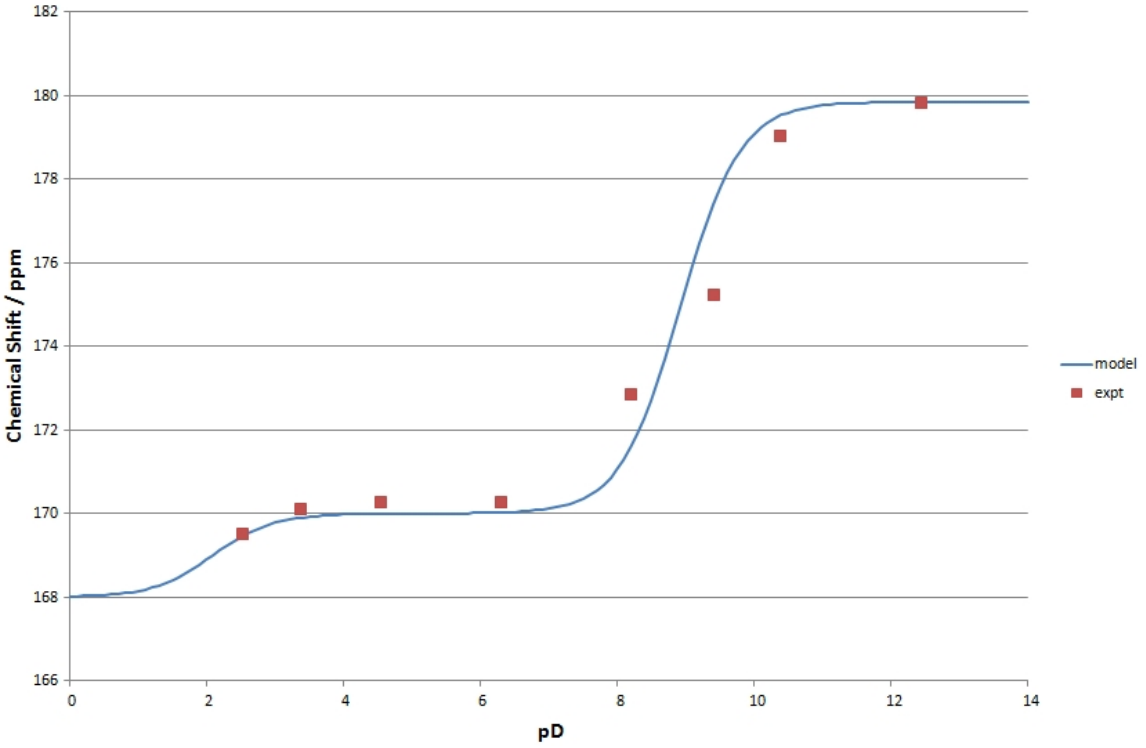

Figure 10: Change in chemical shift of C_1 (COOH) as a function of pD and the model fit for heidi.

These theoretical values obtained for δ_{AH2}, δ_{AH} and δ_{A} can be compared with the experimental data to assess if any complexation is taking place between heidi and the respective metal ions.

Zirconium (IV) : 2 heidi

^{1}H NMR

Zirconium experiments were used as a surrogate for tetravalent actinide ions to avoid radiological concerns in an attempt to model tetravalent actinide ion hydrolysis. The NMR spectra for the zirconium (IV) ion and 2 equivalents of heidi are presented in Figure 11. At low pH (c.a. 1.41), all peaks from heidi slightly shift towards shielded values. The NMR signals from *Ha* and *Hb* (closer to the hydroxyl group) were observed as overlapping triplet and doublet in this system, in comparison to a triplet in a free ligand system. It is postulated that the triplet signals comes from the neighbouring alkyl protons, the doublet is a result of the protonation of the nitrogen group (in the case of tha *Ha* protons) or the signal from a bridging hydroxyl group (in the case of the *Hb* protons).

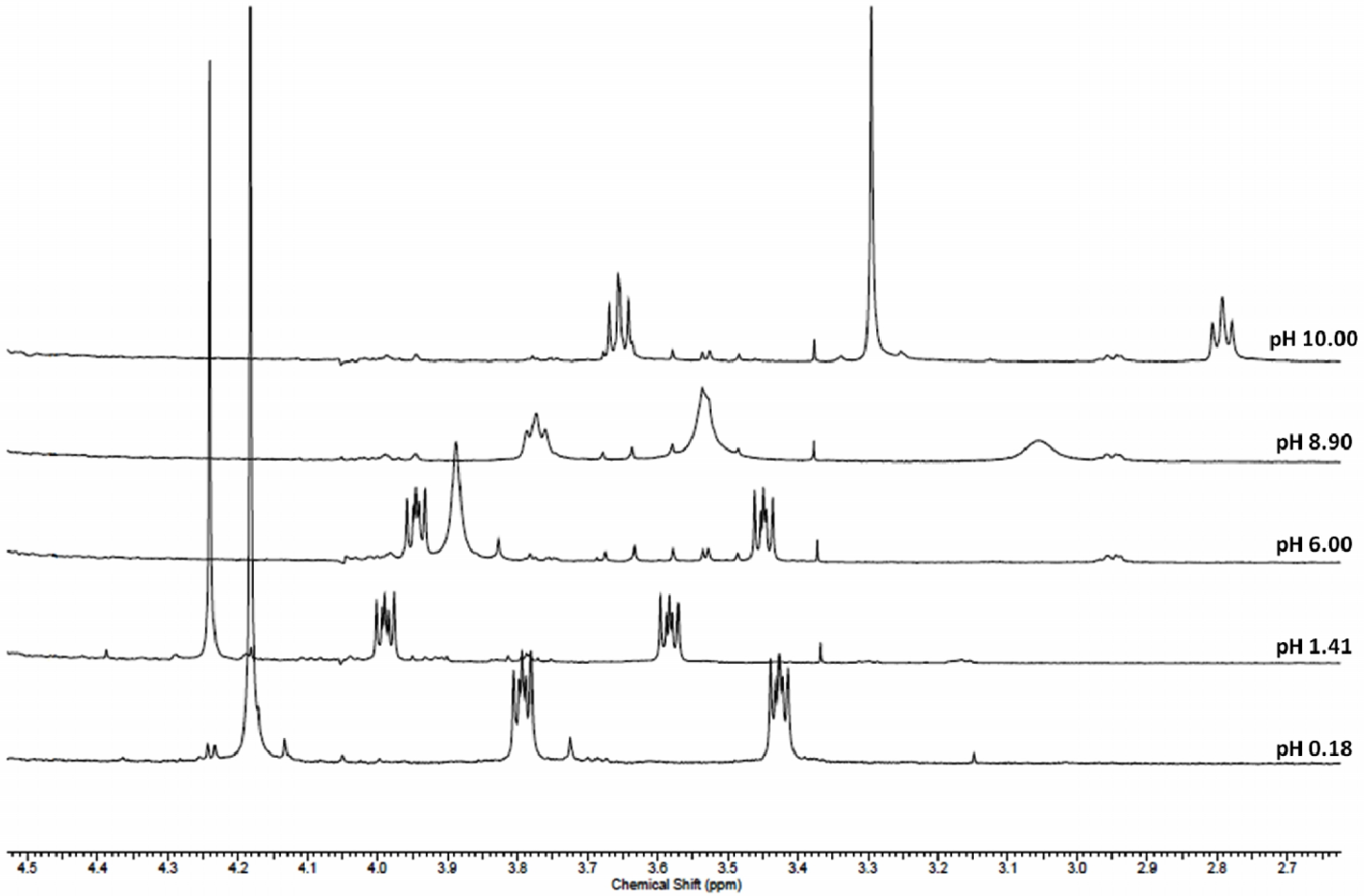

Figure 11: ^{1}H NMR in D_2O for Zr (IV) : heidi at a 1:2 ratio, at 10^{-3} M and I = 0.5 M (NaCl).

At lower pH values (0.18- 6), the chemical shifts observed for the zirconium (IV) ion : 2 heidi system are slightly higher than the chemical shifts observed in a free ligand system. The presence of an electropositive ion such as zirconium (IV) is likely to cause such a shift. However, this observation is not sufficient to confirm absolutely if a complexation interaction between the metal ions and the ligand take place.

At higher pH, free ligand signals were observed. Hydrolysis seems to prevail over heidi complexation when pH is around 10. The ligand is removed from the coordination of zirconium by hydrolysis, possibly by an olation or oxolation mechanism.

^{13}C NMR

^{13}C NMR spectra were recorded in order to study the complexation between the zirconium (IV) ions and the ligand. Similar chemical shifts were observed for the free ligand and the zirconium (IV) : 2 heidi systems (Table 2). These results, as well as the potentiometric data (Fig. 7), show that no quantitative complexation exists between zirconium (IV) ions and the ligand under the experimental conditions. The $[Zr(heidi)_2].9H_2O$ monomer observed in the solid state was obtained at low pH values (below 1) after a month. The strong acidic experimental conditions have probably limited zirconium (IV) ion hydrolysis, and so the metal ions were available to bind to the ligand. Hence, $[Zr(heidi)_2].9H_2O$ species observed in the solid state may not be relevant to aqueous studies and decommissioning issues.

pH	*Zr(IV)*	*heidi*
1.41 – 2.1	168.87	169.53
3.89 - 4.13	-	170.3
5.9 – 6.6	170.51	170.3
7.8 - 8	-	172.87
9 – 9.3	175.63	175.26
10 – 10.35	179.17	179.06
12	179.99	179.85

Table 2: ^{13}C chemical shifts (ppm) from the carbons belonging to the carboxylate groups (C_1) for heidi on its own and Zr (IV): 2 heidi

Thorium (IV) : 2 heidi

^{1}H NMR

Thorium was used as a model for studying hydrolysis in tetravalent actinides. In aqueous media, it is only present as the thorium (IV) ion, which is helpful since it avoids redox reactions.

As for the zirconium (IV) ion, the thorium (IV) system (Fig. 12), is very pH dependent. The signals are broad which is likely due to ligand exchange and not to paramagnetic behaviour. At pH 2, the *Hc* protons show no shift; the *Hb* signal was observed as a broad band between 3.8 to 3.6 ppm. However, the *Ha* protons seem more influenced, as their signal shifted from c.a. 3.4 ppm to c.a. 2.9 ppm in the presence of the thorium (IV) ion. At low pH, the nitrogen atom of heidi can interact with protons, which could shield the *Ha* proton environment and may explain the observed shift.

Signals from the *Hc* protons shift towards lower δ values across the studied pH range, following the trend of the free ligand. Their exact assignment was difficult between pH 2 and 10, as new features appeared in the ^{1}H NMR spectra (Figure 12).

At a given pH, protons from the ligand shifted to more shielded values, which may indicate some complexation between the thorium (IV) metal ions and heidi. Free ligand was also observed at high pH values, indicating a return to hydrolysis.

The NMR spectra reported here show that spectra recorded with thorium are very complex; a complicated pattern of multiplets was observed between pH 4 and 10. Hydrolysis strongly depends on the Z^2/r ratio so a large ionic radius, such as that a smaller metallic ion such as zirconium (IV) (r_{Zr}^{4+} = 98 pm [25]) is more reactive to hydrolysis than thorium (IV) ions (8 coordinate, r_{Th}^{4+} = 119 pm [25]). However, ^{1}H NMR for thorium (IV) ions and heidi seem to show a more complex mixture of species in solution than zirconium (IV) in the presence of the ligand. It is postulated that the broader peaks observed in the thorium (IV) - heidi system were due to quick exchange between the ligand molecules, within the metal ion inner sphere, with heidi molecules from the bulk solution.

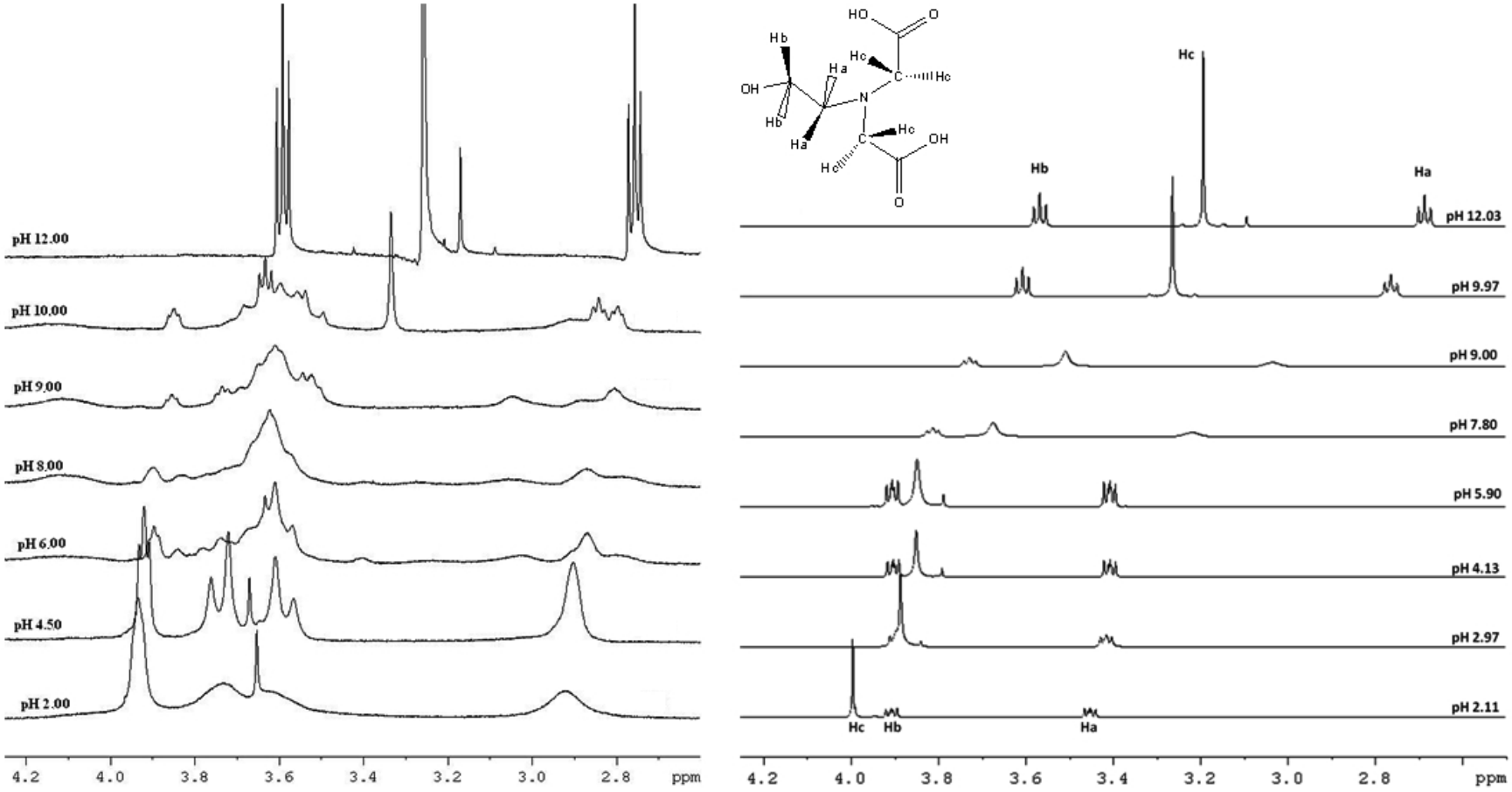

Figure 12: ^{1}H NMR of Th (IV) : heidi at a 1:2 ratio (left) and heidi (right) at 10^{-3} M, I = 0.5 M.

^{13}C NMR

The thorium (IV) : 2 heidi system was also studied using ^{13}C NMR spectroscopy. Signals recorded for the thorium (IV) ions in the presence of heidi are significantly higher than the chemical shifts observed in a free ligand system in the pH range of 1.4-9.3. Above these pH values (10-12), the thorium (IV) : 2 heidi system ^{13}C NMR signals were similar to the free ligand data. This is in accordance to the results observed with ^{1}H NMR spectroscopy. It is however difficult to assess the exact speciation of the thorium (IV) : 2 heidi system in these conditions. It was not possible to prove the existence of the $[Th_2(heidi)_4]^{4-}$ dimer in solution, even when combining solid state, potentiometric and NMR results.

pH	*Th(IV)*	*heidi*
1.41 – 2.1	181.64	169.53
3.89 - 4.13	181.78	170.30
5.9 – 6.6	182.22	170.30
7.8 - 8	182.30	172.87
9 – 9.3	182.70	175.26
10 – 10.35	182.81	179.06
12	179.95	179.85

Table 3: ^{13}C chemical shifts (ppm) from the carbons belonging to the carboxylate groups (C_1) for heidi on its own and Th (IV) : 2 heidi

Uranium (IV) : 2 heidi

The NMR spectra recorded for the uranium (IV) : heidi system are reported in Figure 13. The signals observed were broad and unresolved below pH 4. An intense peak was observed at c.a. 4.7 ppm corresponding to H_2O, as the ligand is hygroscopic. The spectrum at pH 2.57 ppm showed an intense broad band around 4.7 ppm. At pH 4, the spectrum looked similar to a free ligand spectrum at pH 8 (Fig. 8). From pH 4, the profile of the NMR results for uranium (IV) ions in the presence of

2 equivalents of heidi were similar to the data observed for the free ligand. At a pH value of 7, the NMR profile resembles that of a free ligand data set. The chemical shift of *Hc* for heidi in the presence of uranium (IV) ions was observed at 3.90 ppm, whilst the *Hc* signal was observed at 3.67 ppm for the free ligand under similar experimental conditions (Table 4). It was deduced that no quantitative complexation between uranium (IV) ions and heidi was observed. The ligand seemed to be removed from the metal inner sphere from c.a. pH 4.

Free ligand signals were observed around pH 6 for zirconium (IV) ions and around pH 10 for thorium (IV) ions. Therefore, in the presence of heidi, uranium (IV) is more susceptible to hydrolysis than either zirconium (IV) or thorium (IV) ions.

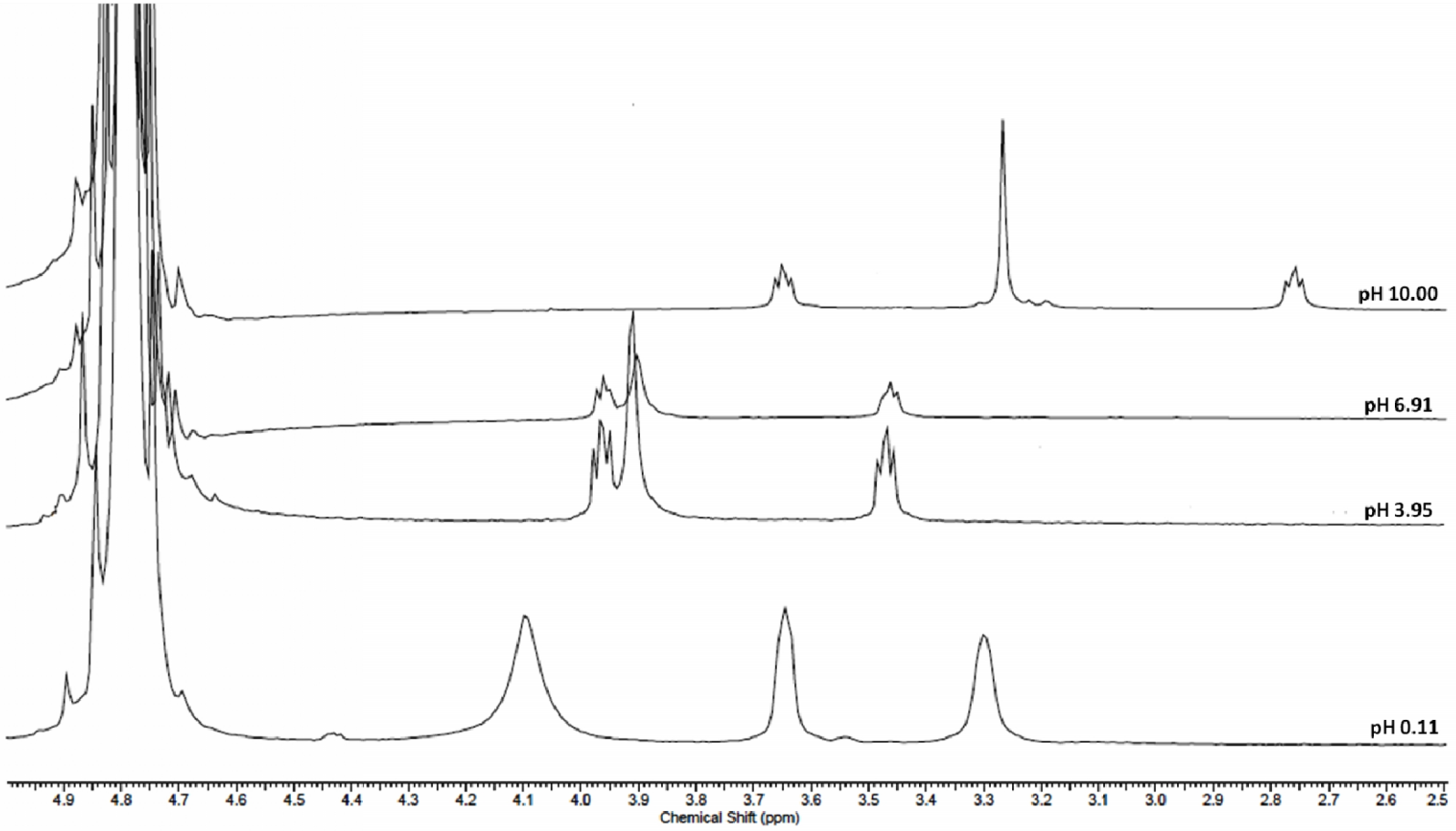

Figure 13: ^{1}H NMR of U (IV) : heidi at a 1:2 ratio at 10^{-3} M, I = 0.5 M.

Uranium (VI) : 2 heidi

When uranyl nitrate was in the presence of 2 equivalents of heidi (Fig. 14) broad peaks were observed below pH 10. Among the labelled protons, slight shifts were observed. For instance, *Hb* protons were observed at approximately 4 ppm in the presence of uranyl ions for pH values of 4, 6 and 8, compared to around 3.8 ppm in the ^{1}H NMR spectra of the free ligand. Most NMR signals are broad and unresolved. This may be due to the presence of several species coexisting in solution, as well as ligand exchange processes. Hydrolysis seems to occur above pH 9 as the NMR spectrum obtained is similar to a free ligand spectrum.

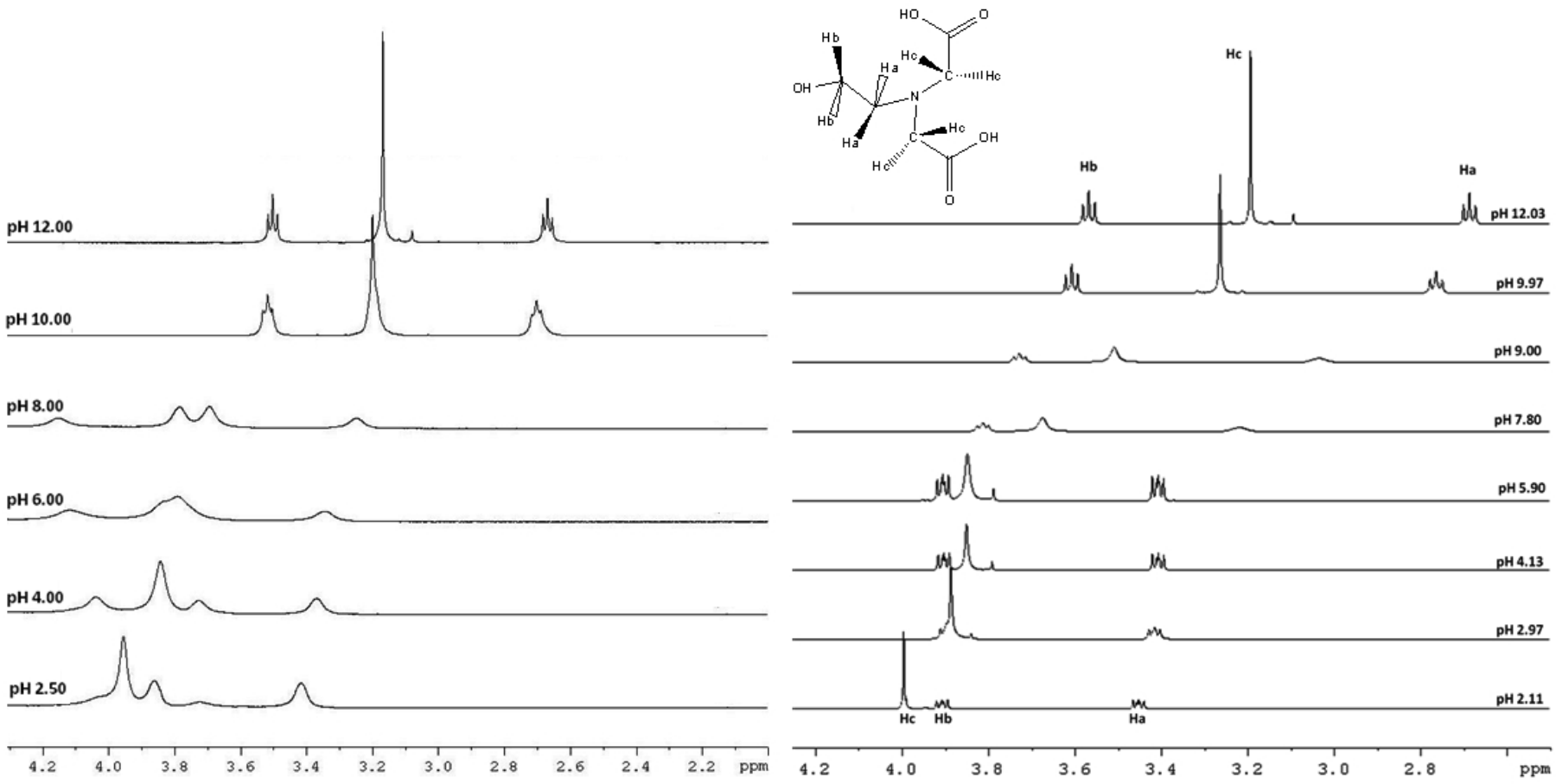

Figure 14: ^{1}H NMR of U(VI):heidi at a 1:2 ratio (left) and heidi (right) at 10^{-3} M, I = 0.5 M.

Neptunium (IV) : 2 heidi

The ^{1}H NMR spectra of the Np (IV) : 2 heidi system are presented in Figure 15. A high affinity between neptunium (IV) ions and heidi was observed as free ligand was only detected above pH 9. A broad and intense water signal was obtained at 4.7 ppm due to the experimental difficulties in keeping the Np (IV) precursor anhydrous. Nevertheless, it was still possible to observe that the ^{1}H NMR signals from heidi shifted to higher values. The spectra resemble those of the free ligand at pH values above 9.

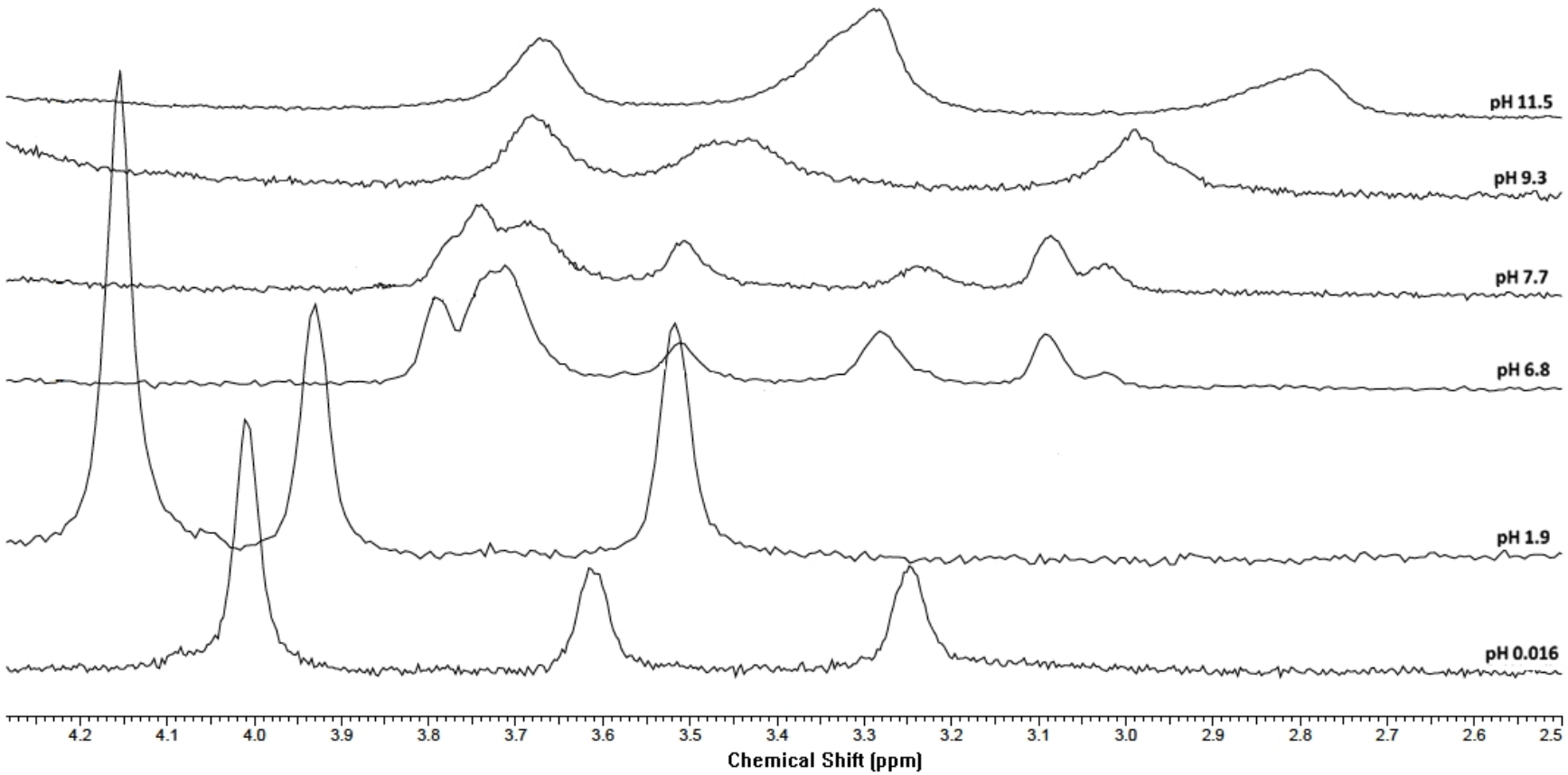

Figure 15: ^{1}H NMR of Np (IV) : heidi at a 1:2 ratio, I = 0.5 M.

Neptunium (VI) : 2 heidi

The ^{1}H NMR spectra of the Np (VI) : 2 heidi system are presented in Figures 16 and 17. A broad and intense water signal was observed at c.a 4.7 ppm, due to the experimental difficulties in keeping an anhydrous Np (VI) precursor, which masked the ^{1}H NMR signals from the neptunium (VI) : 2 heidi system. Free ligand signals were only detected around pH 12, UV-vis spectroscopy was also used to study the behaviour of neptunium (VI) metal ions in the presence of heidi and is presented subsequently in this paper.

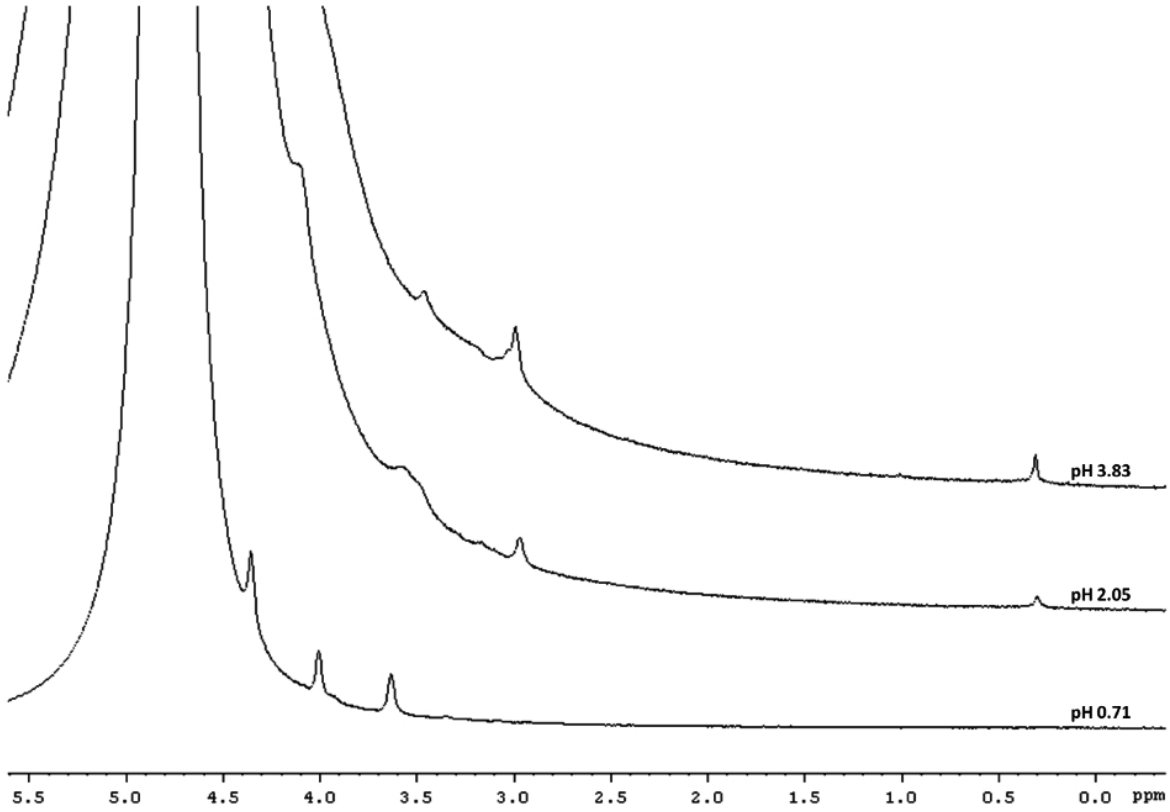

Figure 16: ^{1}H NMR of Np (VI) : heidi at a 1:2 ratio, for pH values below 4, I = 0.5 M.

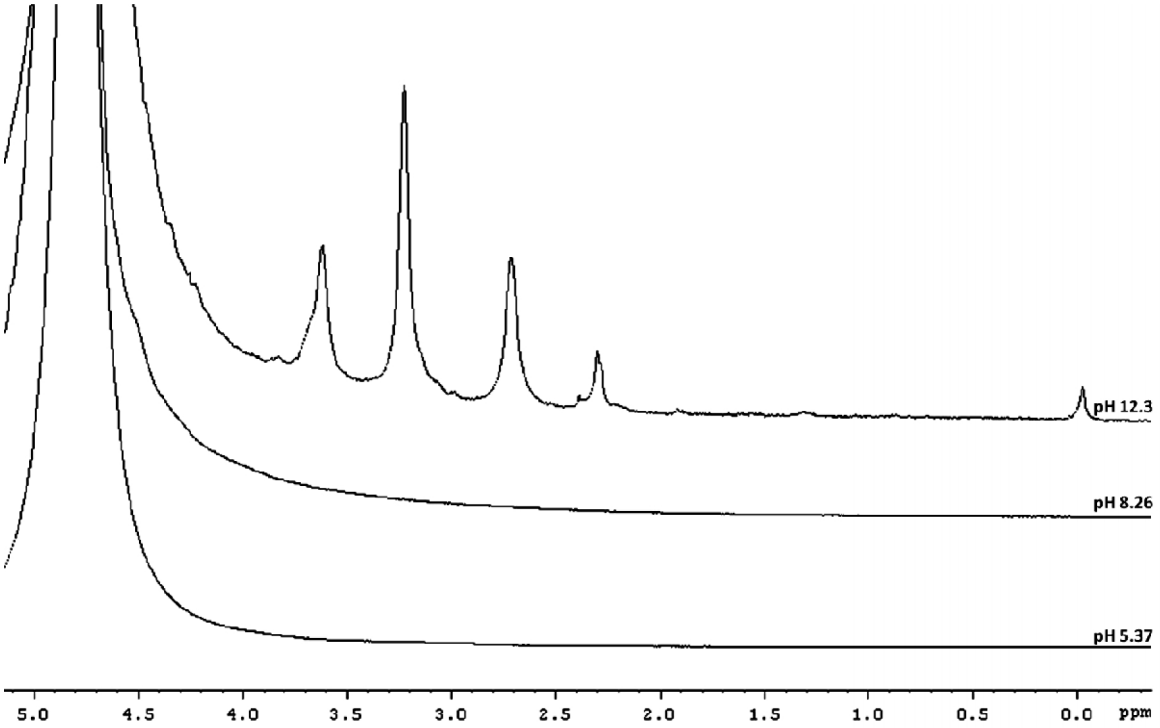

Figure 17: ^{1}H NMR of Np (VI) : heidi at a 1:2 ratio for pH values above 4, I = 0.5 M.

General ^{1}H and ^{13}C NMR data

A list of heidi NMR shifts from the *Hc* protons are reported in Table 4 for different tetravalent metal ion systems. Specific hydrolysis species were difficult to identify *via* NMR spectroscopy. ^{1}H NMR data sets did not allow the identification of an exact speciation; however they were able to provide qualitative information about the complexation of the metal ions and the ligand at a given pH. Some metal ions, in the presence of the ligand such as thorium (IV) and neptunium (IV), showed complex signals and greater chemical shifts in comparison with free heidi results. This indicates a possible metal – ligand complexation. Other metal ions, such as uranium (IV) and zirconium (IV), showed NMR signals profiles similar to a free ligand system; it seems that in these cases, the interaction between the metal ions and the ligand was weaker. The presence of free ligand was also detected in all systems above a pH value that depended on the metal ions. ^{13}C NMR experiments (Table 5) reinforce this observation. As discussed previously, signals recorded for the thorium (IV) ions in the presence of heidi are significantly higher than the chemical shifts observed in a free ligand system in the pH range of 1.4-9.3. On the other hand, the chemical shifts observed for heidi in the presence of zirconium (IV) ions were similar to the free ligand signals.

pH	*Zr(IV)*	*Th(IV)*	*U(IV)*	*Np(IV)*	*Heidi*
0.0 – 1.9	4.18		4.1	4.01	-
2	4.08	3.93		4.15	3.99
4	3.97	3.76 - 3.56	3.91		3.85
6	3.89				3.85
7			3.90		3.67
9	3.53				3.51
10	3.3	3.33	3.26		3.26
12	3.24	3.26	3.23	3.29	3.19

Table 4: ^{1}H chemical shifts (ppm) from the protons of the carboxylate groups (previously labelled *Hc*) in heidi in the presence of tetravalent elements (Zr, Th, U, Np)

pH	*Zr(IV)*	*Th(IV)*	*Heidi*
1.41 – 2.1	168.87	181.64	169.53
3.89 - 4.13	-	181.78	170.3
5.9 – 6.6	170.51	182.22	170.3
7.8 - 8	-	182.30	172.87
9 – 9.3	175.63	182.70	175.26
10 – 10.35	179.17	182.81	179.06
12	179.99	179.95	179.85

Table 5: ^{13}C chemical shifts (ppm) from the carbon atoms neighbouring the carboxylate groups (previously labelled C_1) within heidi and in presence of zirconium (IV) and thorium (IV) ions

3.3. UV-vis-nIR Spectroscopy

Uranium (VI) : 2 heidi

The uranyl ion has been previously and thoroughly studied in aqueous media by different spectroscopic methods (UV-Vis, Raman, NMR). [26] Consequently, several aquo species have been identified, such as UO_2^{2+} ($\varepsilon_{421.8}$ = 101 ± 0.21 $dm^3.mol^{-1}.cm^{-1}$), $U(O_2)_2(OH)_2^{2+}$ ($\varepsilon_{413.8}$ = 9.7 ± 0.21 $dm^3.mol^{-1}.cm^{-1}$) and $U(O_2)_3(OH)_5^{+}$ (ε_{429} = 474 ± 71 $dm^3.mol^{-1}.cm^{-1}$). [27] The data reported in Figure 18 for the bare uranyl ion in aqueous solution were compared to the system consisting of uranyl in the presence of 2 equivalents of heidi at pH values 2-4; spectra for higher pH values are reported in Figure 19.

The spectrum of uranyl ion on its own has resolved peaks at c.a. 420 nm, which correspond to the uranyl ion fingerprint. [28] Absorption values for free uranyl ion and for uranyl in the presence of heidi were similar below pH 4. For instance, for the free uranyl ion experiment, an absorption of 0.075 at 414 nm was recorded for a 5 x 10^{-3} M solution at pH 2; A = 0.085 at 416 nm was observed when uranyl (VI) was mixed with two equivalents of heidi. The following respective values were obtained at pH 4: A = 0.212 at 421 nm and A = 0.208 at 421nm. Values above pH 4 are reported and discussed below in Figure 19. A gradual shift observed in the band position with increasing pH was similar whether uranium (VI) was on its own or in the presence of heidi.

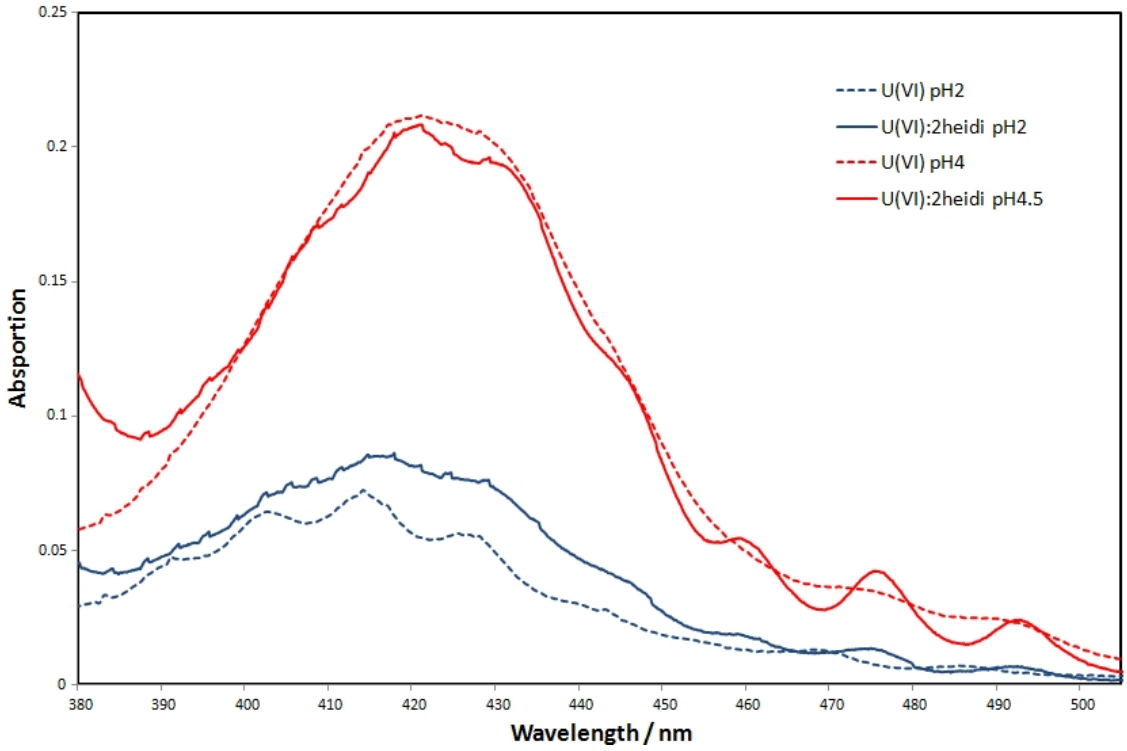

Figure 18: Comparison of UV-vis spectra of U (VI) and U (VI) : heidi at the 1:2 ratio, at 10^{-3} M, pH= 2 and 4, I = 0.5 M.

Figure 19 illustrates the experimental data obtained from pH 6 to 12 for the bare uranyl ion and a system containing uranyl in the presence of 2 equivalents of heidi. A significant broad band was observed at approximately 420 nm, which is characteristic of uranyl bare ions. From pH 6 onwards, the absorption profile coincided with spectra obtained for uranyl (VI) ion in the presence of heidi; the peaks observed were very broad and intense. The absorption values of free uranyl ion are significantly higher than values encountered in the presence of heidi (A = 0.46 at 429 nm for uranyl in the presence of heidi; A = 1 .88 at 423 nm for free uranyl ions at pH 8).

In the presence of the ligand, new features appeared in the spectra at 460, 475 and 492 nm. Signals at 460 and 475 nm were more prominent at lower pH values. As the pH was increased, the peaks broadened and gradually shifted to higher wavelength values (main band at 416 nm at pH 2 and 430 nm at pH 12). The overall absorption also increased with increasing pH. At pH 2, the 416 nm band had an absorption maximum of A = 0.085; its value increased to A = 1.4 at pH 12.

Experiments at lower and higher pH showed a difference in the absorption values which may indicate complexation between the uranyl ions and heidi.

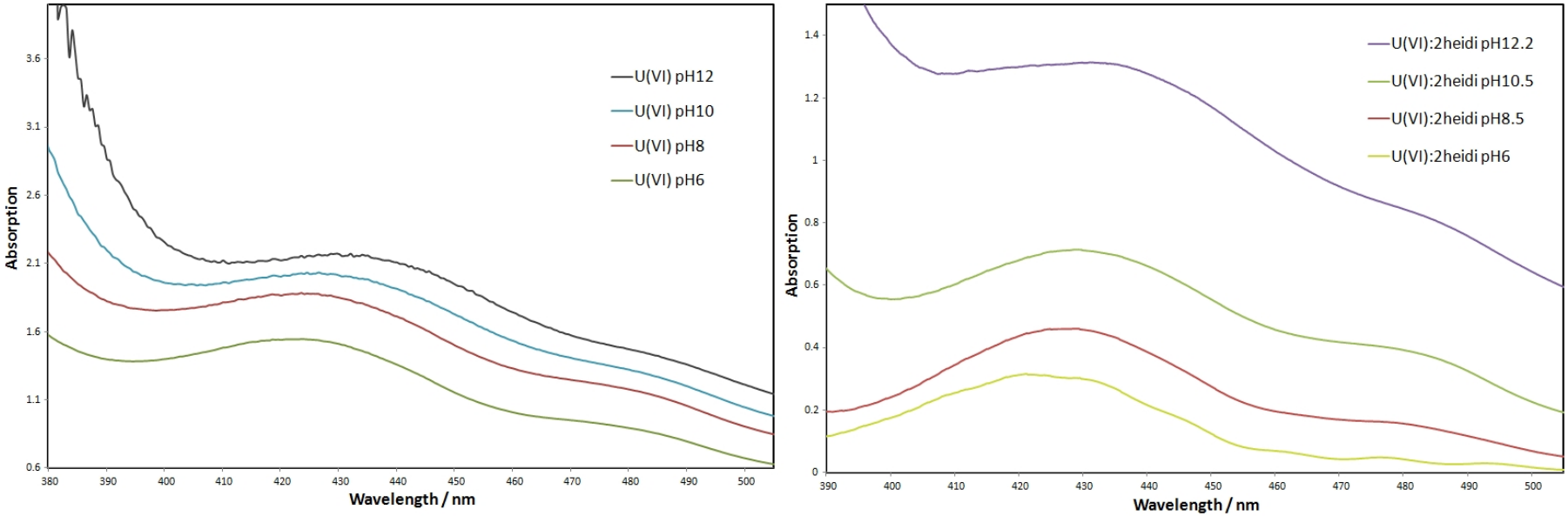

Figure 19: Comparison of UV-vis spectra of U (VI) and U (VI):heidi at the 1:2 ratio, 10^{-3} M, pH > 6, I = 0.5 M.

NMR and UV-vis results seem to show some complexation between the ligand and U(VI) is reducing the hydrolysis of U(VI), especially for pH values below 6. From pH 10 onwards, the formation of oxohydroxo uranium species was observed. The UV-vis results show that heidi might be reducing the hydrolysis as absorptions observed in the presence of the ligand were significantly lower than those observed with free U(VI). The uranyl trans dioxo geometry, does not seem to prevent complexation. Therefore, the ligand must bind through the equatorial plane of U(VI).

Neptunyl (VI) : 2 heidi

Figure 20 illustrates the titration of neptunyl (VI) in the presence of 2 equivalents of heidi followed by nIR spectroscopy. Neptunium was oxidised to the +VI state from its +V state by $HClO_4$. The sample was then dried and redissolved in HNO_3 (1 M). However, under these conditions the reduction of neptunyl (VI) to neptunyl (V) was observed which has also been reported previously. [29] In 1M HNO_3, the wavelength at 1230 nm (ε = 43 $dm^3.mol^{-1}.cm^{-1}$) is characteristic of a neptunyl (VI) species; the band at 980 nm (ε = 365 $dm^3.mol^{-1}.cm^{-1}$) is characteristic of neptunyl (V) species. [28] It was then established, using the Beer-Lambert law, that 88.05 % of neptunium was present as neptunyl (VI) and 11.95 % as neptunyl (V).

Two equivalents of heidi were then introduced to the solution, which resulted in a decrease in the absorption profile for both the neptunyl (V) and neptunyl (VI) species at pH 0.71. Above this value, no neptunyl (VI) species were detected. The position of the 980 nm peak seemed to shift; although, the recorded values were at the edge of the nIR window, which could be affecting the data accuracy. Heidi does not seem to stabilise neptunium in its + VI oxidation state in a 1M HNO_3 solution.

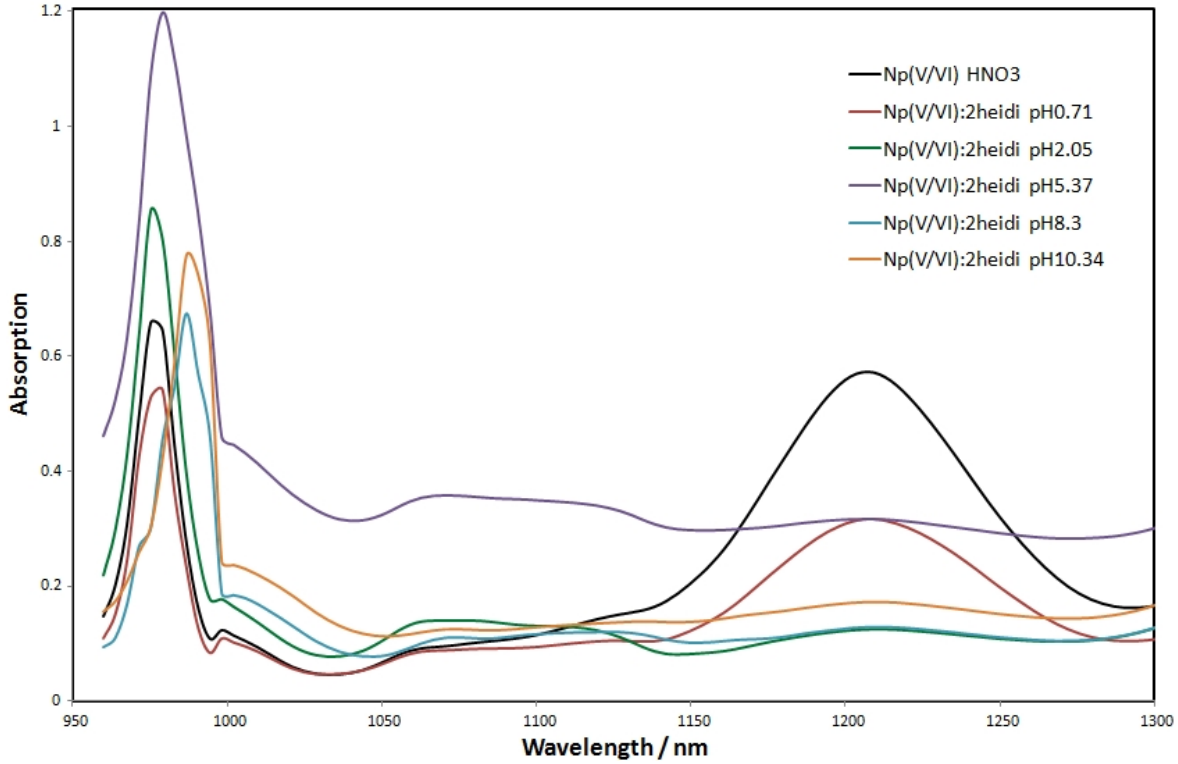

Figure 20: Solution nIR spectra of Np(V/VI) and Np(V/VI): heidi, at a 1:2 ratio, along a 0.7-10 pH range, I = 0.5 M.

Uranium (IV) : 2 heidi

In order to study the solution chemistry of this system, UV-vis-nIR spectroscopy was also used in conjunction with the NMR experiments. This technique allowed us to verify the metal oxidation state and to characterise the chemical behaviour in solution, as the uranium and neptunium ions can easily undergo redox reactions. Figure 21 shows the results for uranium (IV) for wavelengths between 300 and 700 nm (visible region) and Figure 22 shows the spectra for wavelengths between 800 and 1100 nm (near IR region). The spectra reported are representative of all the results observed across the whole pH range.

Two different behaviours were observed in the spectra, *i.e* below pH 4 and above pH 4. The pH 0.11 spectrum was recorded when heidi was added to the metal ion, before any addition of NaOH. At this point, the metal ion does not seem to complex with the ligand as the spectrum was identical to free uranium (IV) ions in a 1 M HCl solution. However, the spectrum observed after the addition of NaOH, at pH 0.75 and 2.5, changed drastically, which could be due to some complexation between the metal ion and the ligand.

From pH 4 onwards, the spectrum resembles that of the free uranium (IV) ion, but differs by the broadening of the peaks, as well as a decrease in intensity, which is probably due to hydrolysis. The NMR data also follows this trend above pH 4, and so the ligand does not seem to be able to complex with uranium (IV) ion significantly. The reported formation constant also suggests low affinity between the uranium (IV) ion and heidi. [22]

Tetravalent actinides have a very low solubility in water, [30] and tend to precipitate as oxides and oxy-hydroxide solids. Their solubility quickly decreases with increasing pH. The fact that UV-vis spectra were recorded at high pH values is evidence of complexation between heidi and the uranium (IV) ion. This may be suggesting that the ligand deprotonates the metal ions and binds to them, preventing hydrolysis to occur, until the ligand molecules coordinated to the metal ions are exchanged by HO- ions, due to the increase of their concentration during titration. This is inconsistent with the potentiometric and ^{1}H NMR data reported previously in Figures 7 and 13 respectively. It is noted that it is difficult to assess the exact origin of the hydrogen atoms in potentiometric data and the interaction between U(IV) and heidi could be weak and therefore not promote significant chemical shift during ^{1}H NMR experiments. Unfortunately, ^{13}C NMR experiments were inconclusive and cannot be used to explain this discrepancy.

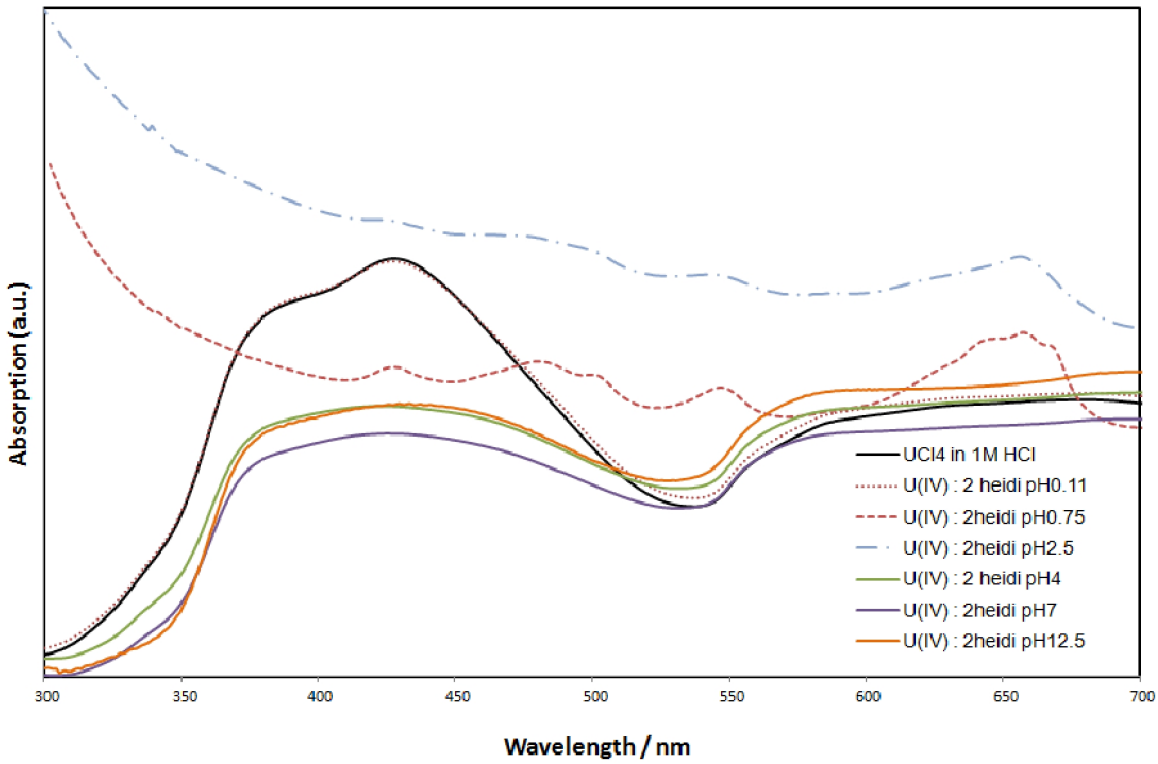

Figure 21: UV-vis spectra of U(IV) and U(IV) : 2 heidi at 10^{-3} M, I = 0.5 M.

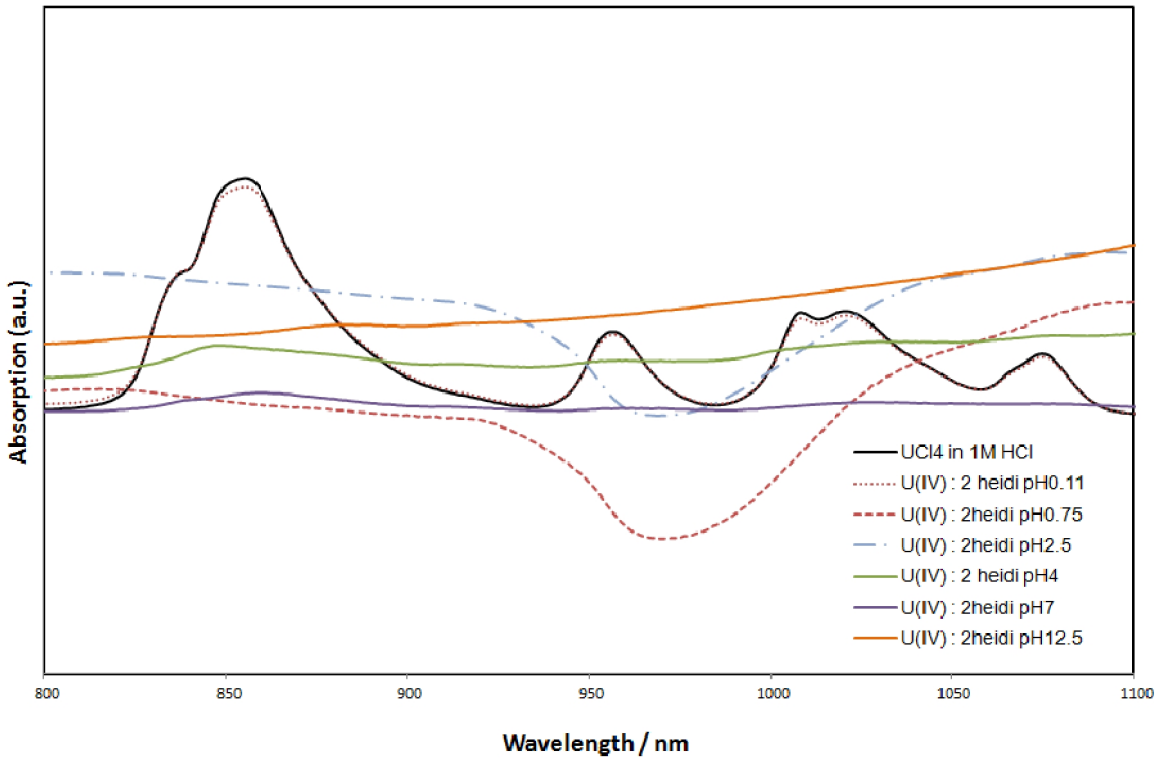

Figure 22: Near IR spectra of free U (IV) metal ions in aqueous solution and U (IV) : 2 heidi at10^{-3} M, I = 0.5 M.

Neptunium (IV) : 2 heidi

The same experiment was performed with neptunium (IV) and two equivalents of heidi, and the results can be seen in Figure 23. The Np(IV) spectrum is mainly characterised by two peaks, a broad multiplet at 723 nm and a sharp signal at 960 nm (ε = 147 and 215 $dm^3.mol^{-1}.cm^{-1}$ respectively [31]). As soon as the ligand was added to the solution, new peaks were observed at 775 and 967 nm, the broad 820 nm shifted to 832 nm, and this peak gradually fades away, and it was not observed around pH 9. Some shifting was also observed towards higher wavelengths, from 723 to 741 nm and from 960 to around 980 nm for the second peak. However, sharp signals around 980 nm are normally the fingerprint of Np(V) species in aqueous media. Eberle and Paul also reported the same phenomenon and assumed the shifting was due to complexation between Np(IV) and heidi. [32] The spectrum at pH 0.1 is similar to the spectrum at pH 9 apart from the offset along the absorption axis. Once again, UV-vis spectra were recorded at high pH values where neptunium (IV) normally precipitates as an oxide or oxy-hydroxide material. Therefore, it is postulated that complexation between the ligand and the neptunium (IV) ions was observed across the pH range, and this result is consistent with the ^{1}H NMR data reported in Figure 15.

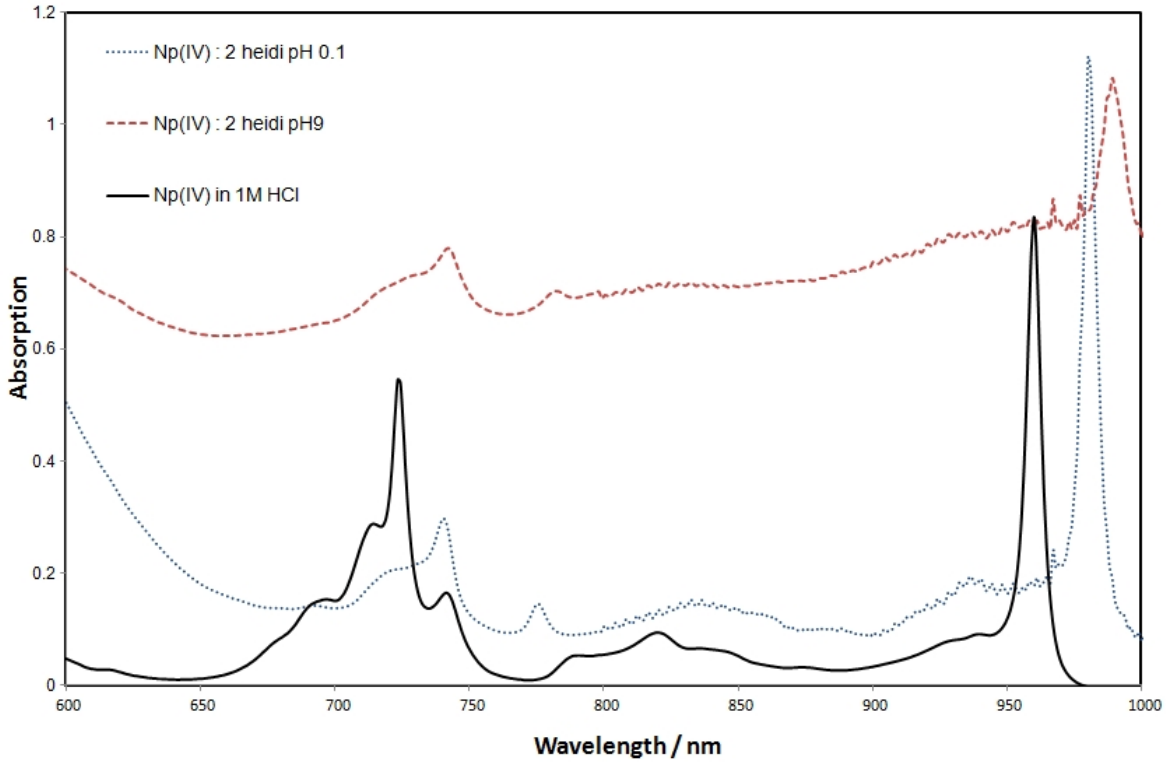

Figure 23: UV-vis-nIR data of Np (IV) and Np(IV) : 2 heidi at 10^{-3} M, I = 0.5 M.

3.4. Synthesis and Characterisation of $[UI(O\text{-}i\text{-}Pr)_2.(HO\text{-}i\text{-}Pr)_4]I$ (1)

The novel U(IV) iodo alkoxide monomer, $[UI(O\text{-}i\text{-}Pr)_2.(HO\text{-}i\text{-}Pr)_4]I$ (**1**), is shown in Figure 24. It was obtained by the dissolution of uranium metal in 2-propanol, and in the presence of iodine. The method was previously observed by Van Der Sluys *et al.* where a $U_2I_4(O\text{-}i\text{-}Pr)_4.(HO\text{-}i\text{-}Pr)_2$ dimer was reported. [33] However, the intermediate monomer compound was never characterised, even though its existence has been predicted. [33] $UI_2(O\text{-}i\text{-}Pr)_2.(HO\text{-}i\text{-}Pr)_2$ has been postulated as a possible intermediate, but the number of isopropanol molecules surrounding the uranium centre was underestimated. Only one iodide anion was observed in the inner sphere of compound **3**, although two iodides were expected.

$[UI(O\text{-}i\text{-}Pr)_2.(HO\text{-}i\text{-}Pr)_4]I$ (**1)** (Fig. 24) only exists in the solid state. The monomer loses isopropanol molecules when it is dissolved in a suitable organic solvent (*i.e.* toluene) and turns into a dimer $[U_2I_4(O\text{-}i\text{-}Pr)_4.(HO\text{-}i\text{-}Pr)_2]$ containing alkoxo bridges. [33] The reaction was shown to be reversible when isopropanol was added to a concentrated toluene solution of the compound and stored at -25 ^{o}C. This process produced lavender crystals of **1**.

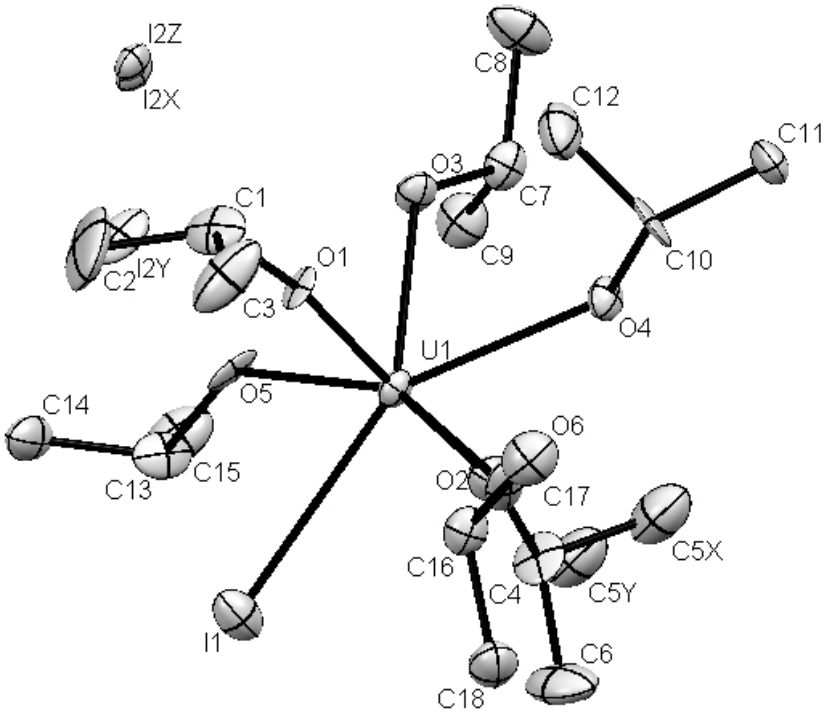

Figure 24: ORTEP representation of $[UI(O\text{-}i\text{-}Pr)_2.(HO\text{-}i\text{-}Pr)_4]I$, **(1)**, hydrogen atoms are not displayed for clarity.

The uranium centre within compound **1**, is bound to three different types of ligands: two isopropoxide groups, four isopropanol groups and one iodide ion. The representative bond lengths and angles of **1** are displayed in Tables 6 and 7 and the list of atomic coordinates is reported in Table 8. The shorter U-O distance of 2.014(13) Å, found for U(1)-O(2), corresponds to an isopropoxide group. The longer U-O distance of 2.564(10) Å was observed for U(1)-O(4), which corresponds to the binding of the uranium ion to an isopropanol group. The binding of isopropanol to one uranium ion has also been reported previously by Van Der Sluys *et al.;* both type of bonds are within expected values for U(IV) species. [33,34] The terminal iodide ligand was found at a distance of 3.110(13) Å, which is slightly longer than the previously reported value of 3.05(3) Å for $[U_2I_4(O\text{-}i\text{-}Pr)_4.(HO\text{-}i\text{-}Pr)_2]$. However, it is closer to the U-I distance within $UI_3(THF)_4$, which has been observed between 3.103(2) and 3.167(2) Å. [35] The atoms labelled I2(X), I2(Y) and I2(Z) are found 4.6 to 5 Å away to the uranium ion, and therefore there is no bond drawn between those atoms.

In comparison with the $[U_2I_4(O\text{-}i\text{-}Pr)_4.(HO\text{-}i\text{-}Pr)_2]$ complex, most of the angles of $[UI(O\text{-}i\text{-}Pr)_2.(HO\text{-}i\text{-}Pr)_2]I$ (Table 7) have similar values; however, a significant difference can be observed in the angle between isopropanol, an iodide and the uranium ion, such as O(3)-U(1)-I(1). Values of around 147 ^{o} were observed whereas the analogous angle for the

previously reported dimer was approximately 170 ^{o}. Intense regions of electronic density in several positions were observed and the refinement showed that the iodide counter ion is disordered.

Selected bond lengths	Bond lengths (Å)
U(1)-O(2)	2.014(13)
U(1)-O(1)	2.056(9)
U(1)-O(6)	2.473(11)
U(1)-O(5)	2.502(10)
U(1)-O(3)	2.526(10)
U(1)-O(4)	2.564(10)
U(1)-I(1)	3.110(13)

Table 6: Selected bond lenghts for $[UI(O\text{-}i\text{-}Pr)_2.(HO\text{-}i\text{-}Pr)_2]I$ (1)

Selected angles	Angles (°)
O(2)-U(1)-O(1)	176.8(5)
O(2)-U(1)-O(6)	92.1(5)
O(1)-U(1)-O(6)	89.5(4)
O(2)-U(1)-O(5)	87.9(4)
O(1)-U(1)-O(5)	91.9(4)
O(6)-U(1)-O(5)	155.4(4)
O(2)-U(1)-O(3)	92.2(4)
O(1)-U(1)-O(3)	84.6(4)
O(6)-U(1)-O(3)	134.8(4)
O(5)-U(1)-O(3)	69.8(4)
O(2)-U(1)-O(4)	78.3(4)
O(1)-U(1)-O(4)	99.7(4)
O(6)-U(1)-O(4)	67.6(4)
O(5)-U(1)-O(4)	136.1(4)
O(3)-U(1)-O(4)	69.4(4)
O(2)-U(1)-I(1)	91.9(4)
O(1)-U(1)-I(1)	91.2(3)
O(6)-U(1)-I(1)	77.5(3)
O(5)-U(1)-I(1)	77.9(3)
O(3)-U(1)-I(1)	147.2(3)
O(4)-U(1)-I(1)	143.1(2)
C(1)-O(1)-U(1)	170.7(11)
C(4)-O(2)-U(1)	167.3(12)
C(7)-O(3)-U(1)	126.2(9)
C(10)-O(4)-U(1)	130.3(9)
C(13)-O(5)-U(1)	134.5(9)
C(16)-O(6)-U(1)	132.8(9)

Table **7**: Representative angles for $[UI(O\text{-}i\text{-}Pr)_2.(HO\text{-}i\text{-}Pr)_2]I$ (1)

	x	y	z	U(eq)
U(1)	6958(1)	7404(1)	7561(1)	16(1)
I(1)	6114(1)	7571(1)	9769(1)	31(1)
I(2X)	12133(6)	7680(2)	6566(4)	18(1)
I(2Y)	10730(20)	8902(16)	7553(16)	31(4)
I(2Z)	12230(20)	7402(13)	6542(16)	17(1)
O(1)	8640(11)	5673(9)	7559(8)	17(2)
O(2)	5362(14)	9108(12)	7486(9)	30(3)
O(3)	8667(12)	7696(11)	6101(8)	21(2)
O(4)	6070(12)	7086(10)	6051(8)	21(2)
O(5)	8522(11)	8513(10)	8013(9)	22(2)
O(6)	5097(13)	6397(12)	7862(8)	28(3)
C(1)	9830(20)	4541(16)	7705(14)	35(4)
C(2)	10720(30)	4910(30)	8350(20)	70(8)
C(3)	9260(20)	3585(19)	8100(20)	51(6)
C(4)	4280(20)	10372(15)	7637(14)	31(4)
C(5X)	3720(30)	10810(30)	6730(20)	48(7)
C(5Y)	4020(90)	11350(80)	7320(70)	48(7)
C(6)	2890(20)	10250(20)	8398(16)	52(6)
C(7)	8228(19)	8630(16)	5391(13)	24(3)
C(8)	9380(20)	8170(20)	4479(13)	38(5)
C(9)	8110(20)	9898(17)	5771(14)	34(4)
C(10)	6370(20)	5936(17)	5492(11)	27(4)
C(11)	5980(20)	6286(18)	4510(11)	28(4)
C(12)	7960(20)	5160(20)	5399(15)	40(5)
C(13)	8330(20)	9401(16)	8779(13)	30(4)
C(14)	9560(20)	8741(19)	9350(13)	32(4)
C(15)	8430(20)	10596(18)	8390(17)	43(5)
C(16)	4945(19)	5403(16)	8485(12)	24(3)
C(17)	5060(20)	4280(18)	7866(14)	35(4)
C(18)	3470(20)	5948(19)	9184(13)	32(4)

Table 8: Atomic coordinates (x 10^4) and equivalent isotropic displacement parameters ($Å^2$x 10^3) for $[UI(O\text{-}i\text{-}Pr)_2.(HO\text{-}i\text{-}Pr)_2]I$ (1). U(eq) is defined as one third of the trace of the orthogonalised Uij tensor

Conventional precursors containing uranium (IV) and (VI) ions are sparingly soluble in toluene, and therefore no direct comparison between uranium (IV) and (VI) complexes in an organic phase was allowed. However, the intense UO_2^{2+} signal ($\varepsilon_{421.8nm}$ = 101 ± 0.21 $dm^3.mol^{-1}.cm^{-1}$) [36] was not observed for the dissolved compound **1** and the spectrum, Figure 25, was comparable to those of others uranium (IV) alkoxides. [37] This led to the conclusion that the uranium ion is tetravalent. This was also confirmed by X-ray diffraction of the $[UI(O\text{-}i\text{-}Pr)_2.(HO\text{-}i\text{-}Pr)_4]I$ compound (Fig. 24).

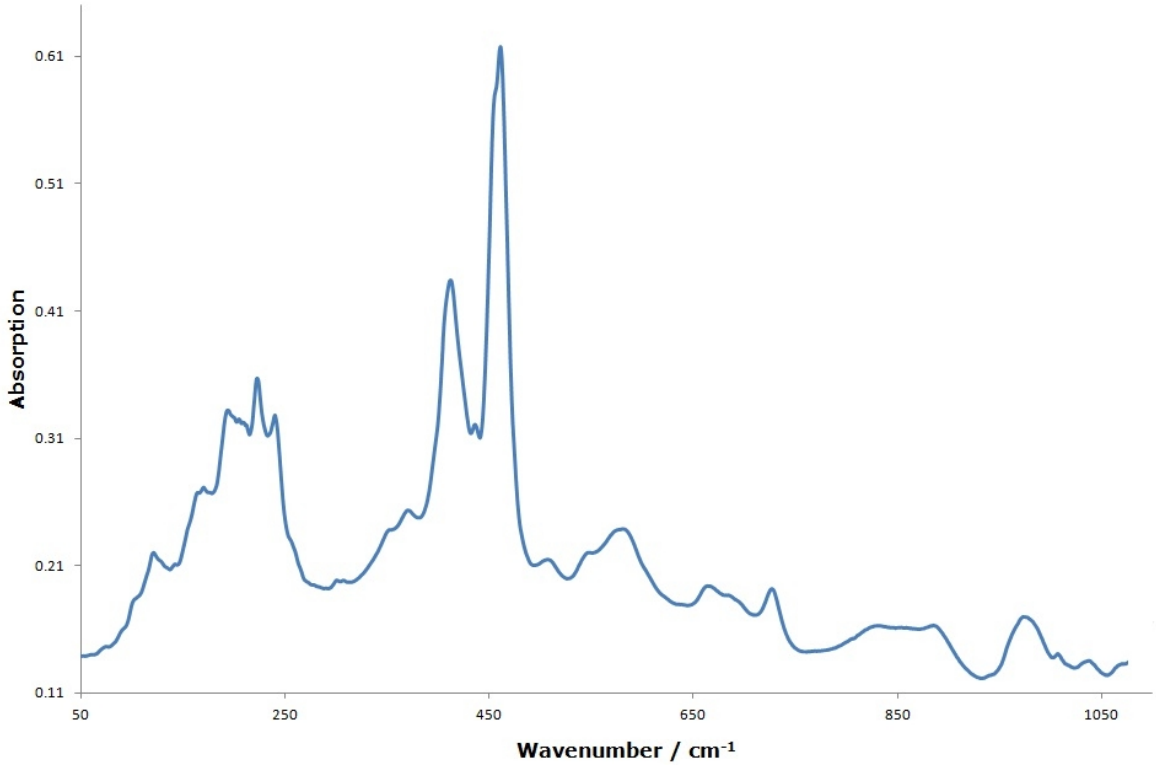

Figure 25: UV-vis spectrum of $[UI(O\text{-}i\text{-}Pr)_2.(HO\text{-}i\text{-}Pr)_2]I$, **(1)**, in toluene [$8.10^{-3}$ M].

4. CONCLUSION

The behaviour of ligands with amino-acid features, such as heidi, still need to be clearly demonstrated for transition metals and for actinide metal ions. Therefore, mechanisms of "ligand controlled hydrolysis" reactions are still under investigation.

This preliminary investigation shows that polycarboxylate ligands, such as heidi, have an effect on actinide hydrolysis. The complexation and speciation of the studied metal ions with heidi can sometimes be difficult to define precisely due to the presence of several coexisting species and fast exchange processes, as shown by the NMR studies. However, an increase in solubility was observed as it was possible to obtain analytical data of tetravalent actinides at relatively high pH values.

Spectroscopic data showed that hydrolysis seems to take place above pH 9 for most metal ions reported here, in the presence of two equivalents of heidi. However, the data was inconclusive for the U(IV) : 2 heidi system. In this case, potentiometric and ^{1}H NMR data showed no quantitative complexation between U(IV) and heidi, however, UV-vis experiments may be suggesting that some interaction occurs. It is also difficult to assess the speciation of metal ions in the presence of heidi, even when combining several analytical techniques with solid state data.

Solution chemistry results with the zirconium (IV) ion seemed similar to neptunium (IV), and previous solid state data suggested that the iron (III) ion behaved like the thorium (IV) ion in the presence of heidi.

The attempt of synthesising new precursors for controlled hydrolysis led to isolating the novel $[UI(O\text{-}i\text{-}Pr)_2.(HO\text{-}i\text{-}Pr)_2]I$ compound its structure was solved by single crystal X-ray diffraction and only exists in the solid state. In solution the monomer turns into a dimer $[U_2I_4(O\text{-}i\text{-}Pr)_4.(HO\text{-}i\text{-}Pr)_2]$.

5. FURTHER WORK

The combined solution and crystal structure information could be used to improve models of environmentally mobile actinide colloid and cluster species formation in aqueous media. In order to progress in this area, the solution chemistry results presented here could be compared to solid state studies. Additionally, in the past solution chemistry experiments have proved to be efficient in setting up solutions that allow crystallisation for systems such as those used in this study.

Different spectroscopic data should be combined with potentiometric data in order to determine equilibrium constants and the speciation of a given metal. This requirement is evident as no thermodynamic or solid state data have been reported so far with plutonium and heidi for instance. This is currently under investigation at the Institute for Transuranic Elements (ITU) in Karlsruhe, Germany. Similar polycarboxylic acids are also being investigated under the same conditions, such as 5-Me-HXTA.

The syntheses of novel actinide alkoxide are still underway. New routes should be explored. Preliminary studies of 'controlled' hydrolysis of $[UI(O\text{-}i\text{-}Pr)_2.(HO\text{-}i\text{-}Pr)_2]I$ were performed However, the results were inconclusive and no structural data was obtained. These experiments should be repeated to promote novel compounds *via* hydrolysis of this organometallic precursor.

6. REFERENCES

[1] C.F. Baes and R.E. Mesmer, *American Journal of Sciences*, 1981, **281**, 935-962.

[2] V. Neck, J.I. Kim, B.S. Seidel, C.M. Marquant, K. Dardenne, M.P. Jensen and W. Hauser, *Radiochimica Acta*, 2001, **89**, 439-446.

[3] S. Hietnan, *Acta Chemica Scandinavica*, 1956, **10**, 1531-1546.

[4] W. Runde, *Los Alamos Science*, 2000, **II**, N^{o} 26.

[5] International Atomic Energy Agency, Technical reports series, no. 441, ISSN 0074–1914, STI/DOC/010/441, ISBN 92–0–104605–7, 2006.

[6] S. A. Nikitina, T. A. Demyanova, A. V. Stepanov, A. A. Lipovskii, M. A. Nemtsova, *Journal of Radioanalitycal and Nuclear Chemistry*, 1979, **51**, 393 -399.

[7] J.P. Jolivet, ; J. Livage; M. Henry, *Metal oxide chemistry and synthesis: from solution to solid state,* 2000, John Wiley, ISBN: 0471970565.

[8] C.M. Mydlowski, *Aminopolycarboxylate complexes of d- and f- block metal ions: a synthetic and structural study*, Thesis of The University of Manchester, 2009.

[9] H. Kipton, J. Powell and E. Fenton, *Analytica Chimica Acta*, 1996, **334**, pp. 27-38.

[10] J.C. Goodwin, R.Sessoli, D. Gatteschi, W. Wernsdorfer, A.K. Powell and S.L. Heath, *Journal of the Chemical Society*, *Dalton Transactions*, 2000, **12**, 1835-1840.

[11] S.L. Heath, P.A. Jordan, I.D. Johnson, G.R. Moore, A.K. Powell, M. Helliwell, *Journal of Inorganic Biochemistry*, 1995, **59**, 785-794.

[12] J.C. Goodwin, S.J. Teat and S.L. Heath, *Angewandte Chemie International Edition*, 2004, **43**, 4037-4041.

[13] L. Soderholm, P.M. Almond, S. Skanthakumar, R.E. Wilson and P.C. Burns, *Angewandte Chemie International Edition*, 2008, **47**, 298-302.

[14] D.C. Bradley, R.C Mehrotra and D.P. Gaur, *Metal Alkoxides*, 1978, London Academic Press.

[15] T. Moeller, *Inorganic Synthesis*, 1957, McGraw-Hill Book Company, New York, **144**.

[16] G.R. Fulmer, A.J.M. Miller, N.H. Sherden, H.E. Gottlieb, A. Nudelman, B.M. Stolz, J.E. Bercaw and K.I. Goldberg, *Organomettallics*, 2010, **29**, 2176-2179.

[17] G.M. Sheldrick, SHELX-97, *A program for crystal structures determination*, University of Gottingen, Germany, 1997

[18] G.R. Choppin, *Marine Chemistry*, 2006, **99**, 83-92.

[19] R.F Bogucki and A.E. Martell, *Journal of the American Chemical Society*, 1958, **80**, 4170-4174.

[20] G.H. Coleman, *The Radiochemistry of Plutonium*, 1965, AEC Contract No. W-7405.

[21] A.E. Martell, R.M. Smith, *Critical Stability Constants Volume One*, 1974, Plenum Press, New York and London.

[22] A. E. Martell & R. M. Smith, *Critical Stability Constants, Volume Three: Other Organic Ligands*, 1977, Plenum Press, New York and London.

[23] G.H. Carey, R.F. Bogucki, A.E. Martell, *Inorganic Chem*istry, 1964, **3**, 1288-1295.

[24] R. Telchadder, *Spectroscopic Studies of Uranyl Solution Phase Complexation by Short Chain β-Hydroxy Carboxylic Acids,* thesis from the University of Manchester, 2010.

[25] R.D. Shannon, *Acta Crystallographica*, 1976, **A32**, 751.

[26] Z. Szabó, T. Toraishi, V. Vallet, I. Grenthe, *Coordination Chemistry Reviews*, 2006, **250**, 784-815.

[27] G. Meinrath, *Journal of Alloys and Compounds*, 1998, **275-277**, 777-781.

[28] J.J. Katz, G.T. Seaborg and L.R. Morss, The Chemistry of Actinides Elements, 2nd Ed., 1986, Vol. 2, Chapman and Hall Ltd, ISBN 0 412 27370 5.

[29] B.J. Mincher, Proceedings of the First ACSEPT International Workshop, 2010, CP FP7-EURATOM 211267.

[30] V.Neck, J.I. Kim, B.S. Seidel, C.M. Marquant, K. Dardenne, M.P. Jensen and W. Hauser, *Radiochimica Acta*, 2001, **89**, 439-446.

[31] L. Bonin, C. Den Auwer, E. Ansoborlo, G. Cote and Ph. Moisy, *Radiochimica Acta*, 2007, **95**, 371-379.

[32] S.H. Eberle and M.Th. Paul, *Journal of Inorganic and Nuclear Chemistry*, 1971, **33**, 3067-3075.

[33] W.G Van Der Sluys, J.C. Huffman, D.S. Ehler and N.N. Sauer, *Inorganic Chemistry*, 1992, **31**, 1316-1318.

[34] S. Fortier, G. Wu and T. Hayton, *Inorganic Chemistry*, 2008, **47**, 4752 – 4761.

[35] L.R. Avens, S.G. Bott, D.L. Clark, A.P. Sattelberger, J.G. Watkin and B.D. Zwick, *Inorganic Chemistry*, 1994, **33**, 2248-2256.

[36] G. Meinrath, *Journal of Alloys and Compounds*, 1998, **275-277**, 777-781.

[37] W.G. Van Der Sluys and A.P. Sattelberger, *Polyhedron*, 1990, **9**, 1843-1848.

Chapter 6:

CONCLUSIONS AND SUGGESTIONS FOR FURTHER WORK

CONCLUSION

In this thesis metal oxides were synthesised by two methods: solid state chemistry and a wet route. The latter also encouraged a parallel solution chemistry study. The experiments involved several fields of expertise (e.g. ceramics as wasteforms, synthesis of organometallic compounds in anaerobic and dry conditions, hydrolysis of actinide ions), all of them being relevant to the nuclear industry (decommissioning or waste management).

The synthesis and structural study of novel potential wasteforms ($Y_{2-x}Ce_xTi_{2-x}Fe_xO_7$ and $Y_2T_{i2-2x}Fe_xNb_xO_7$) have been reported. The $Y_{2-x}Ce_xTi_{2-x}Fe_xO_7$ system is a potential host for tetravalent actinide cations by substitution at the Y^{3+} site. Substitution of Fe^{3+} on the Ti^{4+} site was used as a charge balance. Structural investigation (XRD patterns, Mössbauer spectroscopy) confirmed that $Y_{2-x}Ce_xTi_{2-x}Fe_xO_7$ undergoes several phase transitions. Compositions with $x \leq 0.1$ adopt the pyrochlore structure. In contrast, compositions with $0.5 \leq x \leq 0.6$ adopt the unusual zirconolite-3T structure which appears to be stabilised by a 5-fold Fe^{3+} site. Compositions above $x = 0.7$ were found to comprise a mixture of zirconolite-3T and a fluorite phase (CeO_2), which were detected by SEM/EDX experiments.

The reported $Y_2T_{i2-2x}Fe_xNb_xO_7$ material is a potential host for trivalent actinide species which may be substituted in the Y^{3+} site. Compositions with $0.0 < x < 0.5$ adopt the pyrochlore structure with substitution of Fe^{3+} on the octahedral Ti^{4+} site. In contrast, compositions with $0.7 < x < 0.9$ adopt an unusual zirconolite-3T structure, which was confirmed by X-ray and neutron diffraction. Thus, as proved by Mössbauer spectroscopy, it appears that the new zirconolite 3T phase is stabilised by formation of a FeO_5 species. Compositions with $0.4 < x < 0.7$ were found to comprise a mixture of both pyrochlore and zirconolite and $x > 0.9$ consist of a zirconolite-3T and a fluorite phase.

In both the $Y_{2-x}Ce_xTi_{2-x}Fe_xO_7$ and $Y_2T_{i2-2x}Fe_xNb_xO_7$ systems, the observation of a two phase region in the phase diagram implies that the free energy of the pyrochlore and zirconolite phases must be similar.

Metal oxide ceramics can also be synthesised *via* a wet or semi-wet route. This method promotes an intimate mixture of the precursors and enhances the homogeneity of the reactants, thus minimising compositional inhomogeneities within the products. Inorganic or organic compounds can be used as precursors. This PhD project explored the synthesis of actinide alkoxides. This resulted in the preparation and characterisation of a novel monomeric homoleptic U(IV) alkoxide, $[UI(O\text{-}i\text{-}Pr)_2.(HO\text{-}i\text{-}Pr)_4]I$. Unfortunately, all attempts to obtain new actinide oxide compounds by hydrolysing $[UI(O\text{-}i\text{-}Pr)_2.(HO\text{-}i\text{-}Pr)_4]I$ *via* a Sol-Gel approach were unsuccessful. Therefore, these experiments are not reported in this thesis.

A wasteform is subject to various mechanisms that can decrease its effectiveness as a barrier to radionuclide migration. The corrosion and dissolution of wasteforms are crucial issues for the management of nuclear waste. A clear understanding of actinide hydrolysis is therefore necessary. This PhD project focussed on the hydrolysis of metal ions in the presence of an organic ligand with amino acid features relevant to the environment.

The hydrolysis of several metal ions (*e.g.* Zr (IV), Th (IV), U (IV), U (VI), Np (IV) and Np (VI)) was investigated in the presence of a polycarboxylate ligand, N-(2 hydroxyethyl)iminodiacetic acid (heidi), as part of a study that is developing models of environmentally mobile actinide colloids and cluster species. Solid state data have been reported previously for the 1:2 metal to ligand ratio, however, without any discussion of solution chemistry data. Analytical results for the same ratio have been reported here for the elements listed above.

All experiments showed complex speciation profiles where several coexisting species and fast exchange processes take place, and the behaviour is very pH dependent. An increase in solubility in the presence of heidi was observed, as it was possible to obtain analytical data for the tetravalent actinides at high pH values. Hence, the presence of the ligand is able to retain metal ions in solution in the neutral pH range, where they would otherwise precipitate. However, hydrolysis does take place for most metal ions above pH 9. Surprisingly, during the solution chemistry experiments zirconium (IV) ions seem to behave similarly to neptunium (IV). Previous solid state data reported by Heath *et al*. has suggested that under certain experimental conditions, iron (III) ions have a comparable behaviour to that of thorium (IV) ions. [1,2]

FURTHER WORK

Additional data could further elucidate the structure and bonding of $Y_{2-x}Ce_xTi_{2-x}Fe_xO_7$ materials. For instance, X-ray absorption spectroscopy (XAS) spectroscopy is sensitive to oxidation state in redox active elements. Such data could confirm that Ce is found as Ce^{4+}. Moreover, solid state ^{89}Y NMR could produce structural information on the atomic scale.

This thesis focused only on titanate ceramics, but zirconate ceramics, analogous to $Y_{2-x}Ce_xTi_{2-x}Fe_xO_7$ and $Y_2Ti_{2-x}Fe_xNb_xO_7$, should also be explored. The zirconate compounds may be structurally similar to their titanate equivalents, but the introduction of zirconium atoms in the B-site may affect intrinsic properties of the materials.

All the materials obtained via solid state chemistry in this thesis (pyrochlore, zirconolite, fluorite) are known to be chemically robust and resistant to radiation damage. Very few examples of

zirconolite-3T are reported in the literature. Therefore, it would be useful to investigate their chemical resistance and susceptibility to radiation damage effects. These features are very dependent on the ceramic formulation and co-substitutions could improve or depreciate such properties. Further investigation of their suitability as actinide hosts is consequently crucial.

New synthetic routes to obtain actinide alkoxides should be designed. Hydrolysis experiments should be pursued on potential novel actinide alkoxides and with $[UI(O\text{-}i\text{-}Pr)_2.(HO\text{-}i\text{-}Pr)_4]I$.

The ligand heidi has been shown previously to form cluster compounds with d-transition metals. Further investigation with heidi and actinide metals should be undertaken by using different bases and metal to ligand ratios. Higher nuclearity species containing metal ions of non-zero spin could have interesting magnetic properties, which could aid the understanding of the bonding of actinide ions.

Trimetallic compounds of Th (IV) and U(IV) were obtained during a similar study on cluster growth *via* controlled hydrolysis. [2] The ligand used in that case was 5-Me-HXTA, a bulkier polycarboxylic acid. The solution chemistry of this system should also be investigated in depth.

The behaviour of several metal ions with heidi showed the complexity of actinide hydrolysis. As there is still no clear understanding of "ligand controlled hydrolysis" reactions, the speciation of actinide ions with heidi other ligands should be pursued.

The table below gives the structure of this PhD and the contributions of others to the work reported in this thesis.

Chapter 1	Introduction	No other contribution
Chapter 2	Experimental Techniques and Methods	No other contribution
Chapter 3	Synthesis and Characterisation of a possible host for tetravalent actinides: $Y_{2-x}Ce_xTi_{2-x}Fe_xO_7$	Neutron data refinement – Prof Neil Hyatt Mössbauer analysis help – Dr Martin Stennet
Chapter 4	Synthesis and Characterisation of New Pyrochlore Zirconolite Solid Solutions for actinide immobilisation: $Y_2Ti_{2-2x}Fe_xNb_xO_7$	Neutron data refinement – Prof Neil Hyatt Mössbauer analysis help – Dr Martin Stennet TEM - Dr Martin Stennet SQUID – Dr Floriana Tuna

Chapter 5	Oligomeric Complexes of Actinides Formed Through Ligand Controlled Hydrolysis and the Preparation of a Novel Uranium (IV) Iodo Isopropoxide Isopropanol	Single crystal refinement help – Dr Sarah Heath
Chapter 6	Conclusions and Further Work	No other contribution

[1] J.C. Goodwin, R.Sessoli, D. Gatteschi, W. Wernsdorfer, A.K. Powell and S.L. Heath, *Journal of the Chemical Society*, *Dalton Transactions*, 2000, **12**, 1835-1840.

[2] C.M. Mydlowski, *Aminopolycarboxylate complexes of d- and f- block metal ions: a synthetic and structural study*, Thesis of The University of Manchester, 2009.